2019

Development of Diffusion MRI Methodology to Quantify White Matter Integrity Underlying Post-Stroke Anomia

Emilie Tuijnder McKinnon
Medical University of South Carolina

DEVELOPMENT OF DIFFUSION MRI METHODOLOGY TO QUANTIFY WHITE MATTER INTEGRITY UNDERLYING POST-STROKE ANOMIA

A dissertation
presented to
the academic faculty

By

Emilie Tuijnder McKinnon

In partial fulfillment
of the requirements for the degree
Doctor of Philosophy in Biomedical Imaging

Department of Neurology

College of Graduate Studies
Medical University of South Carolina

June 2019

DEVELOPMENT OF DIFFUSION MRI METHODOLOGY TO QUANTIFY WHITE MATTER INTEGRITY UNDERLYING POST-STROKE ANOMIA

A dissertation presented to the academic faculty

By

Emilie Tuijnder McKinnon

In partial fulfillment of the requirements for the degree Doctor of Philosophy in Biomedical Imaging

Department of Neurology
College of Graduate Studies
Medical University of South Carolina
June 2019

Approved by:

Leonardo Bonilha, MD, PhD
Chairman Advisory Committee
Medical University of South Carolina

Chris Rorden, PhD
University of South Carolina

Jens H. Jensen, PhD
Co-chairman Advisory Committee
Medical University of South Carolina

Steven Kautz, PhD
Medical University of South Carolina

Julius Fridriksson, PhD
University of South Carolina

Andy Y. Shih, PhD
Seattle Children's Research Institute

Joseph A. Helpern, PhD
Medical University of South Carolina

Date Approved: June 27, 2019

Nothing in life is to be feared, it is only to be understood. Now is the time to understand more, so that we may fear less.

Marie Curie

I would like to dedicate this dissertation to the teachers who inspired me.

You are appreciated.

ACKNOWLEDGEMENTS

To say it takes a village to write a PhD thesis would be an understatement. First, I want to sincerely express my gratitude to my mentors. Jens, I will forever be grateful for all the physics knowledge you patiently shared with me over the last few years. You never made me feel inadequate and you always made time to answer my (many) questions - Thank you! Leo, thank you for teaching me to always keep an eye on application. You helped me with the decision to pursue (and keep pursuing) the MD-PhD, and I am positive I will increasingly understand your points of view throughout medical school. I also want to thank you for your patience, I realize I can be very opinionated and you were always happy to discuss things at length. Joe, I will never forget how we met 5 years ago, you took a chance on me and rekindled my passion for science. I am forever grateful for that. The lab environment you created is truly inspirational, and I am honored to have been a part of it. One day, I hope to model my lab after your own. Thank you for always being there for me when I needed advice or a shoulder to cry on. In many ways, I really have considered you a father figure. Thank you.

Second, I need to thank my family. Jared, there are no words that express how much I appreciate you. You motivate me when times get rough, you care for me when I am overwhelmed, you always know just what I need - you really are my “rots in the branding”. I know you will always be rooting for my success, and I could not have done this without your support. Mom and dad, thank you for making me the person I am today. Dad, I am so grateful for having inherited your scientific curiosity and your rigor. You have been an inspiration to me throughout this journey. Mom, you taught me to always aim high, and that there is nothing I can not do. You taught me to take opportunities as they arise, speak up when I need to be heard, and make friends along the way. I would not be where I am today without you. Big sister, being separated from you the last 5 years has been rough, I miss you more than you know. However, I know that I can always count on you for anything.

Please know that I admire your resilience, your view on life, and that I look up to you. Thank you for your unwavering support, and I hope we will be together again soon. My "little" brothers, I am so proud of how far you have come and how much you have grown. I hope I have set a good example for you and that you are proud to follow in my footsteps. Luc, Birgit, know that I love and appreciate you too, and that I miss all of you very much.

A third group of people that deserve more thanks that I can give is the many friends I made since coming to Charleston. Thank you all so much for being there when I needed to forget this dissertation. Maggie and Corinne, thank you for taking me for a night on the town and for letting me vent a little (or sometimes a lot). Kayti, Andrew, and Sid, you are more friends to me than colleagues, thank you for always making it a joy to come to work and for providing me with the many laughs on slack. In addition, I want to thank you for coming to me with all your questions, I am proud and humbled that you turn to me for advice and I love working with all of you! Hunter, it has been a pleasure to brain storm together. Sorry if I wasn't always as patient as I should have been, but I am sure you will take all our projects to the next level! Last but not least, I want to thank my roller derby team. Thank you, for being patient with me when I needed to spend time on work, for helping me let out my frustrations on the track, and for just being the best of friends. Thank you.

Lastly, I want to thank my committee for all the feedback they provided and for taking the time to read this work. I want to thank Dr. Dubno for the financial support, thank Truman and the MSTP for putting together this amazing educational environment, and thank all the other members from the lab for their support and advice.

Thank you again,
Emilie

TABLE OF CONTENTS

Acknowledgments v

Acronyms xii

Symbols xviii

List of Tables xix

List of Figures xxi

Summary xxxiv

Chapter 1: Diffusion Weighted Magnetic Resonance Imaging and the Measurement of White Matter Microstructure 1

1.1 Introduction 1

1.2 Diffusion Magnetic Resonance Imaging 2

1.2.1 General principles 2

1.2.2 Pure Physics Parameters 7

1.2.3 Tissue Modeling Parameters 13

1.3 Tractography 19

1.4 Clinical Applications of dMRI 21

1.5 Challenges and Unanswered Questions 22

Chapter 2: Current Understanding of Naming and Naming Impairments after Stroke 24

2.1 Introduction 24

2.2 Word Production 25

2.2.1 Cognitive Theory: The Lemma Model 25

2.2.2 Neurobiological Theories 27

2.3 Anomia 32

2.4 Magnetic Resonance Imaging and the Study of Anomia 34

2.4.1 Structural Imaging: T1-weighted and T2-weighted MRI 34

2.4.2 Functional Magnetic Resonance Imaging 36

2.4.3 Diffusion Weighted Magnetic Resonance Imaging 36

2.5 Challenges and Unanswered Questions 37

Chapter 3: Impact of Regional White Matter Integrity on Post-Stroke Linguistic Deficits Underlying Anomia and Anomia Recovery 39

3.1 Introduction 39

3.2 Types of Naming Errors in Chronic Post-Stroke Aphasia are Dissociated By Dual Stream Axonal Loss 40

3.2.1 Introduction 40

3.2.2 Materials and Methods 43

3.2.3 Results 52

3.2.4 Discussion 57

3.3 Neuroplasticity: Structural Plasticity of the Ventral Stream and Aphasia Recovery 63

3.3.1 Introduction 63

3.3.2 Material and Methods 64

3.3.3 Results 65

3.3.4 Discussion 67

3.4 Perilesional White Matter Microstructure and Aphasia Recovery 70

3.5 Synergism between cortical damage and white matter disconnection contributes to aphasia severity 71

3.6 Development of a Neuroimaging Pipeline Optimized for the Study of Whole Brain White matter Integrity Post-Stroke 73

Chapter 4: Validation, Development, and Optimization of a Novel Tissue Model using Direction-Averaged High b-value Diffusion MRI 75

4.1 Introduction 75

4.2 Dependence on b-Value of the Direction-Averaged Diffusion-Weighted Imaging Signal 77

4.2.1 Introduction 77

4.2.2 Material and Methods 78

4.2.3 Results 83

4.2.4 Discussion 88

4.2.5 Conclusion 92

4.3 Modeling White Matter Microstructure with Fiber Ball Imaging 92

4.3.1 Introduction 92

4.3.2 Theory 94

4.3.3 Methods 102

4.3.4 Results 105

4.3.5 Discussion 113

4.3.6 Conclusion . . . 118

4.4 Measuring Intra-Axonal T_2 in White Matter With Direction Averaged Diffusion MRI . . . 119

4.4.1 Introduction . . . 119

4.4.2 Theory . . . 120

4.4.3 Methods . . . 122

4.4.4 Results . . . 125

4.4.5 Discussion and Conclusions . . . 130

4.5 Simple Scheme for Correcting Bias in Axonal Water Fraction due to Differences in Compartmental Transverse Relaxation Times . . . 135

4.5.1 Introduction . . . 135

4.5.2 Methods . . . 136

4.5.3 Results . . . 137

4.5.4 Discussion . . . 137

Chapter 5: The Advantages of Studying Post-Stroke White Matter Integrity with Fiber Ball imaging and the Fiber Ball White Matter Model . . . 140

5.1 Introduction . . . 140

5.2 Microstructure . . . 141

5.3 Tractography . . . 142

5.4 Limitations: Case Study - Power-law fits for direction-averaged diffusion MRI signal in neonatal brain as a function of b-value . . . 144

Chapter 6: Overall Conclusion . . . 150

Appendix A: Section 3.2 . . . 154

Appendix B: Section 4.3 158

Appendix C: Section 4.4 160

Appendix D: Publications 161

D.1 Publications in Journals 161

D.1.1 Related to Dissertation 161

D.1.2 Unrelated to Dissertation 162

D.2 Publications in Conference Proceedings 162

D.2.1 Oral Presentations 162

D.2.2 Abstracts 163

References 184

ACRONYMS

ACR Anterior Corona Radiata. 124, 133

AD Axial Diffusivity. 10

AFQ Automated Fiber Quantification. 49, 50, 64, 65

AG Angular Gyrus. 51, 72

AIC Akaike Information Criterion. xxxi, 145, 146, 148

AK Axial Kurtosis. 11

ALIC Anterior Limb of the Internal Capsule. 124

AWF Axonal Water Fraction. xx, xxiii, xxiv, xxvii, xxviii, xxx, xxxiv, 15, 17–19, 42, 43, 45, 46, 49–54, 56–58, 60–62, 76, 93, 95, 98–101, 103, 104, 106, 109, 112, 114, 116–118, 136–139, 142, 151

BCC Body of the Corpus Callosum. 124

BOLD Blood Oxygen Level Dependent. 36

CHARMED Composite Hindered and Restricted Model of Diffusion. 13, 14, 23

CSF Cerebro Spinal Fluid. xxiii, 17, 34, 35

DKE Diffusional Kurtosis Estimator. 47, 48, 64, 70, 103, 123

DKI Diffusional Kurtosis Imaging. xx, xxi, xxiii, xxv, xxvii, xxxiii, xxxiv, 7, 8, 10–12, 14, 16, 19, 37, 39, 40, 42, 43, 45–47, 49, 63, 64, 73, 99, 103, 104, 106, 108, 109, 111–113, 116

dMRI Diffusion Magnetic Resonance Imaging. xxi, xxix–xxxiv, 1, 6, 7, 12–14, 17, 19, 21–23, 34, 36, 42, 43, 45–47, 58–60, 63, 67, 71, 73, 76, 78, 92–97, 99–101, 113–120, 122, 125, 128, 130–132, 134–138, 140–147, 150–152

dODF diffusion Orientation Distribution Function. xxi, xxiii, 11, 12, 19, 46, 47

DSI Diffusion Spectrum Imaging. 7

DTI Diffusion Tensor Imaging. xxi, xxiii, xxxi, 1, 7, 8, 10, 12, 19, 46, 47, 72, 99, 100, 103, 113, 143

DWI Diffusion Weighted Images. 11, 18, 45, 47, 73, 76–78, 88, 91, 102, 103

EC External Capsule. 124

EEG Electroencephalogram. 34

EM Electron Microscopy. 1

EPI Echo Planar Imaging. 5

FA Fractional Anisotropy. xxvi–xxxi, 9, 21, 22, 42, 43, 45, 48–53, 56, 57, 64, 65, 67, 70, 74, 78, 84, 86, 88, 89, 98, 103–105, 107–111, 123, 125–128, 130, 131, 139, 141, 146, 148, 149

FAA Fractional Anisotropy for the Axons. xxvii, xxviii, xxx, 98, 107–111, 142, 159

FBI Fiber Ball Imaging. xx, xxvii, xxviii, xxxi, xxxiv, 13, 17–19, 23, 75, 76, 93–96, 98–101, 104–111, 113, 115–118, 140–144, 151

FBWM Fiber Ball White Matter. xx, xxvii, xxviii, xxx, xxxiv, 76, 94, 95, 100, 101, 103–113, 115–118, 136–138, 140–142, 144, 151, 152

fMRI functional Magnetic Resonance Imaging. 30, 34, 36, 51, 59

fODF fiber Orientation Distribution Function. 17, 19, 20, 76, 93, 95, 97, 98, 103, 113, 116, 143

FOV Field of View. 45, 64, 79, 82, 102, 122, 136, 145

FSL FMRIB Software Library v5.0. 47, 48

GA Gestational Age. 144

GCC Genu of the Corpus Callosum. 123

HARDI High Angular Resolution Diffusion Imaging. xxvi, xxviii, 75, 77, 78, 86, 87, 93, 96, 97, 99, 102, 103, 105, 112, 114, 117, 118

HCP Human Connectome Project. xxvii, 82, 87–90

IFG Inferior Frontal Gyrus. 28, 51

IFOF Inferior Frontal-Occipital Fasciculus. 61, 143

ILF Inferior Longitudinal Fasciculus. xx, xxiii–xxv, xxxiii, 46–48, 50–54, 56–61, 63–69, 72, 73, 143

IRB Institutional Review Board. 43, 122

ITG Inferior Temporal Gyrus. xxiv, 58, 59, 72

JHU Johns Hopkins University. 47–51, 61, 64, 72, 73, 80, 137

MD Mean Diffusivity. xxvii, 10, 65, 70, 74, 101, 103, 108, 109, 111, 123

MK Mean Kurtosis. xxvii, 11, 65, 74, 103, 104, 108, 109, 111, 123

MPRAGE Magnetization-Prepared Rapid Gradient Echo. xxvi, 79, 80, 82, 84, 86, 88, 102

MR Magnetic Resonance. 4, 18, 34

MRI Magnetic Resonance Imaging. xxii, xxv, 1, 3–5, 15, 22, 23, 34, 37, 64, 68, 70–72, 78, 119, 121, 122, 141, 144, 160

MTG Middle Temporal Gyrus. xxiv, 31, 51, 58–60, 72

NAA N-acetyl-L-aspartate. 90

NODDI Neurite Orientation Density and Dispersion Imaging. 13, 14, 17, 23

PCR Posterior Corona Radiata. 124

PDF Probability Distribution Function. 2, 7, 10

PET Positron Emission Tomography. 34

PGSE Pulsed Gradient Spin Echo. xxi, 3, 5, 6

PLIC Posterior Limb of the Internal Capsule. 123, 126, 133

pMFG posterior Middle Frontal Gyrus. 51

pMTG posterior Middle Temporal Gyrus. 51, 72

PNT Philadelphia Naming Test. 33, 44, 52

PPT Pyramids and Palm Trees Test. 44, 52

pSTG Posterior Superior Temporal Gyrus. 51, 72

PTR Posterior Thalamic Radiation. 123, 124

RD Radial Diffusivity. 10, 70

RF Radio Frequency. 5

RK Radial Kurtosis. 11, 70

ROI Region of Interest. xxvi, xxvii, xxxi, 20, 21, 40, 48, 50, 51, 72, 74, 80–84, 86–89, 145–149

SCC Splenium of the Corpus Callosum. 124

SCR Superior Corona Radiata. 124

SLF Superior Longitudinal Fasciculus. xx, xxiv, xxxiii, 47, 48, 50–54, 56–61, 73, 124, 143

SLP Speech Language Pathologists. 33, 44

SMG Supra Marginal Gyrus. xxiv, 29, 51, 57, 59, 72

SNR Signal to Noise Ratio. xxviii, 80, 83, 87, 88, 105, 111–113, 117

SPM Statistical Parametric Mapping. 48, 64, 72, 79

SPT Sylvian Temporal-Parietal. 32, 61

STG Superior Temporal Gyrus. xxiv, 29, 51, 59, 72

tDCS Transcranial Direct Current Stimulation. xxv, 70, 71

TE Echo Time. 45, 64, 76, 79, 82, 90, 102, 122–126, 129, 134–137, 145

TI Inversion Time. 45, 79, 82, 102

TMS Transcranial Magnetic Stimulation. 34

TR Repetition Time. 45, 64, 79, 82, 102, 122, 136

VLSM Voxel-based Lesion Symptom Mapping. 35, 36, 59, 141

WAB-AQ Western Aphasia Battery - Aphasia Quotient. 52, 70, 72

WAB-R Western Aphasia Battery-Revised. 44, 70, 72

WMTI White Matter Tract Integrity Model. xxi, xxviii, 13–15, 17, 23, 49, 62, 76, 94, 104, 105, 107, 110, 116–118

SYMBOLS

D_a Intra-axonal diffusivity. xxvii, xxviii, xxx, 15, 17, 18, 76, 81, 82, 91, 93, 95, 97–99, 101, 103, 104, 107–114, 117, 120, 121, 124, 129, 131, 137, 158, 160

$D_\perp$ Radial Diffusivity. 10, 104, 109, 111

$D_\parallel$ Axial Diffusivity. xxviii, 10, 103, 109, 111, 113

$D_{e,\perp}$ Extra-Axonal Radial Diffusivity. xxvii, xxviii, 16, 101, 103, 104, 107–111

$D_{e,\parallel}$ Extra-Axonal Parallell Diffusivity. xxvii, xxviii, 16, 101, 103, 104, 107–111, 117

D Diffusion Coefficient. xxi, 2, 3, 5–9, 46

G Gradient Strength. 6

$K_\perp$ Radial Kurtosis. 11

$K_\parallel$ Axial Kurtosis. 11

K Diffusional Kurtosis. 7, 10, 11, 46

T_1 Longitudinal Relaxation Time. xxiii, xxvi, xxvii, 34, 35, 70, 72, 73, 86, 89, 141

T_2 Transverse Relaxation Time. x, xxi, xxiii, xxx, xxxiv, 5, 6, 22, 34–36, 70, 72, 76, 117, 119, 121, 130, 131, 133, 135–139, 141, 143, 151

T_{2a} Intra-axonal Transverse Relaxation Time. xxix, xxx, 76, 119–139, 160

T_{2e} Extra-axonal Transverse Relaxation Time. xxx, 76, 121, 124, 127, 128, 131, 134–139, 160

Δ Time between diffusion gradients. 6, 136

α Tortuosity. 16

$\bar{D}_e$ Mean Extra-Axonal Diffusivity. xxvii, xxviii, 93, 101, 103, 104, 107–113, 142

$\bar{D}$ Mean Diffusivity. 10, 21, 22, 43, 64, 65, 67, 101, 137

$\bar{K}$ Mean Kurtosis. xxv, 11, 64–69, 137

$\boldsymbol{D_a}$ Intra-axonal Diffusion Tensor. 14–16, 19, 97–99, 158, 159

$\boldsymbol{D_e}$ Extra-axonal Diffusion Tensor. 14, 16, 19, 95, 99, 101, 103

δ Pulse Width. 5, 6, 136

γ Gyromagnetic Ratio. 6

D Diffusion Tensor. xxvii, 8–12, 22, 99, 101, 103, 104, 113

W Kurtosis Tensor. 11, 15

ζ Zeta. xxvii, xxviii, 18, 86, 87, 98, 99, 101, 103, 104, 107–113, 116, 117

f Axonal Water Fraction. xxvii, xxviii, xxx, 15, 16, 18, 81, 82, 91, 95, 98–101, 103, 104, 107–114, 117, 129, 135–137, 139, 160

t Diffusion time. 2

r 3D vector describing a position in space (x,y,z). 2, 3

LIST OF TABLES

3.1 Summary of all correlation coefficients between average AWF, calculated along the length of the ILF and the SLF, and both phonemic and semantic paraphasias. (* p<0.05, corrected for multiple comparisons) 54

3.2 Summary of all correlation coefficients between FA, calculated along the length of the ILF and the SLF, and both phonemic and semantic paraphasias. (* p<0.05, corrected for multiple comparisons) 55

4.1 Estimates for the exponent α and the scale constant C obtained by fitting Equation 4.3 to the direction-averaged DWI data from the six b-value shells for each of the subjects and the considered anatomical regions. The quality of the fits is indicated by the coefficient of determination R^2, and the uncertainties, in parentheses, indicate standard errors as determined with linear regression. 85

4.2 Mean values ($\pm$ std. dev.) of diffusion parameters in white matter as estimated with DKI, FBI, and FBWM. *Estimated with DKI. †Estimated with FBI. ‡Estimated with FBWM. 111

A.1 Subject demographics and language battery results. (M=male; F=female) . 155

A.1 Subject demographics and language battery results. (M=male; F=female) . 156

A.1 Subject demographics and language battery results. (M=male; F=female) . 157

LIST OF FIGURES

1.1 The displacement probability distribution function: Gaussian free diffusion (in blue) and restricted non-Gaussian diffusion (in red). 3

1.2 Famous analogy for the spin echo phenomenon given by Hahn in 1953 on the cover of physics today (drawing by Kay Kaszas) [6]. "*Cover art from Physics Today 6.11 (1953) reproduced with the permission of the American Institute of Physics.*" 4

1.3 (a) Top: Diagram of the PGSE experiment. Bottom: The phase-evolution of the spins. (b) Raw dMRI image. Voxel A has a higher D than voxel B (in the direction of the gradient pulse) resulting in a difference in signal intensity. Assuming the voxels have a similar T_2. 6

1.4 Comparison of DTI and DKI fitting models. For DTI, the logarithm of diffusion-weighted signal intensity (circles) as a function of the b-value is fit, for small b-values, to a straight line. In brain, this fit is often based on the signal for $b = 0$ and $b = 1000\,\mathrm{s/mm^2}$. For DKI, the logarithm of the signal intensity is fit, for small b-values, to a parabola. In brain, this fit may be based on the signal for $b = 0$, $b = 1000$, and $b = 2000\,\mathrm{s/mm^2}$. *Reproduced from Jensen, Jens H., and Joseph A. Helpern. "MRI quantification of non-Gaussian water diffusion by kurtosis analysis." NMR in Biomedicine 23.7 (2010): 698-710 with the permission of John Wiley and Sons.* 8

1.5 An example of a Gaussian dODF (left) and a kurtosis dODF (right). The amplitude of the dODF reflects the likelihood of diffusion in each direction. The direction of the dODF maxima is commonly considered to equate to the direction of the underlying fiber bundle. By definition, Gaussian dODFs are limited to one maximum. The kurtosis dODF can have multiple maxima and thus represent voxels with multiple fiber bundles. 12

1.6 Graphical representation of the output parameters from the WMTI model. *Figure created by Andreana Benitez, PhD (reprinted with permission).* . . . 15

1.7 Illustration of a set of Watson distributions with the same mean orientation but different orientation dispersion index: $OD = [0.04, 0.16, 0.5, 0.84, 1.0]$. The Watson distribution is cylindrically symmetric, hence showing only the cross-sectional view through the symmetry axis which coincides with its mean orientation. *Reproduced from J. Zhang, Hui, et al. "NODDI: practical in vivo neurite orientation dispersion and density imaging of the human brain." Neuroimage 61.4 (2012): 1000-1016. with the permission of Elsevier.* 18

1.8 Example of whole brain fiber tractography. 19

1.9 Wholebrain tracking can be launched from the white matter (left) or from the white mattergray matter interface, where the fibers are known to originate from (right). *Reproduced from Jeurissen, Ben, et al. "Diffusion MRI fiber tractography of the brain." NMR in Biomedicine 32.4 (2019): e3785. with the permission of John Wiley and Sons.* 21

1.10 The number of publications on PubMed with the key words diffusion and MRI 23

2.1 Serial two-system architecture of the Lemma model: the two stages of lexical selection and three stages of form encoding [40]. *Reproduced from Levelt, Willem JM. "Spoken word production: A theory of lexical access." Proceedings of the National Academy of Sciences 98.23 (2001): 13464-13471. Copyright (2001) National Academy of Sciences, U.S.A* 25

2.2 Form encoding of the word *horses*. (left) The upper stratum shows nodes representing morphemic phonological codes and their phonemic spellouts. The lower stratum shows nodes representing syllabic articulatory scores. (right) Corresponding form-processing stages. ω = phonological word; σ = syllable [40]. *Reproduced from Levelt, Willem JM. "Spoken word production: A theory of lexical access." Proceedings of the National Academy of Sciences 98.23 (2001): 13464-13471. Copyright (2001) National Academy of Sciences, U.S.A* 26

2.3 Wernicke-Lichtheim-Geschwind "house" model. *Reproduced from On aphasia. By L. Lichtheim, MD, Professor of Medicine in the University of Berne. Brain 1885; 7: 433484.* 28

2.4 Top row: Location of Broca's area (left) and Wernicke's area (right) that received the most votes in a survey done by the society for the neurobiology of language. Bottom row: Original location as put forward by Broca (left) and Wernicke (right). Numbers in the bottom left corner represent the percentage of votes received. *Figure is an adapted version of figure 2 and figure 3 from Tremblay, Pascale, and Anthony Steven Dick. "Broca and Wernicke are dead, or moving past the classic model of language neurobiology." Brain and language 162 (2016): 60-71. with permission from authors* 29

2.5 An emerging picture of perisylvian long association fiber pathways supporting language. The image on the left shows the "classic" arcuate fasciculus. The image on the right shows the additional fiber pathways that possbily support language. *Reproduced from Tremblay, Pascale, and Anthony Steven Dick. "Broca and Wernicke are dead, or moving past the classic model of language neurobiology." Brain and language 162 (2016): 60-71. with the permission of Elsevier.* 31

2.6 Anatomical location of regions involved in word naming. As proposed by the dual stream model of language (left) and the Levelt model (right). *Figure on the left is an adapted version of Figure 1 from Hickok, Gregory, and David Poeppel. "The cortical organization of speech processing." Nature reviews neuroscience 8.5 (2007): 393., with permission from authors and the Figure on the right is an adapted version of Figure 5 from Indefrey, Peter, and Willem JM Levelt. "The spatial and temporal signatures of word production components." Cognition 92.1-2 (2004): 101-144.* 32

2.7 Liquids like CSF have long T_1 and T_2 relaxation times resulting in a bright appearance on a T_2-weighted image (right) and a dark appearance on a T_1-weighted image (left). 35

3.1 A: DKI allows for voxel-wise estimation of the number of fiber directions through the calculation of a kurtosis dODF, while the dODF estimated from DTI provides only a single direction. B: The AWF is the voxelwise ratio of intra-axonal water (orange) to the total water content (orange+blue). C: (Left) The ILF estimated using kurtosis-based deterministic tractography with streamlines color-coded according to directionality. (Right) The ILF color-coded according to the underlying AWF values. Augmenting tractography with microstructural information paints a more complete picture of the underlying environment. 46

3.2 Image processing pipeline used to construct the average SLF and ILF for a representative individual. Individual seedmasks (left) for the ILF (beige) and the SLF (pink) were constructed and used as starting points for deterministic tractography. Lesioned voxels (blue) were excluded from each seedmask. The tractography results were cropped (middle), averaged and divided into 4 different segments (right) in each of which we calculated the average AWF 50

3.3 Scatterplots demonstrating the relationship between AWF and percent semantic paraphasias. Average AWF was calculated for different segments of equal size along the length of the ILF. A significant association was seen between the AWF and semantic paraphasias in the two most posterior segments (I & II; r=-0.67, r=-0.63) (after correction for multiple comparisons). 53

3.4 Scatterplots demonstrating the relationship between AWF and percent phonemic paraphasias. Average AWF was calculated for different segments along the length of the SLF. A significant association was seen between the AWF and phonemic paraphasias in the two most posterior segments (I; r=-0.68) (after correction for multiple comparisons). 56

3.5 Left: Semantic paraphasias have been associated with damage to a multitude of temporal gray matter regions (e.g., temporal pole, STG, ITG, and MTG) [101, 65, 99, 62, 102, 63]. Here, we demonstrated that axon density of the ILF relates to the frequency of semantic paraphasias in individuals with post-stroke aphasia. The ILF interconnects these gray matter regions [103] likely supporting parts of a semantic network [66]. Right: Damage to the Precentral Gyrus, Postcentral Gyrus and the SMG has been shown to result in phonemic paraphasias [61, 62, 66, 67]. These areas are interconnected primarily through the SLF and arcuate fasciculi, which bridge perisylvian frontal, parietal, and temporal cortices. A greater degree of axonal loss in the posterior SLF related to a larger number of phonemic paraphasias. 59

3.6 Along-tract diffusion metrics (y-axis) are demonstrated along equally spaced measurement points in the ILF (0 to 100, anterior to posterior) (x-axis). The solid line represents the average patient value, with the standard error of the mean shown as the shaded area. Ipsilesional ILF values are shown in dark gray, and contralesional ILF values are shown in light gray. The rightmost image illustrates an example of a participants core right and left ILF. 66

3.7 The relationship between along-tract ILF $\bar{K}$ values and the chronic stroke lesion (in pink). A. The data from one representative participant is shown in a lateral view to demonstrate the lowest $\bar{K}$ in perilesional areas (color bar). B. The ILF and the lesion are shown for this subject (panel A) and all others using medial views to illustrate their anatomical relationship. Note that the lesion was excluded from the seeding mask during ILF tractography. 66

3.8 A. (top) The scatter plot demonstrates the relationship between pre- to post-therapy changes in $\bar{K}$ measured at the ILF bottleneck, and pre- to post-therapy changes in semantic paraphasias ($r = -0.90$ and $p < 0.05$ corrected). A. (bottom) Table summarizing $\bar{K}$ values for the four MRI acquisitions for all subjects. The table also includes individual changes in the number of semantic paraphasias with treatment (in number of words) and the percent overlap between the stroke lesion and the ILF. The scatterplot in A (top) depicts the relationship between change $\bar{K}$ (second to last column) and change in semantic paraphasias (last column). (BL=baseline; FU=follow-up; MK=mean kurtosis) B. Pre- and post-treatment $\bar{K}$ values along the ILF from a representative participant are shown anatomically. The ILF bottleneck, which is marked with a black arrow, demonstrates an increase in $\bar{K}$ towards normal values from before to after therapy. The stroke lesion is demonstrated in pink. This participant demonstrated a 55% improvement in semantic errors. 68

3.9 Perilesional axial diffusivity (left) and kurtosis (right) significantly related to changes in correct response ($r = 0.47$, $p < 0.05$; $r = -0.49$, $p < 0.05$) correcting for lesion size, pre-treatment aphasia severity and tDCS application. 71

3.10 Proposed new neuroimaging pipeline optimized for the study of whole brain white matter integrity post-stroke. Left: Tractography starts and ends at the gray/white matter boundary. The boundary is segmented into different cortical regions as determined by a predefined atlas. Middle: Deterministic DKI-based tractography is executed for each pair of gray matter ROIs. All tracts belonging to the same pair of ROIs are colored with the same color. This example shows left hemisphere tractography only. All fibers are subsequently divided into 100 equidistant segments $[1 - 100]$. Right: The average DKI metrics are calculated for each segment and are stored in a 100 different matrices. Each matrix elements (i,j) contains the value for the connection between gray matter ROI i and gray matter ROI j. 73

4.1 Locations of the seven ROIs considered in the quantitative analysis superimposed on the average $b0$ image for one subject. Each ROI represents the core of a different anatomical region. Cerebellar peduncle (violet), splenium (cyan), internal capsule (blue) and frontal white matter (green) are all regarded as white matter regions, for the purposes of this study, while cerebellar gray matter (red), putamen (yellow) and thalamus (white) are classified as gray matter. 81

4.2 (a) Log-log plot showing the relationship between the direction-averaged DWI signal $\bar{S}$ from each ROI (normalized by dividing by the signal without diffusion weighting, S_0) and the six b-values (1000, 2000, 3000, 4000, 5000 and $6000\,\mathrm{s/mm^2}$) for all the ROIs of Subject 1. The reference b-value b_1 is set to $1000\,\mathrm{s/mm^2}$. The error bars show the standard deviations of the measurements. The fits to Equation 4.1 for white and gray matter regions are indicated by solid and dashed lines, respectively. (b) Linear scale plot showing the same data, but without normalization and error bars in order to better demonstrate the quality of the fits. WM = white matter; GM = gray matter. 83

4.3 Parametric maps of the exponent α for a single axial slice from each subject. For reference, the corresponding FA and a similar MPRAGE (T_1) images are also shown. In white matter, α is close to 0.5, while for gray matter regions the exponent is consistently larger. 86

4.4 Axial maps of estimates for the quantity ζ, as given by Equation 4.1, for a single human subject as a function of the b-value. From the theory of Ref. 10, the estimates in white matter are expected to converge, for large b-values, to a level that is characteristic of the tissue microstructure. The scale bar is in units of $ms^{1/2}/\mu m$. 87

4.5 (a) The quantity ζ for the four white matter ROIs as estimated with Equation 4.1 and the HARDI data for b = $4000\,\mathrm{s/mm^2}$. (b) Mean ζ values for all the white matter ROIs as a function of the b-value. The mean values for b = 4000, 5000, and $6000\,\mathrm{s/mm^2}$ are all similar, in consistency with the theory of Reference [29]. All error bars indicate standard deviations. SP = splenium; CP = cerebellar peduncle; FWM = frontal white matter; IC = internal capsule. 87

4.6 (a) Log-log plot showing the relationship between the direction-averaged DWI signal $\bar{S}$ from each ROI (normalized by dividing by the signal without diffusion weighting, S_0) and the four b-values (1000, 3000, 5000, $10.000\,\mathrm{s/mm^2}$) for all the ROIs in the HCP dataset (Similar to Figure 4.2a). (b) The exponent α for each ROI and subject. The HCP estimates are similar to those from the primary dataset. (c) Parametric maps of the exponent α and FA for a single axial slice from the HCP dataset. A similar T_1 slice is provided as an anatomical reference. All error bars indicate standard deviations. SP = splenium; CP = cerebellar peduncle; FWM = frontal white matter; IC = internal capsule, TH = thalamus, PU = putamen, CGM = cerebellar gray matter. 89

4.7 Flow chart showing the data analysis pipeline for FBWM. The parameters c_{2l}^m and ζ are determined with FBI, while the total diffusion tensor **D** is found with DKI. The cost function $C(f)$ is then constructed from c_{2l}^m, ζ, and **D**. By minimizing $C(f)$, one obtains a best estimate for the AWF. Finally, the AWF, together with the FBI and DKI results, is used to calculate the additional microstructural parameters of D_a, $\bar{D}_e$, $D_{e,\parallel}$, and $D_{e,\perp}$. 104

4.8 Representative FBWM cost functions for three individual voxels from the splenium of the corpus callosum (SP), frontal white matter (FW), and the internal capsule (IC). The only adjustable parameter in the cost function is the AWF, since all other quantities are fixed with information supplied by DKI and FBI. For most white matter voxels, the cost function has a single local minimum, as illustrated here. 106

4.9 Parametric maps for selected diffusion measures from a single anatomical slice for Subject 1. Two independent datasets (Runs 1 and 2) were acquired within a single scan session in order to test reproducibility. The parameters in Columns 1 and 3 were calculated with DKI (MD, FA, MK) and FBI (ζ, FAA), while the parameters in Columns 2 and 4 were calculated with FBWM. The corresponding maps for Run 1 and Run 2 are fairly similar for all metrics, indicating that they are not overly sensitive to signal noise. The calibration bars for the diffusivities (MD, D_a, $\bar{D}_e$, $D_{e,\parallel}$, $D_{e,\perp}$) are in units of $\mu m^2/ms$, and the calibration bar for ζ is in units of $\sqrt{ms}/\mu m$, while all other quantities (FA, MK, FAA, f) are dimensionless. The FBI and FBWM results are only meaningful in white matter regions. 108

4.10 Median absolute percent difference between Runs 1 and 2 for selected diffusion measures in white matter. These were calculated for all three subjects on a voxelwise basis by using all voxels considered as white matter (i.e., MK ≥ 1). In most cases, the percent difference is about 10% or less. However, the extra-axonal diffusivites ($\bar{D}_e$, $D_{e,\parallel}$, $D_{e,\perp}$) differed by up to 20% for Subject 3. All quantities were obtained with either DKI (MD, FA, MK), FBI (ζ, FAA), or FBWM (f, D_a, $\bar{D}_e$,$D_{e,\parallel}$,$D_{e,\perp}$). 109

4.11 Selected diffusion measures versus FA. All white matter voxels for all three subjects and both imaging runs were pooled. The solid data points are averages calculated with either FBI (ζ, FAA) or FBWM (f, ζ/f, D_a, $\bar{D}_e$, $D_{e,\parallel}$, $D_{e,\perp}$), while the open data points are all averages calculated with WMTI. The error bars indicate standard deviations. For the FBI/FBWM parameters, D_a,$\bar{D}_e$, and ζ/f vary little with FA, but an FA dependence is discernible for the other metrics. The WMTI averages are relatively close to the FBI/FBWM values for ζ, $\bar{D}_e$, and $D_{e,\perp}$, at least for FA > 0.5 where the assumptions underlying WMTI are better justified. Otherwise substantial differences are apparent. In particular, the WMTI estimates for D_a are much smaller than the FBWM estimates over the full range of FA 110

4.12 Numerical simulations of the effect of signal noise on parametric maps of the AWF and the intrinsic intra-axonal diffusivity for a single anatomical slice. The ground truth data are based on the signal model of Equations 4.25 together with the FBWM fits for Subject 1 (same slice as in Figure 3.8). Rician noise was added to create SNR values ranging from 10 to 100 (defined with respect to the $b = 0$ images), and the simulated data were processed according to our standard analysis pipeline. In white matter regions, where the FBWM approach is expected to apply, the parameter values are fairly insensitive to the added noise, for SNR values of 20 and above. The calibration bar for D_a is in units of $\mu m^2/ms$, while that for f is dimensionless. 112

4.13 Mean values of ζ, f, $D_\parallel$, and $\bar{D}_e$ over all white matter voxels for simulated data with varying amounts of added noise (solid data points). The ground truth values are indicated by the dotted lines, and the open data points give the simulated results with the denoising step omitted from the processing pipeline. The error bars indicate standard deviations. With denoising, the FBI/FBWM estimates agree well with the ground truth values for SNRs of 20 and above. Without denoising, both accuracy and precision are noticeably reduced, particularly for $D_\parallel$. 113

4.14 Results for selected diffusion measures from simulations with varying numbers of diffusion coding directions $(30, 64, 128, 256)$ for the $b = 6000\,\mu\mathrm{m}^2/\mathrm{ms}$ HARDI shell. The data points reflect average values over all white matter voxels from the simulated dataset, and error bars indicate standard deviations. The SNR is fixed at 50, which is similar to that of our experiments, and the number of directions is set to 30 for both the $b = 1000$ and $b = 2000\,\mu\mathrm{m}^2/\mathrm{ms}$ shells. The parameter estimates are all similar for 64 directions and above, but are much less accurate for f and D_a when only 30 directions are used for the HARDI shell. 114

4.15 Direction-averaged dMRI signal as function of TE for individual voxels from selected regions of interest using (A) a monopolar (MP) sequence and (B) a bipolar (BP) sequence. All data points were obtained from a single subject (Subject 1) with a b-value of $6000\,\mathrm{s/mm^2}$. The lines are best fits using the monoexponential form of Equation 4.31. The error bars indicate the standard error for the signal noise. 125

4.16 Parametric maps of T_{2a} for a single anatomical slice from Subject 1, as determined with a monopolar sequence (center) and a bipolar sequence (right), along with the corresponding color FA map (left) for anatomical reference. The two T_{2a} maps are qualitatively similar, although somewhat higher values are apparent for the bipolar sequence in most white matter voxels. Note that T_{2a} values are only meaningful in white matter regions, because the assumptions underlying the estimation method are invalid in gray matter. The calibration bars are labeled in units of milliseconds. 126

4.17 Scatter plot of T_{2a} for white matter voxels from the same anatomical slice as in Fig. 4.16. The monopolar and bipolar values are strongly correlated (r = 0.9), but those for the bipolar sequence are mostly higher, with the best fit line having a slope of 1.1. Thus the extra refocusing pulse of the bipolar sequence tends to increase the apparent T_{2a}. 127

4.18 Histograms of T_{2a} for all white matter voxels from three healthy subjects. The dMRI data were acquired with a monopolar sequence and a b-value of $6000\,\mathrm{s/mm^2}$. Most of the T_{2a} values lie between $50\,\mathrm{ms}$ and $110\,\mathrm{ms}$. 128

4.19 Bar graphs showing the median T_{2a} for selected regions of interest from all three subjects, as acquired with a monopolar sequence and a b-value of $6000\,\mathrm{s/mm^2}$. The median values range from a low of about $64\,\mathrm{ms}$ to a high of about $94\,\mathrm{ms}$, and the error bars indicate standard deviations. PLIC = posterior limb of internal capsule; ALIC= anterior limb of internal capsule; SLF = superior longitudinal fasciculus; EC = external capsule; GCC = genu of corpus callosum; BCC = body of corpus callosum; SCC = splenium of corpus callosum; ACR = anterior corona radiata; SCR = superior corona radiata; PCR = posterior corona radiata. 129

4.20 T_{2a} in white matter as a function of FA for b-values of 4000, 6000, and $8000\,\mathrm{s/mm^2}$ from Subject 2. Similar results are found for all three diffusion weightings, with some small deviations being apparent for very low and very high FA. The dMRI data were acquired with a monopolar sequence. The data points indicate median values, and the error bars reflect the first and third quartile of T_{2a} values within each bin (bin size = 0.05). 130

4.21 T_{2e} in white matter as a function of FA for assumed intra-axonal diffusivities of $D_a = 1.0, 1.5, 2.0$ and $2.5\,\mu\mathrm{m}^2/\mathrm{ms}$, together with T_{2a}. The dMRI data were acquired with a monopolar sequence and a b-value of $6000\,\mathrm{s}/\mathrm{mm}^2$. The data points are the averages of the median values from all three subjects, with the error bars indicating inter-subject standard deviations. For all choices of D_a, T_{2e} is found to be substantially shorter than T_{2a} over the full range of considered FA values. 131

4.22 T_{2a} in white matter voxels with a coefficient of linearity exceeding 0.4 as a function of the angle θ between the principal diffusion tensor eigenvector and the direction of the main magnetic field. The colored lines are median values for individual subjects, while the black line shows the average of these medians. The inter-subject averages of T_{2a} are significantly correlated with θ ($r = -0.41$, $p < 0.0001$), suggesting that T_{2a} is influenced by magnetic field inhomogeneities generated by spatial variations in magnetic susceptibility. The dMRI data were acquired with a monopolar sequence and a b-value of $6000\,\mathrm{s}/\mathrm{mm}^2$. 132

4.23 Distribution of T_{2a} and T_{2e} values in the white matter of one healthy subject. The averages ($\pm$ standard deviations) of T_{2a} and T_{2e} are $80.8\pm 12\,\mathrm{ms}$ and $60.8\pm 26\,\mathrm{ms}$ respectively. 138

4.24 Voxelwise parametric maps showing T_{2a} (middle) and T_{2e} (right) for a single axial slice. A color FA image (left) of the same slice is given for anatomical reference. Substantial regional variability is apparent with the T_{2a} generally being longer than the T_{2e}. The T_{2a} maps appear less noisy than the T_{2e} maps, since they do not rely on any inputs from FBWM. Note that the two compartmental T_2 relaxation times are only meaningful in white matter regions, as the assumptions underlying our method are violated in gray matter [30] 139

4.25 Bar graphs showing the average apparent AWF (f^*, blue) and the corrected AWF (f, yellow) for selected white matter regions of interest. The error bars indicate standard deviations. Differences range from 0.13 in the SLF to 0.03 in the EC. PLIC = posterior limb of internal capsule; ALIC= anterior limb of internal capsule; SLF = superior longitudinal fasciculus; EC = external capsule; GCC = genu of corpus callosum; BCC = body of corpus callosum; SCC = splenium of corpus callosum; ACR = anterior corona radiata; SCR = superior corona radiata; PCR = posterior corona radiata. . . 139

5.1 FBWM metrics calculated for a subject with a chronic ischemic stroke. One slice (a) is from the core of the lesion and the other slice (b) is from the perilesional area. Notice how the FAA looks qualitatively intact in the perilesional slice (b). 142

5.2 Top row: dMRI tractography when using DTI (left) and when using FBI (right) in a patient with severe white matter disease. Bottom row: Axial slice of T2-weighted FLAIR from same patient to demonstrate the extend of the abnormalities. *Figure courtesy Hunter Moss* 143

5.3 Anatomical location of the three ROIs considered in the analyses. Voxels were grouped according to the largest b-value for which the direction-averaged dMRI signal exceeded a noise threshold of 3.9 (arbitrary units). Only voxels for which this largest b-value was at least $b = 6000\,\mathrm{s/mm^2}$ were included, so that the power-law fits would all have at least 4 data points above the noise. The ROIs with largest b-values of 6000, 8000, and $10.000\,\mathrm{s/mm^2}$ are shown in blue, red, and green, respectively. These largely coincide with the cerebellum, brain stem, corticospinal tracts, external capsule, and splenium. 146

5.4 Semi-log plots showing the relationship between the direction-averaged diffusion weighted signal ($\bar{S}$) and the b-values for all three ROIs. The first column has the power-law fits, with the black dashed line showing fits to data points averaged over all voxels within each ROI and the gray lines indicating fits for individual voxels. As a comparison, the second and third columns show similar monoexponential fits without and with including $b = 0$ as a fitting point. The red line indicates the noise threshold of 3.9. 147

5.5 Histogram for the power-law exponent α from all the voxels included in the three ROIs. The overall average value for α is 1.21 ± 0.16. 148

5.6 The AIC as a function of FA (bin size $= 0.05$) for power-law and both types of monoexponential fits. The power law outperforms the monoexponential fits for the full range of considered FA values. The goodness of fit is largely independent of FA. 148

5.7 The power law exponent α grouped according to FA for all three ROIs. The average values decrease from 1.35 ± 0.14, for the ROI with a largest b-value of $6000\,\mathrm{s/mm^2}$, to 1.08 ± 0.07 for the ROI with a largest b-value of $10.000\,\mathrm{s/mm^2}$. Notice that α is not strongly dependent of FA. 149

A.1 Lesion Location: Lesion overlap of all participants (N=32). The different colors represent a different amount of patients with lesions in that area. . . . 154

SUMMARY

In 1909 German neurologist Korbinian Brodmann wrote “functional localization of the cerebral cortex without the lead of anatomy is impossible... In all domains, physiology has its firmest foundations in anatomy [1]”. While histology is the current gold standard for studying brain microstructure, it is primarily a post-mortem technique that has an average resolution of one micrometer making it impractical for studying the entire brain. Diffusion Magnetic Resonance Imaging (dMRI) is ideally suited to study whole-brain tissue microstructure by sensitizing the MRI contrast to water diffusion, which has a length scale on the order of micrometers. Even though dMRI is applied clinically for the detection of acute ischemia, the relation between tissue microstructure and the dMRI signal is complex and not fully understood. The focus of this dissertation was the validation and development of a new biophysical model of the dMRI signal. Notwithstanding, it is important to keep in mind the potential clinical applications of these models, so in parallel we studied the relationship between white matter integrity and language impairments in post-stroke anomia. This application is of interest since response to language treatment is variable and it is currently difficult to predict which patients will benefit. A better understanding of the underlying brain damage could help inform on functionality and recovery potential. Our work resulted in 9 peer-reviewed papers in international journals and 13 abstracts in proceedings at national and international conferences.

Using data collected from 32 chronic stroke patients with language impairments, we studied the relation between baseline naming impairments and microstructural integrity

of the residual white matter. An existing dMRI technique, Diffusional Kurtosis Imaging (DKI), was used to assess the tissue microstructure along the length of two major white matter bundles: the Inferior Longitudinal Fasciculus (ILF) and the Superior Longitudinal Fasciculus (SLF). The frequency of semantic paraphasias was strongly associated with ILF axonal loss, whereas phonemic paraphasias were strongly associated with SLF axonal loss. This double dissociation between semantic and phonological processing is in agreement with the dual stream model of language processing and corroborates the concept that, during speech production, knowledge association (semantics) depends on the integrity of ventral pathways (ILF), whereas form encoding (phonological encoding) is more localized to dorsal pathways (SLF). Using a smaller dataset of 8 chronic stroke subjects whom underwent speech entrainment therapy, we assessed if naming improvements were supported by underlying changes in microstructure. Remarkably, we saw that a decrease in semantic errors during confrontational naming was related to a renormalization of the microstructure of the ILF. Together, these two studies support the idea that white matter integrity (in addition to regional gray matter damage) impacts baseline stroke impairments and disease progression. Acquiring accurate information about a patient's linguistic disorder and the underlying neuropathology is often an integral part to developing an appropriate intervention strategy.

However, DKI metrics describe the general physical process of diffusion, which can be difficult to interpret biologically. Different pathological processes could lead to similar DKI changes further complicating interpretation and possibly decreasing its specificity to disease. A multitude of biophysical models have been developed to improve the specificity of dMRI. Due to the complexity of biological tissue, assumptions are necessary, which can differ in stringency depending on the dMRI data at hand. One such assumption is that axons can be approximated by water confined to impermeable thin cylinders. In this dissertation, we provide evidence for this "stick model". Using data from 2 healthy controls we show that the dMRI signal decay behaves as predicted from theory, particularly at strong

diffusion weightings. This work validated the foundation of a biophysical model known as Fiber Ball Imaging (FBI), which allows for the calculation of the angular dependence of fiber bundles. Here, we extend FBI by introducing the technique Fiber Ball White Matter (FBWM) modeling that in addition provides estimations for the Axonal Water Fraction (AWF) and compartmental diffusivities. The ability to accurately estimate compartment specific diffusion dynamics could provide the opportunity to distinguish between different disease processes that affect axons differently than the extra-axonal environment (e.g. gliosis). Lastly, we were able to show that FBI data can also be used to calculate compartmental transverse relaxation times (T_2). These metrics can be used as biomarkers, aid in the calculation of the myelin content, or be used to reduce bias in diffusion modeling metrics.

Future work should focus on the application of FBI and FBWM to the study of white matter in post-stroke anomia. Since FBWM offers the advantage of isolating the diffusion dynamics of the intra- and extra- axonal environments, it could be used to distinguish between pathological processes such as glial cell infiltration and axonal degeneration. A more specific assessment of the structural integrity underlying anomia could provide information on an individual's recovery potential and could pave the way for more targeted treatment strategies. The isolation of intra-axonal water is also beneficial for a technique known as dMRI tractography, which delineates the pathway of fiber bundles in the brain. dMRI tractography is a popular research tool for studying brain networks but it is notoriously challenging to do in post-stroke brains. In damaged brain tissue, the high extra-cellular water content masks the directionality of fibers; however, since FBI provides the orientational dependence of solely intra-axonal water, it is not affected by this phenomenon. It is important to understand that caution should be taken when applying biophysical models (FBWM/FBI vs. DKI) to the diseased brain as the validation we provided in this work was only for healthy white matter and these experiments should be repeated in pathological white matter.

CHAPTER 1
DIFFUSION WEIGHTED MAGNETIC RESONANCE IMAGING AND THE MEASUREMENT OF WHITE MATTER MICROSTRUCTURE

1.1 Introduction

The organization of white matter spans over several orders of magnitude in size. The average diameter of axons is $\sim 1\,\mu\mathrm{m}$ with some axons having lengths up to $1\,\mathrm{m}$ or more. Capturing structural information that encompasses all these different length scales is a major remaining challenge for neuroscience. Techniques like Electron Microscopy (EM) (average resolution of $0.2\,\mathrm{nm}$) are ideally suited to study the smallest structures; however, using EM for studying the entire central nervous system would be extremely time consuming (likely even impossible). In addition, EM does not allow for the study of in vivo samples. On the other hand, Magnetic Resonance Imaging (MRI) is commonly used to study the in vivo brain in its entirety, albeit with resolutions that are on the order of $\sim 1\,\mathrm{mm}$. Diffusion Magnetic Resonance Imaging (dMRI) is an MRI technique that can help us bridge this gap by sensitizing the image to the diffusion of water molecules (a physical process that happens at the $\mu\mathrm{m}$ scale). This chapter will describe the basic principles of dMRI including the physics of diffusion, the diffusion MRI sequence, and the most common ways of interpreting the dMRI signal (e.g. Diffusion Tensor Imaging (DTI)). For more in depth information, the reader can refer to [2]. Once a basic understanding of dMRI is established, we will cover how it is commonly used in clinical applications. The chapter will conclude with some remaining questions and challenges which will be partially addressed in this work.

1.2 Diffusion Magnetic Resonance Imaging

1.2.1 General principles

Water molecules at temperatures above absolute zero (0 K) are constantly in motion and collisions between the particles will result in their random displacement. This phenomena was first described by the botanist Robert Brown in 1827 who studied pollen grain suspended in water [3]. He observed that the pollen would go on "a random walk" under the microscope and coined the process Brownian motion, which is also known as diffusion. Almost 100 years later, Einstein published the mathematical groundwork behind Brownian motion (an outgrowth of his PhD work), which in turn also served as confirmation for the existence of molecules [4]. Einstein showed that the probability of a particle displacing a certain distance **r** after a time t can be described by a Gaussian Probability Distribution Function (PDF):

$$P(\mathbf{r}, t) = (4\pi Dt)^{-3/2} exp(-\frac{\mathbf{r}^2}{4Dt}), \tag{1.1}$$

with D the diffusion coefficient of that particle. $P(\mathbf{r}, t)$ is also commonly known as the average diffusion propagator, an example of which is shown in Figure 1.1 (blue).

The Gaussian shape of the displacement PDF results in what is known as the Einstein relation of diffusion, which states that the mean square displacement of the particles is directly proportional to the D and the diffusion time (t) :

$$< \mathbf{r}^2 >= 6Dt, \tag{1.2}$$

with the angular brackets denoting the average of **r**.

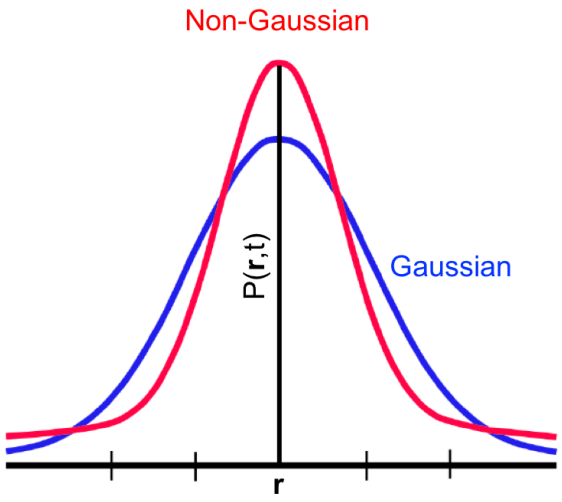

Figure 1.1: The displacement probability distribution function: Gaussian free diffusion (in blue) and restricted non-Gaussian diffusion (in red).

In reality, Equation 1.1 is only valid for free diffusion in unrestricted homogeneous media where the diffusion process can be described by a single scalar (D). In white matter, elements such as cell walls form barriers to the water molecules resulting in displacements that are smaller than to be expected from Equation 1.1. This results in a $P(\mathbf{r}, t)$ that deviates from a Gaussian distribution. An example is depicted in Figure 1.1 (red). Since tissue microstructure has a direct effect on the diffusion dynamics, then studying diffusion can provide information on that underlying tissue microstructure. Two questions remain: 1. How is the diffusion dynamics of biological tissue measured? and 2. How does the diffusion process relate to tissue properties?

In 1963, Stejskal and Tanner proposed an elegant way of sensitizing the MRI signal to diffusion: the Pulsed Gradient Spin Echo (PGSE) technique [5]. Modern diffusion sequences can all be traced back to modifications of the original PGSE experiment. To understand PGSE it is helpful to begin with an intuitive analogy first given by Hahn in 1953 (see Figure 1.2). Picture a group of runners lined up in starting blocks out of which all leave at the same time (Figure 1.2A). Suppose that each runner can only run in their respective lane and that each lane determines the runner's speed, with the runner on the inside running

the slowest and the runner on the outside running the fastest (Figure 1.2B-C). At a certain time the runners are asked to turn around and run back to the start (Figure 1.2D). Since all runners are going at a constant speed determined by their lane they will reach the finish line at the exact same time. A picture is taken as soon as the runners reach the finish (Figure 1.2F). In MRI, where runners are replaced by proton spins, this phenomenon is called an echo and the crossing of the finish line symbolizes the acquisition of the Magnetic Resonance (MR) image. When all runners cross the finish line at the same time the signal is maximized. If the runners were able to switch lanes while turning they would reach the finish line at different time points since their speed would have changed. In this scenario, less runners would be in the picture at the finish line. This "switching of lanes" happens through processes like diffusion, which results in MR signal loss.

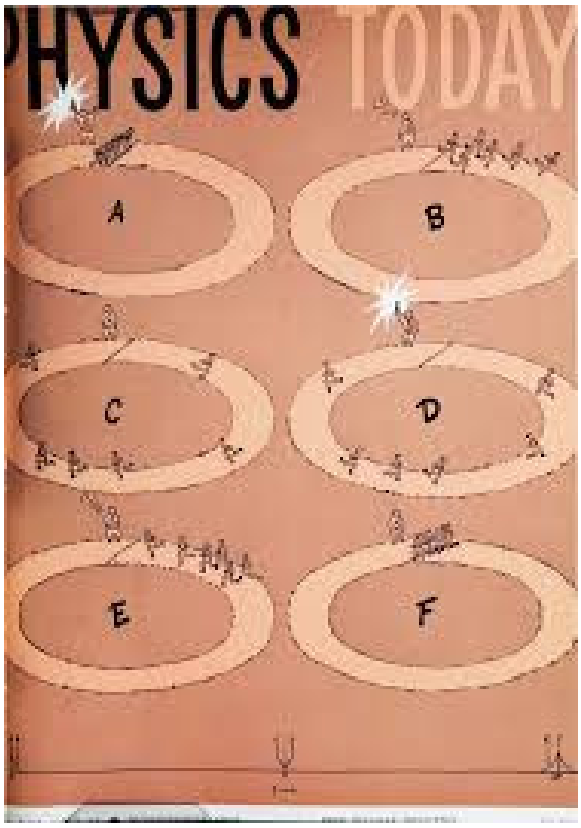

Figure 1.2: Famous analogy for the spin echo phenomenon given by Hahn in 1953 on the cover of physics today (drawing by Kay Kaszas) [6]. "*Cover art from Physics Today 6.11 (1953) reproduced with the permission of the American Institute of Physics.*"

The basic building blocks of the PGSE sequence are demonstrated in Figure 1.3a. Briefly, the initial 90° Radio Frequency (RF) pulse flips all the spins into the transverse (x,y) plane where the signal can be measured (this is standard practice in many MRI sequences). This flip is followed by the first diffusion weighting gradient (diffusion gradient pulse 1) during which the spins undergo a phase shift that is spatially dependent. This spatially dependent shift is analogous to having faster and slower runners determined by their lanes. Gradient pulse one is turned off after a duration δ, which is followed by a 180° RF pulse that flips the spins. Next, the second diffusion gradient pulse is turned on, which is identical to the first one. If the spins are at the same spatial location they will receive the same amount of phase shift as during diffusion gradient pulse 1 and after a time δ all the spins will be back in phase (i.e., creating an echo). If the spins changed location, like during diffusion, the spins will be out of phase after a time δ resulting in signal loss. The spins in voxels with a high D will be out of phase more than the spins in voxels with a low D. This difference in D will manifest itself as a difference in signal attenuation (Figure 1.3b). The direction (x, y, z) of diffusion gradient pulse 1 (and 2) determines in which direction the diffusion is being sensitized. Note that the combination of the two gradient and two RF pulses only sets up the image contrast and has to be followed by another sequence that acquires the image. The image acquisition module that is most frequently used is the Echo Planar Imaging (EPI) sequence, which minimizes the effects of motion.

Stejskal and Tanner also introduced the b-value, which indicates how sensitive the sequence is to diffusion (i.e., the strength of diffusion weighting) in addition to T_2-decay. At low b-values, only voxels with very high diffusivity will experience signal loss, but at high b-values, even low diffusivities will result in phase incoherence.

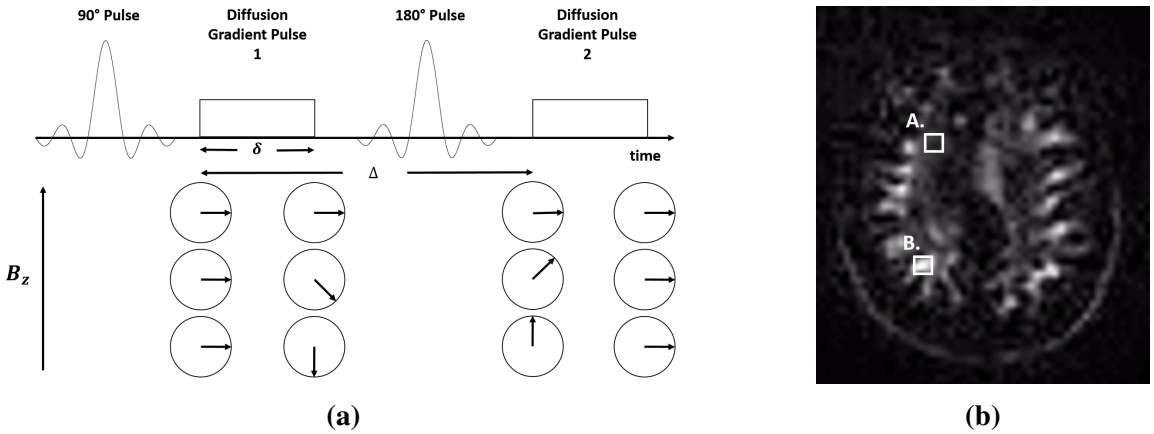

Figure 1.3: (a) Top: Diagram of the PGSE experiment. Bottom: The phase-evolution of the spins. (b) Raw dMRI image. Voxel A has a higher D than voxel B (in the direction of the gradient pulse) resulting in a difference in signal intensity. Assuming the voxels have a similar T_2.

The b-value of a PGSE experiment is calculated by [5]:

$$b = \gamma^2 G^2 \delta^2 (\Delta - \delta/3), \tag{1.3}$$

where γ is the proton gyromagnetic ratio ($267.5 \times 10^6 \cdot \mathrm{rad} \cdot \mathrm{s}^{-1}/\mathrm{T}$), G is the gradient strength, and Δ is the time between the gradient pulses.

The following two sections will cover the most common ways of interpreting the dMRI signal. Research on dMRI signal interpretation is still very active and a consensus has yet to be reached on the most appropriate technique. There are two main strategies to characterizing the dMRI signal: by way of pure physics parameters or by way of tissue modeling parameters. The difference between them will be explained in more detail in the next sections together with the most common strategies to obtain each. These examples are not exhaustive but are intended to give the reader a basic understanding of dMRI modeling. The interested reader can refer to [7, 8] for more details.

1.2.2 Pure Physics Parameters

Pure physics parameters are general physical properties that characterize the water diffusion process (e.g. the diffusivity (D) or the diffusional kurtosis (K)). These metrics have shown to be sensitive to tissue properties but they have no explicit connection to the underlying microstructure. That is, these parameters can be used to describe any diffusion process in any setting. Pure physics parameters are calculated by fitting mathematical functions to the dMRI signal (e.g., diffusion signal attenuation curve) as closely as possible. These functions are often referred to as "model-free" functions since they do not make any assumptions about the geometry or composition of the underlying tissue (for a contrasting approach see tissue modeling parameters in Section 1.2.3). We will briefly go over the basics of three commonly used techniques: DTI, Diffusional Kurtosis Imaging (DKI), and the bi-exponential signal model. Q-space imaging (e.g., Diffusion Spectrum Imaging (DSI)) also belongs to this category but will not be covered in this thesis. Interested readers are referred to [9].

Diffusion Tensor Imaging

DTI was developed in the early 90s and can be considered as one of the simplest dMRI analysis techniques [10, 11]. Notwithstanding, it has produced some strong research, and it is still the most widely used tool for clinical applications. The starting point for DTI is the series expansion of the diffusion NMR signal derived by Tanner [12]:

$$ln[S(b, \mathbf{n})/S_0] = -bD + O(b^2), \tag{1.4}$$

with $S(b, \mathbf{n})$ the measured dMRI signal in a direction $\mathbf{n}$ at a predefined b-value, D the diffusivity, and S_0 the measured dMRI signal without diffusion weighting (i.e., $b = 0\,\mathrm{s/mm^2}$). DTI assumes that the diffusion dynamics can be accurately described by a Gaussian PDF, which justifies neglecting the higher order terms in Equation 1.4 ($O(b^2)$). In this case,

Equation 1.4 simply describes a line with the slope equal to the diffusivity D. This is illustrated in Figure 1.4. In brain, DTI is only accurate at low b-values (up to $b = 1000\,\mathrm{s/mm^2}$), at higher b-values the behavior deviates from linear and more complicated equations are needed (e.g., see Section 1.2.2 *Diffusional Kurtosis Imaging*).

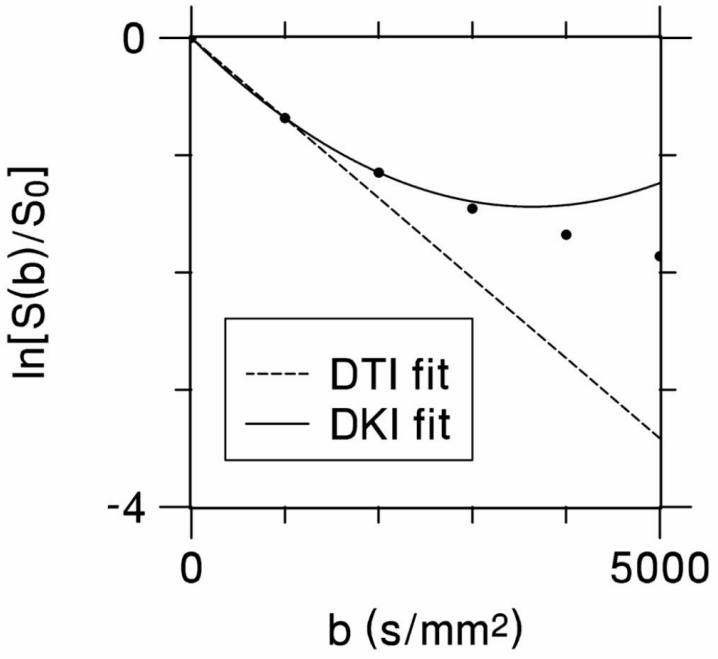

Figure 1.4: Comparison of DTI and DKI fitting models. For DTI, the logarithm of diffusion-weighted signal intensity (circles) as a function of the b-value is fit, for small b-values, to a straight line. In brain, this fit is often based on the signal for $b = 0$ and $b = 1000\,\mathrm{s/mm^2}$. For DKI, the logarithm of the signal intensity is fit, for small b-values, to a parabola. In brain, this fit may be based on the signal for $b = 0$, $b = 1000$, and $b = 2000\,\mathrm{s/mm^2}$. *Reproduced from Jensen, Jens H., and Joseph A. Helpern. "MRI quantification of non-Gaussian water diffusion by kurtosis analysis." NMR in Biomedicine 23.7 (2010): 698-710 with the permission of John Wiley and Sons.*

When diffusion in tissue is isotropic (i.e., the diffusivity is the same in every direction) measuring the diffusivity in one direction would be sufficient to characterize the whole diffusion process. In white matter however, the diffusion characteristics depend strongly on the chosen direction. This is the result of microstructural ordering (e.g., the existence of fiber bundles), which is still appreciable at the scale of the imaging voxel. In this case, the correct representation would be to use a three-dimensional Diffusion Tensor (**D**) to describe

the anisotropic diffusion process:

$$\mathbf{D} = \begin{bmatrix} D_{xx} & D_{xy} & D_{xz} \\ D_{xy} & D_{yy} & D_{yz} \\ D_{xz} & D_{yz} & D_{zz} \end{bmatrix}. \tag{1.5}$$

D is made up of 6 unique elements: three diagonal elements (D_{xx}, D_{yy}, D_{zz}) which represent the D along each of the major axes, and three off diagonal elements (D_{xy}, D_{yz}, D_{xz}) which correspond to the correlation of the displacements along each pair of principal directions. For anisotropic diffusion Equation 1.4 can be rewritten as:

$$ln[S(b, \mathbf{n})/S_0] = -bD(\mathbf{n}) + O(b^2), \tag{1.6}$$

with

$$D(\mathbf{n}) = \sum_{i,j=1}^{3} n_i n_j D_{ij}. \tag{1.7}$$

Since **D** contains 6 unknowns, in practice $S(b, \mathbf{n})$ is measured at a minimum of 6 different directions resulting in 6 equations with 6 unknowns (using Equation 1.6 and 1.7), which can be solved using methods such as linear least squares to find **D**.

Four metrics are commonly derived from **D**:

- Fractional Anisotropy (FA) [13]: Characterizes the degree of diffusion anisotropy. When FA = 1, the diffusivity is maximised along one direction while all other directions have a diffusivity of 0. When FA = 0, the diffusivity is equal in all directions.

$$\text{FA} = \frac{1}{2} \frac{\sqrt{(\lambda_1 - \lambda_2)^2 + (\lambda_2 - \lambda_3)^2 + (\lambda_1 - \lambda_3)^2}}{\sqrt{\lambda_1^2 + \lambda_2^2 + \lambda_3^2}}, \tag{1.8}$$

  $\lambda_1, \lambda_2, \lambda_3$ are the three eigenvalues of **D** and $\lambda_1 \geq \lambda_2 \geq \lambda_3$.

- Mean Diffusivity (MD): The average diffusivity over all directions.

$$\bar{D} = \frac{\lambda_1 + \lambda_2 + \lambda_3}{3} \tag{1.9}$$

- Axial Diffusivity (AD): The diffusivity along the principal direction of diffusion.

$$D_{\parallel} = \lambda_1 \tag{1.10}$$

- Radial Diffusivity (RD): The average diffusivity perpendicular to the principal direction of diffusion.

$$D_{\perp} = \frac{1}{2}(\lambda_2 + \lambda_3) \tag{1.11}$$

The **D** is also used to determine the path of least hindrance to diffusion [14, 15]. In DTI this is simply the direction of the principal eigenvector of **D**, which is also considered to be the local fiber orientation. These voxel-wise local orientations can subsequently be used for different types of fiber tractography (see Section 1.3).

Diffusional Kurtosis Imaging

DKI is a natural extension of DTI which takes into account the non-Gaussian effects of water diffusion [16]. As mentioned in Section 1.2.1, tissue microstructure can cause the PDF to deviate from a Gaussian. From statistics, we know that the non-Gaussianity of any probability distribution can be quantified through its Kurtosis (K). Intuitively, K can be considered a measurement of tissue complexity since it reflects barriers to diffusion. DKI starts with the same series expansion as DTI (Equation 1.6) but now includes the second

order term [16]:

$$ln[S(b,\mathbf{n})/S_0] = -bD(\mathbf{n}) + \frac{1}{6}b^2D^2(\mathbf{n})K(\mathbf{n}) + O(b^3). \tag{1.12}$$

$K(\mathbf{n})$ is the diffusional kurtosis K in direction $\mathbf{n}$ and is defined as:

$$K(\mathbf{n}) = \frac{\overline{D}^2}{D^2(\mathbf{n})} \sum_{i,j,k,l=1}^{3} n_i n_j n_k n_l W_{ijkl}, \tag{1.13}$$

with W_{ijkl} an element of the kurtosis tensor (**W**). **W** is a 4th order tensor with 15 unique elements. Equation 1.12 now contains a total of 21 unknowns (6 from $D(\mathbf{n})$ and 15 from $K(\mathbf{n})$) implying that at least 21 Diffusion Weighted Images (DWI) are necessary for DKI (not counting S_0). Notice that for $K = 0$ (Gaussian diffusion) Equation 1.12 reduces to Equation 1.6. Figure 1.4 demonstrates how the addition of the K term in Equation 1.12 results in a better fit of the diffusion data up to $b \approx 3000\,\mathrm{s/mm^2}$. In brain, a typical DKI protocol exists of two b-values (e.g. $b = 1000-2000\,\mathrm{s/mm^2}$) with a minimum of 30 gradient directions and a handful of $b = 0\,\mathrm{s/mm^2}$ images.

Three metrics are commonly derived from **W**:

- Mean Kurtosis (MK)($\bar{K}$): The average kurtosis over all directions.
- Axial Kurtosis (AK) ($K_\parallel$): The kurtosis along the principal direction of diffusion.
- Radial Kurtosis (RK) ($K_\perp$): The average kurtosis perpendicular to the principal direction of diffusion.

The **W** can also be used in combination with the **D** to define the likelihood of diffusion in each direction. The directional probability of diffusion is more commonly referred to as the diffusion Orientation Distribution Function (dODF) (see Figure 1.5) [17]. The maxima of these functions are considered to be the local fiber orientations and can be used for fiber tractography (see Section 1.3). An important difference between the local fiber orientations

as calculated by DTI is that the kurtosis based dODF can have multiple maxima and thus can represent multiple fiber bundles within one voxel. Figure 1.5 shows an example of a Gaussian dODF based on the **D** alone and the kurtosis dODF based on both the kurtosis and the diffusion tensor. The details on how to calculate the kurtosis dODF are beyond the scope of this work but can be found in [18].

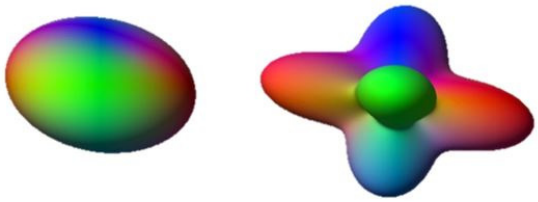

Figure 1.5: An example of a Gaussian dODF (left) and a kurtosis dODF (right). The amplitude of the dODF reflects the likelihood of diffusion in each direction. The direction of the dODF maxima is commonly considered to equate to the direction of the underlying fiber bundle. By definition, Gaussian dODFs are limited to one maximum. The kurtosis dODF can have multiple maxima and thus represent voxels with multiple fiber bundles.

Bi-Exponential

An alternative approach to DKI is to model the non-linear behavior of the dMRI signal as a function of b-value (Figure 1.4) by a bi-exponential function [19, 20]. As we have seen previously, Gaussian diffusion can be described by:

$$S(b, \mathbf{n}) = S_0 \cdot e^{-bD}, \tag{1.14}$$

which is analogous to Equation 1.4 (the mathematical foundation of DTI) without the second order term. The bi-exponential model assumes that diffusion in the brain can be accurately characterized by two distinct Gaussian diffusion processes with their own respective diffusivities (D_1 and D_2):

$$S(b, \mathbf{n}) = f \cdot S_0 \cdot e^{-bD_1} + (1 - f) \cdot S_0 \cdot e^{-bD_2} \tag{1.15}$$

and f is the fraction of the signal coming from compartment 1. Equation 1.15 can be fit to the acquired data to get estimations of D_1, D_2 and f. In practice, the bi-exponential model tends to accurately explain the dMRI signal behavior well in human brain when using one exponential with a low diffusivity and the other with a high diffusivity up to $b \approx 6000\,\mathrm{s/mm^2}$ [19]. Initially, it was thought that these two Gaussians represented the intra- and extracellular space respectively. However, experimental data has shown that this is likely not the case (for a review see [21]). This last step of interpreting the pure physical fitting parameters in the context of tissue microstructure is what is done by tissue modeling and what will be discussed in the next section.

1.2.3 Tissue Modeling Parameters

Tissue models are developed to provide specific measures (i.e., tissue modeling parameters) of the underlying microstructure that attempt to give biological meaning to the pure physical properties of diffusion. They are often tissue specific (e.g., white matter) and require simplifications to deal with the heterogeneous nature of biological tissue. The dMRI signal response is then predicted for this simplified system which in turn is fit to the experimental data. These simplifications have turned out to be difficult to validate and is one of the biggest remaining challenges in dMRI. This section will briefly cover four different tissue models: the Composite Hindered and Restricted Model of Diffusion (CHARMED), the White Matter Tract Integrity Model (WMTI), Neurite Orientation Density and Dispersion Imaging (NODDI) and Fiber Ball Imaging (FBI). These models were chosen specifically because they highlight the progression of tissue modeling throughout the years upon which we will further build in this work. A multitude of other models exist but are beyond the scope of this thesis. The reader is referred to [22] and [8] for review.

Composite Hindered and Restricted Model of Diffusion (CHARMED)

While preceded by a handful of other models [23, 24], CHARMED was the first geometrical model to successfully be applied to human dMRI data in vivo [25, 26]. CHARMED uses a two-compartment model to characterize white matter diffusion. It includes one compartment with restricted diffusion that represents the axons as impermeable cylinders with a predefined distribution of diameters, and another compartment for the extra-axonal space which is modeled using an anisotropic Gaussian wherein all other cell-types are considered to be in fast exchange. The amount of parameters that need to be estimated is large. CHARMED requires at a minimum the estimation of 11 parameters for voxels with only one fiber orientation and a minimum of 15 parameters for voxels with crossing fibers. This is not only a challenging non-linear optimization problem, it also requires a large amount of dMRI data (around 169 data points at a minimum) with b-values up to $10.000\,\mathrm{s/mm^2}$. Such a dataset is challenging to acquire on clinical scanners and within clinically feasible scan times. The following two models (WMTI and NODDI) were the first two attempts to create clinically applicable tissue models.

White Matter Tract Integrity Model

The WMTI model is a tissue model created specifically for the interpretation of DKI data [27]. By leveraging the information captured in the diffusion and kurtosis tensors, WMTI does not require complicated non-linear fitting (like CHARMED). In contrast to the pure physical DKI metrics, WMTI parameters are more specific to the underlying microstructure while still only requiring the acquisition of a DKI dataset (i.e., $b = 0 - 2000\,\mathrm{s/mm^2}$ and a minimum of 21 gradient directions). Before discussing the output parameters, it is important to understand that the model is only valid in white matter and that it makes a couple of key assumptions further restricting its validity to specific parts of the brain. WMTI models white matter as two non-exchanging Gaussian compartments using two diffusion tensors (intra-axonal ($\boldsymbol{D_a}$) and extra-axonal ($\boldsymbol{D_e}$)). In general, this approximation only holds for

bundles of axons that are largely colinear (for more information see [27]).

The WMTI output parameters are visualized in Figure 1.6 and include:

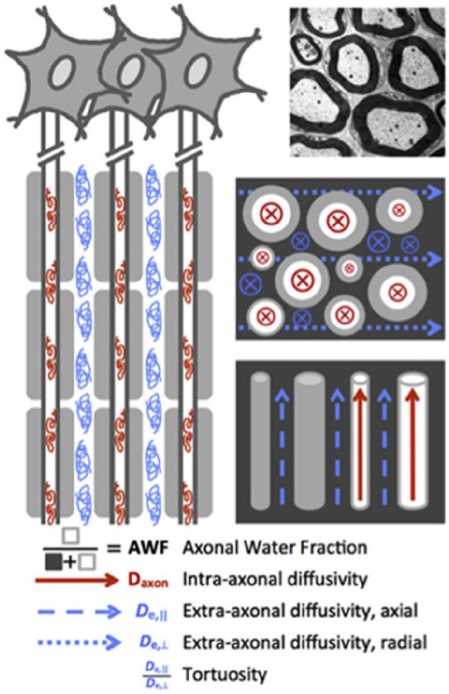

Figure 1.6: Graphical representation of the output parameters from the WMTI model. *Figure created by Andreana Benitez, PhD (reprinted with permission).*

- Axonal Water Fraction (AWF) (f): The percentage of MRI visible water that is contained in axons.

$$f = \frac{K_{max}}{K_{max} + 3}, \tag{1.16}$$

with K_{max} being the maximal directional kurtosis that can be calculated from $\mathbf{W}$.

- Intra-axonal diffusivity (D_a): The diffusivity along the axis of the axons.

$$D_a = tr(\boldsymbol{D_a}), \tag{1.17}$$

with tr symbolizing the trace operator and $\boldsymbol{D_a}$ is the intra-axonal diffusion tensor.

- Extra-axonal parallel diffusivity ($D_{e,\parallel}$): The Diffusivity along the primary direction of diffusion in the extra-axonal space.

$$D_{e,\parallel} = \lambda_{e,1}, \tag{1.18}$$

with $\lambda_{e,1}$ the principal eigenvalue of the extra-axonal diffusion tensor $\boldsymbol{D_e}$.

- Extra-axonal radial diffusivity ($D_{e,\perp}$): The average extra-axonal diffusivity along the directions perpendicular to the principal direction of diffusion in the extra-axonal space.

$$D_{e,\perp} = \frac{\lambda_{e,2} + \lambda_{e,3}}{2}, \tag{1.19}$$

with $\lambda_{e,2}$ and $\lambda_{e,3}$ the second and third eigenvalue respectively of $\boldsymbol{D_e}$.

- The Tortuosity of the extra-axonal space (α):

$$\alpha = \frac{D_{e,\parallel}}{D_{e,\perp}} \tag{1.20}$$

$\boldsymbol{D_a}$ and $\boldsymbol{D_e}$ can be calculated from the directional diffusivities and kurtoses as determined by DKI by:

$$D_{e,i} = D_i[1 + \sqrt{\frac{K_i f}{3(1-f)}}] \tag{1.21}$$

$$D_{a,i} = D_i[1 - \sqrt{\frac{K_i(1-f)}{3f}}] \tag{1.22}$$

Neurite Orientation Dispersion and Density Imaging (NODDI)

Neurite Orientation Density and Dispersion Imaging (NODDI) is probably the most widely used tissue model [28]. NODDI's popularity can be attributed to its clinically feasible protocol, the active imaging framework, and the availability of easy to use software. It assumes a three compartment model: an intra-cellular thin cylindric compartment, an extra-cellular compartment with hindered diffusion, and a CSF compartment with isotropic free diffusion. As the name implies, it has two major outputs: the neurite density (which is closely related to the AWF) and the neurite orientation dispersion. The neurite dispersion is modeled through a cylindrically symmetric Watson distribution (see figure 1.7), which implies the existence of only one main neurite orientation. Notice that the collective word neurite is used which encompasses both axons (i.e., white matter) and dendrites (i.e., gray matter). Since the data acquisition is relatively sparse (around 90 diffusion weighted images), NODDI relies on a multitude of assumptions to diminish the number of parameters that need to be estimated. Most importantly, the intra-axonal diffusivity D_a is assumed fixed at $1.7\,\mu\mathrm{m}^2/\mathrm{ms}$, and the extra-axonal diffusivities are all fully determined by the orientation dispersion and the neurite density.

Fiber Ball Imaging

Fiber Ball Imaging (FBI), on the other hand, is not a multi-compartment model. Instead, FBI assumes that at strong diffusion weightings (i.e., high b-values) the dMRI signal is dominated by only one compartment: the intra-axonal compartment [29, 30, 31]. Similar to WMTI and NODDI, the axons are modeled by impermeable, thin, and straight cylinders. However, their distribution is now fully described by a fiber Orientation Distribution Function (fODF), which allows for complex geometries. This concept was first introduced by Jespersen et al [32]. fODFs describe the density of fibers in each direction (x, y, z) and are useful both for tissue modeling and tractography (see Section 1.3).

The key result of FBI is that the fODF can be estimated directly from the dMRI signal

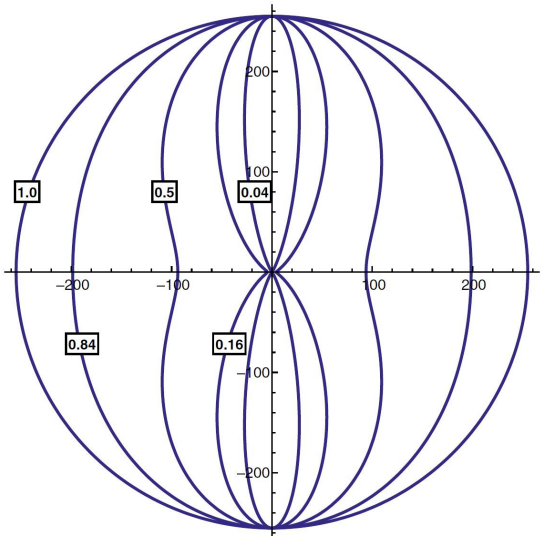

Figure 1.7: Illustration of a set of Watson distributions with the same mean orientation but different orientation dispersion index: $OD = [0.04, 0.16, 0.5, 0.84, 1.0]$. The Watson distribution is cylindrically symmetric, hence showing only the cross-sectional view through the symmetry axis which coincides with its mean orientation. *Reproduced from J. Zhang, Hui, et al. "NODDI: practical in vivo neurite orientation dispersion and density imaging of the human brain." Neuroimage 61.4 (2012): 1000-1016. with the permission of Elsevier.*

at high b-values through [29]:

$$f(\mathbf{n}) = \sqrt{\frac{bD_a}{\pi}} T_F^{-1}(S/S_0, \mathbf{n}), \tag{1.23}$$

where T_F^{-1} is the inverse Funk transform. In practice, the inverse Funk transform is calculated using a spherical harmonic expansion of the DWI signal S/S_0 [33]. The FBI theory also provides an estimation for the parameter ζ, which reflects the microstructure of the underlying voxel. Specifically, ζ is the ratio between the AWF and the square root of the intra-axonal diffusivity (D_a) and can be estimated by:

$$\zeta = \frac{f}{\sqrt{D_a}} = a_0^0 \frac{\sqrt{b}}{\pi}, \tag{1.24}$$

with a_0^0 the lowest order spherical harmonic of the DWI signal. A standard FBI MR protocol would include a set of $b = 4000$ - $6000\,\mathrm{s/mm^2}$ images with a minimum of 64 gradient directions and a couple of $b = 0\,\mathrm{s/mm^2}$ images. FBI will be explained in greater detail

in Chapter 4 - Section 4.3 where we extend this theory to also provide estimations for the AWF and the compartmental diffusion tensors $\boldsymbol{D_a}$ and $\boldsymbol{D_e}$.

1.3 Tractography

The previous two sections explained how the dMRI signal can be used to find voxelwise fiber orientations using for example: the principal eigenvector in DTI, the maxima of the kurtosis dODF in DKI, or the fODF maxima in FBI. Tractography is the process of connecting all these local fiber orientations into a global set of fiber bundles. Figure 1.8 shows an example of whole brain tractography. There are three main fiber tracking algorithms: deterministic tractography, probabilistic tractography, and global tractography. Herein, we will only focus on deterministic tractography, which will be important to understand the following chapters. The interested reader can refer to [34] and [35] for a complete overview of all tractography strategies.

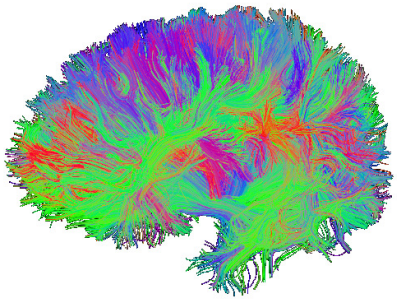

Figure 1.8: Example of whole brain fiber tractography.

Before delving into specifics, it is important to understand that the resulting fiber tracts are only indirectly related to axons. In DTI and DKI, we trace the path of least hindrance to diffusion, which is likely related to the underlying fiber bundles but certainly not identical. For example, since DTI by definition only has one principal diffusion direction, the local fiber orientation will essentially be an average of all underlying fiber directions. Naturally, this becomes problematic if more than one fiber direction is present in which case the local fiber orientation will not accurately reflect the underlying fibers. Even the kurtosis dODF

will suffer from this same problem when fiber bundles intersect at a very small angle. fODFs are an attempt to resolve this issue as they represent the density of fibers in each direction (in comparison to the most likely path of diffusion). However, fODFs require axons to be modeled, which as we discussed previously, has been notoriously difficult to validate. In any case, fiber tracts should never be interpreted as individual axons (or even axon bundles) and one needs to be extremely cautious when using tracts directly for quantification.

After determination of the local fiber orientation, the starting points of the fiber tracking algorithm need to be defined. These starting points are commonly called seeds and can either be placed in a Region of Interest (ROI) (i.e., a specific subset of voxels), or they can cover the whole brain. In ROI-based tractography, the primary interest is the subset of fibers that start from this pre-defined region, which can either be manually drawn or determined by an atlas. Care needs to be taken when specifying pure gray matter ROIs since the diffusion orientation tends to be ill-defined here. Whole-brain tractography on the other hand, attempts to map the entire brain-network as is commonly done in the field of connectomics. For this the seeds can be placed exclusively in white matter, which has the advantage of providing more accurate orientations but which tends to over-represent long fibers. An alternative strategy would be to seed at the gray-white matter boundary. An example of the two commonly used seeding strategies is given in Figure 1.9.

Once a seed is placed, the next step is to integrate the local fiber orientations. The most basic form of integration is called the Euler method, which follows the orientation of the seed voxel for a predefined step-size and then re-assess the orientation at the adjacent voxel. Higher order integration methods exist and details can be found in [34]. The Euler method requires the orientations to be known at locations that do not always coincide with the voxel-grid. This is done through interpolation of the fiber orientations. The simplest interpolation algorithm is called nearest-neighbour, which as the word implies simply

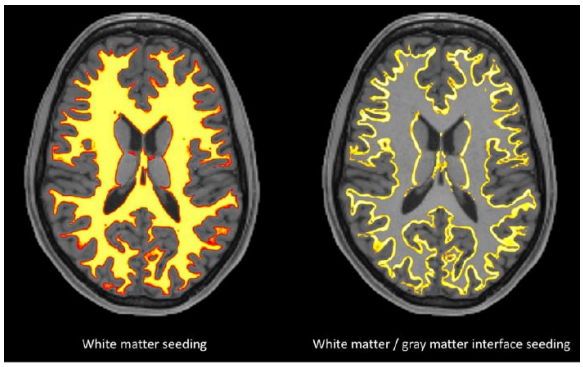

Figure 1.9: Wholebrain tracking can be launched from the white matter (left) or from the white mattergray matter interface, where the fibers are known to originate from (right). *Reproduced from Jeurissen, Ben, et al. "Diffusion MRI fiber tractography of the brain." NMR in Biomedicine 32.4 (2019): e3785. with the permission of John Wiley and Sons.*

adopts the orientation of the nearest neighbouring voxel. Nearest-neighbour interpolation is not recommended since it results in large interpolation errors. The most common form of interpolating the orientations is tri-linear interpolation. In tri-linear interpolation, the orientation of all 8 neighbouring voxels is taken into account in a weighted sum based on the distance to each voxel. Lastly, some criteria need to be set that define when the fiber tracking ends. Two popular strategies are to use an FA threshold and an angular threshold. If a voxel is reached with an FA value below the threshold the tracking algorithm assumes it entered gray matter and will terminate. The angular threshold sets a biologically plausible maximum to the angle between two consecutive orientations. In addition, one can also define a termination ROI, which will terminate the tract as soon as the fiber reaches a voxel specified within this ROI. Once the fiber tract is complete, the algorithm will move to the next seed until a predefined number of seeds or tracts is reached.

1.4 Clinical Applications of dMRI

Bread and butter dMRI is used daily in the hospital for the assessment of acute ischemia, for the characterization of tumors and infections, and at a lower frequency for surgical planning. For a review see [36]. In the early nineties, researchers discovered that ischemia leads to a drop in $\bar{D}$ which is detectable within minutes of onset and before any changes

are apparent on conventional T_2-weighted sequences [37]. The sensitivity and specificity for acute ischemia is higher with dMRI than with CT or conventional MRI making it the modality of choice if time permits. In addition, dMRI is ideally suited for dating the lesion since the $\bar{D}$ changes follow a well-known trajectory of diminished values in the acute phase, pseudo normalization, and increased values in the chronic phase. The dating of the lesion helps with treatment planning and prognosis. dMRI is also commonly used for differentiating different types of tumors and infections. The benefit seems to arise largely from the differentiation between vasogenic and cytotoxic edema. Both types of edema have an increased T_2 but only cytotoxic edema has a drop in $\bar{D}$. Gaining popularity is the use of dMRI tractography for neurosurgical planning. For example, tractography can be used to map out the fiber bundles surrounding a tumor informing the surgeon on how to optimally approach the resection. In other cases, the major motor and/or language bundles can be mapped pre-surgery in an attempt to avoid causing damage to these crucial functions.

1.5 Challenges and Unanswered Questions

dMRI is a popular research tool that has seen exponential growth since the early nineties. Figure 1.10, which shows the amount of publications on PubMed over time with key words diffusion and MRI is a nice demonstration of this growth. Unfortunately, the clinical application of dMRI has not followed this same trend. All clinical applications use either the raw dMRI signal, the $\bar{D}$, or in rare cases the full $\mathbf{D}$, which were all developed in the early days of dMRI. A big remaining problem is the lack of specificity to microstructural change of the conventional pure physical diffusion parameters (i.e., $\bar{D}$ or FA). For example, a voxelwise drop in $\bar{D}$ could have a multitude of origins ranging from cell swelling to inflammation. In fact, after almost thirty years it is still not fully understood what biological changes cause the famous diffusivity drop in acute ischemia. This lack of specificity has caused a considerable amount of confusion in the field and has given rise to sets of papers with contradictory conclusions. It is worth mentioning here that the bulk of translational

imaging studies use large databases to study disease severity and progression. While these studies are critical for advancing our understanding of disease, they are not useful for clinical decision-making, which happens on an individual basis. It is our hope that the discovery of more specific metrics will allow for the development of more individualistic tools.

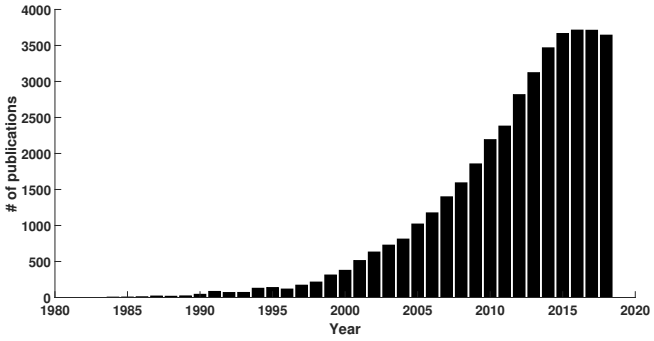

Figure 1.10: The number of publications on PubMed with the key words diffusion and MRI

In 1997, Stanisz et al. were among the first to use a comprehensive tissue model to estimate specific microstructural metrics of excised optic nerve tissue [24]. CHARMED was an extension of this idea to human in-vivo brain [26]. It quickly became obvious that these techniques required large amounts of data and complicated algorithms. In reaction to this, several simpler models were developed (e.g. NODDI [28] and WMTI [27]), which required much stronger assumptions about the underlying biology. Since there is no agreement on what these assumptions should be, a myriad of tissue models have been developed over the past years all with their own unique solutions [7, 8]. Many models turned out to be oversimplified and FBI was developed as a compromise by using a simple model but only at a very specific imaging regime [29]. Knowing which assumptions are valid when will be critical for the future of dMRI and the field is slowly switching its focus from the development of new models to the validation of current ones. In Chapter 4, we provide some validation for the commonly used thin cylinder approximation for axons, which we then use to further develop a better founded tissue model in Section 4.3.

CHAPTER 2
CURRENT UNDERSTANDING OF NAMING AND NAMING IMPAIRMENTS AFTER STROKE

2.1 Introduction

Today, approximately 1 in 250 people in the United States live with an acquired language impairment (i.e., aphasia) resulting from brain injury [38]. A hallmark symptom of post-stroke aphasia is anomia or the inability to accurately name words. Word production is a fundamental feature of what makes us human, and losing this trait is debilitating and can cause a considerable amount of suffering and frustration. This chapter will discuss how anomia typically manifests post-stroke, as well as how it is studied. Even though we will focus solely on spoken word production, it is important to mention that similar deficits can arise in other modes of communication such as in sign language [39]. Since anomia can be extremely diverse, it is useful to start by understanding how naming occurs. We will focus on the initial steps of speech production using the well supported lemma model, which spans from "thinking of speaking" to word selection with its respective phonetic form [40]. The final steps of speech production, which govern motor system control (e.g., articulation) will not be covered in this work since anomia is an impairment of linguistic and not motor capabilities. Several competing models of naming exist and the reader is referred to [41] for a review. After covering the cognitive theory of word production, for which evidence comes largely from the study of error patterns and response times, we will switch to the neural substrates of word production. In this context, we will discuss the elementary Wernicke-Lichtheim-Geschwind "house" model and the more modern dual stream model of language. The chapter will end with some challenges and unanswered questions that will be our focus in this dissertation.

2.2 Word Production

2.2.1 Cognitive Theory: The Lemma Model

According to the lemma model, word production is a serial two-step process consisting of lexical selection and form encoding [40] (see Figure 2.1).

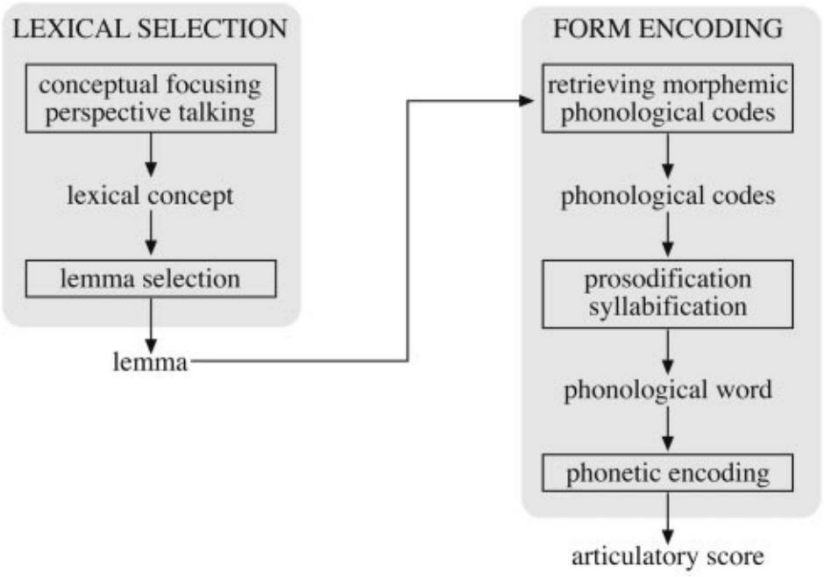

Figure 2.1: Serial two-system architecture of the Lemma model: the two stages of lexical selection and three stages of form encoding [40]. *Reproduced from Levelt, Willem JM. "Spoken word production: A theory of lexical access." Proceedings of the National Academy of Sciences 98.23 (2001): 13464-13471. Copyright (2001) National Academy of Sciences, U.S.A*

Levelt first introduced the different steps of the lemma model by making use of a picture naming task. Upon viewing a picture, one starts sifting through the mental dictionary, called the lexicon, in search for its meaning. Formally, "the meaning" is called the lexical concept commonly denoted by all capital letters. For example, upon viewing a picture of a horse a likely choice would be the lexical concept HORSE but depending on the context the answer could also be ANIMAL or FARM. After a lexical concept is selected, the appropriate lemma is activated. The lemma is identical to the word listed in the dictionary, while the lexical concept is a broader term that consists of all semantic features related to

that lemma. Intuitively, lexical selection can be considered as the translation of thoughts into words. A key concept of the lemma model is that lexical selection is subject to competition. Different lexical concepts and their respective lemmas will be activated but only one will be selected for the next step that prepares the chosen lemma for articulation: form encoding. The transition from lexical selection to form encoding is called crossing the rift. The rift's presence is responsible for the well-known tip of the tongue feeling by occasionally hindering the access to the sound structure of the desired word (form encoding) after already having accessed the meaning of the word (lexical selection).

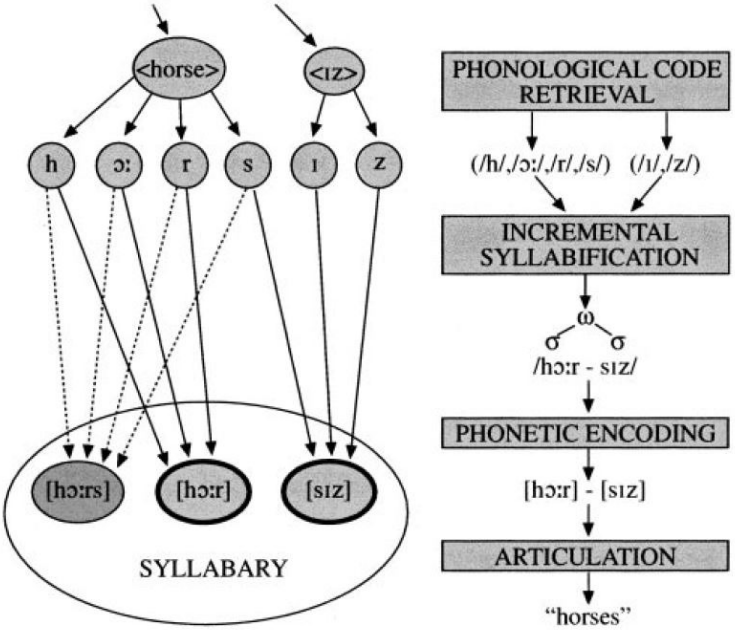

Figure 2.2: Form encoding of the word *horses*. (left) The upper stratum shows nodes representing morphemic phonological codes and their phonemic spellouts. The lower stratum shows nodes representing syllabic articulatory scores. (right) Corresponding form-processing stages. ω = phonological word; σ = syllable [40]. *Reproduced from Levelt, Willem JM. "Spoken word production: A theory of lexical access." Proceedings of the National Academy of Sciences 98.23 (2001): 13464-13471. Copyright (2001) National Academy of Sciences, U.S.A*

Figure 2.2 demonstrates the steps involved in form encoding of the plural noun horses: 1) retrieval of the morphemic phonological code, 2) prosodification and syllabification, and 3) phonetic encoding. Activation of the lemma horse (marked for plural use) triggers the morpheme <horse> and the morpheme <iz>. Morphemes are the smallest unit in a lan-

guage with meaning, which are coupled to their phonemic code in the mental lexicon (in this case: /h/, /ɔː/, /r/,/s/ and /l/,/z/) (step 1). Prosodificiation on the other hand, which in the English language mainly consists of the formation of syllables (step 2), happens while speaking. This is necessary because syllabification is context dependent. For example, the syllabification of horses and horse is different even though they are both associated with the same lexical concept HORSE. To increase efficiency, linguists have suggested that the phonetic encoding (step 3) of the most common syllables are prepared and ready to access in a mental structure called the syllabary (see Figure 2.2). The syllable boundaries (from step 2) are passed to the phonetic encoding mechanism which in turn searches the syllabary for a match. During phonetic encoding it is also decided how the syllabi can be fluently stringed together (the concatenation). These two types of information: the phonetic encoding and their concatenation is called the articulatory score which is sent to the motor apparatus for execution and word production. For a more detailed discussion on the Levelt model and its challenges see [42]. Cognitive models, such as the Levelt model, help us understand what steps are involved in the production of words and aid in the formation of a hypothesis on how the brain controls word production. The following section describes two models that attempt to unravel the neurobiological basis of language namely the Wernicke-Lichtheim-Geschwind model and the dual stream model of language.

2.2.2 Neurobiological Theories

Early Aphasiology: Wernicke-Lichtheim-Geschwind model

In the late 19th century physicians Paul Broca, Carl Wernicke, and Ludwig Lichtheim laid the foundation for the first localizationist model of language. Through the study of post-mortem brains from patient's with language impairments they introduced the first known language centers of the human brain (Figure 2.3): Broca's area that was believed to control speech planning and production (area M) [43], Wernicke's area that was believed to store information on word sounds for speech comprehension (area A) [44], and a concept center

(introduced by Lichtheim) that was believed to store the meaning of words (area B) [45]. According to early beliefs, damage to any of these centers would result in a unique set of language impairments and in a particular aphasia subtype (e.g., a lesion in Broca's area tends to lead to Broca's aphasia). Figure 2.3 depicts the organization of these three different language centers as proposed by Lichtheim in 1885 [45]. Geschwind revitalized the model, almost a 100 years later, and further emphasized that efficient communication between these language centers is required and that their mere disconnection would also result in aphasia [46]. This theory is most commonly known as the Wernicke-Lichtheim-Geschwind model, the classic model, or the house model.

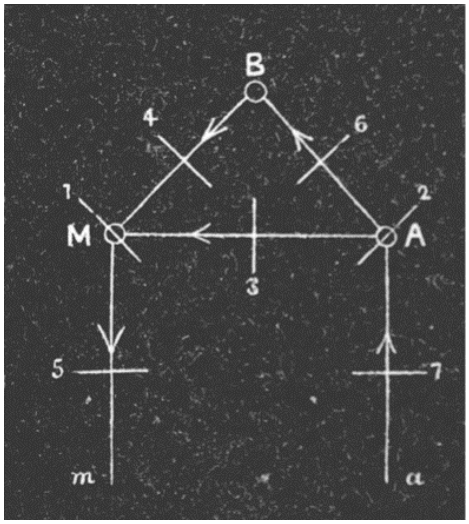

Figure 2.3: Wernicke-Lichtheim-Geschwind "house" model. *Reproduced from On aphasia. By L. Lichtheim, MD, Professor of Medicine in the University of Berne. Brain 1885; 7: 433484.*

The exact anatomical location of these language centers is not entirely well established. A recent survey done by the society for the neurobiology of language showed that 50% of participants (mostly highly experienced language researchers) agreed on the location of Broca's area but only 26% agreed on the anatomical location of Wernicke's area [47]. Figure 2.4 shows both the original definition and location with the majority vote for Broca's and Wernicke's area. The most popular definition coincided with the pars opercularis and pars triangularis of the Inferior Frontal Gyrus (IFG) for Broca's area, and with the posterior

part of the Superior Temporal Gyrus (STG) and the inferior part of the Supra Marginal Gyrus (SMG) for Wernicke's area. Unfortunately, the location of the concept or meaning center was not part of the survey and its whereabouts is also under debate. Lichtheim himself proposed that it was located somewhere subcortically, but the latest research points to the existence of a widely distributed semantic network that interacts with many of the other sensory systems (e.g., vision, gustatory) [48]. The left temporal lobe, however, does seem to play a key role in the final word selection process.

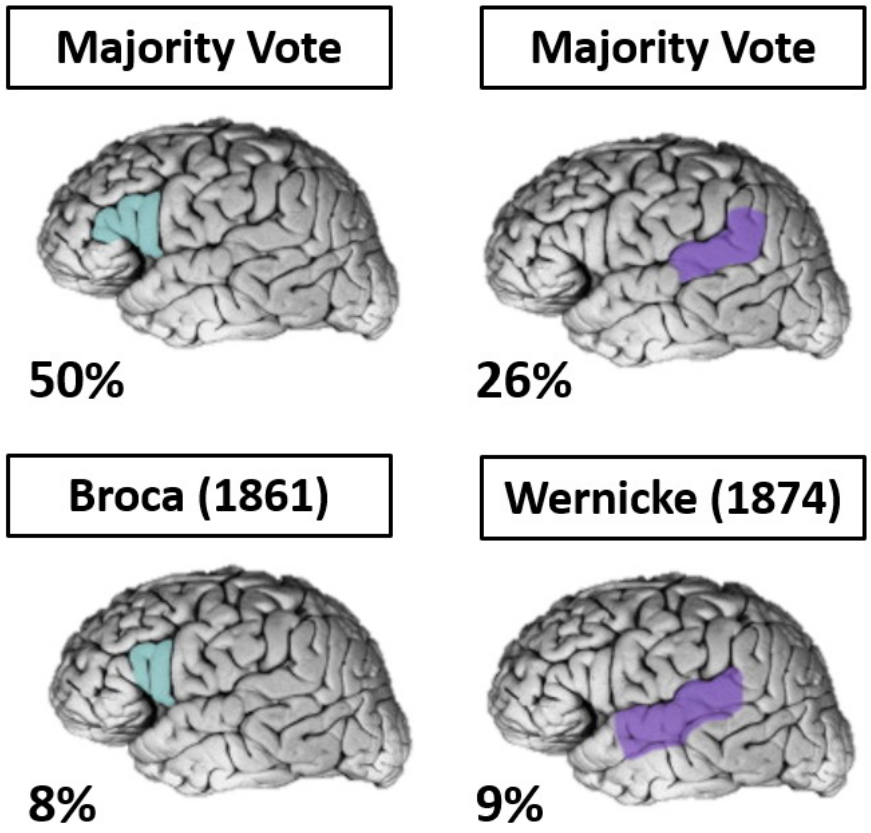

Figure 2.4: Top row: Location of Broca's area (left) and Wernicke's area (right) that received the most votes in a survey done by the society for the neurobiology of language. Bottom row: Original location as put forward by Broca (left) and Wernicke (right). Numbers in the bottom left corner represent the percentage of votes received. *Figure is an adapted version of figure 2 and figure 3 from Tremblay, Pascale, and Anthony Steven Dick. "Broca and Wernicke are dead, or moving past the classic model of language neurobiology." Brain and language 162 (2016): 60-71. with permission from authors*

In 2004, Indefrey and Levelt conducted a meta-analysis, including results of approximately a 100 papers, to resolve the neurobiological origins of the Lemma model [49]. They showed that Wernicke's area is implicated in phonological code retrieval by comparing functional Magnetic Resonance Imaging (fMRI) studies that looked at the activation of language tasks that depend on the phonological code (e.g. picture naming) with activation patterns of tasks that didn't (e.g., pseudoword reading). In the same paper, they demonstrated the involvement of Broca's area in the syllabification of words during naming.

The house model is still included today as a part of all medical school curricula to teach the classification of the different aphasia subtypes, but it is considered mostly obsolete by the research community. One of the main problems with the model is that it is focused on a handful of solitary gray matter areas that function as language hubs. The more modern perspective is that language is supported by a small amount of different language networks. For example, Broca's area is unlikely the sole control center for speech production but likely plays a crucial part in a speech production network. The existence of networks perhaps explains why it is hard to pinpoint a single anatomical location for these language regions. Geschwind already advocated for a more connectionist point of view by introducing the arcuate fasciculus as one of the key language regions (Figure 2.5 left) but we now know that many more white matter structures support language (Figure 2.5 right). Researchers are working on revising and extending the house model, but unfortunately, there is currently not one agreed upon alternative theory. The interested reader can go to [50] for a review.

Dual Stream Model of Language

One such elaborate extension of the house model is the dual stream model of language introduced by Hickok and Poeppel in 2000 (further revised in 2004 and 2007) [51]. It is comparable to the two-stream hypothesis of the visual system, with the basic principle being that the sensory system (in this case the primary auditory cortex) interacts both with a

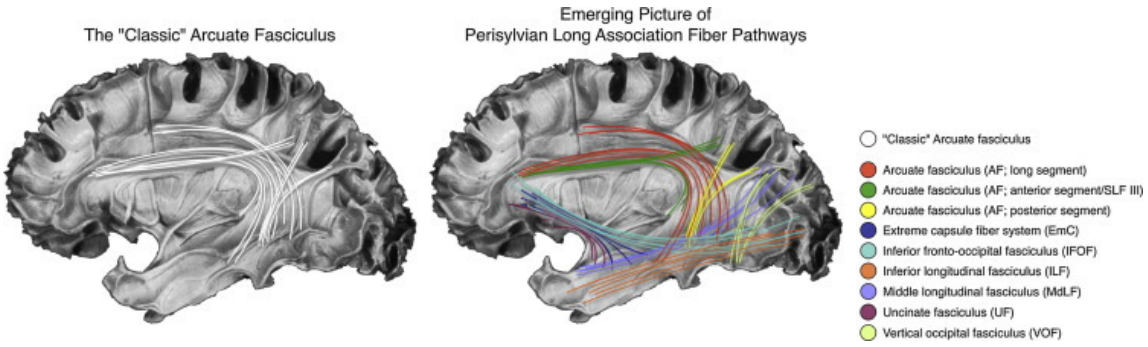

Figure 2.5: An emerging picture of perisylvian long association fiber pathways supporting language. The image on the left shows the "classic" arcuate fasciculus. The image on the right shows the additional fiber pathways that possbily support language. *Reproduced from Tremblay, Pascale, and Anthony Steven Dick. "Broca and Wernicke are dead, or moving past the classic model of language neurobiology." Brain and language 162 (2016): 60-71. with the permission of Elsevier.*

conceptual network (i.e, the ventral stream) and with a network that encodes motor control (i.e., the dorsal stream). Humans rely heavily on both systems while deciding "what word to say" (ventral stream) and "how to say it" (dorsal stream). Convincing evidence for the existence of the two streams comes from the old aphasia literature, which established a double dissociation between speech repetition and auditory comprehension. For example, subjects with transcortical sensory aphasia are able to repeat sentences without understanding them, while patients with conduction aphasia are able to grasp the content of a sentence but are unable to reproduce it. Based on this existing literature, Hickok and Poeppel worked out the most probable segments in each stream and their approximate locations are shown in Figure 2.6left: the ventral stream (pink) encompasses the middle and inferior portions of the temporal lobe, and the dorsal stream (blue) spans from the parietal-temporal junction to Broca's area. Notice how the emerging picture of important Perisylvian white matter pathways for language (from Figure 2.5) overlaps nicely with the black arrows as drawn by Hickok and Poeppel.

Indefrey and Levelt also found evidence in their meta-analysis for the involvement of the temporal lobe in word naming, specifically they implicated the left mid MTG in lemma retrieval and lemma selection (Figure 2.6 right). This area is adjacent to part of the ventral

stream (i.e., lexical retrieval area) as proposed by Hickok and Poeppel which functions as a relay station between phonological representations and semantic content. In addition, the dual stream's phonological network overlaps with the anatomical area put forward by Indefrey and Levelt (i.e., mid-post Superior Temportal Sulcus) for phonological code retrieval. Lastly, both models also point to the Sylvian Temporal-Parietal (SPT) area as a relevant contributor to the interface between the phonological network and the articulatory network. Figure 2.6 summarizes the similarities between the dual stream model (left) and the study done by Indefrey and Levelt that demonstrate the neurobiological underpinnings of their cognitive model (right). To an approximation, we can see that the ventral stream is involved in the first step of word production (i.e, lexical selection) and that the dorsal stream governs the subsequent steps of form encoding and articulation.

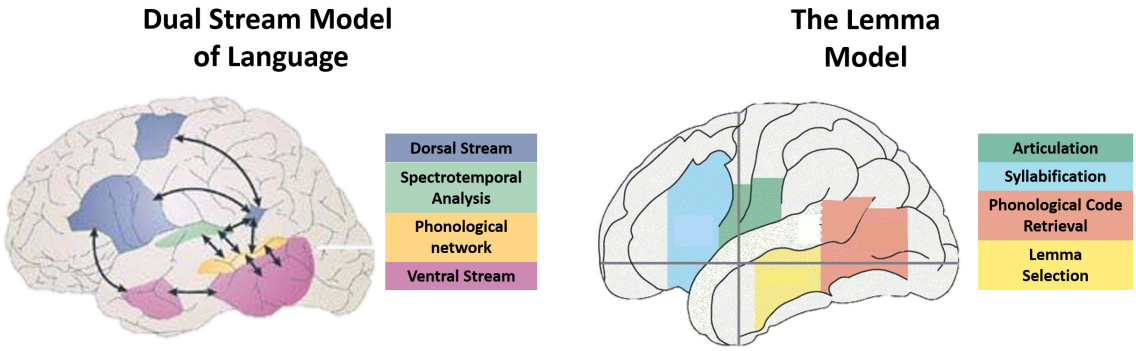

Figure 2.6: Anatomical location of regions involved in word naming. As proposed by the dual stream model of language (left) and the Levelt model (right). *Figure on the left is an adapted version of Figure 1 from Hickok, Gregory, and David Poeppel. "The cortical organization of speech processing." Nature reviews neuroscience 8.5 (2007): 393., with permission from authors and the Figure on the right is an adapted version of Figure 5 from Indefrey, Peter, and Willem JM Levelt. "The spatial and temporal signatures of word production components." Cognition 92.1-2 (2004): 101-144.*

2.3 Anomia

Essentially everybody with aphasia experiences word finding difficulties, or anomia, to some degree. Anomia is extremely diverse and manifestations depend on where in the

word retrieval process (see section 2.2) the problems arise. Identifying at which level the naming difficulties occur is useful to determine the best treatment approach. The most common strategy is to study error patterns during word naming using a confrontational naming test (e.g., Philadelphia Naming Test (PNT)). Naming deficits are often targeted by Speech Language Pathologists (SLP) since they tend to reflect overall communication skills and language therapy has proven to be beneficial for individuals with anomia both at the acute and the chronic state. However, treatment results are inconsistent.

Section 2.2 discussed how word naming is largely a two step process starting with lexical selection and ending with form encoding governed by two anatomically distinct streams. Not surprisingly, confrontational naming in subjects with aphasia is often characterized by two different types of error outputs called semantic and phonemic paraphasias. Breakdowns in the initial steps of word naming (i.e, lexical selection) will result in semantic paraphasias or errors related to the meaning of a word. For example, uttering the semantically related word *table* when shown a picture of a chair. A disruption further down the word forming pipeline will result in a type of speech production error known as phonemic paraphasia. In this case, the spoken word contains incorrect phonemes (e.g., *fable* in stead of *table*). If there is little to no resemblance to the phonemes of the target word the error is classified as a neologism. In some severe cases, mistakes against both semantic content and phonemes can be made at the same time in which case the error is labelled as a mixed paraphasia. Breakdowns can also occur either before lexical selection and/or after form encoding; however, these impairments are not considered under the umbrella that is anomia. For example, failures after form encoding will result in motor control and not linguistic issues, which is defined as apraxia of speech. Failures before lexical selection can arise from deficits in visual and/or conceptual processing. A cognitive test (e.g., pyramid and palm trees) is commonly done to assess impairments in the understanding of words. Often, subjects with anomia are not impaired in their understanding but they are unable to access the correct linguistic construction. Note, that it can be challenging to distinguish

these types of non-linguistic errors from paraphasias.

2.4 Magnetic Resonance Imaging and the Study of Anomia

Our understanding of naming and naming impairments has increased a lot since the early works from Broca and Wernicke, which was largely driven by the development of new technologies. Broadly speaking, there are two approaches to study language: 1) "the theoretical approach", which entails studying the nature of language through response times, error patterns and dissociations, and 2) "the methodological approach", which combines brain mapping techniques and language batteries to unravel its neurobiological origin. Next, we will briefly discuss a few popular brain-mapping methods used to study the brain-language interaction. Even though a wide variety of technologies are used for the study of the brain, e.g.: Electroencephalogram (EEG), Positron Emission Tomography (PET), Transcranial Magnetic Stimulation (TMS), this section will focus on the most common applications of MRI to the study of naming impairments. Specifically, we will briefly cover structural imaging (T_1- and T_2- weighted sequences), functional Magnetic Resonance Imaging (fMRI), and dMRI.

2.4.1 Structural Imaging: T1-weighted and T2-weighted MRI

Tissues types tend to have unique longitudinal (T_1) and transverse relaxation (T_2) times. Some MR sequences take advantage of this difference in relaxation time and use it as their dominant contrast mechanism for visualization (e.g., T_1-weighted or T_2-weighted imaging). For example, liquids like Cerebro Spinal Fluid (CSF) have both a prolonged T_1 and T_2 compared to other brain tissues, which is why CSF appears bright on a T_2-weighted image and dark on a T_1-weighted image (see figure 2.7).

Brain lesions, such as those caused by ischemia, are often clearly visible on T_1- and T_2-weighted images and can be delineated by an expert reader. Lesion maps by them-

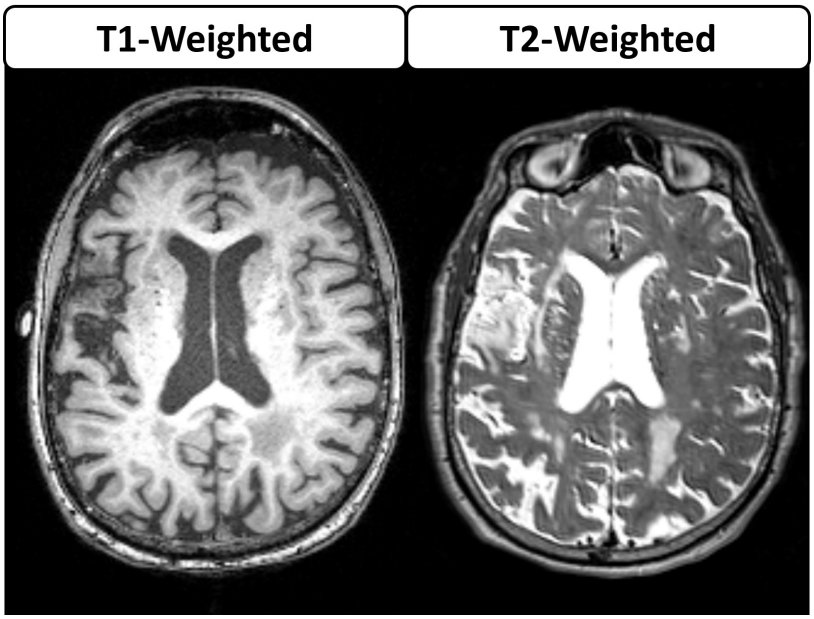

Figure 2.7: Liquids like CSF have long T_1 and T_2 relaxation times resulting in a bright appearance on a T_2-weighted image (right) and a dark appearance on a T_1-weighted image (left).

selves, however, are difficult to interpret but when converted into standard space comparisons between patients are feasible. Two group-analysis strategies are popular: 1) lesion subtraction analysis [52] and 2) Voxel-based Lesion Symptom Mapping (VLSM) [53]. The former method requires one to categorize all subjects into two groups; one group wherein everyone shares a particular deficit and another wherein the deficit is absent. The lesion locations can then be subtracted between both groups and the remaining voxels are often designated as those responsible for the language deficit under study. A disadvantage of this technique is the challenge of creating both groups since language deficits are often not binary. An alternative strategy is VLSM, which entails running a t-test for each voxel to determine if there is a significant difference in a particular behavioral metric between the subjects that have this voxel lesioned versus those that do not. If the t-test is significant, it is often assumed that this particular voxel is important for the behavioral metric under study. Since there are tens of thousands of voxels in the brain, it is important to correct for multiple comparisons. An issue that is worth mentioning here is that traditionally this test is run in a mass univariate way, that is, all voxels are considered to be independent of one

another. However, we now know that the damage between voxels can be highly correlated since they can be part of the same vascular supply [54]. One solution is to do multivariate lesion symptom mapping [55]. VLSM, both uni- and multivariate, is widely used today to study anomia.

2.4.2 Functional Magnetic Resonance Imaging

Blood Oxygen Level Dependent (BOLD) fMRI has been called one of the "greatest methodological success stories in science in the past 20 years". BOLD fMRI visualizes activated brain regions by taking advantage of the difference in magnetic properties between oxyhemoglobin and deoxyhemoglobin in combination with the fact that blood oxygen content changes when oxygen is in higher demand. During activation, neurons require more oxygen and the body's autonomic reaction is to send extra oxygen to these areas. Since deoxyhemgolobin is paramagnetic (shortens T_2), an influx of extra oxygen after activation will result in an increase of the signal. BOLD fMRI has been used extensively by all branches of neuroscience to study the brain behavior relationship. Most commonly, the BOLD signal at rest will be compared to the BOLD signal during a particular task (e.g., word naming). Areas with a significantly lower signal during rest are suggested to be recruited by the brain to complete the task at hand.

2.4.3 Diffusion Weighted Magnetic Resonance Imaging

Chapter 1 explained in detail the theory behind dMRI and how it can be used to probe tissue microstructure. dMRI has been gaining popularity in recent years to study anomia since it is ideally suited to probe white matter connections and their integrity (for more details see section 2.5). Unfortunately, the interpretation of dMRI is still a challenge, which this thesis attempts to improve upon in Chapter 4.

2.5 Challenges and Unanswered Questions

Even though 60% of persons with aphasia exhibit near or complete spontaneous recovery within the first 6 months, many have long-lasting language deficits. As mentioned earlier, the treatment for chronic aphasia consists of speech therapy, which can lead to remarkable improvement. However, because post-stroke brain damage is different for each patient, the clinical outcomes are unpredictable. Unfortunately, conventional metrics of cortical post-stroke damage can only partly explain the severity of aphasia and the likelihood of treatment success; moreover, this limitation may likely be related to the degree of white matter damage beyond the stroke lesion that is pervasive after strokes and not usually mapped. Cerebral ischemia can result in significant gray and white matter injury, with previous studies showing that white matter, after adjusting for metabolic demands, might actually be more vulnerable to ischemia than gray matter. Notwithstanding, many studies focus on cortical necrosis or lesion overlap on structural MRI as an indicator for clinical representation and recovery potential(see section 2.4.1). Previous studies in our lab have shown that white matter damage can continue beyond the necrotic stroke lesion, suggesting that white matter integrity is compromised in an area larger than initially expected, and connectivity (not only lesion overlap) between gray matter regions should be included. Thus, a more detailed evaluation of white matter networks in aphasia is central to a better understanding of linguistic deficits and recovery outcomes. Several connectivity studies have already attempted to resolve this issue, although those studies mostly investigated the number of tracts present. This approach has been criticized in the past as it can be influenced by diffusion anisotropy, curvature, and the length of connections independent of connectivity strength. It is likely more informative to study the microstructure of the residual language network (e.g., using DKI). In addition, the white matter connections of the dual stream model of language remain largely unexplored. Having empirical validation of this model would help us better understand the neurobiology of naming and speech

production. Chapter 3 of this dissertation will focus on the assessment of residual white matter networks in patients with aphasia in order to serve two aims: 1) to determine the crucial networks supporting semantically and phonologically correct speech production, and 2) to quantify longitudinal changes in WM microstructure (neuroplasticity) and how they support treatment-mediated recovery.

CHAPTER 3

IMPACT OF REGIONAL WHITE MATTER INTEGRITY ON POST-STROKE LINGUISTIC DEFICITS UNDERLYING ANOMIA AND ANOMIA RECOVERY

This chapter is based on the following publications:

- **McKinnon, Emilie T.**, Julius Fridriksson, Alexandra Basilakos, Gregory Hickok, Argye E. Hillis, M. Vittoria Spampinato, Ezequiel Gleichgerrcht, Chris Rorden, Jens H. Jensen, Joseph A. Helpern, and Leonardo Bonilha. "Types of naming errors in chronic post-stroke aphasia are dissociated by dual stream axonal loss." Scientific reports 8, no. 1 (2018): 14352.

- **McKinnon, Emilie T.**, Julius Fridriksson, G. Russell Glenn, Jens H. Jensen, Joseph A. Helpern, Alexandra Basilakos, Chris Rorden, Andy Y. Shih, M. Vittoria Spampinato, and Leonardo Bonilha. "Structural plasticity of the ventral stream and aphasia recovery." Annals of neurology 82, no. 1 (2017): 147-151.

- **McKinnon, Emilie T.**, Jensen H. J., Rorden C.,Basilakos A., Gleichgerrcht E., Fridriksson J, Helpern A. Joseph and Bonilha Leonardo. Perilesional white matter microstructure and aphasia recovery. Abstract presented at SNL 2018. Proceedings of the Society for the neurobiology of language; 2018 August 16-18; Quebec City, Canada.

- **McKinnon, Emilie T.**, Marebwa B., Rorden C.,Basilakos A., Gleichgerrcht E., Fridriksson J. and Bonilha Leonardo. Synergism between cortical damage and white matter disconnection contributes to aphasia severity. Oral presented at SNL 2018. Proceedings of the Society for the neurobiology of language; 2018 August 16-18; Quebec City, Canada.

3.1 Introduction

In this chapter, we investigate if the regional integrity of the white matter network is a strong predictor of specific linguistic deficits as predicted by the dual stream model (Section 3.2). We hypothesized that a double dissociation exists, where residual structural dorsal stream integrity is a determinant of phonological processing, whereas ventral stream integrity is a determinant of semantic processing. We employed DKI-based tractography to locate white matter pathways focusing on the superior and inferior longitudinal fasciculi (dorsal and ventral stream, respectively) and quantified their integrity using DKI-based diffusion metrics. Using a multivariate analysis we assessed their contribution, along with cortical

damage and aphasia characteristics, to phonological and semantic paraphasias during naming prior to therapy. In section 3.3, we also explored if improvements on confrontational naming tasks were supported by changes in white matter microstructural integrity of existing fibers. Recovery related neuroplasticity is often associated with the strengthening or the reestablishment of structural connections. We hypothesized that therapy-related improvements in semantic and phonological processing would result in detectable changes in the ventral and dorsal stream respectively. DKI-based metrics calculated along the streams before and after therapy were used in a multivariate analysis to assess if their local reconfigurations related to improvements in phonological and semantic processing after therapy. Next, we present some preliminary pilot data on predicting therapy outcomes from baseline white matter integrity (Section 3.4) and on the synergism between gray and white matter damage (Section 3.5)

The last section, section 3.6, will cover the development of a new and improved pipeline for the study of anomia after stroke. The studies performed in Section 3.2 and 3.3 were limited in their study of whole brain white matter integrity. That is, they focused on specific white matter tracts without taking into account the integrity of most other fiber bundles. In addition, there was no knowledge of the cortical regions that were being connected by the white matter bundles under study. The new pipeline provides the opportunity to do a whole brain white matter integrity assessment between hundreds of cortical ROIs.

3.2 Types of Naming Errors in Chronic Post-Stroke Aphasia are Dissociated By Dual Stream Axonal Loss

3.2.1 Introduction

Many stroke survivors experience language impairments (aphasia) beyond six months after a dominant hemisphere stroke [56]. One of the most common and debilitating impairments in individuals with chronic aphasia is the inability to accurately produce language,

commonly represented by difficulties in naming objects or actions (anomia) [57, 58, 59]. Naming is often assessed in the clinical setting through confrontational naming tests, during which the individual with anomia is either unable to produce the correct name for a target item, or generates words that are related in sound or meaning with the target (paraphasias). Paraphasias are erroneous attempts that relate to the target, but are inaccurate regarding the chosen speech units (phonemic paraphasias), or are real words that relate in meaning to the intended word (semantic paraphasias). For example, when shown a picture of a pencil, a phonemic paraphasia could be an utterance such as wencil, whereas a semantic paraphasia could be pen.

Paraphasias offer a critical window into the mechanisms of speech production because they represent discrete deficits regarding 1) the spoken sound structure (phonemic) vs. 2) speech related knowledge association (semantic). They provide the opportunity to determine if these processes dissociate into different anatomic-functional pathways. Notably, they permit the assessment of a recent neurolinguistic theory, the dual stream model of speech processing, which suggests that distinct anatomical streams map phonological and lexical-semantic content retrieval during speech processing [51]. The model suggests the existence of two streams: a ventral, or what stream, which maps between lexical and semantic representations of knowledge associations, and a dorsal, or how stream, that maps between auditory and articulatory-motor representations for phonological production. In the context of a naming task, both networks are assumed to participate at integrated different levels of the naming process, lexical-semantic (ventral networks) and phonological encoding (dorsal networks). Paraphasias have been explored in the context of the dual stream model using computer simulations of speech data [60], lesion symptom mapping [61, 62, 63, 64, 65, 66, 67], and direct electrical cortical and subcortical stimulation in the intra-operative setting [68]. However, the relationship between residual white matter network integrity, subcortical networks (specifically in relationship to core tracts in the ventral and dorsal streams), and speech production errors is not yet fully defined.

As introduced in Chapter 1, dMRI is ideally suited to study post-stroke residual white matter integrity non-invasively and to test the hypothesis that semantic and phonological processing dissociates between the ventral and dorsal white matter pathways. Specifically, dMRI permits the estimation of the remaining anatomical connections between brain regions through tractography, as well as an assessment of the microstructural integrity of these connections. The quantification of pathway-specific white matter integrity in stroke survivors with chronic aphasia allows for the evaluation of the relationship between regional white matter integrity and specific types of language deficits. This process is analogous to classical neuropsychological approaches which relate brain lesions to behavioral deficits, but it can leverage white matter tractography to identify residual pathways associated with language processing. Moreover, since dMRI also provides measures sensitive to axonal integrity, it can improve the sensitivity in determining which pathways are associated with phonological vs. semantic deficits and resolve the underlying neurobiological mechanisms of regional brain damage that contribute to speech production errors. In contrast with lesion-symptom mapping, which can provide information on damage to white matter regions, without directly testing the integrity of specific pair-wise connections, dMRI can provide information on the integrity and microstructural properties of residual regional connections.

The AWF, i.e., the ratio of intra-axonal water to total MRI-visible water, reflects axonal density by assessing the portion of tissue water that resides inside axons. Multi-shell dMRI permits an estimation of AWF through the calculation of the diffusional kurtosis by fitting a second-order Taylor expansion to the decay of the logarithm of the dMRI signal as a function of diffusion weighting strength following the theory for DKI [27, 16]. FA is a dMRI measure more commonly used to investigate white matter microstructure [69]. However, FA is a generic indicator of diffusion anisotropy [70]. AWF can indicate brain damage through axonal loss [71] and provides information complementary to FA that allows for a more comprehensive quantification of brain tissue properties. More microstructure specific

diffusion metrics (e.g. AWF) should be used in conjunction with more traditional metrics (e.g. FA, $\bar{D}$) to enhance our understanding of the mechanisms underlying FA and $\bar{D}$ changes, and ultimately brain pathology.

In this study, we examined whether the degree of ventral vs. dorsal stream damage dissociates the proportion of phonemic and semantic paraphasias in a group of individuals with chronic aphasia. We employed multi-shell dMRI, DKI post-processing and the quantification of AWF and FA along stream-specific fiber pathways obtained from each individual with aphasia. Tract-specific measures were assessed in relation with paraphasias using multivariate statistical analyses. We hypothesized that in chronic stroke axonal loss, reflected by a decreased AWF in the ventral but not dorsal stream, would directly associate with semantic but not phonological paraphasias and vice versa.

3.2.2 Materials and Methods

Subjects

We studied 32 participants with chronic post-stroke aphasia (age: 57 $\pm$ 11 y, time post-stroke: 35 $\pm$ 30 mos, gender: 8 women). All subjects were recruited through local advertisement at the Medical University of South Carolina. They were right-handed native English speakers with a history of a single previous ischemic in the left hemisphere at least 6 months before enrollment. Demographics and behavioral information is presented in supplementary Table A.1. Participants with a history of developmental language disorders, other neurological or psychiatric problems, brain surgery or with seizures during the previous 12 months were excluded. This study was approved by the Institutional Review Boards at the Medical University of South Carolina and the University of South Carolina. Written informed consent was obtained from all participants or their legal guardians. All methods were performed in accordance with guidelines and regulations from our Institutional Review Board (IRB).

Assessment of naming

Participants were tested using the Western Aphasia Battery-Revised (WAB-R) [72] to screen different language abilities and obtain a global measure of aphasia. The Pyramids and Palm Trees Test (PPT) [73] was used to determine semantic knowledge, and the PNT [74] was used to test confrontational naming. The PNT was repeated within one week to determine intra-subject variability. During the PNT, participants had 10 seconds to produce a response. The last complete attempt was used for scoring. Semantic paraphasias were defined as all incorrect real word responses related to the target in meaning. Phonological paraphasias were defined as real word attempts with phonological similarities as well as non-word attempts with incorrect phonemes that preserved more than 50% of the target word. Circumlocutions were scored as no response; dysfluency as articulation errors, and partially phonologically related words were considered to be phonological errors (or, if it was more than 50% different than the target, a neologism). In the case of visual errors (e.g., person says "house" for the "garage"), we redirected the subjects and clarified so they knew which part of the picture to respond to. If the visual errors persisted they were coded as semantic paraphasias. Mixed paraphasias and articulation errors were not included in the analysis. The PNT results from both sessions were averaged, and semantic and phonemic paraphasias were expressed as a percentage of naming attempts excluding the number of no responses since we were interested in semantic and phonemic paraphasias when naming was attempted. All standardized speech and language tests were administered and scored by an experienced American Speech-Language-Hearing Association-certified SLP.

Image Acquisition

All participants were scanned on a Siemens 3T TIM Trio MRI scanner (Siemens Healthcare, Erlangen, Germany) using a 12-channel head coil at the Medical University of South Carolina. Data were acquired in three series, with three degrees of diffusion weighting (b-value = 0, 1000, $2000\,\mathrm{s/mm^2}$), using 30 diffusion-encoding directions acquired twice

for each $b = 1000$ and $b = 2000$, as well as eleven additional images without diffusion weighting ($b = 0$), for a total of 131 volumes. Additional acquisition parameters were: TE = $101\,\mathrm{ms}$, TR = $6100\,\mathrm{ms}$, $2.7\,\mathrm{mm} \times 2.7\,\mathrm{mm} \times 2.7\,\mathrm{mm}$ isotropic voxels, pixel bandwidth = $1355\,\mathrm{Hz/px}$. All DWI were acquired using a twice-refocused gradient scheme to minimize the contributions of eddy currents and without partial Fourier encoding. High resolution $1\,\mathrm{mm}^3$ isotropic T2-weighted images were acquired for lesion demarcation utilizing a 3D-TSE SPACE protocol (Field of View (FOV) = $256\,\mathrm{mm} \times 256\,\mathrm{mm}$, 160 sagittal slices, Repetition Time (TR) = $3200\,\mathrm{ms}$, Echo Time (TE) = $212\,\mathrm{ms}$, turbo factor = 129, echo trains per slice = 2, echo train duration = $432\,\mathrm{ms}$) and, for anatomical reference, T1-weighted images were gathered using an isotropic 1 mm MPRAGE sequence: FOV = $256\,\mathrm{mm} \times 256\,\mathrm{mm}$, 9° flip angle, Inversion Time (TI) = $925\,\mathrm{ms}$, TR = $2250\,\mathrm{ms}$, TE = $4.15\,\mathrm{ms}$.

Image Data Processing

The assessment of tract-specific microstructure included the calculation of scalar diffusion metrics along the length of the white matter fibers. The terms fiber or bundle are used here to indicate the deterministic paths identified by diffusion tractography, which are the biophysical representation of large collections of axonal projections in white matter. In this study, we employed three novel forms of structural white matter analyses: a) patient specific white matter tractography was performed using DKI, a technique that requires a multi-shell diffusion acquisition and dedicated post-processing procedures to improve upon tractography through the delineation of fiber crossings [75, 76]; b) the integrity of individual fibers was described using microstructural modeling metrics (i.e. AWF) derived from DKI [27], which provide a more specific description of the underlying microstructure than conventional dMRI metrics (i.e. FA); and c) AWF and FA- were assessed in a fine grained pattern along specific tracts, enabling a detailed assessment of where and how post-stroke integrity can affect language. Figure 3.1 highlights these methodologies; all techniques are explained in further detail below.

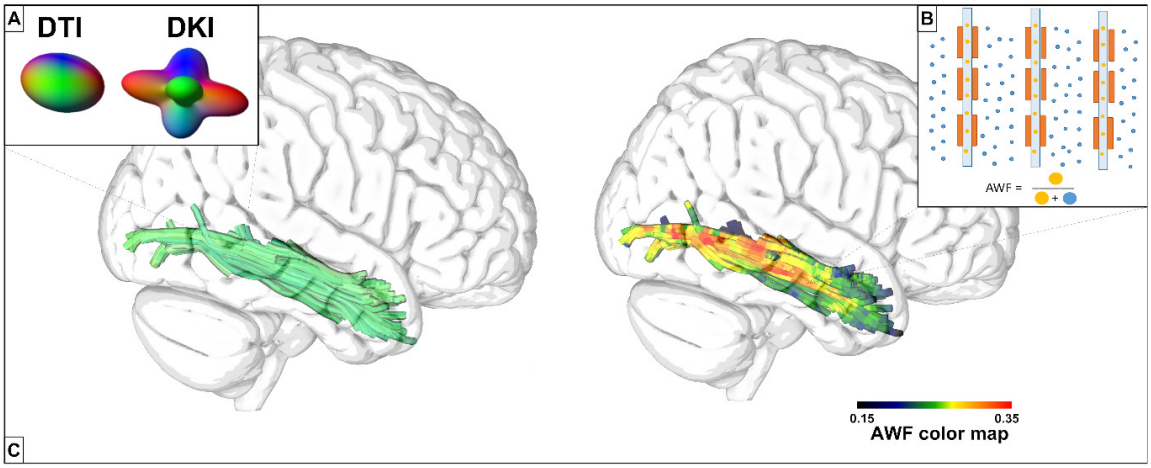

Figure 3.1: A: DKI allows for voxel-wise estimation of the number of fiber directions through the calculation of a kurtosis dODF, while the dODF estimated from DTI provides only a single direction. B: The AWF is the voxelwise ratio of intra-axonal water (orange) to the total water content (orange+blue). C: (Left) The ILF estimated using kurtosis-based deterministic tractography with streamlines color-coded according to directionality. (Right) The ILF color-coded according to the underlying AWF values. Augmenting tractography with microstructural information paints a more complete picture of the underlying environment.

DKI Tractography

As introduced in section 1.2.2 *Diffusional Kurtosis Imaging*, DKI is an extension of the more conventional DTI method [11] that provides a more thorough characterization of white matter microstructure, as well as allowing for more accurate fiber tractography [75, 16]. In addition to the standard diffusion measures available with DTI, DKI also estimates the diffusional kurtosis, which quantifies the non-Gaussianity of the underlying water diffusion process [16]. The dMRI signal model for DTI can be expressed as:

$$ln[S(b,\mathbf{n})/S_0] \approx -bD, \tag{3.1}$$

while the signal model for DKI is

$$ln[S(b,\mathbf{n})/S_0] \approx -bD(\mathbf{n}) + \frac{1}{6}b^2D^2(\mathbf{n})K(\mathbf{n}). \tag{3.2}$$

where $S(b)$ is the measured dMRI signal at diffusion weighting b, S_o is the signal intensity for $b = 0\,\mathrm{s/mm^2}$, D is the apparent diffusion coefficient, and K is the apparent

diffusional kurtosis.

Analogous to the diffusion tensor, a kurtosis tensor, which describes the kurtosis dependence on direction, can be constructed with DKI [16]. The kurtosis tensor permits the assessment of the underlying microstructure through scalar metrics of kurtosis, which characterize the complexity of the brain cytoarchitecture, and it provides a voxel-wise description of fiber orientations and their crossings through the calculation of a kurtosis dODF (Figure 3.1) [18]. This is in contrast to other commonly used methods that explicitly model fiber crossings (e.g. bedpostX) [77]. Previous work has demonstrated high sensitivity to pathology when using mean kurtosis as a measure of tissue microstructure [78, 79, 80, 81, 82, 83], as well as tractography that identifies intra-voxel fiber crossings that are not apparent with DTI [76].

Diffusion and kurtosis tensors were estimated using publicly available post-processing software known as Diffusional Kurtosis Estimator (DKE) [84] (Medical University of South Carolina, Charleston, USA, https://www.nitrc.org/projects/dke/). To improve the signal-to-noise ratio, raw dMRI images were first denoised using a principal components analysis approach [85], and, Gibbs ringing artifacts were removed using the method of Kellner et al. [86, 87]. All DWI acquisitions including the additional images with b = 0 were linearly coregistered between themselves using FMRIB Software Library v5.0 (FSL)[88] before averaging them into a final set of 61 image volumes which was used as the input for DKE.

To localize ventral and dorsal stream white matter, we constructed tractography seed masks for two major components of the dual stream pathway: Inferior Longitudinal Fasciculus (ILF) (ventral stream) and Superior Longitudinal Fasciculus (SLF) (dorsal stream). For each participant, we located the core of each white matter bundle by calculating the intersection between the Johns Hopkins University (JHU) atlas [89] (SLF thresholded at

21% (20/97) and ILF at 25% (20/79)) and a white matter probability mask (thresholded at 50%) created using Statistical Parametric Mapping (SPM)12, while excluding any lesioned voxels that were drawn on the T2-weighted images. Lesions included the entire post-stroke cavity as well as areas with laminar necrosis and gray and white matter gliosis. Enantiomorphic unified segmentation-normalization [90] was employed to calculate the spatial transformation between MNI and native T1-space (Clinical Toolbox, SPM12 [91]) taking into account lesions. This transformation was used to transfer the JHU atlas to native T1-weighted space, while the linear transformation from native T1-weighted to native diffusion space was calculated using FSL

The individual ILF and SLF seed masks were used for deterministic kurtosis-based white matter tractography using the FT-toolbox from DKE, which estimates fiber directions from both diffusion and kurtosis tensors. Streamlines were removed when the probability of belonging to a neighboring white matter bundle, defined by the overlap between the streamline coordinates and the JHU ROIs, was larger than the probability of belonging to the target bundle. Additional tractography parameters were FA-threshold = 0.1, angular threshold = $35°$, minimum track length = $20\,\mathrm{mm}$, step size = $1\,\mathrm{mm}$ and seed number = 1000.

White matter lesion overlap was calculated as the cross-section between the manually delineated lesion mask and the third quartile of the JHU SLF and ILF ROIs. The third quartile was chosen to provide an inclusive representation of white matter lesion overlap, i.e., regions of the tract that were damaged. Crucially, all analyses were performed in native diffusion space, reducing interpolation artifacts.

Microstructural Modeling: Axonal Water Fraction

As established in Section 1.2.3, from the kurtosis tensor it is also possible to calculate information related to specific microstructural compartments (i.e., axonal vs. extra-axonal)

[27]. AWF is a metric, obtained through the WMTI method, which estimates the relative amount of water inside axons to the total water content within one voxel (Figure 3.1) [27]. Specifically, AWF is estimated by

$$AWF = \frac{K_{max}}{K_{max} + 3}, \tag{3.3}$$

where K_{max} is the maximal directional kurtosis calculated from the kurtosis tensor over all possible directions. Tissue modelling leverages neurobiological characteristics from tissue structure, which are translated into biophysical properties as follows: 1) axons can be approximated to long impermeable thin cylinders that are mostly coplanar, 2) diffusion in the extra-axonal water pool can be approximated as Gaussian, and 3) water exchange between compartments is negligible during the MRI sampled diffusion time ($\sim 50\,\mathrm{ms}$). Except for the coplanarity condition, these are generally accepted properties of white matter that have been assumed in a variety of different tissue modeling approaches [92]. Because Equation 3.3 requires the axons to be coplanar, it may not be accurate in some white matter regions with complex patterns of fiber crossings [27]. In summary, we focused on the conventional metric FA, calculated from the diffusion tensor, and the tissue modeling metric AWF, determined from the kurtosis tensor (Equation 3.3). AWF was calculated from the kurtosis tensor using in-house scripts. FA was calculated using a DKI-based approach to improve its accuracy [93].

Along Tract Metrics

Figure 3.2 demonstrates how FA and AWF were quantified along the length of two distinct white matter fiber bundles. To enable comparisons between individuals, we isolated the core of each bundle using a methodology based in part on Automated Fiber Quantification (AFQ) [94]. While the AFQ pipeline performs whole brain seeding and uses the JHU atlas to assign each streamline to their respective fiber bundle, we created different seed masks to locate the specific bundles. The isolation of the core was performed based

on the methods proposed in the original AFQ description with the exception that a straightforward averaging was used to identify the final values compared to a distance-weighted average in AFQ. Specifically, each subjects fiber bundle was cropped at similar locations employing the JHU-ROIs [95], with each streamline being interpolated into 100 equidistant points using cubic B-splines [96] (Figure 3.2, middle). Cropping provides the streamlines with similar starting and ending points, which facilitates the identification of the core components of each tract. By assessing equivalent segments across patients, it is possible to relate their integrity with individualized naming performance through statistical analyses. AWF and FA values were quantified at each point, but to facilitate statistical analysis, we assigned the average metric to each point along the fiber bundles geometric mean resulting in 100 values along the length of the ILF and SLF sections that were ultimately binned into 4 segments containing 25 nodes each (Figure 3.2). In what follows, these midsections will be referred to as the SLF and ILF.

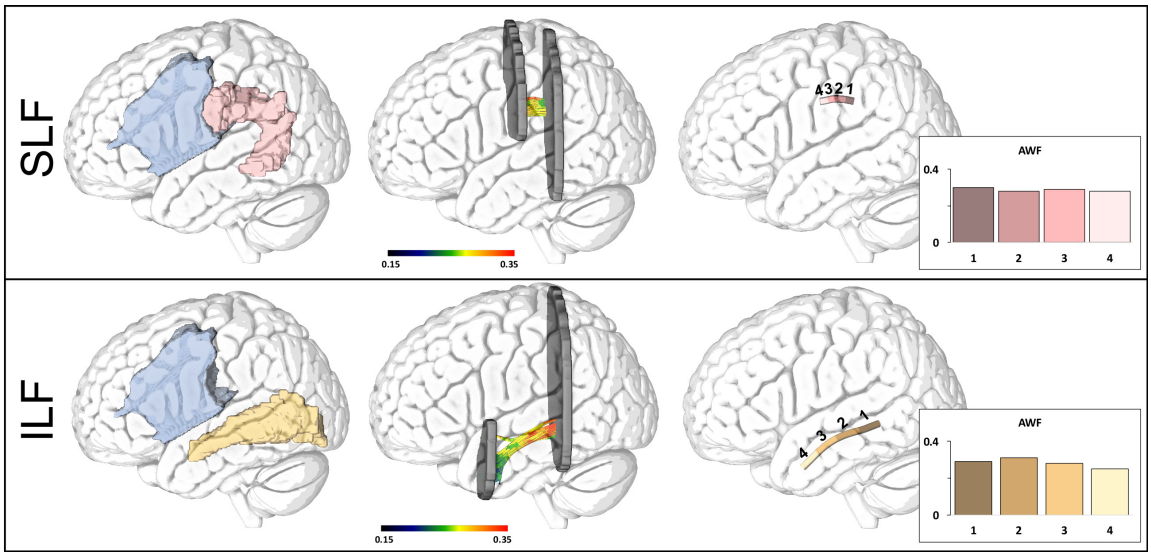

Figure 3.2: Image processing pipeline used to construct the average SLF and ILF for a representative individual. Individual seedmasks (left) for the ILF (beige) and the SLF (pink) were constructed and used as starting points for deterministic tractography. Lesioned voxels (blue) were excluded from each seedmask. The tractography results were cropped (middle), averaged and divided into 4 different segments (right) in each of which we calculated the average AWF

Gray Matter Necrosis

To investigate the interaction between dual stream gray matter necrosis and white matter integrity, we defined three gray matter ROIs: supra-Sylvian language-processing gray matter regions (dorsal stream) infra-Sylvian language-processing gray matter regions (ventral stream) identified using fMRI [97] and the SMG. Gray matter necrosis was calculated as the percent overlap between the stroke lesion and the gray matter ROIs as defined by the JHU atlas [98]. Suprasylvian gray matter included the left posterior Middle Frontal Gyrus (pMFG), the left IFG pars opercularis, the left IFG pars triangular, and the left Angular Gyrus (AG). Infrasylvian gray matter was composed by the STG, the pole of the STG, the MTG, the Posterior Superior Temporal Gyrus (pSTG) and the posterior Middle Temporal Gyrus (pMTG). Damage to the SMG was also quantified since it has been implicated in phonological processing [62]. Lesion locations can be found in supplementary Figure A.1.

Statistical Analysis

We created multiple linear regression models to assess the relationship between paraphasias and integrity of the ventral and the dorsal streams. Specifically, we used the percentage of semantic or phonemic paraphasias as dependent variables in two separate multiple linear regression models with SLF integrity (i.e., AWF and FA), as well as ILF integrity at four distinct tract locations as predictors controlling for white matter lesion overlap. We also assessed whether the inclusion of gray matter damage influenced the model. All reported correlation coefficients are Pearson r. P-values were adjusted using the Bonferroni correction. Fisher r-to-z transformations were performed to investigate if the dissociations between the dorsal and the ventral stream integrity and semantic and phonemic paraphasias were statistically significant.

3.2.3 Results

Language Tests

Western Aphasia Battery - Aphasia Quotient (WAB-AQ), aphasia types and average PNT results for all individuals are summarized in supplementary table A.1. Aphasia ranged from severe to mild (WAB-AQ = [20.1-93.7]), with an average ($\pm$ standard deviation) WAB-AQ of 54.1 ($\pm$ 22.5). During confrontational naming, participants elicited an average of 36.0% ($\pm$ 27.1) correct responses. Incorrect responses were identified as semantic paraphasias 14.7% ($\pm$ 12.5) and phonemic paraphasias 7.1% ($\pm$ 8.3) of the time. The PPT [73] demonstrated that the semantic association pathway between pictures and their meaning was relatively preserved in the majority of subjects (45 $\pm$ 5).

Tract-Based Integrity Analysis

As explained in the methods, we used along tract quantification to assess AWF and FA along the longitudinal length of individual fiber bundles in order to provide a more detailed evaluation of tract integrity. Both the residual ILF and SLF were identified in 18 out of 32 subjects, while only the residual ILF was located in an additional 11 subjects. There were no cases where the SLF was not accompanied by the ILF. All subsequent tract-based analyses were performed on these residual connections. Table 3.1 and 3.2 summarize the interactions between 1) the percentage of semantic and phonemic paraphasias and 2) the average AWF (Table 3.1) and FA (Table 3.2) at different parts along the ILF and SLF. As described in Table 3.1, semantic paraphasias had the highest relationship with the average AWF within the posterior portion of the ILF (segment 1: r=-0.67 and segment 2: r=-0.63, p¡0.05 corrected). Figure 3.3 shows the scatter plots (and their line of best fit with 95% confidence intervals) demonstrating the distribution of the percentage of semantic paraphasias and the AWF from each segment of the ILF. The FA of sections 1, 2 and 3 were also significantly correlated with semantic paraphasias (r= -0.66, r= -0.56 and r= -0.58, p¡0.05

corrected). However, neither AWF nor FA along the length of the SLF was associated with the percentage of semantic paraphasias.

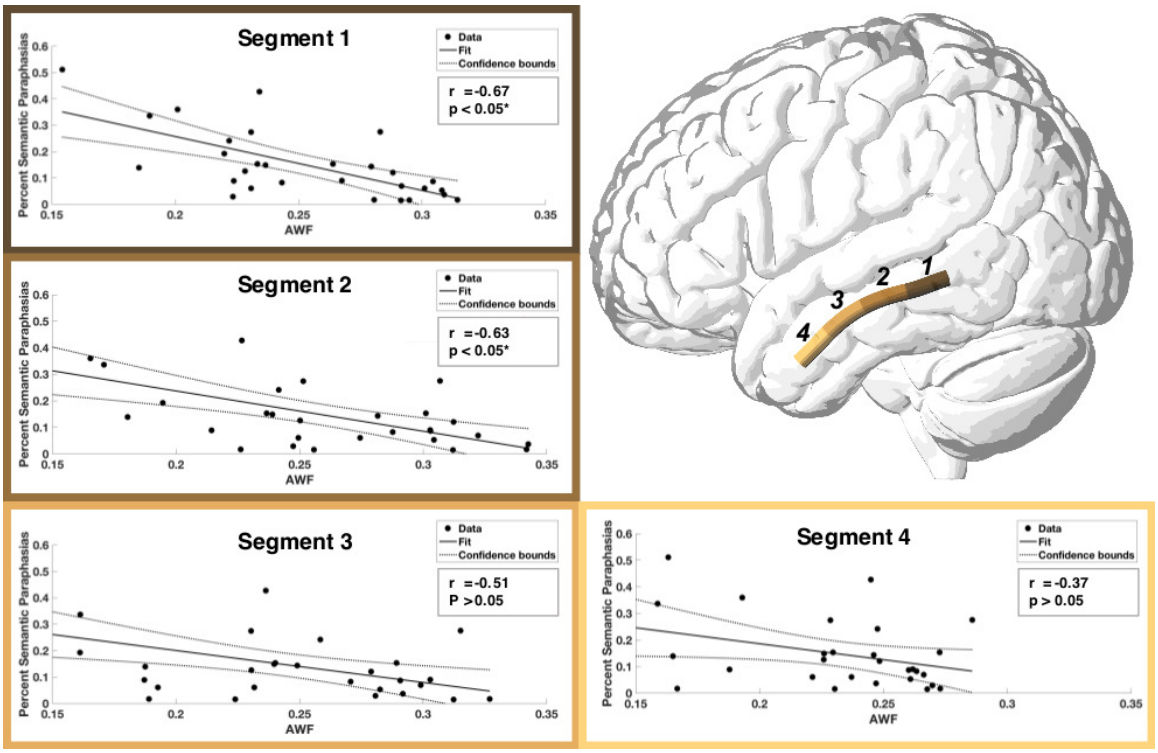

Figure 3.3: Scatterplots demonstrating the relationship between AWF and percent semantic paraphasias. Average AWF was calculated for different segments of equal size along the length of the ILF. A significant association was seen between the AWF and semantic paraphasias in the two most posterior segments (I & II; r=-0.67, r=-0.63) (after correction for multiple comparisons).

The weak association between semantic paraphasias and the SLF diffusion measurements was not related to the smaller sample size of SLF compared to ILF (18 vs. 29). For a similar R-value (0.67), the statistical power from $n = 29$ to $n = 18$ drops from 0.98 to 0.88. We performed 1000 random sampling of the ILF with n=18, the average R-value was 0.65, and $r = 0.21$ was below the 99th percentile of this sample. For this reason, the relationship between the SLF and semantic paraphasias was not significant taking into account the smaller sample size. In addition, Fisher r-to-z demonstrated that the AWF within the ILF (segment 1) related more strongly to semantic paraphasias than the AWF within the SLF (segment 1) ($p < 0.05$).

Table 3.1: Summary of all correlation coefficients between average AWF, calculated along the length of the ILF and the SLF, and both phonemic and semantic paraphasias. (* $p<0.05$, corrected for multiple comparisons)

Dependent Variable	Region	Segment	r	r (corrected for lesion overlap)
Semantic Paraphasias	**ILF**	I	**-0.67***	**-0.49***
		II	**-0.63***	-0.4
		III	-0.51	—-
		IV	-0.36	—-
	SLF	I	0.21	—-
		II	0.35	—-
		III	0.42	—-
		IV	0.31	—-
Phonemic Paraphasias	**ILF**	I	0.25	—-
		II	0.14	—-
		III	0.15	—-
		IV	0.08	—-
	SLF	I	**-0.68***	**-0.65***
		II	-0.52	—-
		III	-0.47	—-
		IV	-0.39	—-

Table 3.2: Summary of all correlation coefficients between FA, calculated along the length of the ILF and the SLF, and both phonemic and semantic paraphasias. (* $p<0.05$, corrected for multiple comparisons)

Dependent Variable	Region	Segment	r	r (corrected for lesion overlap)
Semantic Paraphasias	**ILF**	I	**-0.66***	-0.44
		II	**-0.56***	-0.31
		III	**-0.58**	-0.37
		IV	-0.3	—-
	SLF	I	0.07	—-
		II	0.16	—-
		III	0.25	—-
		IV	0.06	—-
Phonemic Paraphasias	**ILF**	I	0.12	—-
		II	0.13	—-
		III	0.15	—-
		IV	0.16	—-
	SLF	I	-0.46	—-
		II	-0.29	—-
		III	-0.24	—-
		IV	-0.33	—-

Phonemic paraphasias had the most significant association with the average AWF within the most posterior part of the SLF (segment 1: $r = -0.68$, $p < 0.05$) (Table 3.1). The distribution of phonemic paraphasia prevalence and average AWF calculated from the different parts of the SLF is depicted in Figure 3.4. The FA of segment 1 was weakly associated with phonemic paraphasias, albeit not surviving correction for multiple comparisons ($r = -0.46$, $p > 0.05$). The percentage of phonemic paraphasias was not related to any of the diffusion metrics calculated from the ILF. Fisher r-to-z transformations confirmed that phonemic paraphasias were more associated with AWF within segment 1 of the SLF than within segment 1 of the ILF ($p < 0.05$).

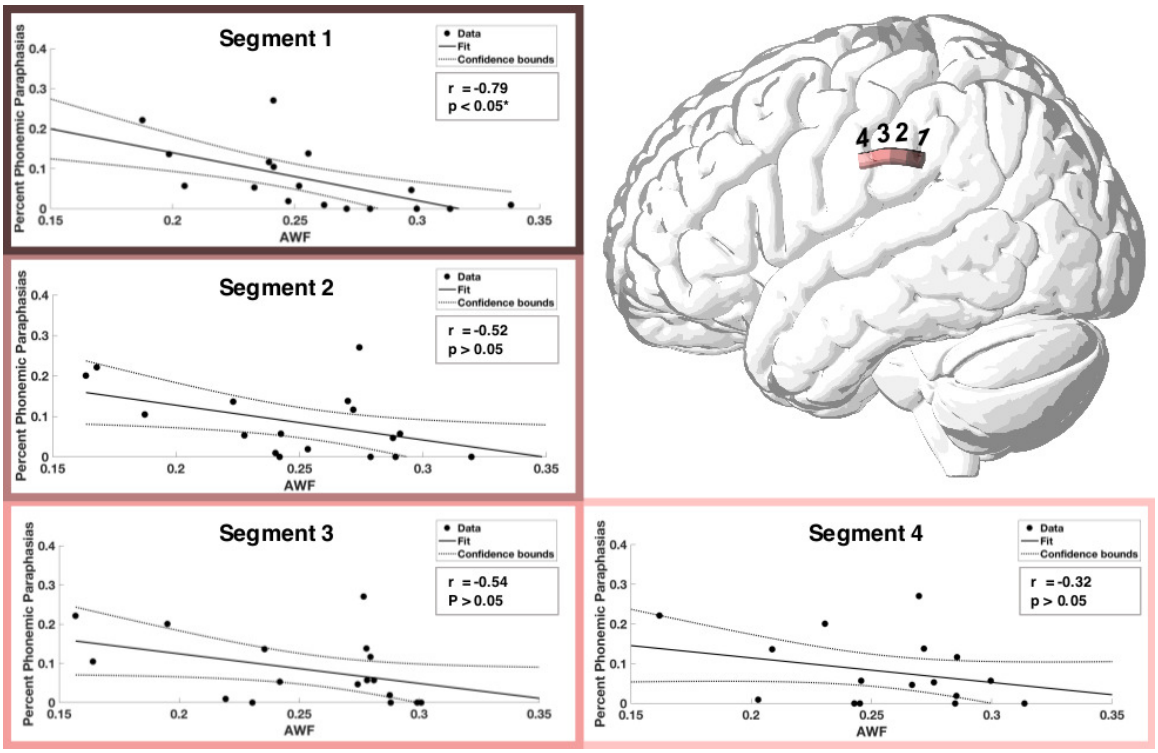

Figure 3.4: Scatterplots demonstrating the relationship between AWF and percent phonemic paraphasias. Average AWF was calculated for different segments along the length of the SLF. A significant association was seen between the AWF and phonemic paraphasias in the two most posterior segments (I; r=-0.68) (after correction for multiple comparisons).

It is important to highlight that ILF lesion burden was associated with the percentage of semantic paraphasias ($r = 0.56$, $p < 0.05$). Therefore, to exclude this potential confounder

from the analyses relating paraphasias with tract-based microstructure, we recalculated the linear models described above (whose r and p values mentioned above did not control for lesion burden) now controlling for lesion overlap with the ILF and SLF. This stricter analysis resulted in two remaining significant correlations between 1) the average AWF in segment 1 of the ILF and the percentage of semantic paraphasias ($r = -0.49$, $p < 0.05$) and 2) the average AWF in segment 1 of the SLF and the percentage of phonemic paraphasias ($r = -0.65$; $p < 0.05$). AWF and FA were strongly correlated (ILF: $r = 0.81$, $p < 0.05$; SLF: $r = 0.74$, $p < 0.05$), but stepwise regression (based on an F-test of the change in the sum of squared error by adding a term) using AWF, FA, and lesion overlap as input variables resulted in a final linear model with AWF as the only variable.

Impact of Gray Matter Necrosis

The degree of infra-Sylvian gray matter necrosis was associated with the frequency of semantic paraphasias made during confrontational naming ($r = 0.42$, $p < 0.05$). However, when correcting gray matter damage for the average AWF of the posterior ILF (segment 1), the relationship did not exceed statistical significance. Conversely, a statistically significant relationship between the AWF of the posterior ILF and semantic paraphasias ($r = -0.67$, $p < 0.05$) remained when adjusting for infra-Sylvian gray matter necrosis ($r = -0.55$ $p < 0.05$). Supra-Sylvian specifc gray matter was not related to percent phonemic paraphasias and thus did not alter the relationship between the AWF of the SLF and phonemic paraphasias. Note that the AWF calculated from SLF's segment 1 was associated with SMG necrosis ($r = -0.55$, $p < 0.05$); however, SMG necrosis only weakly related to the percentage of phonemic paraphasias ($r = 0.31$, $p = 0.21$).

3.2.4 Discussion

In this study, we examined the importance of residual white matter pathways supporting semantic and phonological processing during confrontation naming in individuals with

chronic post-stroke aphasia. We used advanced dMRI post-processing techniques to trace representative large pathways in the ventral and dorsal streams (ILF and SLF, respectively) and to measure a microstructural property of axonal integrity (AWF) along the fibers in each tract. Our results indicated a double dissociation between white matter axonal loss and semantic vs. phonemic naming impairments: AWF in the ILF (particularly in the posterior aspect of the tract) was associated with the number of semantic paraphasias, but not with the number of phonemic paraphasias. Conversely, AWF in the SLF (also more strongly in the posterior aspect of the tract) was related to the number of phonemic paraphasias, but not with the number of semantic paraphasias.

These findings are in line with the dual stream model of language, which proposes the presence of functionally and anatomically distinct processing routes for lexical access (i.e., ventral stream) and phonological form encoding (i.e., dorsal stream). Importantly, they provide anatomical confirmation at the white matter network level and complement existing lesion based studies, which mostly focus on regional damage, not residual white matter connections. Moreover, these results also provide information on the relevance of the biological nature of damage, i.e., axonal loss, and their location within the white matter tracts.

Multiple studies have demonstrated that regional post-stroke brain damage can be associated with naming errors, with damage to dorsal regions relating mostly to phonemic paraphasias, and damage to ventral regions predominantly associated with semantic paraphasias. Figure 3.5 demonstrates the positioning of the ILF and SLF relative to the gray matter regions most often implicated in naming impairments. Different studies have reported that semantic errors are related to lesion involvement of the temporal pole [63, 61], the Inferior Temporal Gyrus (ITG) [99], as well as different portions (anterior, mid and posterior) of the MTG [62, 64, 65, 61, 100]. Taken together, it is possible that the intactness of these areas, in combination with the successful integration within the language network

is required for unimpaired lexical access. The association between neuronal damage and word production errors has recently been further explored in relation to the Dell speech production model [100]. It is important to note that these studies did not focus on the residual integrity of the white matter as quantified by dMRI, but instead focused on lesion location using structural MRI. We believe that our results complement their conclusions highlighting the importance of residual white matter integrity in concordance with cortical and white matter damage as shown on structural MRI.

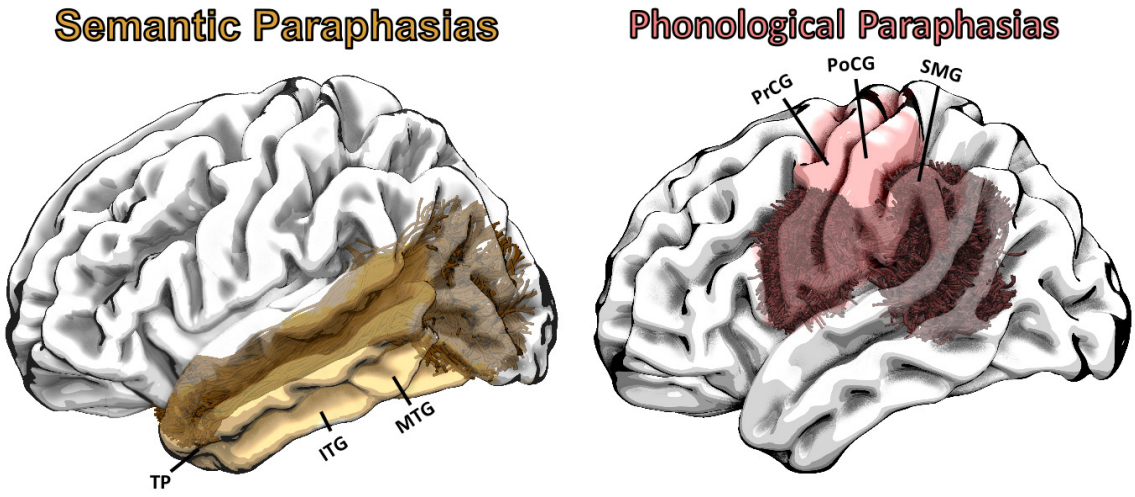

Figure 3.5: Left: Semantic paraphasias have been associated with damage to a multitude of temporal gray matter regions (e.g., temporal pole, STG, ITG, and MTG) [101, 65, 99, 62, 102, 63]. Here, we demonstrated that axon density of the ILF relates to the frequency of semantic paraphasias in individuals with post-stroke aphasia. The ILF interconnects these gray matter regions [103] likely supporting parts of a semantic network [66]. Right: Damage to the Precentral Gyrus, Postcentral Gyrus and the SMG has been shown to result in phonemic paraphasias [61, 62, 66, 67]. These areas are interconnected primarily through the SLF and arcuate fasciculi, which bridge perisylvian frontal, parietal, and temporal cortices. A greater degree of axonal loss in the posterior SLF related to a larger number of phonemic paraphasias.

The ILF, whose fibers link the superior- middle- and inferior temporal gyri [103], has been suggested by task-based fMRI studies to support such a semantic network [66, 101]. Phonology and articulatory representations are supported by the dorsal stream, and damage to the SMG and post-central gyrus has especially been related most frequently to impaired phonological encoding [66, 62, 67, 61]. Schwartz et al. postulated in a structural VLSM

analysis that phonological paraphasias might also arise from damage to dorsal stream white matter pathways [62]. Here, we directly located the residual white matter pathways using dMRI, and demonstrated that the axon density of the residual SLF indeed relates to the frequency of phonemic paraphasias, confirming the hypothesis by Schwartz et al. In addition, we also demonstrated that the degree of axonal loss of the residual ILF relates with semantic paraphasias during confrontational naming, independent of the degree of damage to the MTG. Our results provide evidence that damage to the gray matter regions as well as the integrity of the remaining connections between them should be considered when studying naming impairments after stroke. More specifically, damage to the brain at the white matter network level can directly influence ventral and dorsal stream processing and lead to speech production errors. In comparison with the existing literature, this is the main novel finding from this study.

It is important to note that the diffusion imaging methods used in this study are relatively different from conventional fiber tracing methods [104]. We employed an approach to best define the integrity of the residual white matter networks in stroke survivors and elucidate the nature and location of the white matter post-stroke damage. The specific innovations of the methods used here are threefold: 1) the use of DKI to track white matter fibers and ameliorate tracing inaccuracies in areas of fiber crossing or complex curvature; 2) the use of DKI tissue modeling (i.e., WMTI) to approximate axonal loss (AWF); and 3) the quantification of microstructural tissue properties along the main axis of each tract. This allows for the direct assessment of the local integrity of specific tracts since it entails the actual tracing of each tract in each individual. Since tracts can follow unusual paths in lesioned brains, scalar diffusion metrics obtained from ROI or skeletonized based analyses, without tracing connections, could miss important individual details.

Studying changes along the main axis of the fibers was pioneered through a technique known as automated fiber quantification (AFQ) [94], which is particularly useful when dis-

ease affects different parts of a fiber bundle to a different degree or when different segments of white matter pathways are composed of branches to different parts of gray matter. In a recent study, we used AFQ and demonstrated that aphasia recovery mediated plasticity varies along the length of a specific tract [83]. Here, we used the same principles of AFQ to determine AWF along the tracts, and we observed that damage to the posterior parts of the ILF and the SLF was more significantly associated with paraphasias highlighting the importance of local white matter integrity. While the explanation for these observations remains unclear, it may be related to the regional integration performed by these parts of the ILF, and SLF, with their posterior relationship to somatosensory processing areas in the temporal-parietal region, such as area SPT [105]. Alternatively, information transmission could preferably flow posteriorly to anteriorly where damage to segment 1 would impact the functioning of the downstream segments 2, 3, and 4. Lastly, it could be due to the posterior parts being more commonly lesioned after middle cerebral artery strokes and thereby strengthening the statistical association between damage and paraphasias in those areas. From our findings, we can conclude that posterior damage to either stream is a strong marker of paraphasias, but a more detailed dissection focusing on the regions connected by the specific streams is necessary.

It is a limitation of this study that only the ILF and the SLF were studied in a small number of cases without the assessment of other tracts and other naming errors related to the multiple subnetworks that form the dual stream system. It is important to emphasize that the nomenclature of white matter fibers is inconsistent throughout the literature (e.g., arcuate fasciculus vs. SLF). In this paper, the names ILF and SLF were chosen in accordance with the JHU atlas labeling convention used to seed the tracks. The SLF, however, likely includes fibers from both the SLF and the arcuate fasciculus, since no filtering algorithm based on fiber curvature was implemented. Similarly, the posterior location of the ILF also highly overlaps with the location of the Inferior Frontal-Occipital Fasciculus (IFOF). A thorough dissection of the tracks is however beyond the scope of this paper, and future

work should focus on studying white matter connections between specified gray matter regions. Another caveat would be that the AWF is based on assumptions and simplifications about the properties of axons. For example, the WMTI model assumes that in a voxel all axons lie in the same plane, which might be more or less accurate in different locations [27]. In lesioned brains, extra-cellular and glial changes could add confounders, but these are likely less pronounced in chronic strokes, where the brain parenchyma is more stable and inflammatory responses and edema are minimal. Regardless, the metric will always represent a specific property of the underlying water diffusion processes, albeit not necessarily the axon density. Finally, a decrease in AWF could also be related to an increase in water in the extra-axonal compartment. However, that seems unlikely to occur in isolation without the loss of any axons. Note that the same error types have been associated with more than one cause and revealing a one to one relationship between brain damage and paraphasias would be unrealistic [106]. Future work should focus on determining the integrity of the entire dual stream system and on studying the relationship between its residual structure and naming performance. Studying additional error types and further subcategorizing semantic and phonemic paraphasias might provide additional information about the origin of naming errors in post-stroke aphasia [102, 107].

In summary, our results are in concordance with the dual stream model of language processing and further corroborates the notion that, during speech production, knowledge association (semantics) depends on the integrity of ventral, whereas form encoding (phonemics) is localized to dorsal pathways. These findings also demonstrate the importance of the local residual integrity of specific white matter pathways beyond regional gray matter damage for speech production and underscore how biophysical tissue models can yield more specific and interpretable results for clinical translation.

3.3 Neuroplasticity: Structural Plasticity of the Ventral Stream and Aphasia Recovery

3.3.1 Introduction

Stroke is the leading cause of neurological disability and acquired language problems (aphasia) [56]. For survivors with chronic aphasia, speech therapy can lead to language improvements, but the response is highly variable [108]. The neurobiological bases of therapy-mediated recovery are not completely understood and it remains unclear why some individuals benefit while other exhibit little response. A leading hypothesis suggests that re-strengthening of the residual language network is crucial for recovery in post-stroke aphasia [109]. The dual stream model of language suggests that ventral (parietal temporal) networks are responsible for integrating the lexical-semantic system, whereas dorsal (parietal frontal) networks are related to the motor-articulatory system [51]. In a pioneering work, Schlaug et al. demonstrated non-specific structural changes associated with chronic aphasia improvement [110, 111]; subsequently, Van Hees et al. showed renormalization of the dorsal stream related to phonemic improvement [112]. However, it is unclear if semantic improvements are supported by structural plasticity of the ventral stream. This knowledge could help guide therapy approaches targeting residual brain integrity. We tested if structural plasticity of the ventral stream, represented by a segment of the ILF, was related to linguistic improvements by examining a cohort of individuals with chronic aphasia who underwent speech therapy. We applied DKI [113], a dMRI technique that provides more comprehensive characterization of tissue microstructure, and improves the assessment of white matter tractography [76]. In accordance with the dual stream model, we hypothesized that re-strengthening of the residual ILF would be associated with semantic, but not phonemic, therapy related improvements in naming.

3.3.2 Material and Methods

We recruited eight participants, (52 $\pm$ 7 years, 3 women) with a history of post-stroke aphasia due to a single left hemisphere stroke at least 12 (50.3 $\pm$ 29.8) months prior to the study. The participants had no history of other neurological diseases and were all right-handed. This study was approved by Institutional Review Boards at our institutions. The participants received group-based Intensive Language Action Therapy (constraint induced) [114] for three weeks (five therapy sessions per week lasting four hours each). They were tested for confrontational naming using a short version of the Philadelphia Naming Test [115] within one week prior and post therapy. MRI data was collected using a Siemens 3T TIM Trio (12-channel head coil) at the University of South Carolina. DKI data: two b-values (1000 and $2000\,\mathrm{s/mm^2}$), 30 diffusion-encoding directions, 45 slices, voxel size=$2.7\,\mathrm{mm} \times 2.7\,\mathrm{mm} \times 2.7\,\mathrm{mm}$, TR=$6100\,\mathrm{ms}$, TE=$101\,\mathrm{ms}$, FOV=$222\,\mathrm{mm} \times 222\,\mathrm{mm}$, two averages and 11 non-diffusion weighted images. T1-weighted images: turboflash sequence, FOV=$256\,\mathrm{mm} \times 256\,\mathrm{mm}$, 160 sagittal slices, 9° flip angle, TR=$2250\,\mathrm{ms}$, TE=$4.5\,\mathrm{ms}$, voxel size = $1\,\mathrm{mm} \times 1\,\mathrm{mm} \times 1\,\mathrm{mm}$. All subjects underwent four MRI sessions, two before and two after treatment, within one week prior and post therapy. The image analysis pipeline was optimized to quantify diffusion FA, $\bar{D}$ and $\bar{K}$) along a representative segment of the ILF as defined by the probabilistic JHU white matter atlas [116], which travels from the coronal plane in the posterior edge of the cingulum to the temporal pole. Data from both pre-treatment and post-treatment sessions were combined into a set of 121 diffusion-weighted images, linearly registered to the initial scan using SPM8 to locate the ILF for each subject. DKE was used for deterministic kurtosis-based tractography (https://www.nitrc.org/projects/dke/). A white matter seeding mask was created with SPMs Clinical Toolbox (https://www.nitrc.org/projects/clinicaltbx/), which was normalized to diffusion space by cost function masking with the stroke lesion (drawn on T1 images). Individual whole brain tractography maps were analyzed using AFQ [94], customized to perform analysis in diffusion space. AFQ and DKI were combined as described

previously [78]. AFQ results in a set of ILF fibers, which ultimately is abridged to one centroid. One hundred equidistant measurements along the centroid were obtained for each metric before and after therapy. Since no significant differences were revealed between the pre- or post-treatment scans, they were averaged to reduce noise. To assess the ILFs weakest segment, the location with the highest diffusion abnormality (minima $\bar{K}$ or FA, maximum $\bar{D}$) was determined between nodes 20-80 of the core ILF. We called this highest abnormality the bottleneck, and a 6-node smoothing kernel was applied in this neighborhood to reduce contribution of outliers. All further analyses were carried out in the bottleneck. Pre- to post-treatment structural changes in the ILF were examined in relationship to therapy related improvements in both semantic and phonemic paraphasias using linear regression. Baseline metrics were also related to baseline performance. Corresponding p-values are adjusted for multiple comparisons (n=12) using Bonferroni correction.

3.3.3 Results

As a group, subjects showed significant improvement in the number of correctly named items with therapy (paired t-test, $p = 0.002$), which was driven by fewer semantic errors ($p = 0.01$) and a decrease of no responses ($p = 0.03$). The left ILF was significantly different ($p < 0.001$) from the right ILF for each metric. Compared to the contralateral side, the ipsilateral ILF had a higher MD, lower FA and lower MK (Figure 3.6). Individualized perilesional changes in ILF microstructure in relationship with its proximity to the stroke lesion were also noted. $\bar{K}$ values at greater distances from the lesion are higher, gradually decreasing when closer to the lesion (Figure 3.7).

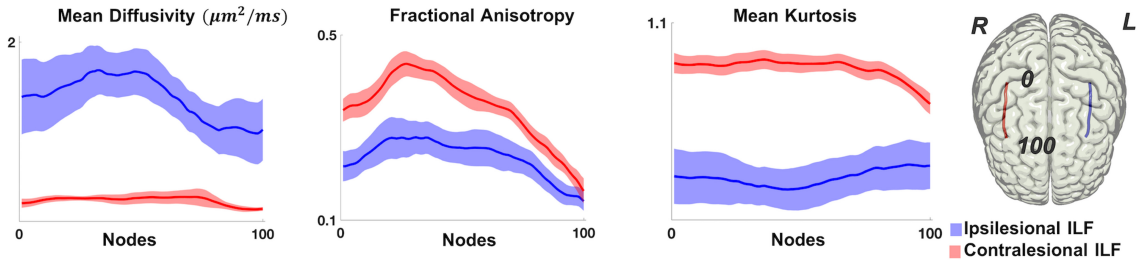

Figure 3.6: Along-tract diffusion metrics (y-axis) are demonstrated along equally spaced measurement points in the ILF (0 to 100, anterior to posterior) (x-axis). The solid line represents the average patient value, with the standard error of the mean shown as the shaded area. Ipsilesional ILF values are shown in dark gray, and contralesional ILF values are shown in light gray. The rightmost image illustrates an example of a participants core right and left ILF.

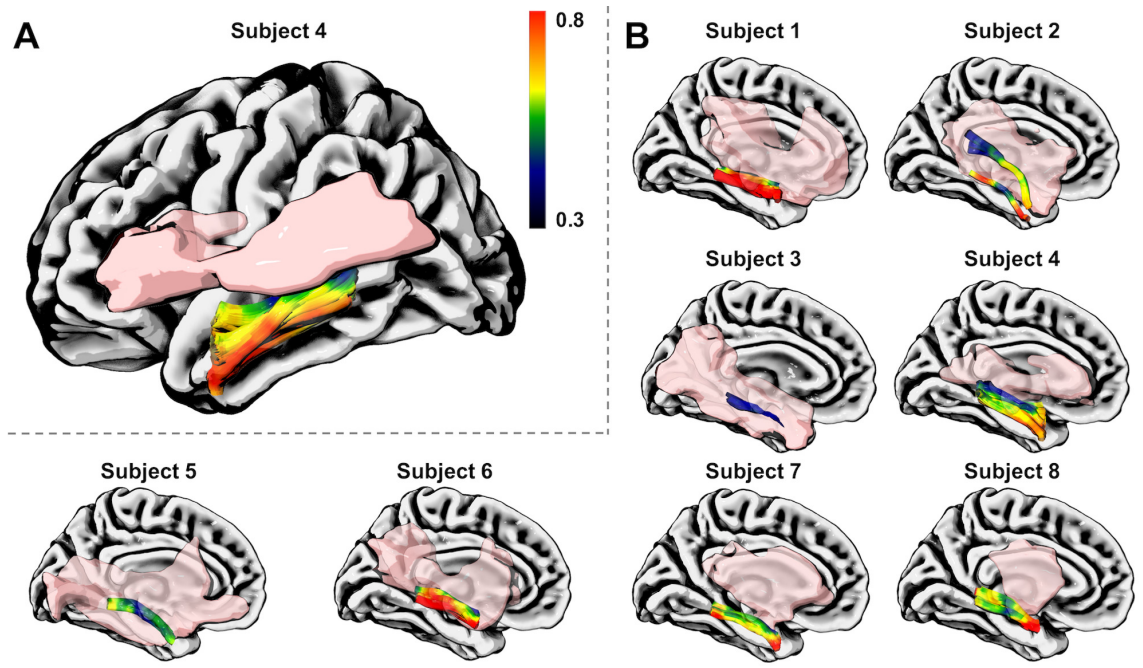

Figure 3.7: The relationship between along-tract ILF $\bar{K}$ values and the chronic stroke lesion (in pink). A. The data from one representative participant is shown in a lateral view to demonstrate the lowest $\bar{K}$ in perilesional areas (color bar). B. The ILF and the lesion are shown for this subject (panel A) and all others using medial views to illustrate their anatomical relationship. Note that the lesion was excluded from the seeding mask during ILF tractography.

Overlap between the lesion core and the left ILF ranged from 0.4% to 94.7% (Figure 3.8a). There was a strongly significant correlation between pre- to post-therapy increment in $\bar{K}$ (renormalization towards normal values [117] in the left ILF (at the bottleneck) and therapy-related improvement in semantic paraphasias ($r = -0.90$, $p < 0.05$; Figure 3.8a).

No relationships were observed for pre- to post-therapy $\bar{K}$ changes and phonemic errors ($r = -0.11$) (semantic vs. phonemic R to Z comparison [Fisher transformation], $p < 0.05$) or for right ILF changes and improvement in semantic paraphasias (left-ILF vs. right-ILF R to Z, $p < 0.05$). The correlations with FA and $\bar{D}$ did not reach significance level at $p < 0.05$. Bottleneck increases in $\bar{K}$ with therapy are shown in the perilesional space of a representative patient (Figure 3.8b; note $\bar{K}$ color-code changes from blue to green). There was a trend towards statistical significance in the relationship between ILF $\bar{K}$ pre-treatment and the number of semantic paraphasias prior to treatment ($r = -0.82$, $p = 0.15$), this association did not increase with treatment. To investigate the effect of lesion burden on recovery, we evaluated the number of residual fibers in each patient. The number of semantic paraphasias prior to therapy was related to ILF lesion burden ($r = -0.65$, $p = 0.07$). However, lesion burden (or track integrity) was not associated with semantic recovery ($r = 0.19$, $p = 0.65$).

3.3.4 Discussion

The present study evaluated the relationship between structural plasticity of the ventral stream and therapy-related improvements in naming in individuals with chronic aphasia. We observed that pre- to post-treatment increases in ILF $\bar{K}$ towards normal values [117], specifically within the areas along the ILF with the highest degree of baseline structural compromise (the diffusion bottleneck), were strongly associated with semantic improvements. These results leverage recent advancements in dMRI and image analysis, which enable the investigation of white matter microstructure with higher sensitivity to microstructural changes [118]. $\bar{K}$ is a biophysical measure less affected by partial volume, which can be higher in the proximity of a stroke lesion [119]. In this study, $\bar{K}$ was the only diffusion metric that reached statistical significance suggesting that conventional diffusion measures may be less sensitive to structural changes associated with recovery, and $\bar{K}$ may be optimally suited for assessing post-stroke neuroplasticity. Larger studies are needed to

A.

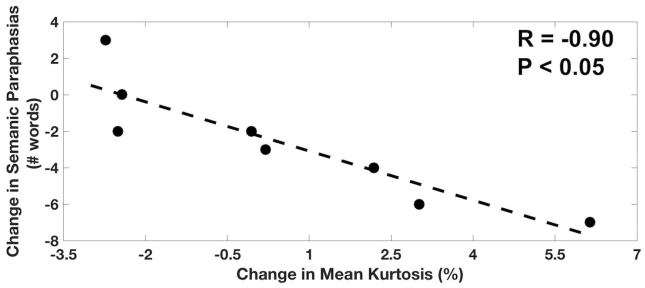

SUBJECT	LESION OVERLAP (%)	BL1	BL2	MEAN BL	FU1	FU2	MEAN FU	CHANGE MK (%)	CHANGE SEMANTIC PARAPHASIAS (#WORDS)
P8	0.8	0.53	0.53	0.53	0.53	0.49	0.51	-2.73	3
P2	10.5	0.55	0.55	0.55	0.54	0.53	0.53	-2.5	-2
P4	0.4	0.78	0.75	0.77	0.75	0.75	0.75	-2.43	0
P6	19.1	0.7	0.79	0.74	0.74	0.74	0.74	-0.06	-2
P7	13.1	0.65	0.65	0.65	0.66	0.64	0.65	0.2	-3
P1	0.5	0.86	0.82	0.84	0.85	0.86	0.86	2.18	-4
P5	66.3	0.46	0.46	0.46	0.47	0.48	0.48	3.01	-6
P3	94.7	0.39	0.40	0.40	0.43	0.41	0.42	6.13	-7

B.

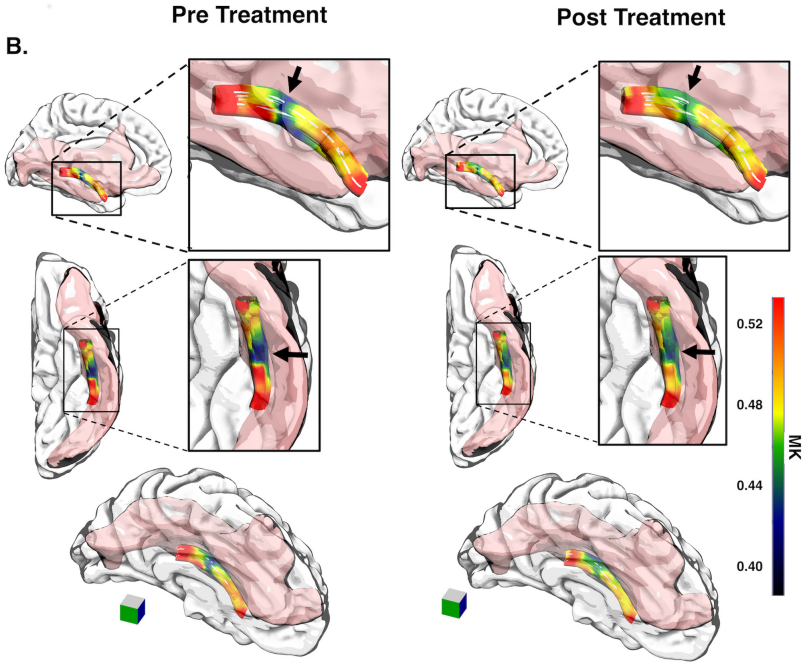

Figure 3.8: A. (top) The scatter plot demonstrates the relationship between pre- to post-therapy changes in $\bar{K}$ measured at the ILF bottleneck, and pre- to post-therapy changes in semantic paraphasias ($r = -0.90$ and $p < 0.05$ corrected). A. (bottom) Table summarizing $\bar{K}$ values for the four MRI acquisitions for all subjects. The table also includes individual changes in the number of semantic paraphasias with treatment (in number of words) and the percent overlap between the stroke lesion and the ILF. The scatterplot in A (top) depicts the relationship between change $\bar{K}$ (second to last column) and change in semantic paraphasias (last column). (BL=baseline; FU=follow-up; MK=mean kurtosis) B. Pre- and post-treatment $\bar{K}$ values along the ILF from a representative participant are shown anatomically. The ILF bottleneck, which is marked with a black arrow, demonstrates an increase in $\bar{K}$ towards normal values from before to after therapy. The stroke lesion is demonstrated in pink. This participant demonstrated a 55% improvement in semantic errors.

replicate these results. The neurobiology underlying $\bar{K}$ changes is likely due to a combination of factors that are known to occur after strokes. Namely, axonal sprouting, changes in axon thickness or neurogenesis, can contribute to an increase in complexity in perilesional tissues, which has been demonstrated in post-stroke experimental studies [120]. However, further specific biophysical tissue models are needed to completely elucidate the basis of post-stroke plasticity. Our findings provide preliminary, but theory-driven, evidence of semantic improvements being supported by structural plasticity of the ventral language processing stream. This knowledge can be used to guide therapies to recruit ventral processing pathways in individuals with residual ILF, or direct stimulation to the ILF for semantic improvement. Of note, Language Action Therapy focuses on the improvement of communication skills in general, and future studies with a larger sample could address whether impairment based interventions (i.e., semantic based treatments for semantic paraphasias) could lead to further enhanced structural neuroplasticity. Moreover, the residual integrity of the language network could help improve the predictions of recovery potential, together with other predictors such as lesion site, lesion load [121], as well as the right language network, specifically the arcuate fasciculus, which has been implicated in recovery by previous studies [110, 122]. In conclusion, therapy-related ventral stream plasticity, quantified

by MK changes within a bottleneck of damage in the ILF, is related to semantic, but not phonemic, improvements due to therapy. These results are in accordance with the theoretical dual stream model of language, which predicts the involvement of the ILF in semantic processing. Furthermore, kurtosis-based tractography is a promising tool for the study of the neurobiology of stroke recovery. Understanding language network integrity and its relationship with clinical performance could advance our knowledge of stroke recovery mechanisms and the basic neurobiology of language.

3.4 Perilesional White Matter Microstructure and Aphasia Recovery

Language therapy has shown to be effective in chronic aphasia, although treatment responses are variable, and predicting outcomes remains challenging. Research has previously shown that left hemisphere perilesional areas contribute to therapy-induced neuroplasticity, but little is known about how perilesional white matter affects treatment outcome. This preliminary study attempts to address this gap in knowledge by relating pretreatment residual perilesional white matter integrity to post-treatment changes in confrontational naming. Thirty-one subjects (age = 57 ± 11 y; 9 females; MRI time post-stroke=36 ± 32 m) with chronic post-stroke aphasia underwent the WAB-R, multimodal MRI, and 15 sessions (5x/week) of self-administered computerized anomia treatment (45 min). Half of the participants received anodal tDCS (1mA) during the first 20 minutes, and the remaining half received sham stimulation. Aphasia severity ranged from severe to mild (WAB-AQ = $[20 - 92]$), with an average ($\pm$ standard deviation) WAB-AQ of 52 ($\pm$ 22). Structural (T_1-w, T_2-w) and diffusional kurtosis images ($b = 0$, 1000, $2000\,\mathrm{s/mm^2}$) were acquired at baseline and DKE was used to estimate diffusion and kurtosis tensors. A perilesional white matter mask was created by dilating lesion drawings (4 voxels) including only those voxels categorized as white matter (>90% probability) by enantiomorphic segmentation. Voxels dominated by cerebral spinal fluid (MD $> 2\,\mu\mathrm{m^2/ms}$) were excluded. Before treatment, subjects elicited an average of 24% ($\pm$ 25%) correct responses during a confrontational naming test consisting of 80 objects. After treatment, participants demonstrated a significant proportional change in correct responses on trained items with an average improvement of 12% $\pm$ 19%. We found that both perilesional axial diffusivity and kurtosis significantly related to changes in correct response ($r = 0.47$, $p < 0.05$; $r = -0.49$, $p < 0.05$) correcting for lesion size, pre-treatment aphasia severity and tDCS application (Figure 3.9). Baseline perilesional FA, RD and RK did not relate to naming improvements ($r = 0.2$, $p > 0.05$; $r = 0.28$, $p > 0.05$; $r = -0.33$, $p > 0.05$). This study shows prelimi-

nary evidence on the relationship between baseline perilesional white matter and language recovery, and demonstrates the possible role image analysis can play in predicting recovery potential from baseline neuroimaging data. If pretreatment MRI contains valuable information about treatment response, then imaging has the potential to become a useful tool for guiding clinical management of aphasia. It would be particularly useful if dMRI could be used to tap into specific recovery potentials, such as comparing room for semantic vs. phonemic improvement.

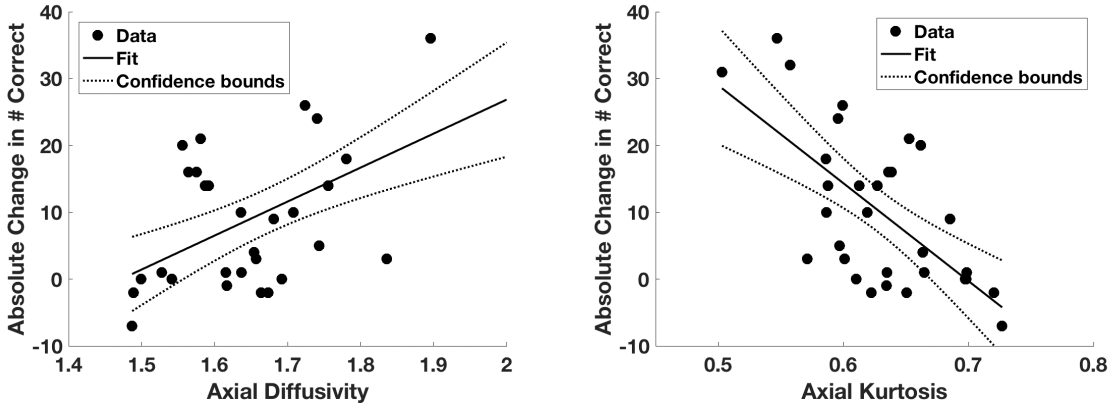

Figure 3.9: Perilesional axial diffusivity (left) and kurtosis (right) significantly related to changes in correct response ($r = 0.47$, $p < 0.05$; $r = -0.49$, $p < 0.05$) correcting for lesion size, pretreatment aphasia severity and tDCS application.

3.5 Synergism between cortical damage and white matter disconnection contributes to aphasia severity

Language impairments are common after a dominant hemisphere stroke, although the relative contribution of damage to cortical areas and white matter pathways to aphasia severity remains poorly understood. In this preliminary study, we assessed if our understanding of aphasia severity and linguistic skills could be improved by quantifying damage to both gray and white matter areas often implicated in language. Specifically, we hypothesized that cortical disconnection aids in the explanation of critical differences in language function

particularly when cortical areas are largely intact. We recruited 90 right handed participants (age 58.8 ± 12.1 years, 34 females; 42.8 ± 50 months post stroke) with a single left hemisphere stroke that underwent MRI imaging (T_1-w, T_2-w and DTI ($b = 0, 1000\,\mathrm{s/mm^2}$) and the WAB-AQ (mean 63 ± 28). In addition, we scanned 60 older self-reported cognitively normal participants (47 females, age 55.1 ± 8.6 years). T_1-weighted images were segmented into probabilistic gray and white matter maps using either SPM12's unified segmentation-normalization or enantiomorphic normalization. The probabilistic gray matter map was divided into JHU anatomical regions, and white and gray matter parcellation maps were registered into diffusion imaging space where pairwise probabilistic DTI fiber tracking was computed. Weighted connectomes were constructed based on the number of streamlines corrected by distance traveled and by the total gray matter volume. Lesions were drawn on T_2-weighted images and proportional damage to ROIs was determined by the intersection of lesion drawings and JHU ROIs. ROIs were considered disconnected when the number of connections was less than 2 standard deviations away from the mean number of connections in the non-brain damaged cohort. Our results focused on a language specific subnetwork consisting of Broca's area, SMG, AG, STG, MTG, ITG and the pSTG and pMTG. Disconnection within this subnetwork significantly aided in the explanation of aphasia severity (WAB-AQ) when cortical areas suffered between $21 - 91$ % damage. Outside of this range, disconnection did not significantly help explain the variability in aphasia quotient. In an additional ROI-based analyses, damage to the left superior longitudinal fasciculus explained an extra 31% of variance ($r = -0.56$, $p < 0.05$) in WAB-R-fluency scores in addition to 29% variance explained by damage to Broca's area alone. Likewise, individual auditory comprehension scores were explained by the quantification of damage to the ILF ($r = -0.23$, $p < 0.05$) in addition to quantified damage to Wernicke's. In conclusion, quantifying damage to white matter pathways can help explain individual language impairments in subjects with chronic aphasia. Our results suggest that this benefit is largest in areas with average cortical damage.

3.6 Development of a Neuroimaging Pipeline Optimized for the Study of Whole Brain White matter Integrity Post-Stroke

The studies covered in Sections 3.2 - 3.3 assesses the integrity of specific white matter bundles (i.e, the SLF and the ILF) separately. Ideally, the white matter network should be studied as a whole since damage to different white matter bundles is not independent. Additionally, the origin and end point of the specific white matter fibers was not known further complicating interpretation. To alleviate these issues, we developed a new neuroimaging pipeline that ultimately provides the user with a way to assess the microstructure (as determined by DKI metrics) between a set of gray matter ROIs determined by an atlas (e.g., JHU atlas). The software is available to download at:

https://github.com/neurolabusc/nii_preprocess/tree/DKI_pipeline.

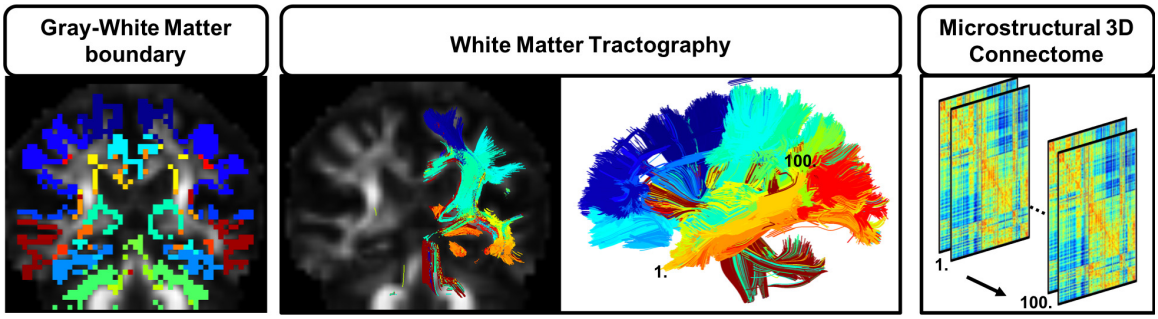

Figure 3.10: Proposed new neuroimaging pipeline optimized for the study of whole brain white matter integrity post-stroke. Left: Tractography starts and ends at the gray/white matter boundary. The boundary is segmented into different cortical regions as determined by a predefined atlas. Middle: Deterministic DKI-based tractography is executed for each pair of gray matter ROIs. All tracts belonging to the same pair of ROIs are colored with the same color. This example shows left hemisphere tractography only. All fibers are subsequently divided into 100 equidistant segments $[1 - 100]$. Right: The average DKI metrics are calculated for each segment and are stored in a 100 different matrices. Each matrix elements (i,j) contains the value for the connection between gray matter ROI i and gray matter ROI j.

Tractography is performed from the gray/white matter boundary in native dMRI space. The boundary is first located, using the software package MRtrix, on a native T_1-w image using the functions *5ttgen* and *5tt2gmwmi*. Subsequently, it is normalized into native DWI

space using non-linear registration, and each boundary voxel is assigned to a particular gray matter ROI using a predefined gray matter atlas (see Figure 3.10 left). Each pair of gray matter ROIs is then used as a seed and end region in a deterministic tractography algorithm using the function *tckgen* from MRtrix. Ultimately, this results in fiber tracts connecting a known pair of gray matter ROIs, which are rendered in the same color (Figure 3.10 middle). All fiber tracts are divided into 100 equidistant segments (node 1 and 100 in Figure 3.10). In a final step we calculate the average "microstructure" at each node (e.g, MD, FA,MK), which is stored in a matrix where the rows and colums represent the different gray matter ROIs (Figure 3.10 left). This matrix was coined the 3D microstructural connectome. For example, microstructural connectome element (1,2,1) contains the average FA of segment 1 for the tracts connecting gray matter ROI 1 and gray matter ROI 2. The 3D microstructural connectome provides a comprehensive overview of the white matter microstructure at its entirety while keeping track of the cortical areas that are being connected. The large amount of data captured in this matrix is ideally suited to be used with machine learning algorithms.

CHAPTER 4

VALIDATION, DEVELOPMENT, AND OPTIMIZATION OF A NOVEL TISSUE MODEL USING DIRECTION-AVERAGED HIGH B-VALUE DIFFUSION MRI

This chapter is based on the following publications:

- **McKinnon, Emilie T.**, and Jens H. Jensen. "Measuring intra-axonal T2 in white matter with direction-averaged diffusion MRI." Magnetic resonance in medicine (2019): 2985-2994.
- **McKinnon, Emilie T.**, Joseph A. Helpern, and Jens H. Jensen. "Modeling white matter microstructure with fiber ball imaging." NeuroImage 176 (2018): 11-21.
- **McKinnon, Emilie T.**, Jens H. Jensen, G. Russell Glenn, and Joseph A. Helpern. "Dependence on b-value of the direction-averaged diffusion-weighted imaging signal in brain." Magnetic resonance imaging 36 (2017): 121-127.
- **McKinnon, Emilie T.**, and Jens H. Jensen. Simple scheme for correcting bias in axonal water fraction due to differences in compartmental transverse relaxation times. Oral presented at ISMRM 2019. Proceedings of the 27th meeting of the International Society of Magnetic Resonance in Medicine; 2019 May; Montreal, Canada.

4.1 Introduction

The key assumption underlying FBI is that strong diffusion weighting isolates water confined to the intra-axonal compartment, and that this compartment can be approximated by thin impermeable cylinders. The latter is commonly referred to as the "stick model", which is an assumption that has been used by a multitude of tissue models (see Section 1.2.3). To date, few studies have focused on the validation of these assumptions, which is crucial for the accurate estimation of tissue specific parameters. In section 4.2, by comparing experiment and theory, we provide some preliminary evidence for the validity of the "stick model". FBI theory predicts that the direction averaged b-value signal decays as $1/\sqrt{b}$. High Angular Resolution Diffusion Imaging (HARDI) data were acquired from two human volunteers with 128 diffusion-encoding directions and six b-value shells ranging from 1000 to $6000\,\mathrm{s/mm^2}$ in increments of $1000\,\mathrm{s/mm^2}$. The direction-averaged signal

was calculated for each shell and the signal was plotted as a function of b-value for selected regions of interest. We demonstrate that the direction-averaged DWI signal in white matter varies, to a good approximation, as $1/\sqrt{b}$ providing strong evidence for the validity of FBI.

The original FBI framework provides a means of calculating the fODF in white matter from dMRI data obtained over a spherical shell with a b-value of about $4000\,\mathrm{s/mm^2}$ or higher. We show that by supplementing this FBI-derived fODF with dMRI data acquired for two lower b-value shells, it is possible to estimate several microstructural parameters, including the AWF and the intrinsic intra-axonal diffusivity (D_a) (Section 4.3). This FBWM modeling method is demonstrated for dMRI data acquired from healthy volunteers, and the results are compared with those of the WMTI method. An important practical advantage of FBWM is that the only nonlinear fitting required is the minimization of a cost function with just a single free parameter, which facilitates the implementation of efficient and robust numerical routines.

In Section 4.4, we demonstrate how the T_2 relaxation time of the intra-axonal water in white matter can be measured with direction-averaged dMRI for b-values larger than about $4000\,\mathrm{s/mm^2}$. Since the direction-averaged dMRI signal from white matter at high b is dominated by the contribution from water within axons, it enables T_{2a} to be estimated by acquiring data for multiple TE values and fitting a monoexponential decay curve. Given an a priori value of the intra-axonal diffusivity D_a, an extension of the method allows the extra-axonal relaxation time T_{2e} to also be calculated. This approach was applied to estimate T_{2a} in white matter for three healthy subjects at 3T, as well as T_{2e} for a selected set of assumed intra-axonal diffusivities. The straightforward calculation of compartmental relaxation times allows for exploration of their use as potential biomarkers, and importantly they can be used to improve the accuracy of certain tissue modeling parameters like the AWF (Section 4.5).

4.2 Dependence on b-Value of the Direction-Averaged Diffusion-Weighted Imaging Signal

4.2.1 Introduction

The relationship between the DWI signal and brain tissue microstructure is subtle and manifold. In white matter, there is the added complexity of substantial diffusion anisotropy caused by axonal fiber bundles. While there have been a variety of mathematical models proposed to describe this relationship, their relative merits are still debated, and this topic continues to be actively investigated [123, 21]. Previously proposed models include bi-exponentials [124, 20, 125, 19, 126], stretched exponentials [127] and power laws [128, 29]. Although each of these approaches can approximately fit DWI data over significant ranges of b-values, their precise mathematical forms are quite different, as is particularly evident for large b-values. For bi-exponential models, the large b-value behavior will be dominated by the more slowly decreasing term, and so it will approach a simple mono-exponential decay. For stretched exponentials, the signal decay has the form $exp[-(kb)^a]$, where b is the b-value, k is a constant, and a$<$1 parameterizes the degree of stretching. For the statistical model of Yablonskiy and coworkers [128], the signal decays as $1/b$ for large b, while for the model considered by Jensen and coworkers [29], the large b signal decays as $1/b$.

In order to investigate the b-value dependence of the DWI signal, we acquired HARDI data from two healthy volunteers with b-values ranging from 1000 to $6000\,\mathrm{s/mm^2}$ in increments of $1000\,\mathrm{s/mm^2}$ and with 128 uniformly distributed diffusion-encoding directions for each b-value shell. We then averaged the signal for each shell over all of the diffusion-encoding directions in order to reduce the effects of variable degrees of diffusion anisotropy [129]. In effect, this corresponds to determining the powder-averaged signal [130], which should have a less complicated behavior than the full signal. Related data reduction meth-

ods have been applied to dMRI in various contexts [126, 129, 131]. Here our purpose is to suppress the effects of macroscopic diffusion anisotropy, as quantified by metrics such as the FA. Nonetheless, the direction-averaged dMRI signal will still reflect microscopic diffusion anisotropy, as is often studied with double diffusion encoding MRI [132, 133, 134] and magic-angle spinning dMRI [135]. As a supplementary analysis, we also applied similar methods to retrospective dMRI data obtained from the human connectome project (HCP), which includes b-values up to $10.000\,\mathrm{s/mm^2}$ [136].

Remarkably, our results demonstrate a simple power law scaling of the direction-averaged DWI signal throughout the brain parenchyma over the range of b-values considered. Moreover, a distinct qualitative difference is found between white and gray matter, suggesting sharp biophysical differences beyond just macroscopic diffusion anisotropy. We discuss the significance of our observations with respect to the mathematical modeling of the DWI signal. However, our main purpose here is not to compare how well different models fit our data, but rather to describe the empirical dependence on the b-value of the direction-averaged DWI signal and the broader implications of this for modeling.

4.2.2 Material and Methods

Data Acquisition

Data were acquired from two healthy volunteers (Subject 1, female, age 25 yr; Subject 2, male, age 55 yr) under a protocol approved by our institutional review board using a Siemens 3T TIM Trio MRI scanner (Siemens Healthcare, Erlangen, Germany) and a 32 channel head coil (adaptive combine mode). HARDI data were acquired for six b-value shells using a twice-refocused DWI sequence in order to reduce eddy current distortion [137]. The b-values for the shells were 1000, 2000, 3000, 4000, 5000 and $6000\,\mathrm{s/mm^2}$, and each shell had the same 128 uniformly distributed diffusion-encoding directions over half a sphere, determined with an electrostatic repulsion algorithm [138]. Fourteen images

without diffusion weighting (b0 images) were acquired at the beginning of each session, and one additional b0 image was acquired between each b-value shell. Other acquisition parameters were TE = $149\,\mathrm{ms}$, TR = $7200\,\mathrm{ms}$, slice thickness = $3.0\,\mathrm{mm}$, field of view = $222\,\mathrm{mm} \times 222\,\mathrm{mm}$, pixel bandwidth = $1351\,\mathrm{Hz/px}$, echo spacing = $0.82\,\mathrm{ms}$, and parallel imaging factor = 2. The acquisition matrix was 74x74 resulting in an in-plane resolution of $3\,\mathrm{mm} \times 3\,\mathrm{mm}$ with a total scan time of 97 min 31 s.

For anatomical reference, Magnetization-Prepared Rapid Gradient Echo (MPRAGE) images were acquired with 192 sagittal slices, TE = $2.3\,\mathrm{ms}$, TR = $1900\,\mathrm{ms}$, TI = $900\,\mathrm{ms}$ and slice thickness = $1\,\mathrm{mm}$. The FOV was $256\,\mathrm{mm} \times 256\,\mathrm{mm}$, yielding $1\,\mathrm{mm} \times 1\,\mathrm{mm} \times 1\,\mathrm{mm}$ isotropic voxels. The total scan time for the MPRAGE acquisition was 4 min and 26 s.

Image Analysis

Due to the lengthy scan time, a co-registration process was implemented to account for motion, using SPM8 (Wellcome Department of Imaging Neuroscience, London, United Kingdom). The images for each b-value shell were co-registered with a rigid body transformation to the average of the initial set of fourteen b0 images, employing each shells respective intermediate b0 image as the source image. The MPRAGE images were also brought into diffusion space by using the average of all b0 images as a template. To reduce the contribution of signal noise and Gibbs ringing [87], all diffusion-weighted images were smoothed with a Gaussian kernel having a full width at half maximum of $3.75\,\mathrm{mm}$[84].

The direction-averaged diffusion-weighted images were calculated with the following image analysis steps. In order to estimate the average over all gradient directions, one million random points were selected on the surface of a sphere with unit radius and with the origin at the spheres center. For each point, we determined the closest gradient vector by calculating the angle between that point and each of the 128 gradient vectors. Subsequently, a weight was assigned to each gradient vector by the fraction of assigned closest points

over the sphere. This fraction was then applied to calculate a weighted average of all the diffusion-weighted images for each shell. This weighted average is more accurate than an unweighted average, since even uniformly distributed points typically do not have exactly equal spacings [139].

The ROIs were defined by the following semi-automated method. First subcortical segmentations were obtained by using the raw MPRAGE images together with FreeSurfer v5.0 (Freesurfer, Laboratory for Computational Neuroimaging, Charlestown, MA). Details on the FreeSurfer subcortical segmentations are described by Fischl et al. [140]. Next, the segmentations were brought into diffusion space by employing the same affine transformation matrix used to transform the MPRAGE image. Additionally, certain white matter regions, such as the splenium and the cerebellar peduncle, were obtained from the JHU white matter atlas [89]. Finally, the segmentations of FreeSurfer, the JHU white matter labels, and the MPRAGE images were yoked together, and four voxels in the core of each selected anatomical region were defined manually. These small ROIs were chosen to increase the likelihood that they contained a single tissue type without partial volume contamination, possibly introduced by the long acquisition time, low spatial resolution and smoothing. The following anatomical regions were analyzed: cerebellar peduncle, splenium, internal capsule, frontal white matter, thalamus, cerebellar gray matter, and putamen (Figure 4.1). For the purposes of this study, we classified the ROIs drawn for internal capsule, splenium, frontal white matter and cerebellar peduncle as being white matter brain tissue. Conversely, regions selected from thalamus, cerebellar gray matter and putamen were regarded as being gray matter (although the thalamus does contain some white matter). The Signal to Noise Ratio (SNR) was estimated in each ROI from the ratio of the average signal for the $6000\,\mathrm{s/mm^2}$ b-value shell to the average background signal (for a similar number of voxels) multiplied by $\sqrt{\frac{\pi}{2}}$ [141, 142]. All statistical tests performed under Results are paired t-tests, with a significance level of p = 0.05, not corrected for multiple comparisons.

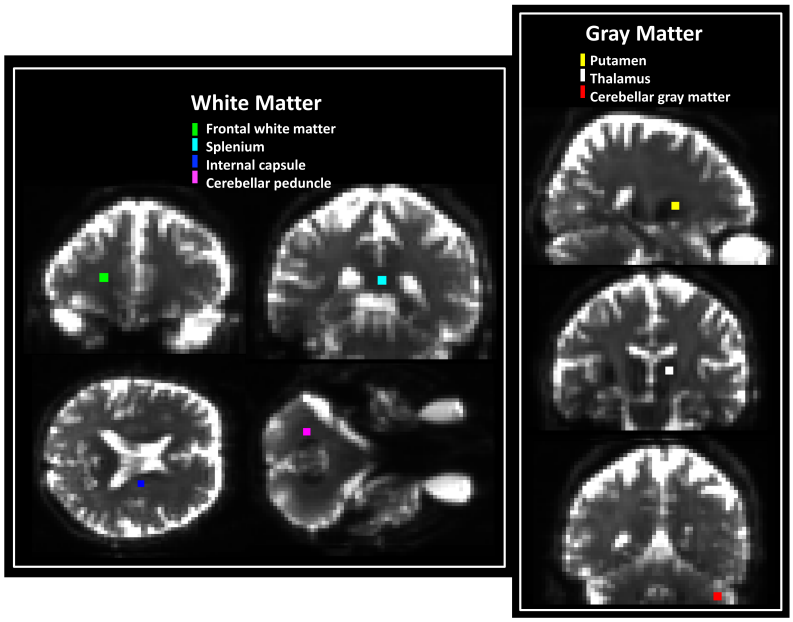

Figure 4.1: Locations of the seven ROIs considered in the quantitative analysis superimposed on the average $b0$ image for one subject. Each ROI represents the core of a different anatomical region. Cerebellar peduncle (violet), splenium (cyan), internal capsule (blue) and frontal white matter (green) are all regarded as white matter regions, for the purposes of this study, while cerebellar gray matter (red), putamen (yellow) and thalamus (white) are classified as gray matter.

The direction-averaged DWI signal for each b-value shell was normalized by dividing by the b0 signal on a voxel-by-voxel basis. For both subjects, this normalized mean signal was further averaged over the selected ROIs, and the resulting data were graphed on a log-log plot. Linear fits to these data were then determined by linear regression, with the slope, intercept and their associated errors determined according to standard methods [143]. We also calculated the quantity

$$\zeta = 2 \cdot \sqrt{\frac{b}{\pi}} \cdot \frac{\bar{S}}{S_0} \tag{4.1}$$

where b is the b-value, $\bar{S}$ is the direction-averaged DWI signal, and S_0 is the signal for $b = 0$. Recent work has argued that

$$\zeta \approx \frac{f}{\sqrt{D_a}} \tag{4.2}$$

for white matter if the b-value is sufficiently large, where f is the fraction of MRI visible water inside axons and D_a is the intrinsic intra-axonal diffusivity (i.e., the along-axis diffusivity of water inside axons) [29].

Supplementary Analysis

In order to test the generalizability of our results, we also performed a retrospective analysis for one subject (female, age between 25-29) from the MGH Adult Diffusion Dataset downloaded from the HCP data repository (https://www.humanconnectome.org). This dataset was acquired on a 3T Siemens Connectom scanner, customized with a 64 channel tight-fitting brain array coil [144] and consists of MPRAGE and diffusion scans with four levels of diffusion weighting. The b-values used were 1000, 3000, 5000 and $10.000\,\mathrm{s/mm^2}$ with respectively 64, 64, 128 and 256 randomly distributed diffusion-encoding directions over a full sphere. Every 14th volume was an image without diffusion weighting (b0) used for motion correction. Other acquisition parameters were TE = $57\,\mathrm{ms}$, TR = $8800\,\mathrm{ms}$, voxel size = $1.5\,\mathrm{mm} \times 1.5\,\mathrm{mm} \times 1.5\,\mathrm{mm}$ isotropic, FOV = $210\,\mathrm{mm} \times 210\,\mathrm{mm}$, pixel bandwidth = $1984\,\mathrm{Hz/Px}$, echo spacing = $0.63\,\mathrm{ms}$ and parallel imaging factor = 3. Additional details can be found in [145]. The MPRAGE acquisition parameters were TE = $1.15\,\mathrm{ms}$, TR = $2530\,\mathrm{ms}$, TI = $1100\,\mathrm{ms}$, and voxel size = $1\,\mathrm{mm} \times 1\,\mathrm{mm} \times 1\,\mathrm{mm}$ isotropic voxels.

These data were analyzed in a manner very similar to that described above for our primary dataset with a few notable differences. First, the Gaussian smoothing kernel had a full width at half maximum of $1.85\,\mathrm{mm}$, due to the higher resolution of the HCP data. Second, we computed the direction-averaged signal for each b-value shell from a simple arithmetic mean. Since the HCP diffusion encoding directions are random, this arithmetic mean corresponds to a conventional Monte Carlo integration divided by the number of directions [146]. Finally, because of the higher resolution of the HCP dataset, each ROI consisted of 16 rather than 4 voxels.

4.2.3 Results

For Subject 1, the SNR at $b = 6000\,\mathrm{s/mm^2}$ ranged from 6.3 to 11.4 in the white matter ROIs and between 3.1 and 6.6 in the gray matter ROIs. For Subject 2, the ranges were 8.5-11.2 for white matter and 3.0-4.9 for gray matter. This suggests that the bias in our data due to rectified noise should be relatively small [141].

The log-log plotted ROI data for Subject 1 together with linear fits are shown in Figure 4.2a. The x-axis corresponds to $ln(\frac{b_1}{b})$, while the y-axis corresponds $ln(\frac{\bar{S}}{S_0})$. Here $b_1 \equiv 1000\,\mathrm{s/mm^2}$ is a reference b-value scale, chosen for convenience. The high quality of these linear fits (average R^2 of 0.996) indicates that, over the range of b-values investigated, the data are well described by power law behavior of the form

$$\frac{\bar{S}}{S_0} \approx C \cdot (\frac{b_1}{b})^{\alpha}, \tag{4.3}$$

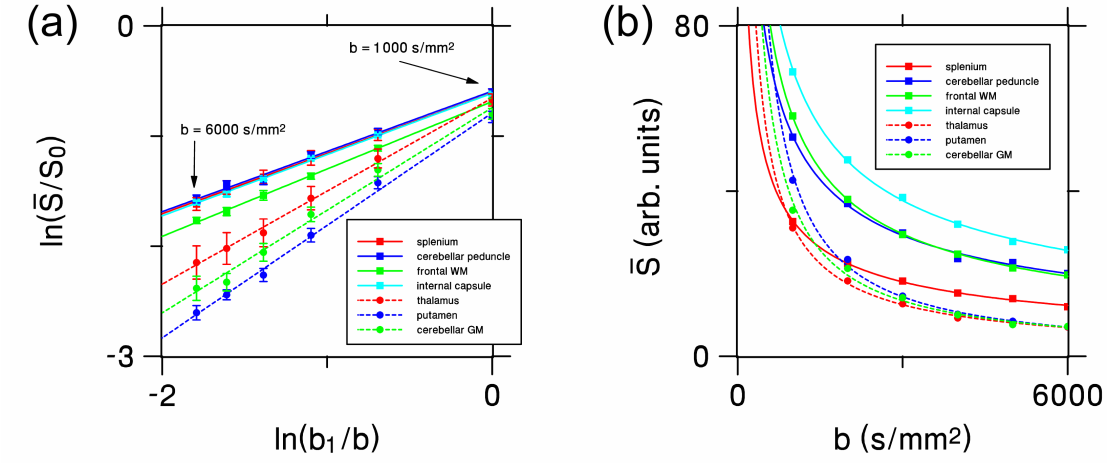

Figure 4.2: (a) Log-log plot showing the relationship between the direction-averaged DWI signal $\bar{S}$ from each ROI (normalized by dividing by the signal without diffusion weighting, S_0) and the six b-values (1000, 2000, 3000, 4000, 5000 and $6000\,\mathrm{s/mm^2}$) for all the ROIs of Subject 1. The reference b-value b_1 is set to $1000\,\mathrm{s/mm^2}$. The error bars show the standard deviations of the measurements. The fits to Equation 4.1 for white and gray matter regions are indicated by solid and dashed lines, respectively. (b) Linear scale plot showing the same data, but without normalization and error bars in order to better demonstrate the quality of the fits. WM = white matter; GM = gray matter.

where the exponent α is the measured slope of the fits and C is a dimensionless constant. The constant C is approximately equal to $\frac{\bar{S}_{1000}}{S_0}$, with $\bar{S}_{1000}$ being the direction-averaged signal for $b \equiv 1000\,\mathrm{s/mm^2}$, and may be calculated directly from the y-intercept of the fits.

The fact that the direction-averaged DWI signal is accurately fit by a power law for $b = 1000$ to $6000\,\mathrm{s/mm^2}$ indicates that two degrees of freedom are sufficient to describes the b-value dependence over this range of diffusion weightings. This is further illustrated in Figure 4.2b by linear scale power law fits of $\bar{S}$ as a function of the b-value. The quality of these fits is remarkable given that they utilize only two adjustable parameters. In contrast, a stretched exponential [127] has three adjustable parameters, while a bi-exponential [126] uses four.

Following Equation 4.3, we computed for each ROI both the exponent α and the constant C, which were derived from the slope and y-intercept of the linear regression analysis of the log data (as in Figure 4.2a). Table 4.1 lists these fitting parameters for both subjects and all the ROIs. In white matter, the mean exponent α is found to be 0.56 $\pm$ 0.05, while the mean gray matter exponent has a substantially larger value of 0.88 $\pm$ 0.11. A paired t-test demonstrates the white and gray matter exponents to be significantly different (p = 0.0005). The fitting constant C is, in contrast, relatively similar over the considered ROIs, with no significant difference between its average values calculated from white matter (0.53 $\pm$ 0.03) and gray (0.48 $\pm$ 0.05).

Parametric maps of α for a single axial slice from each subject are shown in Figure 4.3. Corresponding FA maps [69] and MPRAGE images are also provided for anatomical reference. The FA maps were calculated from a conventional diffusional kurtosis imaging analysis using just the images with diffusion weightings of b = 0, 1000 and $2000\,\mathrm{s/mm^2}$ [84]. Throughout the white matter, the exponent is seen to be relatively close to 0.5, while appreciably larger values are found for gray matter in consistency with our ROI results.

Table 4.1: Estimates for the exponent α and the scale constant C obtained by fitting Equation 4.3 to the direction-averaged DWI data from the six b-value shells for each of the subjects and the considered anatomical regions. The quality of the fits is indicated by the coefficient of determination R^2, and the uncertainties, in parentheses, indicate standard errors as determined with linear regression.

ROI		**Subject 1**			**Subject 2**		
		R^2	α	**C**	R^2	α	**C**
White Matter	**cerebellar peduncle**	0.993	0.548 (-0.022)	0.553 (-0.015)	0.999	0.53 (-0.01)	0.545 (-0.007)
	splenium	0.998	0.548 (-0.013)	0.543 (-0.008)	0.999	0.475 (-0.008)	0.495 (-0.005)
	internal capsule	0.998	0.557 (-0.01)	0.543 (-0.007)	0.999	0.555 (-0.005)	0.537 (-0.004)
	frontal	0.999	0.611 (-0.008)	0.503 (-0.008)	0.999	0.615 (-0.011)	0.482 (-0.006)
Gray Matter	**thalamus**	0.997	0.845 (-0.024)	0.52 (-0.016)	0.998	0.706 (-0.015)	0.481 (-0.009)
	cerebellum	0.989	0.966 (-0.049)	0.485 (-0.03)	0.995	0.957 (-0.034)	0.397 (-0.017)
	putamen	0.995	1.021 (-0.034)	0.543 (-0.02)	0.997	0.81 (-0.022)	0.478 (-0.013)

Voxels containing substantial amounts of cerebrospinal fluid (e.g., ventricles and sulci) also show large values of in Figure 4.3, but this may be of little physical significance as the signal in these regions does not necessarily follow the power law decay of Equation 4.3.

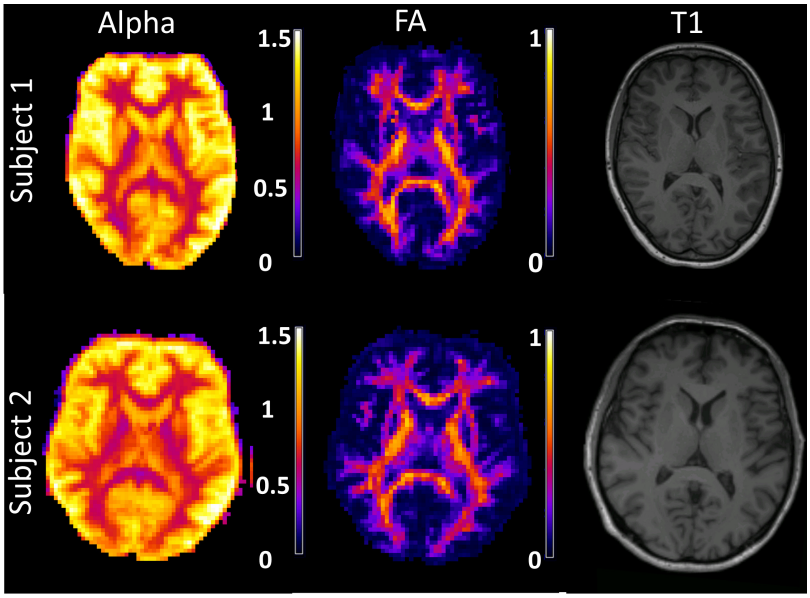

Figure 4.3: Parametric maps of the exponent α for a single axial slice from each subject. For reference, the corresponding FA and a similar MPRAGE (T_1) images are also shown. In white matter, α is close to 0.5, while for gray matter regions the exponent is consistently larger.

By combining Equation 4.1 and Equation 4.2, one finds

$$\frac{\bar{S}}{S_0} \approx 0.5 \cdot \zeta \cdot \sqrt{\frac{\pi}{b}}, \tag{4.4}$$

This has the same form as Equation 4.3 with an exponent $\alpha = 0.5$, which is relatively close to the measured values for white matter shown in 4.1. Thus our observed power law decay is roughly consistent with the behavior predicted by Equation 4.3. Parametric maps of ζ, as derived with Equation 4.1, from one subject for each of the b-values considered in this experiment are shown in Figure 4.4. Within the white matter regions, the ζ estimates for the higher b-values are seen to be relatively consistent with each other, as would be expected for a true tissue property. Bar graphs of the ζ estimates for the white matter ROIs based on the $b = 4000\,\mathrm{s/mm^2}$ HARDI data are given by Figure 4.5a. The mean values

over all of the white matter ROIs are shown as a function of the b-value in Figure 4.5b, again indicating a stable behavior for the larger diffusion weightings. The fact that ζ is a decreasing function for the lower b-values, suggests that including this lower range of b-values in the calculation of the power law exponent tends to increase its value.

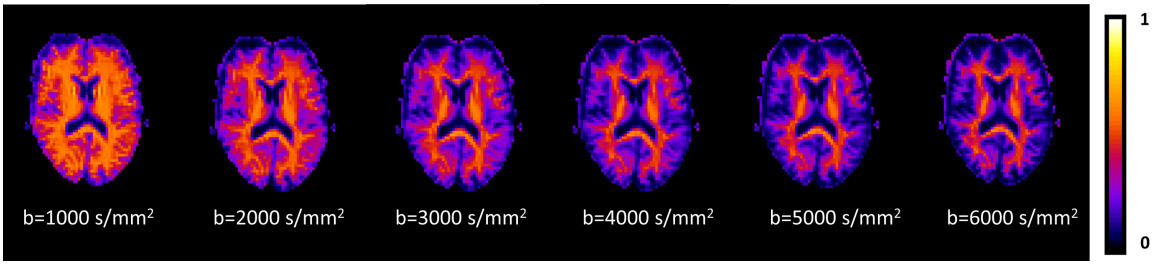

Figure 4.4: Axial maps of estimates for the quantity ζ, as given by Equation 4.1, for a single human subject as a function of the b-value. From the theory of Ref. 10, the estimates in white matter are expected to converge, for large b-values, to a level that is characteristic of the tissue microstructure. The scale bar is in units of $ms^{1/2}/\mu m$.

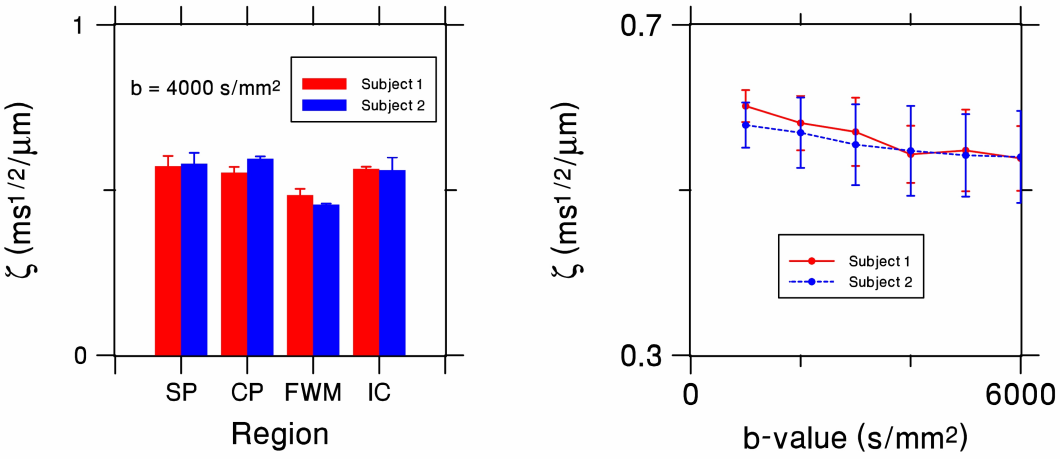

Figure 4.5: (a) The quantity ζ for the four white matter ROIs as estimated with Equation 4.1 and the HARDI data for b = $4000\,\mathrm{s/mm^2}$. (b) Mean ζ values for all the white matter ROIs as a function of the b-value. The mean values for b = 4000, 5000, and $6000\,\mathrm{s/mm^2}$ are all similar, in consistency with the theory of Reference [29]. All error bars indicate standard deviations. SP = splenium; CP = cerebellar peduncle; FWM = frontal white matter; IC = internal capsule.

For the HCP dataset, the SNR at $b = 10.000\,\mathrm{s/mm^2}$ is 3.9-5.4 in white matter ROIs and 3.0-4.9 in gray matter ROIs. For gray matter this is comparable to the SNR of our primary dataset, but the white matter SNR is somewhat lower. The linear regression ROI fits are

shown in Fig. 6a. For all the white matter regions and for the cerebellar gray matter ROI, the data points from all four b-values lie close to the best fit lines, indicating approximate power law decay. The R^2 values for the white matter regions ranges from 0.995 to 0.999, cerebellar gray matter has R^2 = 0.997. The R^2 values for the thalamus and putamen are 0.955 and 0.965, which is somewhat lower than we find with our primary dataset. This may indicate a breakdown of power law scaling, but could also reflect a systematic error in the measurements. The deviation from linearity in these two gray matter regions is most pronounced in the $b = 10.000\,\mathrm{s/mm^2}$ data points, which also correspond to the two data points with the lowest SNR. Although our simple SNR estimates are suggestive of minor noise bias, this is not definitive given the complex nature of noise when parallel imaging is utilized [147]. In this regard, it is important to note that the HCP data was acquired with a parallel imaging factor of 3, while the primary dataset used a parallel imaging factor of 2. The exponents obtained from the best fit lines in Figure 4.6a had an average value of $\alpha = 0.48 \pm 0.05$ for white matter and $\alpha = 0.73 \pm 0.13$ for gray matter, which is fairly similar to, if a bit lower than, the values from our primary dataset. The region-by-region comparison of the HCP exponents with those for the primary dataset is given by Fig 6b. A parametric map of for one slice of the HCP data appears in Fig. 6c, along with FA and MPRAGE images. Overall, in most white matter regions, the values for α are a little above 0.5, but they are visibly lower in high FA areas such as the corpus callosum.

4.2.4 Discussion

The central observation of this paper is the simple power law behavior of the direction-averaged DWI signal, as given by Equation 4.3, for b-values ranging from $1000\,\mathrm{to}\,6000\,\mathrm{s/mm^2}$. In white matter, the average measured exponent is $\alpha = 0.56 \pm 0.05$, while the average gray matter exponent of 0.89 ± 0.11 is substantially larger. This disparity suggests fundamental differences in gray and white matter microstructure. Due to the direction averaging of the DWI signal, we hypothesize that these go beyond those reflected in the familiar macro-

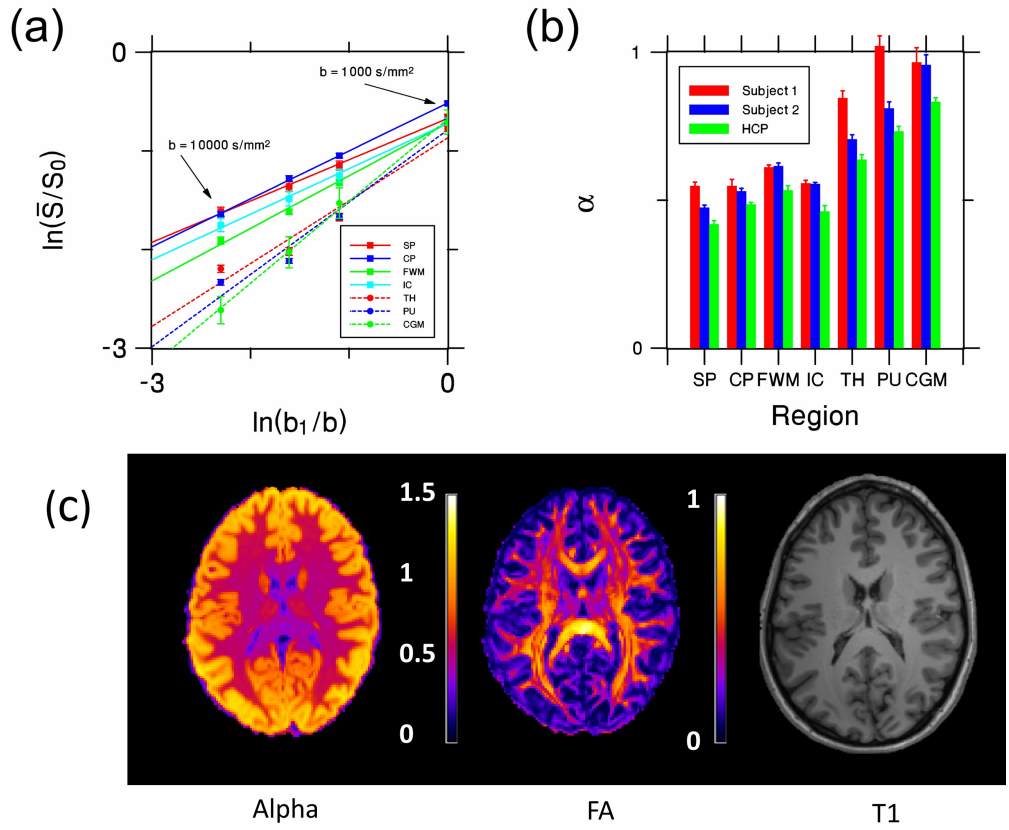

Figure 4.6: (a) Log-log plot showing the relationship between the direction-averaged DWI signal $\bar{S}$ from each ROI (normalized by dividing by the signal without diffusion weighting, S_0) and the four b-values (1000, 3000, 5000, $10.000\,\mathrm{s/mm^2}$) for all the ROIs in the HCP dataset (Similar to Figure 4.2a). (b) The exponent α for each ROI and subject. The HCP estimates are similar to those from the primary dataset. (c) Parametric maps of the exponent α and FA for a single axial slice from the HCP dataset. A similar T_1 slice is provided as an anatomical reference. All error bars indicate standard deviations. SP = splenium; CP = cerebellar peduncle; FWM = frontal white matter; IC = internal capsule, TH = thalamus, PU = putamen, CGM = cerebellar gray matter.

scopic diffusion anisotropy metrics (e.g., FA) [69].

It should be emphasized that our primary data only support power law signal decay for the restricted range of b-values between 1000 and $6000\,\mathrm{s/mm^2}$. For smaller b-values, this scaling behavior must break down as the DWI signal approaches a constant in the limit b0. It could also fail to hold for very large b-values, if, for example, there were a pool of immobile proton spins that contributed a constant to the overall signal. However, our supplementary analysis of HCP data suggests that this picture may indeed hold for b-

values as high $10.000\,\mathrm{s/mm^2}$, although the acquisition parameters for the HCP dataset are quite different from ours. Most importantly, the TE for our dataset is $149\,\mathrm{ms}$, while HCP dataset was acquired with TE = $57\,\mathrm{ms}$. This implies a much shorter diffusion time as well as a larger contribution from myelin water for the HCP dataset, which could potentially affect the quality of the power law decay fits. In addition, the HCP dataset includes only 64 diffusion encoding directions for $b = 1000\,\mathrm{s/mm^2}$ and $3000\,\mathrm{s/mm^2}$, which would reduce the accuracy of the directional averaging, especially in high FA areas such as the corpus callosum.

The exponent of approximately one-half for white matter is consistent with the large b-value limit predicted for a model of water confined to thin, impermeable cylindrical tubes [29, 22], which is commonly used to describe the diffusion dynamics of intra-axonal water [148, 32, 22, 28]. Our results support this as being a reasonable approximation for white matter (Table 1, Figure 4.3). However, the markedly larger exponent found for gray matter points to essential differences in the diffusion dynamics. Since gray matter does contain a large proportion of neurites that are plausibly modeled by thin cylindrical tubes [32, 22, 148, 28], this conclusion may seem surprising. Indeed by using magnetic resonance spectroscopy, Kroenke and coworkers [148] measured the diffusion-weighted signal decay for N-acetyl-L-aspartate (NAA) in rat brain up to b-values of about $20.000\,\mathrm{s/mm^2}$ and showed that this data could be accurately fit with a model based on thin, impermeable cylinders. The volume elements for the experiment were large, but contained substantial amounts of gray matter. Thus, the higher exponent found here for water diffusion most likely reflects a distinction between water and NAA diffusion dynamics, rather than simply the geometry of the cylinder model being inadequate for gray matter. One key distinction is that NAA is confined to neurons [148], while water can cross cell membranes. The discrepancy between the white and gray matter exponents for our experiment could then plausibly be due to gray/white matter differences in water permeability for the cell membranes of neurites, with gray matter having a sufficiently larger permeability to invalidate the model.

Thus, qualitatively different assumptions about brain microstructure may be necessary to accurately model the water diffusion dynamics for white and gray matter.

As discussed by Jensen and coworkers [29], a consequence of the thin cylindrical tube model for axons is that the direction-averaged DWI signal decay in white matter can be related to the microstructural parameter ζ, in the limit of large b-values. Estimates for ζ obtained from our data and Equation 4.1 are shown in Figures 4.4 and 4.5. These estimates are fairly consistent across b-values for $b \geq 4000\,\mathrm{s/mm^2}$. As intrinsic tissue parameters must be independent of the diffusion weighting, this suggests a reasonable minimum b-value of about $4000\,\mathrm{s/mm^2}$ for the applicability of Equation 4.4. Since the estimations of both the intra-axonal diffusivity, D_a, and the axonal water fraction f are topics of substantial recent interest [149], accurate quantification of $\zeta \approx \frac{f}{D_a}$ from data acquired from a single b-value shell could be useful in constraining microstructural models of water diffusion dynamics in brain [134, 123]. As is evident from Figures 4.4 and 4.5, there is some variability in ζ values across white matter regions. From our results alone, it cannot be determined whether this is mainly due to differences in f or D_a. However, individual estimates for these parameters based on explicit modeling suggest that both of these parameters may have significant regional variations [27, 28, 134].

Two other proposed models predict power law signal decay, at least for sufficiently large b-values. One of these is the statistical model of Yablonskiy and coworkers [128], for which the signal decays as $1/b$ for large b. This does not match the power law behavior that we find in white matter, but it is in rough agreement with our exponent for gray matter. Yet another statistical model, based on a gamma distribution of diffusion coefficients, yields a DWI signal of the form [113, 150, 151].

$$\frac{S}{S_0} = \frac{1}{(1 + \frac{b}{b_c})^{\epsilon}}, \tag{4.5}$$

which scales as $(b_c/b)^\epsilon$ for $b \geq b_c$. However, in this case, the exponent ϵ depends on the details of the distribution rather than having a universal value. Nonetheless, it should be emphasized once again that our observation of power law scaling for the direction-averaged DWI signal has only been demonstrated over a restricted range of b-values, and so our results may not be sufficient to fully evaluate either of these two statistical models. Note added in revision: While this paper was under review, an independent study reported similar power law scaling for the direction-averaged DWI signal in white matter with an exponent near one-half up to b-values of $10.000\,\mathrm{s/mm^2}$ [87].

4.2.5 Conclusion

The direction-averaged DWI signal in human brain decreases with increasing b-values approximately as a power law, for b-values ranging from 1000 to $6000\,\mathrm{s/mm^2}$. In white matter, the exponent characterizing this decrease is close to one-half, which is consistent with the large b-value limit of a model in which intra-axonal water diffusion is confined to thin, impermeable cylinders. The exponent for gray matter is substantially larger, indicative of sharp microstructural differences relative to white matter that likely go beyond those associated with diffusion anisotropy. As a consequence, in contrast to some previous approaches, white and gray matter may require distinct tissue modeling strategies in order to obtain the most accurate results.

4.3 Modeling White Matter Microstructure with Fiber Ball Imaging

4.3.1 Introduction

dMRI is widely applied as a tool for investigating brain microstructure in vivo [152]. However, determining specific microstructural properties from measured dMRI data is challenging due to the intricacies of water diffusion within the complex cytoarchitecture of brain tissue [153]. This has led to an assortment of tissue modeling methods being proposed for dMRI, which are still being actively developed and evaluated [154, 155, 156, 8, 123, 157,

22].

A common difficulty associated with dMRI tissue models is managing the multiple local optima that often arise in nonlinear fitting algorithms with several free parameters, which adds to numerical computation times and may increase sensitivity to noise and imaging artifacts [158, 149, 8, 7]. In addition, estimating certain microstructural parameters with good accuracy and precision has proven problematic. This is notably true for the intrinsic intra-axonal diffusivity (D_a), with predictions from different approaches varying by over a factor of two [149, 7, 159]. Here we present a dMRI modeling method based on FBI [29] intended to ameliorate these issues.

FBI is closely related to q-ball imaging [160] and yields estimates for the fODF in white matter from HARDI data, by employing b-values typically in the range of 4000 to $6000\,\mathrm{s/mm^2}$ [29, 30]. It can also be used to calculate several microstructural properties associated with axonal fiber bundles. An advantage of FBI is that the core post-processing step is a straightforward linear transformation of the dMRI signal data that avoids the complications of nonlinear fitting.

In this study, we demonstrate how to augment FBI with lower b-value dMRI data in order to estimate several additional parameters, including D_a, the mean extra-axonal diffusivity ($\bar{D}_e$), and the AWF. While determining these extra quantities does require nonlinear fitting, the proposed algorithm involves the minimization of a cost function having only a single free parameter. This allows the global optimum to be found robustly and efficiently. This approach differs markedly from the conventional tactic of directly fitting the signal model corresponding to the assumed microstructural framework (i.e., the tissue model) to dMRI signal data, which typically leads to a cost function with multiple adjustable parameters and the aforementioned computational challenges. Instead, we regard the outputs of the FBI analysis as fixed inputs upon which the cost function is built. Similarly, we also

use the diffusion tensor, obtained by standard means from the lower b-value dMRI data, as a fixed input. In this way, the number of free parameters that need to be determined by nonlinear optimization is reduced to one, resulting in a simple numerical procedure.

A principal motivation for this Fiber Ball White Matter (FBWM) modeling approach is to improve upon the WMTI method [27, 161], which yields predictions for the same basic physical quantities. An advantage of WMTI is its simple computational algorithm that uses only comparatively low b-value dMRI data. However, WMTI assumes all axons within any given voxel to be aligned in approximately the same direction, which may be a significant source of error particularly in crossing fiber regions. The FBWM approach overcomes this limitation by employing the measured fODF from FBI rather than presuming a specific geometrical arrangement for the axons. In order to investigate the extent to which FBWM and WMTI lead to different predictions, we utilize experimental results obtained from three healthy volunteers.

4.3.2 Theory

Signal Model

We assume the intra-axonal and extra-axonal spaces can be treated as separate compartments, which requires the intra-axonal water exchange time to be large in comparison to the diffusion time for the dMRI sequence. Although this exchange rate is not known with high precision, it has been estimated to be on the order of seconds [162], which is indeed long relative to typical dMRI diffusion times. In addition, we neglect the dMRI signal from myelin water. Myelin water has a T2 of about $10-20\,\mathrm{ms}$ [163], so the myelin water signal will be suppressed by over a factor of 100 for typical clinical scanner dMRI echo times of about $100\,\mathrm{ms}$.

For the intra-axonal space, we idealize axons as thin, straight cylinders, which implies

an intra-axonal dMRI signal of the form

$$S_a(b, \mathbf{n}) = S_0 f \int d\Omega_u F(\mathbf{u}) exp[-bD_a(\mathbf{n} \cdot \mathbf{u})^2], \tag{4.6}$$

where f is the AWF, S_0 is the signal without diffusion weighting, b is the b-value for the dMRI sequence, $\mathbf{n}$ is the diffusion encoding direction unit vector, and $F(\mathbf{u})$ is the fODF as a function of a unit vector $\mathbf{u}$ that indicates the axon orientation. The integral in Equation 4.6 is taken over all possible axon orientations, and the fODF is normalized so that

$$1 = \int d\Omega_u F(\mathbf{u}). \tag{4.7}$$

This corresponds to the widely used stick model for axons [164, 155, 129, 148, 32, 165, 8, 123, 22, 87, 166, 28], and it is also employed in FBI [29]. However, here we adopt a different normalization for the fODF than used in our previous work [29], as this is more convenient for our proposed FBWM modeling approach.

For the extra-axonal space, we treat water diffusion as Gaussian so that the signal in a diffusion encoding direction $\mathbf{n}$ is given by

$$S_e(b, \mathbf{n}) = S_0(1 - f) exp(-b\mathbf{n}^T \boldsymbol{D_e} \mathbf{n})), \tag{4.8}$$

where $\boldsymbol{D_e}$ is the extra-axonal diffusion tensor. This same model has been utilized by Jespersen and coworkers [165] and should be appropriate for b-values small enough so that the intrinsic kurtosis of the extra-axonal space can be neglected. As we shall argue, for FBWM the details of the extra-axonal signal at high b-values should be relatively unimportant, since the intra-axonal signal is then much larger and dominates the full signal, which is simply the sum of S_a and S_e.

Fiber Ball Imaging

FBI requires HARDI data for a single spherical b-value shell with a large number of uniformly distributed diffusion encoding directions. The chosen b-value, b_{FBI}, should be high enough to strongly suppress the dMRI signal from the extra-axonal space, but not so big as to induce a significant noise bias. In practice, b_{FBI} would usually be in the range of $4000\text{-}6000\,\mathrm{s/mm^2}$, depending on scanner performance and the desired spatial resolution [29, 30].

From the HARDI data, one can construct a spherical harmonic expansion for the dMRI signal on the b-value shell as

$$S(b_{FBI}, \mathbf{n}) = S_0 \sum_{l=0}^{\infty} \sum_{m=-l}^{l} a_l^m Y_l^m(\theta, \phi), \tag{4.9}$$

where $S(b, \mathbf{n})$ is the signal magnitude as a function of the b-value and the diffusion encoding direction, a_l^m are the expansion coefficients, Y_l^m are the spherical harmonics, and (θ, ϕ) are the spherical angles corresponding to $\mathbf{n}$. In Equation 4.9, we assume the convention [167]

$$Y_l^m(\theta, \phi) = \sqrt{\frac{2l+1}{4\pi} \cdot \frac{(l-m)!}{(l+m)!}} P_l^m(cos\theta) e^{im\phi}, \tag{4.10}$$

where

$$P_l^m(x) \equiv \frac{(-1)^m}{2^l l!} (1-x^2)^{m/2} \frac{d^{l+m}}{d^{l+m}x} (x^2-1)^l \tag{4.11}$$

is the associated Legendre function. The expansion coefficients for odd l may be set to zero, since reflection symmetry implies $S(b, -\mathbf{n}) = S(b, \mathbf{n})$.

The central result of FBI is then that the fODF is approximately given by [29]

$$F(\mathbf{n}) = \sum_{l=0}^{\infty} \sum_{m=-2l}^{2l} c_{2l}^m Y_{2l}^m(\theta, \phi), \tag{4.12}$$

where

$$C_{2l}^{m} = \frac{a_{2l}^{m} g_0(b_{FBI} D_0)}{\sqrt{4\pi} P_{2l}(0) a_0^0 g_{2l}(b_{FBI} D_0)} \tag{4.13}$$

with $P_l(x) = P_l^0(x)$ being a Legendre polynomial and

$$g_{2l}(x) = \frac{l! x^{l+\frac{1}{2}}}{\Gamma(2l+\frac{3}{2})} {}_1F_1(l+\frac{1}{2}; 2l+\frac{3}{2}; -x) \tag{4.14}$$

In Equation 4.13, D_0 represents an upper bound on D_a, which would usually be chosen as either infinity or as the free water diffusivity at body temperature of about $3.0\,\mu\mathrm{m}^2/\mathrm{ms}$ [168], while in Equation 4.14, ${}_1F_1$ is the confluent hypergeometric function and Γ is the Gamma function. One may verify that Equation 4.12 is normalized in accord with Equation 4.7. For $D_0 = \infty$, Equation 4.13 simplifies to

$$c_{2l}^{m} = \frac{a_{2l}^{m}}{\sqrt{4\pi} P_{2l}(0) a_0^0}, \tag{4.15}$$

since $g_{2l}(\infty) = 1$. In this case, the fODF is proportional to the inverse Funk transform [169] of the dMRI signal for the HARDI shell. In practice, the difference between using a D_0 of infinity or $3.0\,\mu\mathrm{m}^2/\mathrm{ms}$ is typically small, with the fODF being slightly sharper with $D_0 = 3.0\,\mu\mathrm{m}^2/\mathrm{ms}$ [29]. Note that D_0 becomes more irrelevant as b_{FBI} is increased.

From Equation 4.12, one may show that the diffusion tensor for the intra-axonal compartment, within the stick model approximation, is

$$\boldsymbol{D_a} = D_a \mathbf{A}, \tag{4.16}$$

with

$$\mathbf{A} \equiv \frac{1}{C_0^0\sqrt{30}} \begin{pmatrix} \frac{\sqrt{30}}{3}c_0^0 - \frac{\sqrt{6}}{3}c_2^0 + c_2^2 + c_2^{-2} & ic_2^2 - ic_2^{-2} & -c_2^1 + c_2^{-1} \\ ic_2^2 - ic_2^{-2} & \frac{\sqrt{30}}{3}c_0^0 - \frac{\sqrt{6}}{3}c_2^0 - c_2^2 - c_2^{-2} & -ic_2^1 - ic_2^{-1} \\ -c_2^1 + c_2^{-1} & -ic_2^1 - ic_2^{-1} & \frac{\sqrt{30}}{3}c_0^0 + \frac{2\sqrt{6}}{3}c_2^0 \end{pmatrix}. \quad (4.17)$$

Observe that $tr(\mathbf{A}) = 1$. The tensor $\mathbf{A}$ is guaranteed to be real, since $(c_l^m)^* = c_l^{-m}$ as follows from the requirement that the fODF be real. Even though D_a is not known a priori, Equations 4.16 and 4.17 are sufficient to calculate the FA for the intra-axonal space, as well as other related dimensionless properties of $\boldsymbol{D_a}$. More explicitly, this Fractional Anisotropy for the Axons (FAA) is given by

$$FAA = \sqrt{\frac{3\sum_{m=-2}^{2}|c_2^m|^2}{5|c_0^0|^2 + 2\sum_{m=-2}^{2}|c_2^m|^2}}. \quad (4.18)$$

The derivations of Equations 4.16-4.18 are discussed in the Appendix B. FBI also estimates the parameter $\zeta \equiv f/\sqrt{D_a}$ as [29]

$$\zeta = a_0^0\frac{\sqrt{b_{FBI}}}{\pi} \quad (4.19)$$

The FAA is simply related to the axonal dispersion metric by $p_2 = FAA/\sqrt{3 - 2(FAA^2)}$ [7],[166].

Expressions for Intra-Axonal and Extra-Axonal signals in terms of AWF

By combining Equations 4.6 and 4.12, one can show that the spherical harmonic expansion for intra-axonal signal may be expressed as [29]

$$S_a(b, \mathbf{n}) = 2\pi S_0\zeta\sqrt{\frac{\pi}{b}}\sum_{l=0}^{\infty}\sum_{m=-2l}^{2l}P_{2l}(0)g_{2l}(b\frac{f^2}{\zeta^2})c_{2l}^m Y_{2l}^m(\theta, \phi). \quad (4.20)$$

A notable feature of the spherical harmonic expansion in Equation 4.20 is that the only unknown parameter is f, as all the other quantities are determined by FBI. This contrasts with several other white matter modeling approaches that utilize multiple free parameters in order to represent the intra-axonal signal [32, 165, 8, 166, 28]. Consistency of Equations 4.9,4.19, and 4.20 requires that

$$g_0(b_{FBI}D_a) = erf(\sqrt{b_{FBI}D_a}) \approx 1, \tag{4.21}$$

where erf indicates the error function; this approximation holds to better than 0.1% provided $b_{FBI}D_a > 5.5$.

Now let us assume that, in addition to the HARDI b-value shell acquired for FBI, one also obtains low b-value data sufficient for estimating the total diffusion tensor, **D**, as is conventionally done with either DTI [170] or DKI [113]. The diffusion tensor for the extra-axonal space, $\boldsymbol{D_e}$, is related to **D** and $\boldsymbol{D_a}$ by

$$\mathbf{D} = f\boldsymbol{D_a} + (1-f)\boldsymbol{D_e}, \tag{4.22}$$

which implies

$$\boldsymbol{D_e} = \frac{\mathbf{D} - f\boldsymbol{D_a}}{(1-f)}. \tag{4.23}$$

With the help of Equation 4.16 and the definition of ζ, this leads to

$$\boldsymbol{D_e} = \frac{1}{(1-f)}(\mathbf{D} - \frac{f^3}{\zeta^2}\mathbf{A}). \tag{4.24}$$

Except for the AWF, all the quantities on the right-hand side of Equation 4.24 can be directly calculated from either FBI or low b-value dMRI data. For fitting purposes, we can therefore regard $\boldsymbol{D_e}$ as only a function of f. This also applies to the extra-axonal signal of Equation 4.8, which is determined by $\boldsymbol{D_e}$ and f.

Cost Function

The dMRI signal for the full FBWM model is

$$S_{mod}(b, \mathbf{n}) = S_a(b, \mathbf{n}) + S_e(b, \mathbf{n}). \tag{4.25}$$

As we have seen, both S_a and S_e can be thought of as functions of the AWF, given the information provided by FBI and the total diffusion tensor. Therefore, we may consider the total signal S_{mod} to also be a function of the AWF.

In order to determine the AWF, we introduce the cost function

$$C(f) \equiv \frac{1}{S_0}\{\frac{1}{M}\sum_{i=1}^{M}\frac{1}{N}\sum_{j=1}^{N_i}[S_{mod}(b_i, \mathbf{n}_{i,j} - S_{exp}(b_i, \mathbf{n}_{i,j})]^2\}^{1/2}, \tag{4.26}$$

where $S_{exp}(b, \mathbf{n})$ is the magnitude of the measured dMRI signal as a function of b-value and diffusion encoding direction, M is the number of b-value shells, N_i is the number of diffusion encoding directions for the ith shell, b_i is the b-value for the ith shell, and $\mathbf{n}_{i,j}$ is the jth diffusion encoding direction for the ith shell. Normally, one would set $b_M = b_{FBI}$. This cost function represents a weighted root-mean-square difference between the model and experimental signals divided by the signal for $b = 0$, with the weight factors depending on the number of directions for each shell. The best estimate for the AWF is then defined as the value of f that minimizes C.

By construction, we expect the model and experimental signals to agree fairly well for both low and high b-values, even if f is only roughly correct. Thus in order to predict the AWF with useful precision, shells having intermediate b-values should be included in Equation 4.26. By intermediate, we mean b-values larger than the range for which the signals b-value dependence is primarily governed by the total diffusion tensor (as assumed for DTI), but smaller than the b-values for which the intra-axonal signal predominates (as

assumed for FBI). In brain, we expect such intermediate b-values to be roughly 2000 to $3000\,\mathrm{s/mm^2}$, corresponding to the smallest b-values with readily apparent non-Gaussian diffusion effects in the dMRI signal [20, 113]. A minimal FBWM imaging protocol would, therefore, have three nonzero b-value shells, with low, medium, and large b-values.

Microstructural Parameters

Once the AWF has been determined by minimizing C, then several other microstructural parameters are easily calculated. In particular, the intrinsic intra-axonal diffusivity can be found from

$$D_a = \frac{f^2}{\zeta^2}. \tag{4.27}$$

which follows directly from the definition of ζ, and the mean extra-axonal diffusivity is given by

$$\bar{D}_e = \frac{1}{(1-f)}(\bar{D} - \frac{f^3}{3\zeta^2}), \tag{4.28}$$

where $\bar{D} = tr(\mathbf{D}/3)$ is the Mean Diffusivity (MD), which follows from Equation 4.24. If the eigenvalues of $\boldsymbol{D_e}$ are $\lambda_{e,1} \geq \lambda_{e,2} \geq \lambda_{e,3}$, then one can also estimate the axial extra-axonal diffusivity as

$$D_{e,\parallel} \equiv \lambda_{e,1} \tag{4.29}$$

and the radial extra-axonal diffusivity as

$$D_{e,\perp} \equiv \frac{1}{2}(\lambda_{e,2} + \lambda_{e,3}). \tag{4.30}$$

4.3.3 Methods

Imaging

DWI data were acquired for three healthy volunteers on a 3T Prisma MRI scanner (Siemens Healthcare, Erlangen, Germany) under a protocol approved by the Medical University of South Carolina institutional review board. Using a twice-refocused echo planar imaging pulse sequence to minimize eddy current distortion [137], 42 axial brain slices with $3.0\,\mathrm{mm}$ slice thickness and no interslice gap were obtained. The b-values were 0, 1000, 2000, and $6000\,\mathrm{s/mm^2}$. For the 1000 and $2000\,\mathrm{s/mm^2}$ shells, 30 vendor-supplied diffusion encoding directions were employed, while 256 diffusion encoding directions were acquired for the $6000\,\mathrm{s/mm^2}$ (HARDI) shell. For the 0 images, 25 separate signal excitations were utilized for each slice. The HARDI shell had a large number of directions since these data were applied in estimating the spherical harmonic expansion of Equation 4.9. The TE was $98\,\mathrm{ms}$, the TR was $5100\,\mathrm{ms}$, the FOV was $222\,\mathrm{mm} \times 222\,\mathrm{mm}$, and the acquisition matrix was 7474, resulting in isotropic voxels with dimensions of $3\,\mathrm{mm} \times 3\,\mathrm{mm} \times 3\,\mathrm{mm}$. The data were acquired with an in-plane parallel imaging factor of 2 and a multiband acceleration factor of 2, using a bandwidth of $1438\,\mathrm{Hz/pixel}$. Partial Fourier encoding was not employed. This entire DWI scan protocol was then repeated, in the same scan session, in order to allow the reproducibility of our parameter estimates to be tested. The combined scan time for both runs was 59 min 20 s.

For anatomical reference, T1-weighted (MPRAGE) images were also acquired with isotropic $1\,\mathrm{mm}$ voxels for 192 slices. The TE was $2.26\,\mathrm{ms}$, the TI was $900\,\mathrm{ms}$, the TR was $2300\,\mathrm{ms}$, and the total scan time was 5 min 21 s.

Data Analysis

All DWI data were denoised using a principal components analysis approach [85], and the method of moments [142] was applied to reduce noise bias. Subsequently, a Gibbs ringing

correction was employed [86], and all DWI images were co-registered to correct for any subject motion.

The DWI images for 0, 1000 and $2000\,\mathrm{s/mm^2}$ were used to calculate the diffusion tensor with DKE (https://www.nitrc.org/projects/dke/) in order to estimate the total diffusion tensor $\mathbf{D}$ on a voxel-by-voxel basis [84]. This DKI-based approach was employed instead of DTI in order to improve the accuracy of the tensor calculation [93]. The spherical harmonic coefficients of Equation 4.9 were determined with linear least squares from the 0 and HARDI data. For our main results, all harmonics up to degree $l = 6$ were kept in Equation 4.9, but we also considered other maximum degrees in auxiliary calculations aimed at investigating the impact of this cutoff. The spherical harmonic coefficients for the fODF of Equation 4.13 were calculated with $D_0 = 3.0\,\mu\mathrm{m^2/ms}$, and the microstructural parameter ζ was obtained from Equation 4.19.

In order to estimate the AWF, the cost function C of Equation 4.26 was evaluated in each voxel for 100 equally spaced points between $f = 0$ and $f = 1$. For our DWI protocol, we have $M = 3$, $N_1 = N_2 = 30$, $N_3 = 256$, $b_1 = 1000\,\mathrm{s/mm^2}$, $b_2 = 2000\,\mathrm{s/mm^2}$, and $b_3 = b_{FBI} = 6000\,\mathrm{s/mm^2}$. For each value of f, the eigenvalues of $\boldsymbol{D_e}$ were calculated with the help of Equation 4.23. If any of these eigenvalues were less than zero for a particular f, then that value of the AWF was excluded as being unphysical. The optimal AWF was taken as the value that minimized C, among all those that were not excluded. From the optimal AWF, parametric maps of D_a, $\bar{D}_e$, $D_{e,\parallel}$, and $D_{e,\perp}$ were obtained by using Equations 4.27 - 4.30. A flow chart outlining the FBWM data analysis procedure is shown in Figure 4.7. To process a full whole brain dataset for one subject required about 12.5 min on an iMac computer with a 4 GHz Intel Core i7 CPU.

For comparison, the DWI data for 0, 1000 and $2000\,\mathrm{s/mm^2}$ were used with DKE to obtain standard DKI maps of MD, FA, Mean Kurtosis (MK), axial diffusivity ($D_\parallel$), and

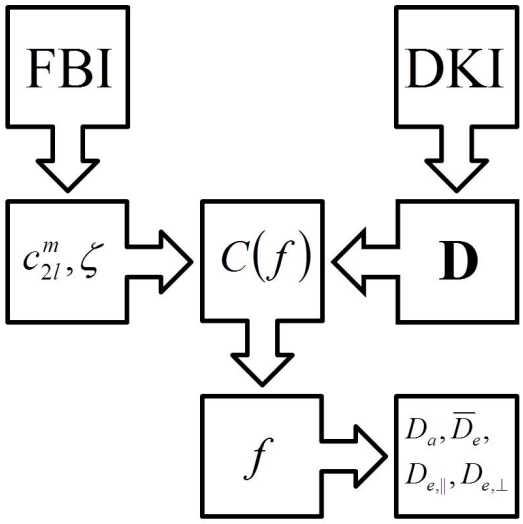

Figure 4.7: Flow chart showing the data analysis pipeline for FBWM. The parameters c_{2l}^m and ζ are determined with FBI, while the total diffusion tensor **D** is found with DKI. The cost function $C(f)$ is then constructed from c_{2l}^m, ζ, and **D**. By minimizing $C(f)$, one obtains a best estimate for the AWF. Finally, the AWF, together with the FBI and DKI results, is used to calculate the additional microstructural parameters of D_a, $\bar{D}_e$, $D_{e,\parallel}$, and $D_{e,\perp}$.

radial diffusivity ($D_\perp$). These same data were also applied to determine ζ, f, D_a, $\bar{D}_e$, $D_{e,\parallel}$, and $D_{e,\perp}$ following the WMTI procedure of Fieremans and coworkers [27]. The parametric maps for all diffusion measures were skull-stripped, and a white matter mask was defined as all brain voxels with MK ≥ 1.0 [119]. The white matter mask was based on MK rather than FA, since the FA can be low in white matter regions with extensive fiber crossing.

To test reproducibility, the two scans for each subject were analyzed independently. The absolute percent difference between the parameter values from Run 1 and Run 2 were then calculated for each white matter voxel. From the full set of these voxels, median absolute percent differences were found for each of the three subjects. We used the median rather than the average difference in order to reduce the effect of outliers, as may arise from imaging artifacts and co-registration errors. In calculating overall means for the various estimated diffusion parameters, all the white matter voxels from both runs were pooled for each subject, with standard deviations being used to indicate the spread in values.

Finally, to compare the FBI and FBWM predictions to those obtained with WMTI, average values were calculated for each parameter by binning all white matter voxels for all three subjects according to FA, with a bin size of 0.1. Even though the application of the WMTI is only recommended for voxels with FA values larger than 0.3 to 0.4 [27, 159], we determined all measures for FA values ranging from 0.15 to 0.75 for the sake of completeness. The validity of the FBI and FBWM estimates is not expected to depend significantly on FA.

Numerical Simulations

In order to investigate the effect of signal noise on our parameter estimates, we conducted numerical simulations by adding varying amounts of Rician noise to a ground truth dataset constructed from our signal model with the model parameters set to those estimated for one of our in vivo scans (Subject 1, Run 1). Using a SNR of 50, we also numerically tested the impact of employing different numbers of diffusion encoding directions (30, 64, 128, 256) for the $6000\,\mathrm{s/mm^2}$ HARDI shell, while keeping the number of directions for $b = 1000$ and $2000\,\mathrm{s/mm^2}$ fixed at 30. In performing the simulations, we utilized the same data analysis pipeline as for the in vivo data, except that co-registration was not performed (since there was no motion to correct) and denoising was skipped in a subset of the simulations in order to demonstrate the effect of this processing step.

4.3.4 Results

In vivo

Our denoising algorithm [85] generated voxelwise noise maps, which were used to estimate the average SNR in white matter. For the b_0 images, the average SNR over all scans was 59 ± 9, while for the $6000\,\mathrm{s/mm^2}$ images the average SNR was 15 ± 5. This latter number was obtained by first averaging the $6000\,\mathrm{s/mm^2}$ images over all of the diffusion encoding directions prior to dividing by the noise. Representative examples of the cost function C

of Equation 4.26 are shown in Figure 4.8, for three different white matter voxels. In most cases, the cost function has a quasi-parabolic shape with a minimum skewed toward higher AWF values. Only 10.4% of white matter voxels had multiple local minima out of a total of 16,184 for all three subjects. In any case, finding the global minima was not problematic due to our exhaustive grid search strategy.

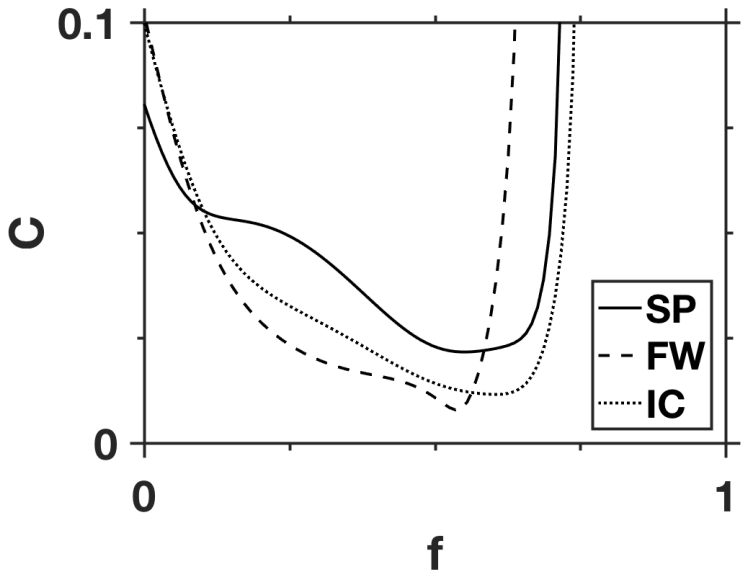

Figure 4.8: Representative FBWM cost functions for three individual voxels from the splenium of the corpus callosum (SP), frontal white matter (FW), and the internal capsule (IC). The only adjustable parameter in the cost function is the AWF, since all other quantities are fixed with information supplied by DKI and FBI. For most white matter voxels, the cost function has a single local minimum, as illustrated here.

Parametric maps of selected diffusion parameters for one anatomical slice from Subject 1 are given in Figure 4.9. The Run 1 and Run 2 maps are derived from independent datasets obtained during a single scan session. The similarity of the corresponding FBWM metrics within white matter regions demonstrates the minimal effect of signal noise (after denoising) on the reproducibility of the method. Outside of white matter, both the FBI and FBWM values have no clear physical meanings, even though our post-processing algorithms generate results for all voxels. The absolute percent differences of all white matter voxels from each subject, for the same set of diffusion parameters as in Figure 4.9, are plotted in Figure

4.10. For Subjects 1 and 2, the voxelwise reproducibility is about 10% or better for all the FBWM measures. For Subject 3, the FBWM measures have a reproducibility of about 20% or better. The axial extra-axonal diffusivity, $D_{e,\parallel}$, has the highest degree of variability for Subjects 1 and 2, while $D_{e,\perp}$ has the highest variability for Subject 3.

In Figure 4.11, FBI, FBWM, and WMTI parameter estimates are plotted as functions of the FA. The ζ values are relatively close for both FBI and WMTI, especially at higher FA, which confirms the findings of a prior study [159]. In addition, the FBWM and WMTI averages for $\bar{D}_e$ and $D_{e,\perp}$ are comparable. For FAA, f, and $D_{e,\parallel}$, WMTI shows similar trends as FBI/FBWM, but the numerical values are quite different. Importantly, the estimates for f found with FBWM are higher than the WMTI values by about 20% or more. Even more striking, D_a as predicted with FBWM is over twice that from WMTI for all FA values. This discrepancy is a manifestation of the well-known difficulty associated with estimating D_a accurately [149, 7]. Finally, Figure 4.11 also shows that the ratio ζ/f for FBI/FBWM (but not for WMTI) to be nearly constant across the full range of FA, with tight error bars. This suggests a high correlation between ζ and f, as estimated with FBI/FBWM, and indeed their voxelwise Pearson correlation coefficient is r = 0.78.

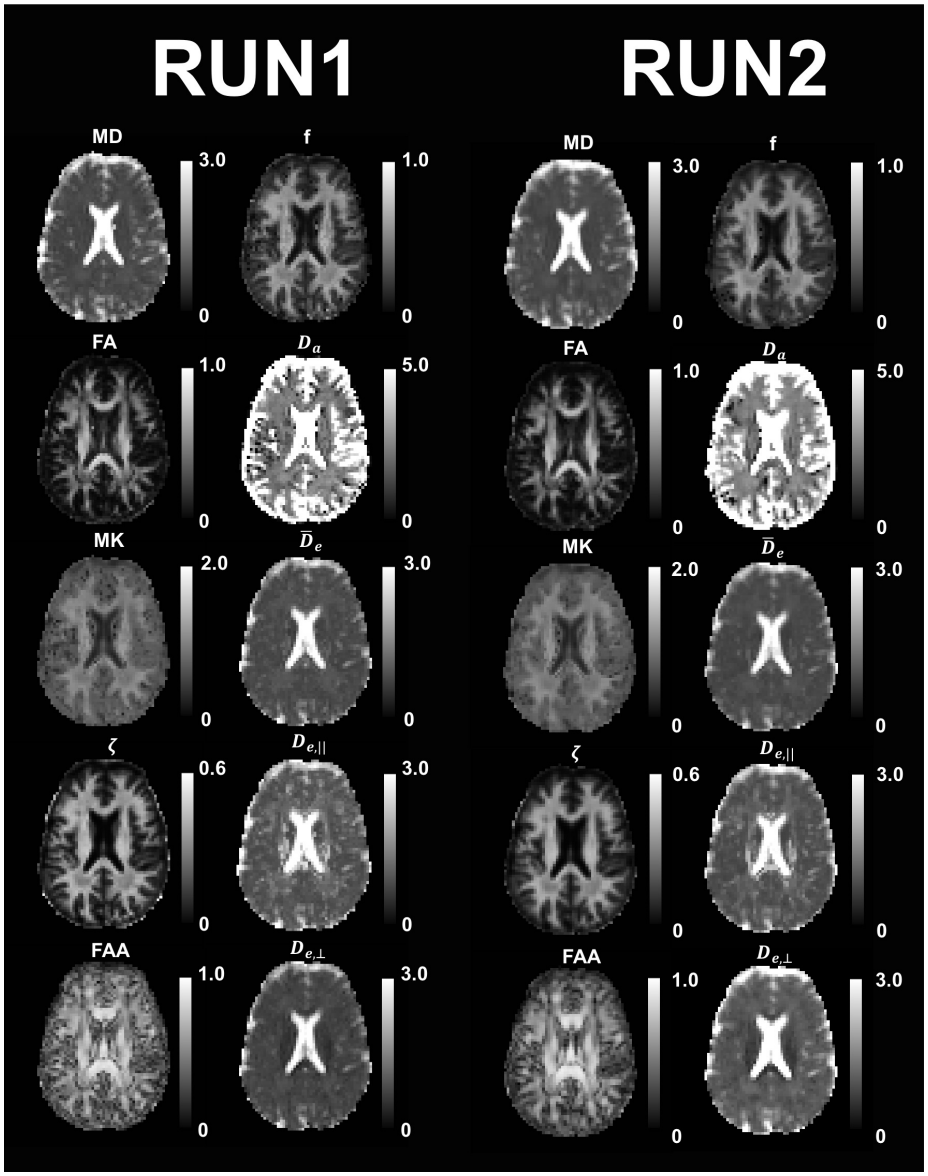

Figure 4.9: Parametric maps for selected diffusion measures from a single anatomical slice for Subject 1. Two independent datasets (Runs 1 and 2) were acquired within a single scan session in order to test reproducibility. The parameters in Columns 1 and 3 were calculated with DKI (MD, FA, MK) and FBI (ζ, FAA), while the parameters in Columns 2 and 4 were calculated with FBWM. The corresponding maps for Run 1 and Run 2 are fairly similar for all metrics, indicating that they are not overly sensitive to signal noise. The calibration bars for the diffusivities (MD, D_a, $\bar{D}_e$, $D_{e,\parallel}$, $D_{e,\perp}$) are in units of $\mu m^2/ms$, and the calibration bar for ζ is in units of $\sqrt{ms}/\mu m$, while all other quantities (FA, MK, FAA, f) are dimensionless. The FBI and FBWM results are only meaningful in white matter regions.

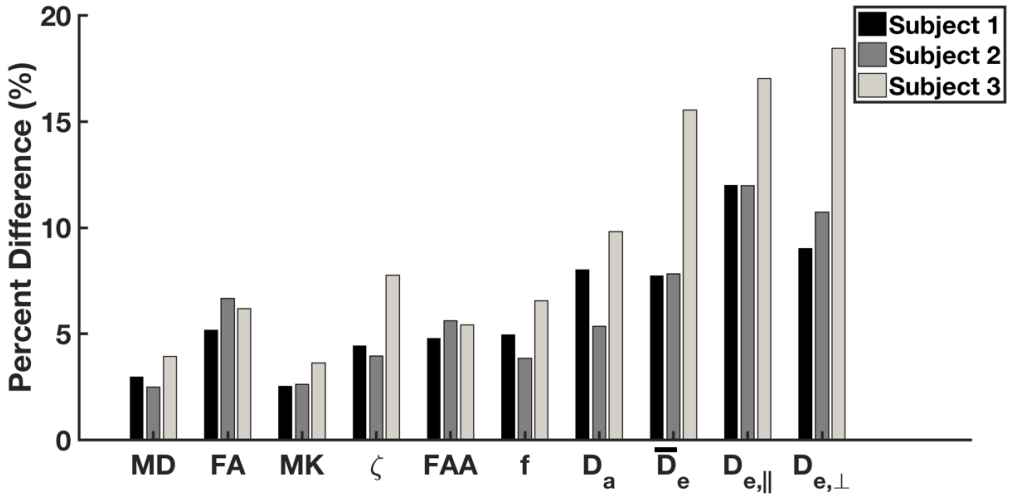

Figure 4.10: Median absolute percent difference between Runs 1 and 2 for selected diffusion measures in white matter. These were calculated for all three subjects on a voxelwise basis by using all voxels considered as white matter (i.e., MK ≥ 1). In most cases, the percent difference is about 10% or less. However, the extra-axonal diffusivites ($\bar{D}_e$, $D_{e,\parallel}$, $D_{e,\perp}$) differed by up to 20% for Subject 3. All quantities were obtained with either DKI (MD, FA, MK), FBI (ζ, FAA), or FBWM (f, D_a, $\bar{D}_e$,$D_{e,\parallel}$,$D_{e,\perp}$).

Average values for the DKI-, FBI-, and FBWM-derived measures over all white matter voxels (both runs) for each of the three subjects are listed in Table 4.2. All the parameters are relatively consistent across subjects. For the FBWM-derived metrics, the coefficients of variation range from 0.08 for the AWF in Subject 1 to 0.27 for the axial extra-axonal diffusivity in Subject 3. Note that the axial diffusivity, $D_{\parallel}$, obtained from the diffusion tensor is very similar to the axial extra-axonal diffusivity but that the radial diffusivity, $D_{\perp}$, from the diffusion tensor is smaller than the radial extra-axonal diffusivity. In our model, the principal eigenvectors for the total diffusion tensor and the extra-axonal diffusion tensor need not be parallel, although on physical grounds one might expect them to be approximately parallel in most white matter voxels. For our data the average absolute angle between the two eigenvectors was $21^{\circ} \pm 21^{\circ}$. Moreover, for about 14% of the white matter voxels, the angle exceeded 45°.

The above FBWM results were calculated by including all spherical harmonics in Equation 4.9 up to and including the degree $l = 6$. In order to investigate how varying this

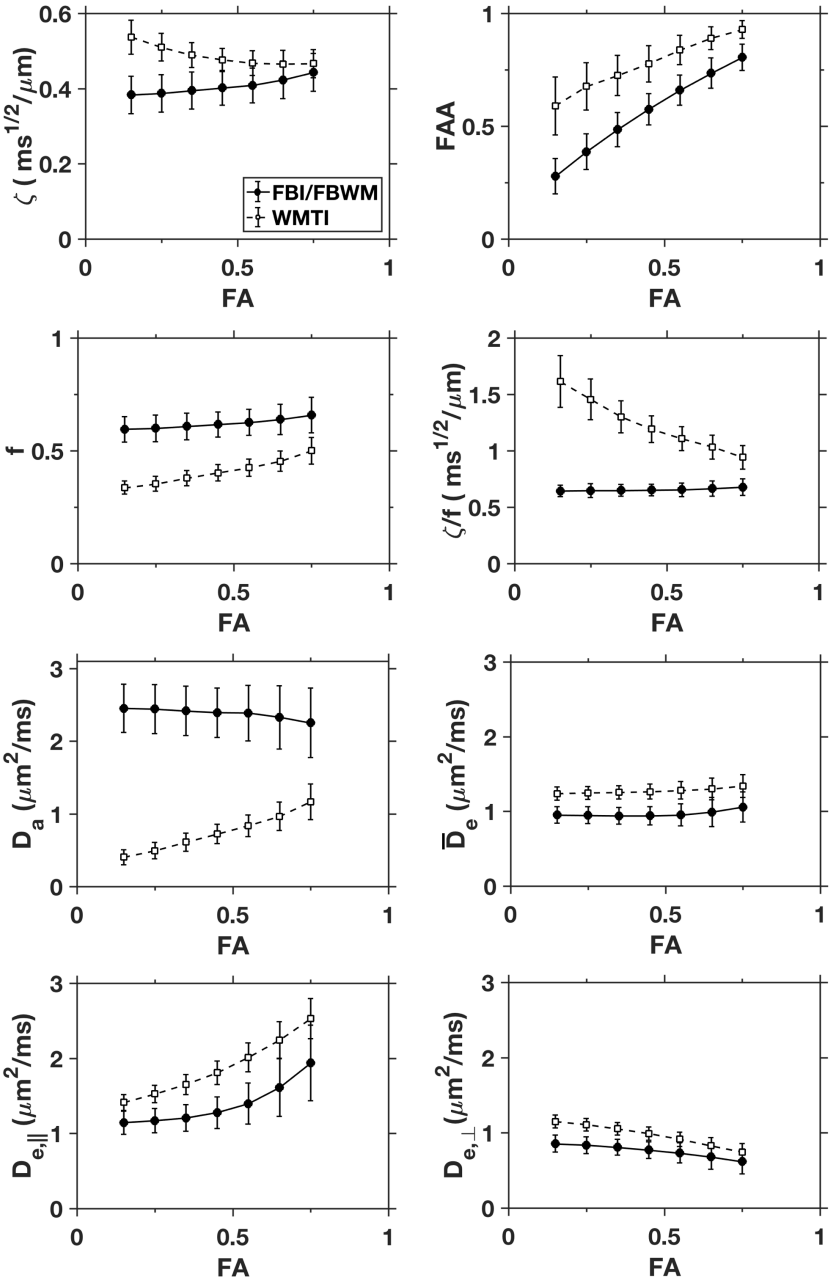

Figure 4.11: Selected diffusion measures versus FA. All white matter voxels for all three subjects and both imaging runs were pooled. The solid data points are averages calculated with either FBI (ζ, FAA) or FBWM (f, ζ/f, D_a, $\bar{D}_e$, $D_{e,\parallel}$, $D_{e,\perp}$), while the open data points are all averages calculated with WMTI. The error bars indicate standard deviations. For the FBI/FBWM parameters, D_a,$\bar{D}_e$, and ζ/f vary little with FA, but an FA dependence is discernible for the other metrics. The WMTI averages are relatively close to the FBI/FBWM values for ζ, $\bar{D}_e$, and $D_{e,\perp}$, at least for FA > 0.5 where the assumptions underlying WMTI are better justified. Otherwise substantial differences are apparent. In particular, the WMTI estimates for D_a are much smaller than the FBWM estimates over the full range of FA

Table 4.2: Mean values ($\pm$ std. dev.) of diffusion parameters in white matter as estimated with DKI, FBI, and FBWM.
*Estimated with DKI. †Estimated with FBI. ‡Estimated with FBWM.

Parameter	**Subject 1**	**Subject 2**	**Subject 3**
MD $[\mu m^2/ms]^*$	0.85 ± 0.06	0.87 ± 0.08	0.85 ± 0.08
FA*	0.46 ± 0.14	0.44 ± 0.14	0.46 ± 0.14
MK*	1.09 ± 0.06	1.14 ± 0.08	1.13 ± 0.08
${D_\parallel}^*$	1.31 ± 0.21	1.32 ± 0.23	1.32 ± 0.26
${D_\perp}^*$	0.62 ± 0.10	0.64 ± 0.12	0.61 ± 0.11
$\zeta[ms^{1/2}/\mu m]^\dagger$	0.40 ± 0.04	0.40 ± 0.05	0.42 ± 0.05
FAA†	0.57 ± 0.14	0.56 ± 0.14	0.58 ± 0.15
$f^\ddagger$	0.60 ± 0.05	0.63 ± 0.06	0.62 ± 0.07
$D_a[\mu m^2/ms]^\ddagger$	2.36 ± 0.31	2.50 ± 0.35	2.23 ± 0.40
$\bar{D}_e[\mu m^2/ms]^\ddagger$	0.95 ± 0.09	0.93 ± 0.13	1.02 ± 0.18
$D_{e,\parallel}[\mu m^2/ms]^\ddagger$	1.31 ± 0.26	1.29 ± 0.32	1.46 ± 0.39
$D_{e,\perp}[\mu m^2/ms]^\ddagger$	0.76 ± 0.11	0.75 ± 0.14	0.80 ± 0.16

maximum degree affects the number of local minima, we also calculated the percentage of white matter voxels, across all subjects, with more than one local minima for maximum degrees of $l = 2, 4,$ and 8, obtaining 45.3%, 13.6%, and 9.6%, respectively. This should be compared to the 10.4% for $l = 6$, as previously stated. Thus increasing the degree cutoff tends to reduce the number of voxels with multiple local minima.

Simulations

Ground truth maps of a single anatomical slice for the parameters f and D_a are given in Figure 4.12 together with the corresponding maps determined with FBWM using different simulated noise levels. The full brain slice is shown, even though FBWM is only expected to yield meaningful results for white matter. Within white matter regions, the FBWM estimates agree fairly well with the ground truth values for SNR of 20 and above, but large discrepancies are apparent for SNR = 10. Here the SNR is defined with respect to the $b = 0$ images.

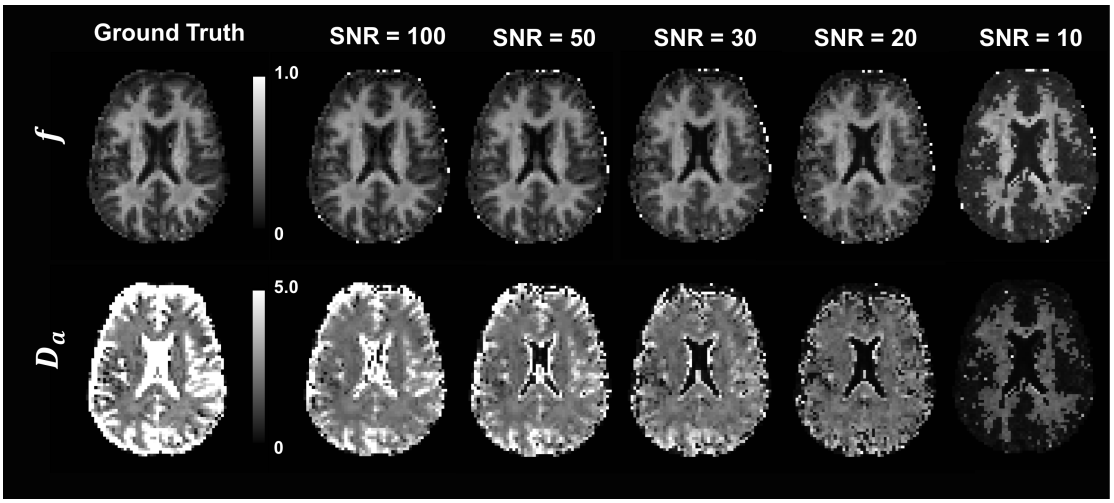

Figure 4.12: Numerical simulations of the effect of signal noise on parametric maps of the AWF and the intrinsic intra-axonal diffusivity for a single anatomical slice. The ground truth data are based on the signal model of Equations 4.25 together with the FBWM fits for Subject 1 (same slice as in Figure 3.8). Rician noise was added to create SNR values ranging from 10 to 100 (defined with respect to the $b = 0$ images), and the simulated data were processed according to our standard analysis pipeline. In white matter regions, where the FBWM approach is expected to apply, the parameter values are fairly insensitive to the added noise, for SNR values of 20 and above. The calibration bar for D_a is in units of $\mu m^2/ms$, while that for f is dimensionless.

Mean values for ζ, f, D_a, and $\bar{D}_e$ from the simulations are plotted in Figure 4.13 as a function of the SNR. The estimates are averages over all 4608 white matter voxels in our simulated dataset. The solid line shows the results for our full analysis pipeline, while the dashed line shows the effect of skipping the denoising step. With denoising, the parameter estimates are close to the ground truth values when the SNR is 20 or higher, but without denoising larger errors are apparent especially for D_a. The small underestimation of D_a at an SNR of 100 is primarily due to systematic errors in the calculation of the diffusion tensor from DKI, which propagate into the cost function.

Simulated results (with denoising) using different numbers of diffusion encoding directions for the HARDI shell are given in Figure 4.14. Little difference in the parameter mean values and standard deviations are seen with $64, 128, or 256$ directions, but both f and D_a are significantly underestimated when only 30 directions are employed.

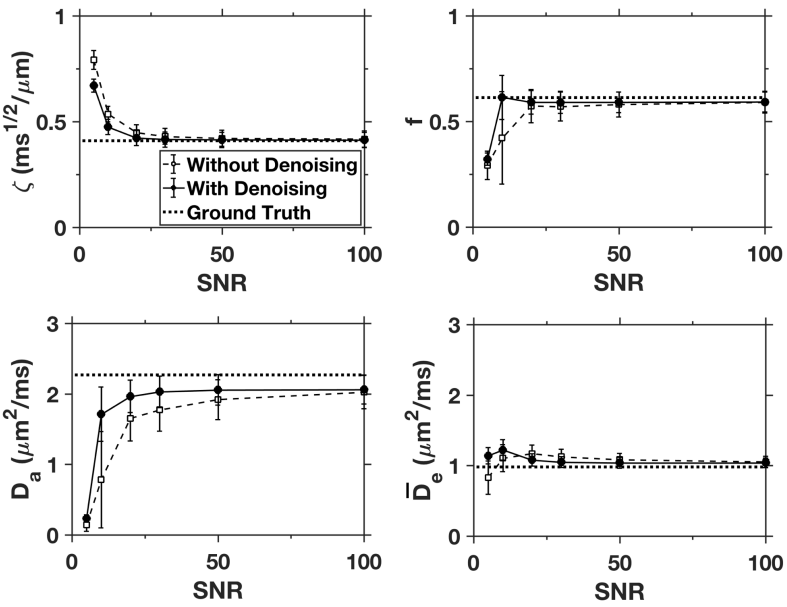

Figure 4.13: Mean values of ζ, f, $D_{\parallel}$, and $\bar{D}_e$ over all white matter voxels for simulated data with varying amounts of added noise (solid data points). The ground truth values are indicated by the dotted lines, and the open data points give the simulated results with the denoising step omitted from the processing pipeline. The error bars indicate standard deviations. With denoising, the FBI/FBWM estimates agree well with the ground truth values for SNRs of 20 and above. Without denoising, both accuracy and precision are noticeably reduced, particularly for $D_{\parallel}$.

4.3.5 Discussion

A premise underlying FBI is that the dMRI signal in white matter is predominately due to intra-axonal water for high b-values, as is strongly supported by the observed decrease of the direction-averaged signal as $1/\sqrt{b}$ for large diffusion weightings [30, 87]. Furthermore, this $1/\sqrt{b}$ drop-off is a signature of diffusion restricted within thin cylindrical pores, which presumably correspond to axons. These facts allow the fODF to be estimated in a simple manner, along with the microstructural parameter $\zeta \equiv \frac{f}{\sqrt{D_a}}$ [29].

For low b-values, the dMRI signal is well-described by the total diffusion tensor $\mathbf{D}$, which is easily estimated with either DTI or DKI. Knowledge of $\mathbf{D}$, the fODF, ζ, and f are sufficient to calculate both the intra-axonal and extra-axonal diffusion tensors via Equations 4.16, 4.17, and 4.24. Of these quantities, f is the only one of the inputs not determined by the combination of FBI and DTI/DKI. Thus one additional condition is needed in order

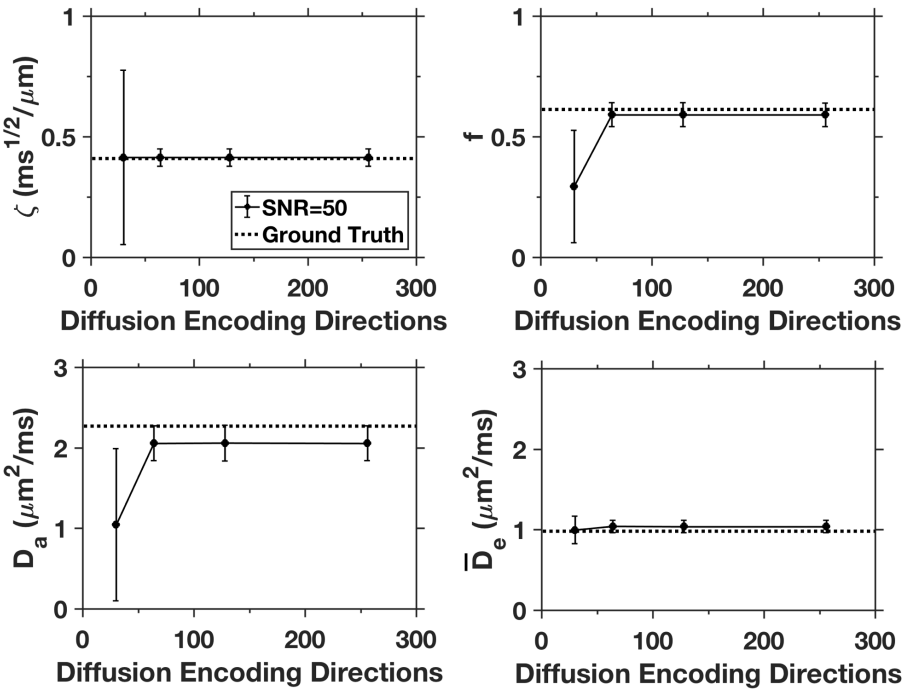

Figure 4.14: Results for selected diffusion measures from simulations with varying numbers of diffusion coding directions $(30, 64, 128, 256)$ for the $b = 6000\,\mu\mathrm{m}^2/\mathrm{ms}$ HARDI shell. The data points reflect average values over all white matter voxels from the simulated dataset, and error bars indicate standard deviations. The SNR is fixed at 50, which is similar to that of our experiments, and the number of directions is set to 30 for both the $b = 1000$ and $b = 2000\,\mu\mathrm{m}^2/\mathrm{ms}$ shells. The parameter estimates are all similar for 64 directions and above, but are much less accurate for f and D_a when only 30 directions are used for the HARDI shell.

to find the AWF and thereby independently characterize the intra-axonal and extra-axonal diffusion environments.

Here we have estimated f by requiring the model dMRI signal of Equation 4.25 to match the measured dMRI signal as closely as possible through minimization of the cost function of Equation 4.26. As formulated, this is a one-dimensional optimization problem that is straightforward to solve numerically, in contrast to some alternative approaches [158, 149, 7]. Moreover, we find empirically that the cost function has a single minimum for most white matter voxels so that potential issues arising from multiple local minima should be minor. From the optimal f, we are then able to calculate the intra-axonal and extra-axonal diffusion tensors, along with a variety of associated diffusion parameters (see Figure 4.9).

A crucial distinction between the FBWM optimization and alternative diffusion modeling approaches that also employ a spherical harmonic expansion of the dMRI signal [32, 165, 8, 31] is that, for the alternatives, the number of free parameters increases with the number of harmonics used, while for FBWM there is always a single free parameter regardless of the number of harmonics. The reason for this is that FBWM uses the harmonic expansion coefficients determined with FBI rather than treating them as fitting parameters.

Our results suggest that harmonics at least up to a degree of about 6 should be kept for numerical calculations, since the occurrence of voxels with multiple local minima increases substantially as the maximum degree is reduced below this, raising concerns regarding unphysical solutions [158, 149, 7, 8]. However, including harmonics with very high degrees may not be beneficial as these are likely dominated by signal noise.

The model for the full dMRI signal is the sum of the intra-axonal and extra-axonal signal models. The intra-axonal signal model of Equation 4.20 follows directly from the theory for FBI. There is, however, no similar basis for the extra-axonal signal model. For our cost function, we have adopted the simplest possibility of regarding water diffusion in the extra-axonal space as Gaussian, which leads to Equation 4.8. It has been argued that treating the extra-axonal space as Gaussian is overly simplistic [129], but we hypothesize that this may be adequate for b-values of $2000\,\mathrm{s/mm^2}$ or less, as would be the case if the kurtosis of the extra-axonal space were not too large. Furthermore, for our high b-value of $6000\,\mathrm{s/mm^2}$, the form of the extra-axonal signal should be irrelevant, since the dMRI signal in white matter is expected mainly arise from intra-axonal water. Thus, Equation 4.8 may be appropriate for our dataset, even if it is less accurate than some other models for intermediate b-values. Indeed, a possible advantage of our method could be a relative insensitivity to the details of the extra-axonal signal model, although further work would be necessary to confirm this.

In this initial study, we have applied our FBWM method to estimate several different microstructural parameters for characterizing diffusion in white matter using data from three healthy volunteers. Most of these parameters have a high degree of reproducibility, as demonstrated by Figures 4.9 and 4.10. Their values are all within physically plausible ranges, although we have no ground truth for comparison. Alternative approaches have yielded variable results, particularly for the intra-axonal diffusivity, which seems to be especially difficult to estimate accurately [149, 7]. Nonetheless, our results are fairly similar to those from the recently proposed spherical mean technique [129], from b-value scaling [87], and from TE dependent diffusion imaging [166], even while these methods employ more complex numerical fitting schemes than used here. More specifically, we find a mean value from FBWM for the intra-axonal diffusivity of $2.46 \pm 0.20\,\mu\mathrm{m}^2/\mathrm{ms}$. This is also quite close to the value of $2.25 \pm 0.03\,\mu\mathrm{m}^2/\mathrm{ms}$ recently reported by Dhital and coworkers [171] based on triple diffusion encoding dMRI and a novel analysis method. The discrepancy between these two results could either be caused by intersubject differences or by systematic errors in the respective estimation methods. It would be of interest to gather data with both techniques on the same subjects to better assess their concordance. Another interesting observation is that the AWF and the microstructural parameter ζ are strongly correlated, indicating that the regional variation in ζ is mainly driven by differences in the AWF rather than in the intra-axonal diffusivity. This fact can be helpful for interpreting FBI results when full FBWM modeling is not available.

A principal motivation for this work is to improve upon the WMTI method, which also uses DKI data. Our basic rationale is that FBI can supply the fODF and thus eliminate the need to assume, as with WMTI, that all axons are approximately aligned in a single direction. In this way, meaningful parameter estimates can be obtained for the entire white matter instead of just a small subset of voxels in which the axons may be regarded as largely unidirectional. Moreover, fixing the parameter ζ with FBI provides an additional constraint that may improve accuracy and precision. Our results show that WMTI and FBWM give

similar results for ζ in high FA regions, as previously reported [159], but the WMTI estimates of both f and D_a are substantially lower in comparison to those from FBWM. We speculate that the FBWM values are more accurate, since the FBWM prediction for D_a is closer to several recent estimates obtained with a variety of techniques, as mentioned above. In addition, experiments employing isotropic diffusion weighting [172] and in fixed spinal cord [173] both indicate that $D_a > D_{e,\parallel}$, which is consistent with our FBWM results but not with WMTI.

Our experimental data were acquired with $3\,\mathrm{mm}$ isotropic voxels and an average SNR of about 59. However, our numerical simulations (Figures 4.12 and 4.13) suggest that an SNR as low as 20 may be adequate as long as denoising is included as part of the post-processing analysis pipeline. Thus higher resolution maps may be attainable with FBWM. In addition, our numerical simulations (Figure 4.14) indicate that as few as 64 diffusion encoding directions could be sufficient for the HARDI shell, which would sharply reduce the dMRI data acquisition time for FBWM to about 12 min from the 30 min of our experimental protocol with 256 HARDI directions. However, actual experiments should be conducted to verify this.

There are two important limitations of our proposed FBWM method. First, it only applies to white matter, since the direction-averaged dMRI signal in gray matter does not obey the $1/\sqrt{b}$ scaling behavior for large diffusion weightings, as required for FBI [30]. This contrasts with several other previously proposed dMRI tissue models that are intended to apply to both gray and white matter [165, 28, 129]. Second, the effect of different T2 values for the intra-axonal and extra-axonal spaces is not accounted for in FBWM. As a consequence, the estimated AWF may be T_2-weighted. In particular, Veraart and coworkers [166] have recently argued that the T_2 of intra-axonal water may be substantially longer than for extra-axonal water. FBWM might therefore overestimate f, depending somewhat on TE.

The primary goals of this paper have been to describe the FBWM approach in detail and to give some preliminary results for healthy human brain. Further work is needed in at least three directions. First, the imaging protocol should be optimized in order to reduce the acquisition time. Specifically, the 256 directions used for the $b = 6000\,\mathrm{s/mm^2}$ HARDI shell could likely be reduced, as our numerical simulations suggest, with minimal impact on the parameter estimates. Second, the predictions of FBWM should be more rigorously validated by comparison with histology and other dMRI methods. Advanced dMRI techniques that employ nonstandard pulse sequences with complex gradient wave forms seem especially promising in this regard, as they can potentially estimate diffusion parameters with fewer modeling assumptions and thereby yield more reliable results [172, 171, 132, 174, 175]. Finally, the relative strengths and weaknesses of FBWM in comparison to the several related alternatives [173, 157] should be more thoroughly investigated. Here we have mainly compared FBWM to WMTI and argued that FBWM is both more comprehensive and more accurate.

4.3.6 Conclusion

By combining FBI with low to intermediate b-value dMRI data, FBWM provides estimates for multiple biophysical parameters that characterize tissue microstructure in white matter. FBI is used to determine the orientation of the axonal fibers, while the low/intermediate b-value dMRI data are employed to find the total diffusion tensor of the system. From these two inputs, a cost function is constructed with the AWF as the sole free parameter. The minimum of this cost function gives the optimal AWF, from which several other microstructural parameters may be calculated. A key advantage of FBWM is the simplicity of cost function, which facilitates efficient and robust numerical algorithms. The predictions of FBWM differ substantially from those of the WMTI approach, particularly for the intrinsic intra-axonal diffusivity, and are in better agreement with results from some alternative methods.

4.4 Measuring Intra-Axonal T_2 in White Matter With Direction Averaged Diffusion MRI

4.4.1 Introduction

Measurements of transverse relaxation in white matter can distinguish three different compartments, which may be identified as intra-axonal water, extra-axonal water, and myelin water [176]. The T_2 relaxation time for myelin water is typically in the range of 10 to 20 ms, while the intra-axonal and extra-axonal T_2 values are substantially longer [163]. Knowledge of compartmental T_2 values is important for understanding how tissue microstructure affects MRI signal data. Most prior studies have been based on multi-exponential fits for spin echo signal decay curves over a broad range of echo times values [176, 177, 178, 179, 180, 181, 182, 183]. Recently, an alternative approach, known as TEdDI, has been demonstrated that employs dMRI data, acquired with multiple b-values and echo times that are fit with a specific model for the diffusion-weighted signal [166]. An advantage of TEdDI is that the extra information provided by applying diffusion sensitizing gradients helps to separate the intra-axonal and extra-axonal compartments, which is hard to do from spin echo signal decay curves alone.

Here we describe a straightforward method of estimating the intra-axonal $T_2(\equiv T_{2a})$ relaxation time from direction-averaged dMRI data obtained with multiple echo times but only a single b-value. Moreover, the signal is fit with a monoexponential decay rather than the more complicated model utilized in TEdDI. The key idea is that the direction-averaged dMRI signal is dominated by intra-axonal water for sufficiently large b-values and echo times. As demonstrated in Section 4.2 and further discussed in other prior studies, b-values of about $4000\,\mathrm{s/mm^2}$ or higher should be sufficient to suppress most of the signal from extra-axonal water ([29, 30, 7, 166]. The echo time need only be large enough to suppress the signal from myelin water. In practice, this implies echo times greater than about $80\,\mathrm{ms}$

for the myelin signal to be reduced by at least a factor of 50. On clinical scanners, echo times for dMRI sequences with large b-values are typically greater than this because of the gradient pulse durations required to generate strong diffusion weightings [184].

To demonstrate our technique, we utilized data acquired from three healthy volunteers. Most of our data were collected using a monopolar (a.k.a. Stejskal-Tanner) diffusion pulse sequence, as this allows for shorter echo times than a bipolar (a.k.a. twice-refocused) sequence. However, for one subject, we also obtained data with a bipolar sequence in order to reduce eddy currents, which could conceivably confound our T_{2a} measurements.

4.4.2 Theory

With increasing b-value, the direction-averaged dMRI signal in white matter has been observed to decay approximately as $b^{-1/2}$ (Section 4.2, for b-values greater than about $4000\,\mathrm{s/mm^2}$ and echo times greater than about $80\,\mathrm{ms}$ ([30, 7, 166]. This scaling behavior is the signature of water confined to thin cylindrical pores, which presumably correspond to axons. It is only evident at high b-values for two reasons. First, the condition $bD_a >> 1$, where D_a is the intra-axonal diffusivity, must be satisfied in order for the signal decay from the intra-axonal water to decrease as $b^{-1/2}$ [29]. Since $D_a \approx 2\,\mu\mathrm{m^2/ms}$ [166, 171], this implies that $b >> 500\,\mathrm{s/mm^2}$. Second, the b-value must be sufficiently high to suppress the signal from the more mobile pool of extra-axonal water within the extra-cellular space, glial cells, blood, and possibly cerebrospinal fluid. Long echo times are needed as well to suppress the signal from myelin water, which has a relatively low diffusivity [185], but at least on clinical scanners this will automatically be the case for large b-values, as the time to play out the diffusion-sensitizing gradients typically forces the echo time to be about $80\,\mathrm{ms}$ or longer [184]. Thus with an appropriate choice of imaging parameters, the direction-averaged dMRI signal is dominated by the contribution of intra-axonal water. As a consequence, the echo time dependence of the direction-averaged dMRI signal, for a

fixed large b-value, will simply be given by

$$\bar{S}(TE) = C_a \cdot e^{-TE/T_{2a}}, \tag{4.31}$$

with C_a being a constant. Equation 4.31 is the basis of our proposed method for estimating T_{2a}. Provided data for two echo times, TE_1 and TE_2, we then have the explicit formula

$$T_{2a} = \frac{TE_2 - TE_1}{ln[\bar{S}(TE_1)/\bar{S}(TE_2)]}. \tag{4.32}$$

When data for more than two echo times are available, Equation 4.31 could instead be fit numerically in order to find T_{2a}, which reduces to a linear problem after taking the logarithm of both sides.

If one also acquires the MRI signal, $S_0(TE)$, without diffusion weighting (i.e., $b = 0$) for the same echo times and if one has an a priori estimate for D_a, then the extra-axonal $T_2(\equiv T_{2e})$ relaxation time may be calculated from

$$F(TE) \equiv S_0(TE) - 2\bar{S}(TE)\sqrt{\frac{bD_a}{\pi}} = C_e \cdot e^{-TE/T_{2e}}, \tag{4.33}$$

where C_e is a constant and b is the b-value for which the direction-averaged signal is measured. A derivation of Equation 4.33 is given in the Appendix (C). In the special case of two echo times, the extra-axonal relaxation time is

$$T_{2e} = \frac{TE_2 - TE_1}{ln[F(TE_1)/F(TE_2)]}. \tag{4.34}$$

However, the accuracy of Equations 4.33 and 4.34 will depend upon the accuracy of the estimate for D_a, which puts these equations on a less firm foundation than Equations 4.31 and 4.32.

4.4.3 Methods

Imaging

Three healthy adult volunteers (ages 26 to 30 yr) were scanned on a 3T Prisma MRI system (Siemens Healthineers, Erlangen, Germany) employing a 32-channel head coil under a protocol approved by the IRB of the Medical University of South Carolina. Diffusion-weighted data were acquired for all three subjects using a monopolar dMRI pulse sequence and 64 diffusion encoding directions with a b-value of $6000\,\mathrm{s/mm^2}$ for TE = 90 , 100 , 110 , 120 , 130 , 140 , and $150\,\mathrm{ms}$. Other imaging parameters were: TR = $3800\,\mathrm{ms}$, voxel size = $3\,\mathrm{mm} \times 3\,\mathrm{mm} \times 3\,\mathrm{mm}$, number slices = 42, FOV = $222\,\mathrm{mm} \times 222\,\mathrm{mm}$, acquisition matrix = 74×74, slice acceleration = 2, phase encoding acceleration = 2, coil combine mode = adaptive combine, and bandwidth = $1438\,\mathrm{Hz/px}$. The diffusion time (Δ) and gradient pulse duration (δ) of the monopolar sequence both depended on TE, with each increasing by $5\,\mathrm{ms}$ for every $10\,\mathrm{ms}$ increase in TE. Thus, Δ varied from $44.1\,\mathrm{ms}$ for TE = $90\,\mathrm{ms}$ to $74.1\,\mathrm{ms}$ for TE = $150\,\mathrm{ms}$, while δ varied from $24.9\,\mathrm{ms}$ for TE = $90\,\mathrm{ms}$ to $54.9\,\mathrm{ms}$ for TE = $150\,\mathrm{ms}$. For every TE, we obtained five additional images with the same parameters except that the b-value was set to zero ($b0$ images). For TE = $90\,\mathrm{ms}$, diffusion-weighted data were also collected using the same monopolar sequence except with 30 diffusion encoding directions, b-values of 1000 and $2000\,\mathrm{s/mm^2}$, and an additional 5 $b0$ images. These low b-value data were used to calculate standard diffusion measures to support our analysis, but not for estimating T_{2a}. For anatomical reference, T1-weighted images were acquired with isotropic $1\,\mathrm{mm}$ voxels, TE = $2.26\,\mathrm{ms}$, and TR = $2300\,\mathrm{ms}$. The total scan time for all of these sequences was 42 min 47 s.

For one subject (Subject 1), we also obtained, during the same scan session, diffusion-weighted data using a bipolar dMRI pulse sequence in order to suppress eddy currents [137]. The imaging parameters were set in the same way as for the monopolar sequence except no data were collected with TE = $90\,\mathrm{ms}$, which was not possible for the bipolar

sequence due to the time needed to include the extra refocusing pulse. The bipolar diffusion scans required 27 min 57 s of additional scan time.

In order to test the dependence of our T_{2a} estimates on the choice of b-value, Subject 2 was scanned, in a separate session, using the monopolar sequence and 64 diffusion encoding directions for b-values of 1000, 2000, 4000, 6000, and $8000\,\mathrm{s/mm^2}$, both with TE = $100\,\mathrm{ms}$ and with TE = $140\,\mathrm{ms}$. The remaining imaging parameters were set to be the same as for the other monopolar diffusion-weighted data. For each combination of b-value and TE, five b0 images were also acquired. A T1-weighted anatomical scan was obtained as well, using the same imaging parameters as in the previous scan session. The total scan time for this session was 51 min 48 s.

Data Analysis

Signal noise in all diffusion-weighted images was reduced by applying a denoising algorithm based on principal components analysis [85]. The denoising algorithm also yielded noise maps, which were used with the method of moments [142] to correct positive signal bias arising from noise rectification in magnitude images. Gibbs ringing artifacts were mitigated by employing the approach of Kellner and coworkers [86]. Image coregistration was accomplished through the standard techniques [186, 88], which included correction of image distortion due to eddy currents (https://fsl.fmrib.ox.ac.uk/fsl/fslwiki/eddy).

Conventional diffusion metrics, including MK, MD, and FA, were calculated from the diffusion-weighted data obtained with the monopolar sequence for TE = $90\,\mathrm{ms}$ and b-values of 0, 1000 and $2000\,\mathrm{s/mm^2}$ by applying in-house software (DKE) [84]. White matter masks for each subject were defined as all cerebral voxels with an MK > 1 and MD $< 1.5\mu m^2/ms$ [119]. In addition, we located specific anatomical regions of interest by reference to a white matter atlas [187]. Eleven white matter regions were considered: Posterior Limb of the Internal Capsule (PLIC), Genu of the Corpus Callosum (GCC), Posterior

Thalamic Radiation (PTR), Anterior Corona Radiata (ACR), Anterior Limb of the Internal Capsule (ALIC), Superior Longitudinal Fasciculus (SLF), External Capsule (EC), Body of the Corpus Callosum (BCC), Splenium of the Corpus Callosum (SCC), Superior Corona Radiata (SCR), and Posterior Corona Radiata (PCR).

In order to estimate T_{2a}, Equation 4.31 was fit in each voxel, using least squares, to the direction-averaged signal with a b-value of $6000\,\mathrm{s/mm^2}$, for the monopolar data with TE ranging from $90\,\mathrm{ms}$ to $150\,\mathrm{ms}$ (Subjects 1-3) and for the bipolar data with TE ranging from $100\,\mathrm{ms}$ to $150\,\mathrm{ms}$ (Subject 1). In order to assess the extent to which the measured T_{2a} depends on the choice of b-value, we employed Equation 4.32 together with the direction-averaged data from the second scan session for Subject 2, with b-values of 4000, 6000, and $8000\,\mathrm{s/mm^2}$ and echo times of $100\,\mathrm{ms}$ (TE_1) and $140\,\mathrm{ms}$ (TE_2).

We also generated parametric maps of T_{2e} for all subjects by fitting Equation 4.33 to monopolar data with b-values of 0 and $6000\,\mathrm{s/mm^2}$ and TE ranging from $90\,\mathrm{ms}$ to $150\,\mathrm{ms}$. The assumed values for D_a were 1.0, 1.5, 2.0, $2.5\,\mu\mathrm{m^2/ms}$, which are representative of estimates obtained from microstructural modeling [166, 129, 159, 92].

Since T_2^* in white matter is known to depend on orientation [188, 189], we investigated the relationship of T_{2a} and the angle of the principal diffusion tensor eigenvector relative to the main magnetic field. We restricted our comparison to voxels with a coefficient of linearity greater than 0.4, because these represent white matter with largely collinear axonal fiber bundles for which any angular variation is most likely to be apparent. Here we defined the coefficient of linearity as $c_l = (\lambda_1 - \lambda_2)/\lambda_1$, where λ_1 and λ_2 are, respectively, the first and second largest eigenvalues of the diffusion tensor [190]. For this analysis, T_{2a} was estimated by using the monopolar data of all three subjects with a b-value of $6000\,\mathrm{s/mm^2}$ and the seven TE values from 90 to $150\,\mathrm{ms}$.

4.4.4 Results

The direction-averaged signal with a b-value of $6000\,\mathrm{s/mm^2}$ as a function of TE is plotted in Figure 4.15 for representative white matter voxels from Subject 1. The error bars indicate standard errors calculated as the standard deviation of the signal noise divided by the square root of the number of diffusion encoding directions. The lines show monoexponential fits with Equation 4.31. The quality of the fits is similar for the monopolar data (A) and bipolar data (B), although T_{2a} is slightly longer for the bipolar data.

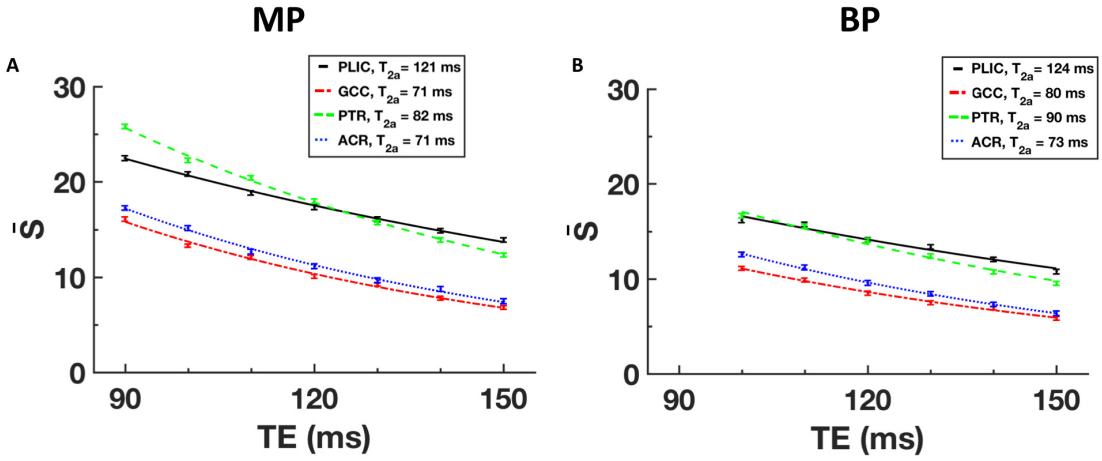

Figure 4.15: Direction-averaged dMRI signal as function of TE for individual voxels from selected regions of interest using (A) a monopolar (MP) sequence and (B) a bipolar (BP) sequence. All data points were obtained from a single subject (Subject 1) with a b-value of $6000\,\mathrm{s/mm^2}$. The lines are best fits using the monoexponential form of Equation 4.31. The error bars indicate the standard error for the signal noise.

Parametric maps of T_{2a} for one anatomical slice from Subject 1 are given by Figure 4.16, along with the corresponding color FA map. It should be emphasized that the T_{2a} values are only meaningful in white matter regions, where the theory underlying our method is expected to hold. The maps generated from the monopolar data and from the bipolar data are qualitatively similar, although a tendency toward higher T_{2a} for the bipolar data is apparent. Figure 4.17 shows a scatter plot of the monopolar and bipolar T_{2a} values for all the white matter voxels from the same slice as in Figure 4.16. The dashed line has a slope

of one and an intercept of zero; thus points lying above this line have a higher T_{2a} for the bipolar data. The solid line is a best fit with a slope of 1.1 and a y-intercept of 3.6 ms, indicating that the bipolar T_{2a} values are, on average, about 10% larger than the monopolar T_{2a} values. The Pearson correlation coefficient is 0.9, reflecting a strong correlation between the monopolar and bipolar data.

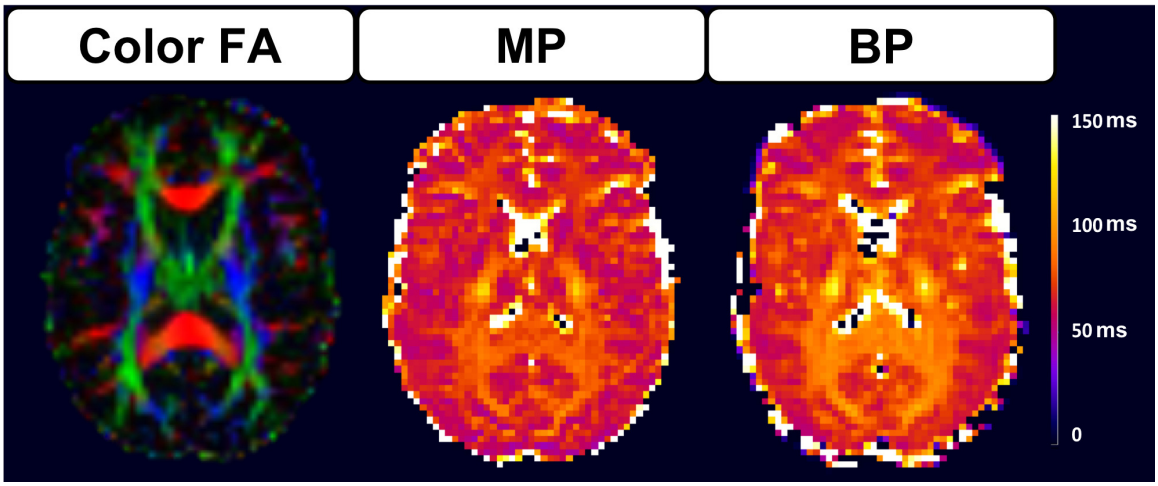

Figure 4.16: Parametric maps of T_{2a} for a single anatomical slice from Subject 1, as determined with a monopolar sequence (center) and a bipolar sequence (right), along with the corresponding color FA map (left) for anatomical reference. The two T_{2a} maps are qualitatively similar, although somewhat higher values are apparent for the bipolar sequence in most white matter voxels. Note that T_{2a} values are only meaningful in white matter regions, because the assumptions underlying the estimation method are invalid in gray matter. The calibration bars are labeled in units of milliseconds.

Histograms of T_{2a} from all white matter voxels for each subject are displayed in Figure 4.18. The data are for the monopolar sequence with a b-value of $6000\,\mathrm{s/mm^2}$ and seven TE values. Most voxels have T_{2a} between 50 and $110\,\mathrm{ms}$, and the average values are 78 ± 11, 81 ± 12, and $78\pm 11\,\mathrm{ms}$ for Subjects 1, 2, and 3, respectively. The median T_{2a} for selected white matter regions is given by Figure 4.19, with median values being used to reduce the effect of outliers. Considerable regional variation is evident, with a lowest median value of $64\pm 7\,\mathrm{ms}$ (EC, Subject 3) and a highest median value of $94\pm 17\,\mathrm{ms}$ (PLIC, Subject 2). There are no significant differences in T_{2a} between the three subjects.

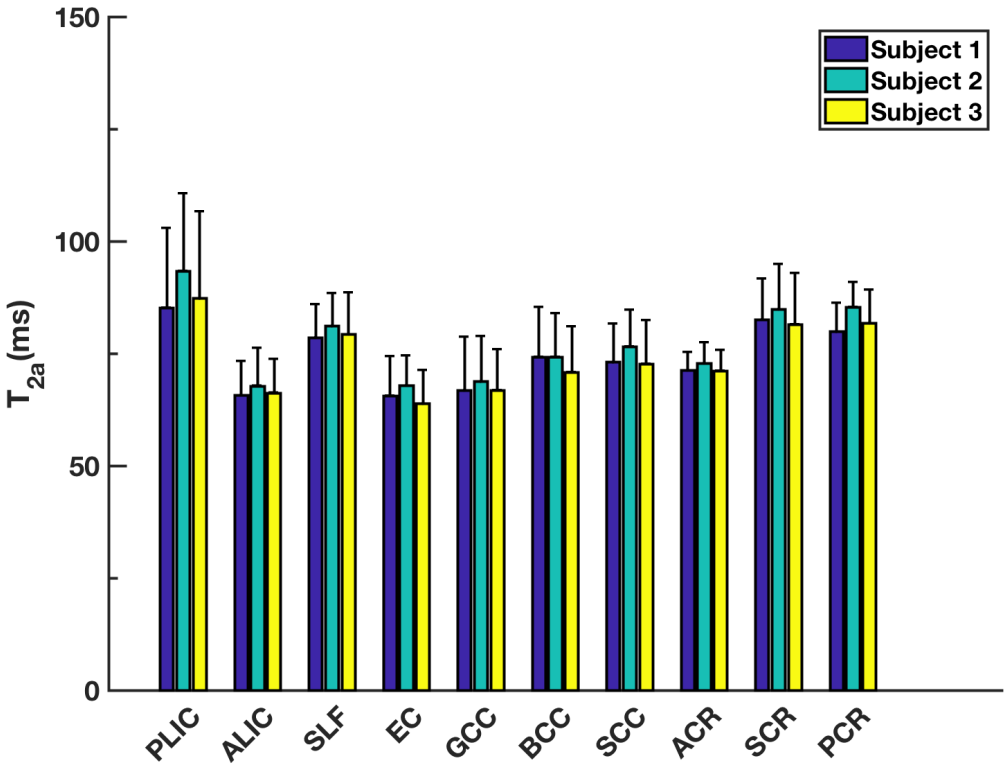

Figure 4.17: Scatter plot of T_{2a} for white matter voxels from the same anatomical slice as in Fig. 4.16. The monopolar and bipolar values are strongly correlated (r = 0.9), but those for the bipolar sequence are mostly higher, with the best fit line having a slope of 1.1. Thus the extra refocusing pulse of the bipolar sequence tends to increase the apparent T_{2a}.

Figure 4.20 is a plot of T_{2a} in white matter from Subject 2 as a function of FA, for b-values of 4000, 6000, and $8000\,\mathrm{s/mm^2}$. The data points represent median values, and the error bars indicate the first and third quartiles for each bin, which spanned an FA interval of 0.05. For $0.2 \leq$ FA ≤ 0.6, similar results are obtained for all three b-values, which includes most of the white matter voxels. Some minor differences are apparent for FA < 0.2 and FA > 0.6, although these might well reflect noise and/or coregistration errors as there are a relatively small number of voxels in these bins. The average T_{2a} values ($\pm SD$) over all white matter voxels are 81 ± 12, 81 ± 13, and $83 \pm 13\,\mathrm{ms}$ for b-values of 4000, 6000, and $8000\,\mathrm{s/mm^2}$, respectively.

The averages of the median T_{2e} and T_{2a} for all three subjects as a function of FA

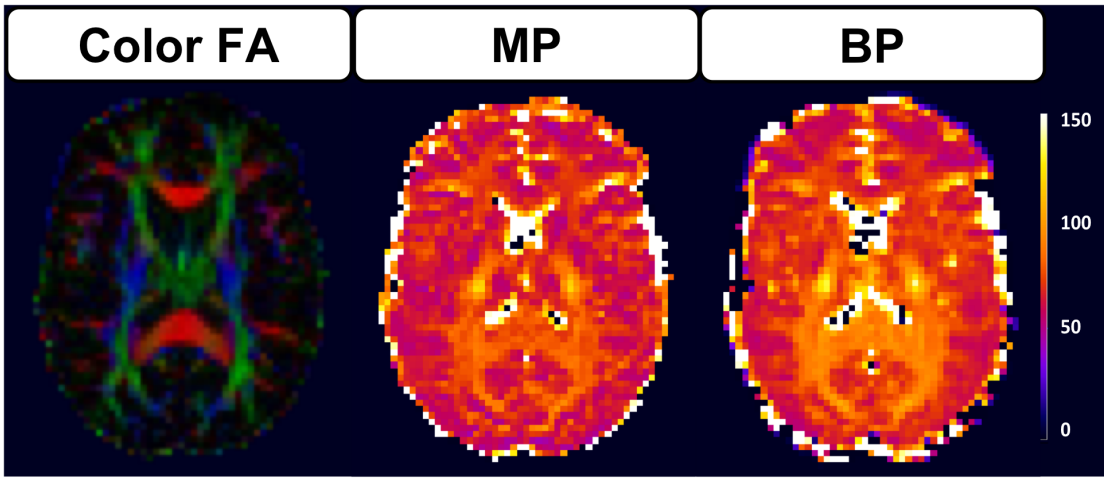

Figure 4.18: Histograms of T_{2a} for all white matter voxels from three healthy subjects. The dMRI data were acquired with a monopolar sequence and a b-value of $6000\,\mathrm{s/mm^2}$. Most of the T_{2a} values lie between $50\,\mathrm{ms}$ and $110\,\mathrm{ms}$.

are given by Figure 4.21. The data are for the monopolar sequence with a b-value of $6000\,\mathrm{s/mm^2}$, with the error bars being inter-subject standard deviations. We calculated T_{2e} for several different choices of the intra-axonal diffusivity, since this has been a difficult quantity to estimate accurately [149], although recent work indicates that it is most likely in the range of 2 to $2.5\,\mu\mathrm{m^2/ms}$ [171]. In all of the cases considered, T_{2a} is substantially longer than T_{2e}, in consistency with prior studies [179, 181, 183, 166]. Interestingly, T_{2e} is markedly shorter for the higher FA values than for lower FA values. Over all white matter voxels, the median values are 64, 62, 59 and $56\,\mathrm{ms}$ for T_{2e} with $D_a = 1.0, 1.5, 2.0$ and $2.5\,\mu\mathrm{m^2/ms}$, respectively, while the median T_{2a} is $78\,\mathrm{ms}$.

The dependence of T_{2a} on the angle θ between the main magnetic field and the principal diffusion tensor eigenvector, for white matter voxels with a coefficient of linearity greater than 0.4, is shown in Figure 4.22. The colored lines are median values for individual subjects, using a bin size of $5°$. The black line is the average of the median values for the three subjects and demonstrates a significant negative correlation between T_{2a} and θ (r = -0.41, $p < 0.0001$). The plot indicates that T_{2a} tends to be longer for axonal fiber bundles that are parallel to the main field than for bundles that are perpendicular. This is similar

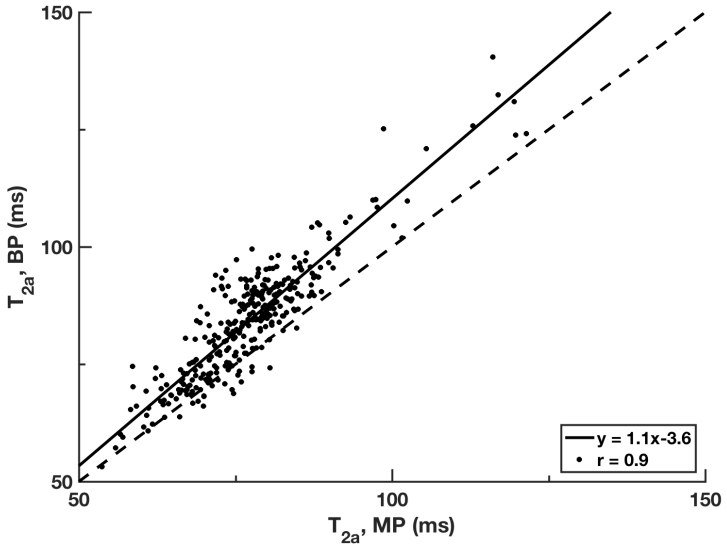

Figure 4.19: Bar graphs showing the median T_{2a} for selected regions of interest from all three subjects, as acquired with a monopolar sequence and a b-value of $6000\,\mathrm{s/mm^2}$. The median values range from a low of about $64\,\mathrm{ms}$ to a high of about $94\,\mathrm{ms}$, and the error bars indicate standard deviations. PLIC = posterior limb of internal capsule; ALIC= anterior limb of internal capsule; SLF = superior longitudinal fasciculus; EC = external capsule; GCC = genu of corpus callosum; BCC = body of corpus callosum; SCC = splenium of corpus callosum; ACR = anterior corona radiata; SCR = superior corona radiata; PCR = posterior corona radiata.

to prior observations of a longer T_2^* in white matter bundles that are parallel to the main field [188, 189], which has been attributed to variations in subvoxel magnetic susceptibility [189].

Although our data does allow the intra-axonal water fraction to be calculated, we can estimate the apparent intra-axonal water fraction for any given value of D_a by using the expression

$$f^*(TE) = 2\sqrt{\frac{bD_a}{\pi}} \cdot \frac{\bar{S}(TE)}{S_0(TE)} \tag{4.35}$$

which follows from Equation [A2]. For the monopolar data with TE = $90\,\mathrm{ms}$, we find $f^* = 0.418 \pm 0.004,\ 0.512 \pm 0.004,\ 0.591 \pm 0.005,\ 0.661 \pm 0.006$, where the values are averages ($\pm$ standard deviations) across all three subjects, for $D_a = 1.0, 1.5, 2.0$ and $2.5\,\mu\mathrm{m^2/ms}$. Thus, the intra-axonal and extra-axonal water fractions should be roughly

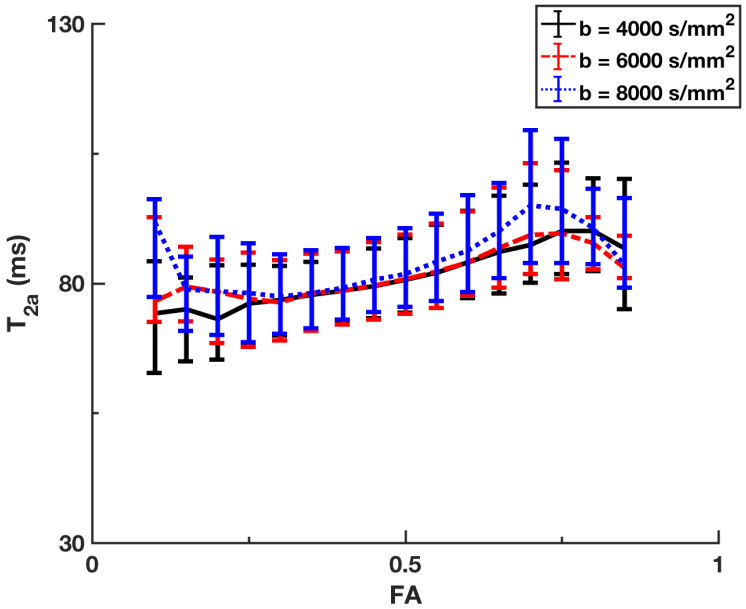

Figure 4.20: T_{2a} in white matter as a function of FA for b-values of 4000, 6000, and $8000\,\mathrm{s/mm^2}$ from Subject 2. Similar results are found for all three diffusion weightings, with some small deviations being apparent for very low and very high FA. The dMRI data were acquired with a monopolar sequence. The data points indicate median values, and the error bars reflect the first and third quartile of T_{2a} values within each bin (bin size = 0.05).

comparable in size, as has also been found in prior work (10,29).

4.4.5 Discussion and Conclusions

In microstructural models for white matter based on dMRI data, differences in the intra-axonal and extra-axonal T_2 values have typically been ignored [156]. This is understandable, considering that the daunting task of linking brain microstructure to dMRI data necessitates simplifying assumptions in order to obtain a tractable mathematical description capable of yielding useful predictions. However, as recent work has shown, intra-axonal and extra-axonal T_2 values do differ significantly, enough to cause a noticeable bias in estimates for the compartmental water fractions if neglected [166].

In this section, we have proposed a simple technique for estimating T_{2a} from monoexponential fits to direction-averaged dMRI data for b-values exceeding about $4000\,\mathrm{s/mm^2}$.

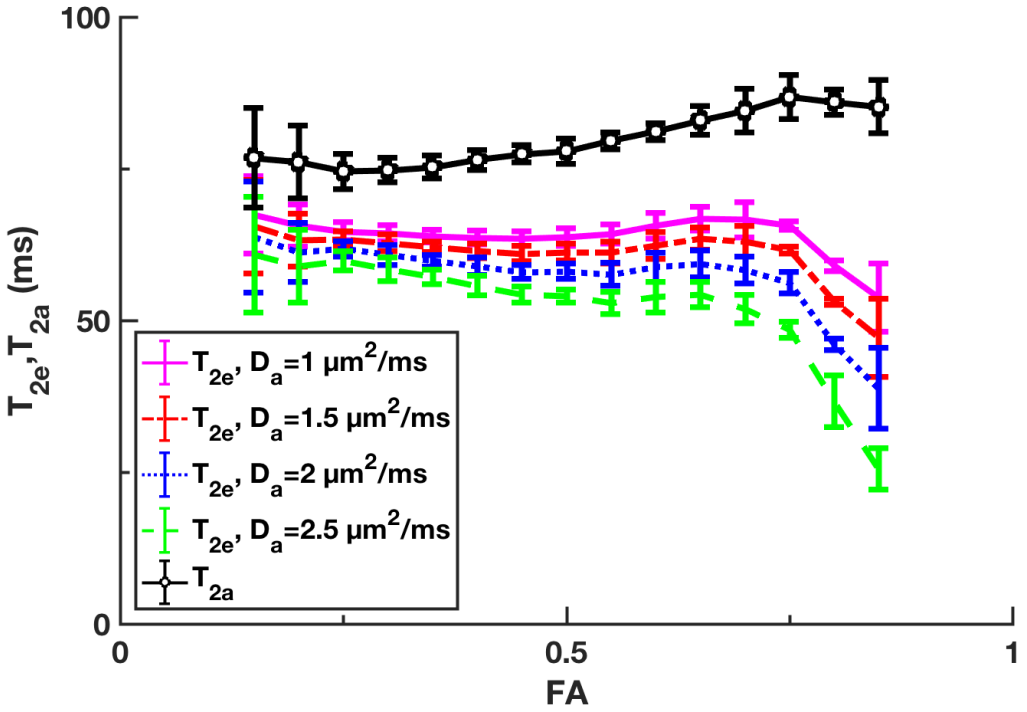

Figure 4.21: T_{2e} in white matter as a function of FA for assumed intra-axonal diffusivities of $D_a = 1.0, 1.5, 2.0$ and $2.5\,\mu\mathrm{m}^2/\mathrm{ms}$, together with T_{2a}. The dMRI data were acquired with a monopolar sequence and a b-value of $6000\,\mathrm{s/mm}^2$. The data points are the averages of the median values from all three subjects, with the error bars indicating inter-subject standard deviations. For all choices of D_a, T_{2e} is found to be substantially shorter than T_{2a} over the full range of considered FA values.

The key idea underlying this method is that the direction-averaged signal is dominated by the contribution from intra-axonal water for large b-values, which is supported by the observed $b^{-1/2}$ scaling behavior [30, 7, 166]. Our results for T_{2a} are largely consistent with those obtained by Veraart and coworkers using the TEdDI method, even though TEdDI differs markedly from our approach in being based on a detailed model for both the intra-axonal and extra-axonal spaces and in requiring complex nonlinear fitting [166]. We have shown here that neither a comprehensive tissue model nor advanced numerical methods are necessary for determining T_{2a}. The advantage of TEdDI, on the other hand, is that it also estimates T_{2e}, along with several diffusion parameters. Another approach for estimating compartmental T_2 is the recently proposed b-tensor method [191].

An important observation is that T_{2a} has a strong regional variation. At first this might

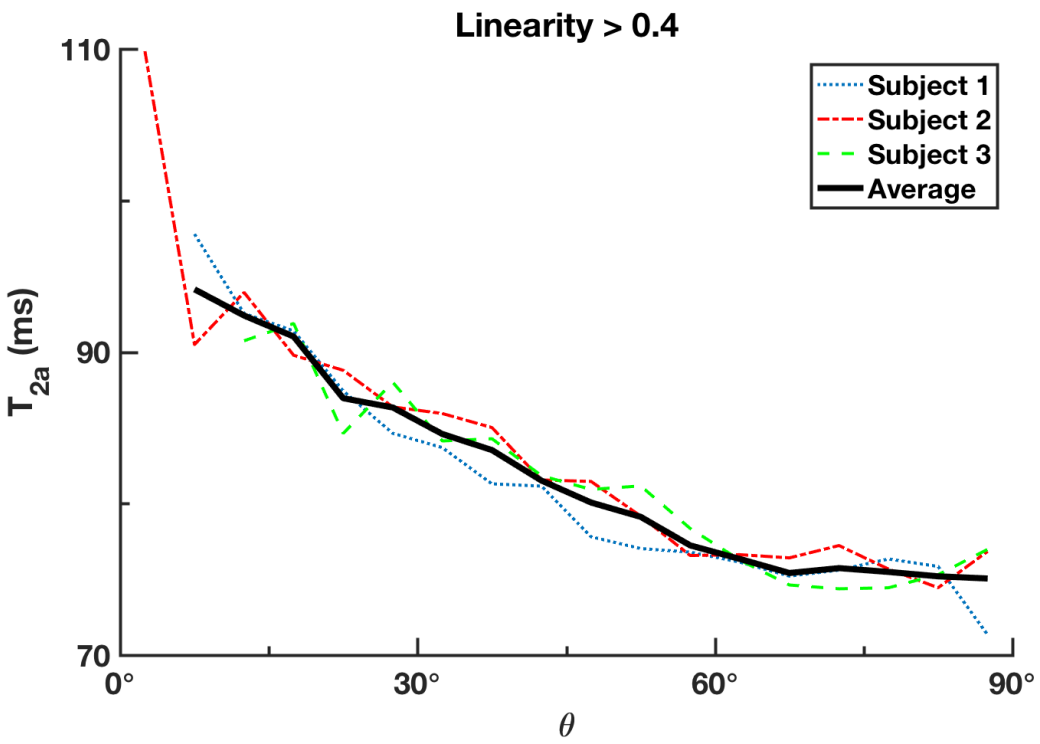

Figure 4.22: T_{2a} in white matter voxels with a coefficient of linearity exceeding 0.4 as a function of the angle θ between the principal diffusion tensor eigenvector and the direction of the main magnetic field. The colored lines are median values for individual subjects, while the black line shows the average of these medians. The inter-subject averages of T_{2a} are significantly correlated with θ ($r = -0.41$, $p < 0.0001$), suggesting that T_{2a} is influenced by magnetic field inhomogeneities generated by spatial variations in magnetic susceptibility. The dMRI data were acquired with a monopolar sequence and a b-value of $6000\,\mathrm{s/mm^2}$.

seem surprising, as the chemical composition of axoplasm is presumably relatively uniform. But a possible explanation is that T_{2a} is altered by spins diffusing across microscopic magnetic field inhomogeneities, generated by adjacent myelin, tissue iron, and deoxyhemoglobin within small blood vessels, that depend on both on the local arrangement of axons as well as their orientation with respect to the main magnetic field. This hypothesis is supported by our observation that T_{2a} is correlated with the angle between the main magnetic field and the principal diffusion tensor eigenvector for voxels with coefficients of linearity exceeding 0.4, which is consistent with prior work on the orientation dependence of T_2^* [188, 189]. It is also conceivable that T_{2a} may be affected by the axon diameter, due perhaps to exchange or surface relaxation effects [191, 192, 193]. Axons with larger di-

ameters would then be expected to have a longer T_{2a}, which is roughly consistent with our results. For example, the cortical spinal tract, which runs through the PLIC, contains many thick axons, while axons in frontal white regions, such as the ACR, have smaller average diameters [194]. Accordingly, we find a significantly longer T_{2a} in the PLIC as compared to the ACR Figure 4.19.

A potential confounding effect for our method is that the eddy currents induced by the strong diffusion sensitizing gradients will vary across echo times, thereby conceivably altering the signal decay curves due to TE-dependent image distortions. In order to mitigate this, we applied eddy current correction to all of our diffusion-weighted images [186]. In addition, for one subject we acquired data with a bipolar sequence, which is designed to strongly suppress eddy currents [137], as well as with the monopolar sequence employed for most of our scans. Any eddy current effects should manifest themselves as differences in the monopolar and bipolar T_{2a} values. Qualitatively, we found a good correspondence between the T_{2a} maps obtained with the two sequences, and the T_{2a} values were strongly correlated. Thus eddy current effects are likely to be small for our experiments. We did observe a somewhat larger T_{2a} for the bipolar sequence. But that may be attributed, at least in part, to the extra refocusing pulse for the bipolar sequence, which reduces the effects of magnetic field inhomogeneities. This is similar to the known increase, as measured using a multiple spin echo sequence, of white matter T_2 with a decrease of interecho time [195, 196]. We chose to use the monopolar sequence for the majority of our scans, because it allows for a shorter minimum echo time, thereby supporting more precise measurements of T_{2a}.

In applying our method, a chief consideration is the choice of b-value. Below about $4000\,\mathrm{s/mm^2}$, systematic errors may be expected because of the contribution to the signal from extra-axonal water, while above $8000\,\mathrm{s/mm^2}$ accurate quantification of T_{2a} is challenging as a result of a low signal-to-noise ratio. For this reason, we utilized a b-value of

$6000\,\mathrm{s/mm^2}$ for most of our experiments, although we found good consistency with results obtained at $4000\,\mathrm{s/mm^2}$ and $8000\,\mathrm{s/mm^2}$. The optimal b-value may also depend somewhat on scanner hardware and the details of the imaging protocol.

A limitation of our experimental design is that the diffusion time Δ and the gradient pulse duration δ for the monopolar sequence varied with TE, which could, in principle, alter the T_{2a} estimates even with a fixed b-value. This is a built-in feature of our vendor supplied sequence, which is constructed so as to allow the maximum possible b-value for any chosen TE. However, changing δ and Δ has little effect on measured diffusion parameters in healthy white matter [197, 198]. As a consequence, the signal attenuation in our experiments due to the diffusion-sensitizing gradients should primarily be determined by the b-value, and we do not expect the variable δ and Δ to appreciably affect our results. Similar considerations hold for the bipolar sequence, although the diffusion time and gradient pulse duration are less well-defined in this case due to the more complicated pulse sequence design [137].

While the focus of this section has been on T_{2a}, we have also shown how T_{2e} can be estimated in a similar way, provided some additional information is available. First, one needs signal data acquired without diffusion weighting for the same echo times used to determine T_{2a}. Second, an a priori value for the intrinsic intra-axonal diffusivity is required, as could be found from any of several proposed dMRI-based microstructural modeling methods [166, 171, 129, 92, 198, 199]. Given these, T_{2e} may once again be obtained from simple monoexponential fits, according to Equation 4.33. For a range of plausible values for the intra-axonal diffusivity, we find the T_{2a} exceeds T_{2e} in the vast majority of white matter voxels, in consistency with the prior studies [179, 181, 183, 166]. The reader should be aware, however, that there has been some controversy regarding the accurate measurement of the intra-axonal diffusivity [171, 159, 149].

An important reason for estimating T_{2a} and T_{2e} is that knowledge of these two parameters can be used to correct values for the axonal water fraction obtained from dMRI-based microstructural modeling, which would typically be T_2-weighted as suggested by Equation C.3, when the difference between T_{2a} and T_{2e} is neglected. Specifically, the corrected axonal water fraction is given by

$$f = \frac{f^* \cdot e^{-TE/T_{2e}}}{f^* \cdot e^{-TE/T_{2e}} + (1 - f^*) \cdot e^{-TE/T_{2a}}}, \tag{4.36}$$

where f^* is the uncorrected (apparent) axonal water fraction determined with dMRI data acquired at an echo time TE. Equation 4.36 can be derived by solving Equation [A3] for f.

In summary, we have demonstrated how T_{2a} in white matter can be found from mono-exponential fits of direction-averaged dMRI data acquired with large b-values and two or more echo times. Our results show a substantial regional variation in T_{2a}. We argue that this is at least partially attributable to the effects of microscopic magnetic field inhomogeneities, as is known to be the case for T_2^* [189], although other effects may well also be important. We also confirm the conclusion of prior studies that $T_{2a} > T_{2e}$. Our method may find application to improving the predictions of dMRI-based microstructural models of white matter.

4.5 Simple Scheme for Correcting Bias in Axonal Water Fraction due to Differences in Compartmental Transverse Relaxation Times

4.5.1 Introduction

Although studies have shown significant differences in the T_2 relaxation times for the intra- and extra-axonal compartments in white matter [200, 178, 179, 181, 183, 166], these differences are often neglected in microstructural models based on dMRI data [32, 27, 28, 92, 201]. This potentially affects the accuracy of estimated modeling parameters, particularly

for compartmental water fractions. More specifically, the intra-axonal T_2 is believed to be longer than the extra-axonal T_2 [179, 181, 183], which may lead to overestimates for the AWF if the T_2 difference is neglected [166]. Here we show how to correct this T_2 bias in the AWF for the dMRI method introduced in Section 4.3: FBWM modeling [92]. FBWM requires data for three b-value shells at a single echo time. To correct for T_2 bias in the AWF, an additional high b-value shell is acquired at a second echo time. The implementation of this correction only involves simple analytic formulae and does not increase the numerical complexity of FBWM

4.5.2 Methods

Monopolar dMRI data from one healthy adult (30 yrs) was acquired on a Siemens Prisma scanner for $b = 1000$, 2000, and $6000\,\mathrm{s/mm}$ with 30, 30, and 64 diffusion-encoding directions, respectively. Other imaging parameters were: TE=$90\,\mathrm{ms}$, TR=$3800\,\mathrm{ms}$, voxel size=$3\,\mathrm{mm}$, number slices=42, FOV=$222\,\mathrm{mm}$, Δ=$44.1\,\mathrm{ms}$, δ=$24.9\,\mathrm{ms}$, and bandwidth=$1438\,\mathrm{Hz/px}$. We obtained an additional $b = 6000\,\mathrm{s/mm}$ dataset using identical gradient directions and imaging parameters except that TE=$140\,\mathrm{ms}$, Δ=$69.1\,\mathrm{ms}$ and δ=$49.9\,\mathrm{ms}$. Each dMRI dataset also included 5 images with $b = 0\,\mathrm{s/mm}$. The total acquisition time was 14min and 12s. Data quality was improved by reducing signal noise [87], removing Gibbs ringing artifacts [86], correcting for Rician noise bias [142], and eddy currents [186].

In 4.4 we proposed a new technique [92] to measure intra-and extra-axonal T_2 (T_{2a}, T_{2e}) from which the corrected AWF can be calculated using

$$f = \frac{f^* \cdot e^{-TE/T_{2e}}}{f^* \cdot e{-}TE/T_{2e} + (1 - f^* \cdot e^{(} - TE/T_{2a}))} \tag{4.37}$$

where f^* is the apparent (i.e., T_2-weighted) AWF determined with FBWM at a given TE.

The parameters f^* and D_a were calculated using FBWM from data with TE=$90\,\mathrm{ms}$. FBWM combines dMRI data for weak and strong diffusion weightings to create a cost function with f^* as the single adjustable parameter. Optimization of the cost function results in estimates of f^*. More details can be found in section 4.3. After calculating the standard FBWM microstructural parameters, we applied our correction scheme to find T_{2a}, T_{2e}, and the corrected AWF, f, within the white matter using the additional data with $b = 6000\,\mathrm{s/mm}$ and TE=$140\,\mathrm{ms}$. Voxels with a $\bar{D} < 1.5\,\mu\mathrm{m/ms}$ and a $\bar{K} > 1.0$ were considered white matter [119]. Diffusion metrics were calculated using standard tensor analyses [84]. Average f and f^* were estimated for 10 regions of interest by reference to the JHU white matter atlas [187].

4.5.3 Results

Figure 4.23 shows the distribution of and values within the white matter. The average and are $80.8 \pm 12\,\mathrm{ms}$ and $60.8 \pm 26\,\mathrm{ms}$ respectively. Voxelwise parametric and maps are given for an anatomical slice in Figure 4.24. The regional variability in is noteworthy with lower values found in the frontal white matter and higher values in the posterior limb of the internal capsule. Average and are reported in Figure 3. Since $T_{2a} > T_{2e}$ in most voxels, is smaller than in all regions considered. On average, AWF values are 16% lower after correcting for the difference in compartmental relaxation times.

4.5.4 Discussion

As in prior studies [200, 178, 166, 179, 181, 183], we find that compartmental T_2 relaxation times are not equal in white matter, with being on average about $20\,\mathrm{ms}$ longer than. Correcting this difference lowers our AWF estimates obtained with FBWM substantially, demonstrating that the uncorrected AWF has a considerable degree of T_2-weighting. This confirms previous work by Veraart and coworkers using the TEdDI method [166]. A crucial difference between our approach and TEdDI is that correcting for the T_2 bias required

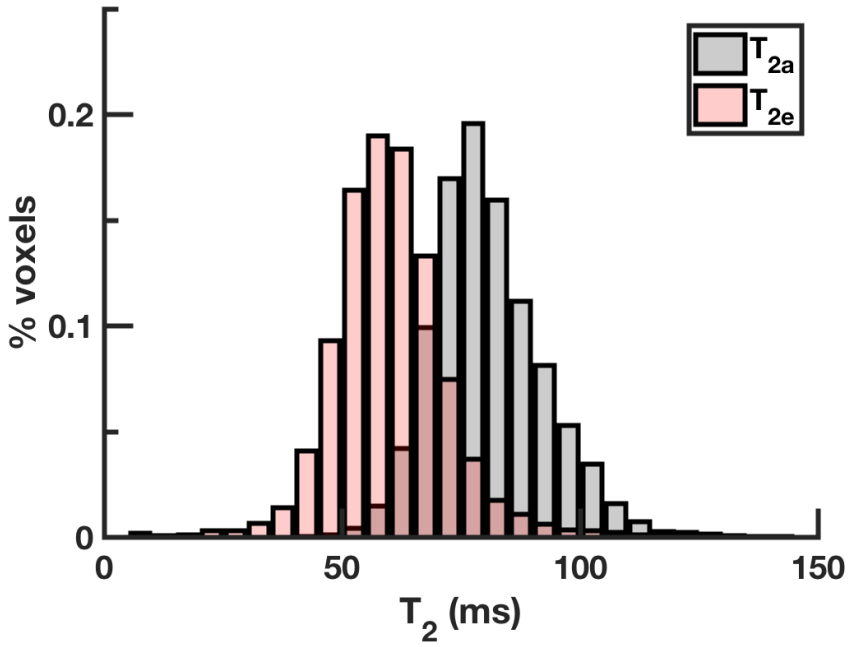

Figure 4.23: Distribution of T_{2a} and T_{2e} values in the white matter of one healthy subject. The averages ($\pm$ standard deviations) of T_{2a} and T_{2e} are $80.8\pm$ 12 ms and $60.8\pm$ 26 ms respectively.

no additional numerical fitting, making it simple to implement and potentially improves accuracy and precision. In summary, we have described a straightforward calculation scheme to correct T_2 bias for the AWF, which requires minimal additional data acquisition. While this approach is particularly well-suited for FBWM, it may also be adapted to other dMRI modeling methods for white matter.

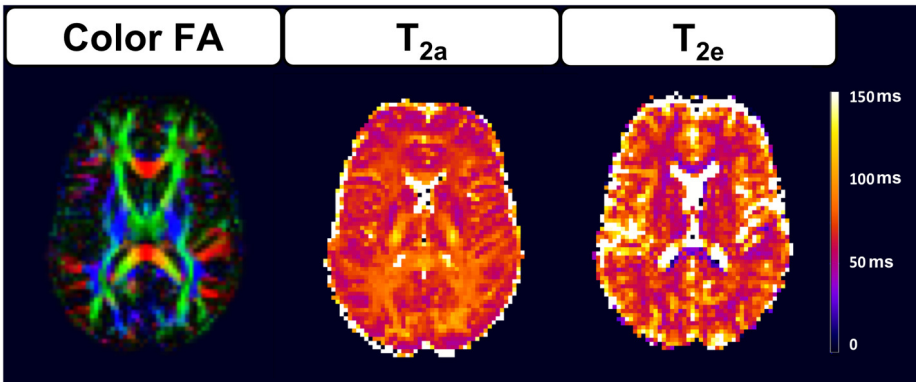

Figure 4.24: Voxelwise parametric maps showing T_{2a} (middle) and T_{2e} (right) for a single axial slice. A color FA image (left) of the same slice is given for anatomical reference. Substantial regional variability is apparent with the T_{2a} generally being longer than the T_{2e}. The T_{2a} maps appear less noisy than the T_{2e} maps, since they do not rely on any inputs from FBWM. Note that the two compartmental T_2 relaxation times are only meaningful in white matter regions, as the assumptions underlying our method are violated in gray matter [30]

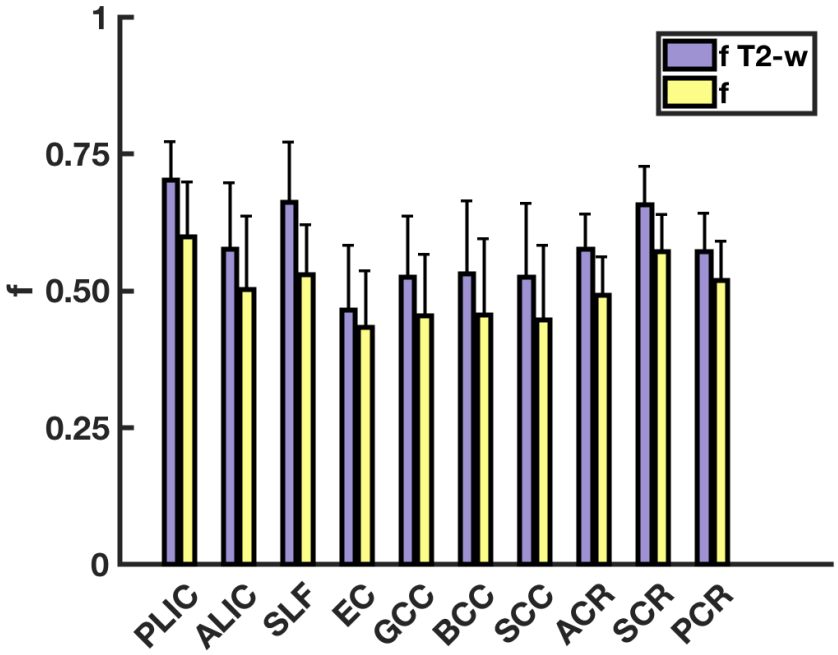

Figure 4.25: Bar graphs showing the average apparent AWF (f^*, blue) and the corrected AWF (f, yellow) for selected white matter regions of interest. The error bars indicate standard deviations. Differences range from 0.13 in the SLF to 0.03 in the EC. PLIC = posterior limb of internal capsule; ALIC= anterior limb of internal capsule; SLF = superior longitudinal fasciculus; EC = external capsule; GCC = genu of corpus callosum; BCC = body of corpus callosum; SCC = splenium of corpus callosum; ACR = anterior corona radiata; SCR = superior corona radiata; PCR = posterior corona radiata.

CHAPTER 5
THE ADVANTAGES OF STUDYING POST-STROKE WHITE MATTER INTEGRITY WITH FIBER BALL IMAGING AND THE FIBER BALL WHITE MATTER MODEL

5.1 Introduction

In 1990, Moseley and colleagues kickstarted the clinical application of dMRI by discovering that acute ischemia results in a large and quick drop in diffusivity, and today dMRI is an indispensable tool in the radiologist's toolbox. Over the last 30 years, dMRI has been used to increase our understanding of impairments post-stroke but it has proven challenging to make the next influential contribution. So far, very little applications have made it to the clinic except dMRI tractography for neurosurgical planning at a few large academic centers.

dMRI has the potential of functioning as an in-vivo microscope that could inform clinicians on phenomena like demyelination, necrosis, or inflammation. As discussed in Chapter 1, the major issue is the lack of specificity of dMRI metrics which currently makes it challenging to distinguish between these pathological processes. A more specific assessment of the affected tissue could make a substantial difference when assessing a patient's recovery potential, and therapy could be targeted to those brain regions that are most viable. The advantage of FBI and FBWM for the study of post-stroke brains is two fold: 1) it provides compartment specific microstructural metrics and, 2) it enables the tracking of intra-axonal water for tractography. More details together with some examples will be given in Section 5.2 and Section 5.3 respectively.

The chapter will conclude with a note of caution. As discussed in extensive detail, the

calculation of more specific dMRI metrics requires the introduction of several assumptions. Even though we provided evidence for the validity of FBI's main assumptions in Chapter 4, there is no guarantee that these assumptions will hold in stroke. Unfortunately, the appropriate dataset was not available to redo the same experiment from Section 4.2 for chronic stroke, but we will demonstrate, using neonatal dMRI data, that care needs to be taken when using FBWM to study diseased white matter.

5.2 Microstructure

Determining the residual functionality and recovery potential of brain regions post-stroke is of significant interest for stroke researchers. As introduced in Chapter 3, structural MRI is commonly used to study the function of brain regions. It is often assumed, (e.g., like in VLSM) that any visibly abnormal voxel on T_1- and/or T_2-weighted MRI has lost its normal function. However, there is a clear difference in contrast throughout the affected tissue and it is not well understood how the underlying microstructure changed and how this impacts functionality. For example, T_2-weighted MRIs of brains from older adults often show bright spots in the white matter and their presence is not necessarily related to cognitive decline.

FBWM allows for a more in depth study of the underlying structure and could potentially provide more insight into the integrity and/or composition of the affected white matter. Specifically, it provides metrics that are compartment specific. Pathological processes that impact axons, like cytotoxic edema, would have an effect on the diffusion dynamics of the intra-axonal compartment, while other phenomena like gliosis would not. Figure 5.1 shows example FBWM metrics for two slices from one chronic stroke patient. One slice is taken through the necrotic core of the lesion (Figure 5.1a), while the other slice is taken from the edge of the lesion (Figure 5.1b). Both the T_1-weighted image and the conventional FA metric show abnormalities for both slices, albeit not to the same degree.

Remarkably, the FBI-derived metric FAA looks qualitatively intact in the perilesional area. From a diffusion perspective, a large FAA value is indicative of highly anisotropic diffusion inside the remaining axons. Biologically speaking, this could be suggestive of perilesional axons that are structurally similar to the axons on the contralesional side. The AWF drop, however, reveals a likely decrease in the total number of axons. The remaining metric, $\bar{D}_e$, complements FAA and suggest substantial changes to the extra-axonal environment. In comparison, the FAA does show severe pathology in the core of the lesion as shown in Figure 5.1a together with changes to AWF and $\bar{D}_e$. These preliminary findings suggest that FAA could potentially be used to categorize lesioned tissue, which potentially relates to their functionality; however, further research is needed to confirm this.

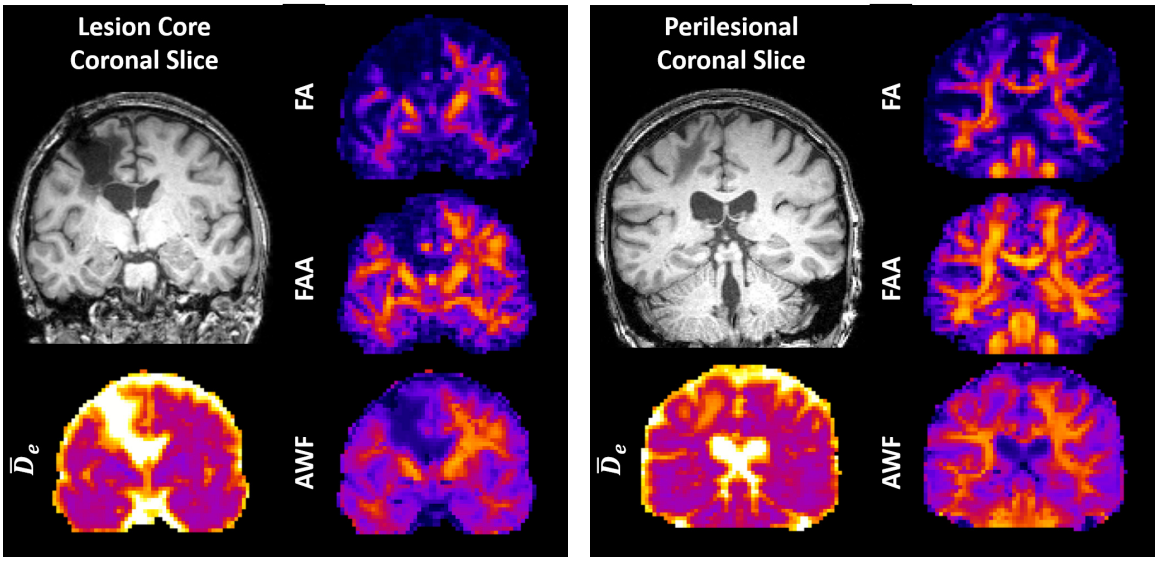

(a) Lesion core **(b)** Peri lesional area

Figure 5.1: FBWM metrics calculated for a subject with a chronic ischemic stroke. One slice (a) is from the core of the lesion and the other slice (b) is from the perilesional area. Notice how the FAA looks qualitatively intact in the perilesional slice (b).

5.3 Tractography

The majority of dMRI tractography techniques make the underlying assumption that the direction of water diffusion equals the directionality of white matter fiber bundles. However,

in diseased brain, an abundance of extra-axonal fluid (e.g., vasogenic edema) can mask the true orientation of the fibers resulting in faulty tractography. In Chapter 4 we showed that high b-values can be used to isolate the intra-axonal compartment, and techniques like FBI leverage this to calculate the fiber density in all directions (i.e., fODF). While FBI tractography is future work for the study of stroke and anomia, Figure 5.2 shows an example of conventional DTI and the newly proposed FBI tractography for a patient with severe leukoaraiosis. The patient reported no significant cognitive decline and was negative for any metabolic, autoimmune, and genetic abnormalities. A structural T_2-FLAIR image is given to demonstrate the severity of the white matter abnormalities. The rendered tracts are: the SLF, the ILF, the IFOF, the corpus callosum, and the cortico-spinal tract. Qualitatively, the FBI tractogram appears much fuller than the DTI tractogram, which is more in line with her normal cognitive presentation. Tracking intra-axonal water is a promising avenue of research for stroke, brain cancers, and other white matter diseases.

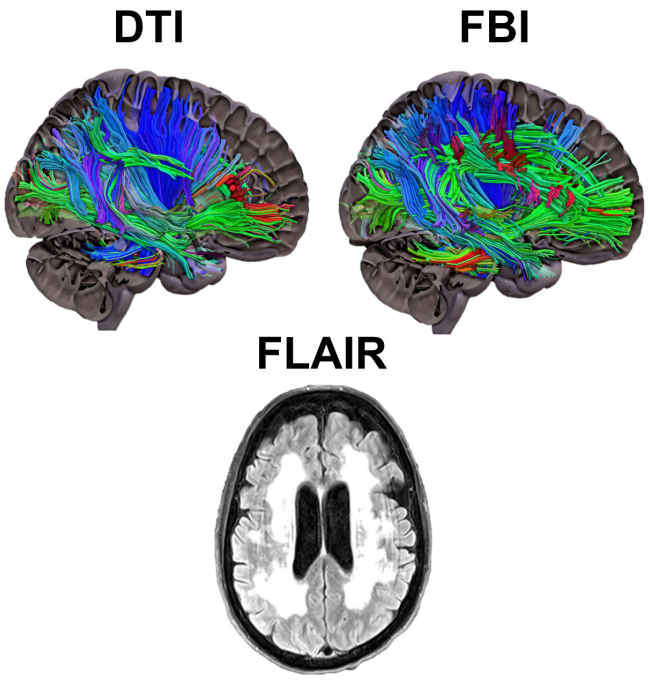

Figure 5.2: Top row: dMRI tractography when using DTI (left) and when using FBI (right) in a patient with severe white matter disease. Bottom row: Axial slice of T2-weighted FLAIR from same patient to demonstrate the extend of the abnormalities. *Figure courtesy Hunter Moss*

5.4 Limitations: Case Study - Power-law fits for direction-averaged diffusion MRI signal in neonatal brain as a function of b-value

Introduction

In Chapter 4 we showed that the direction-averaged dMRI signal in healthy adult brain decays approximately as a power-law [30, 166]. Considering that a power-law fit only has two adjustable parameters, this provides a parsimonious description of the data. Moreover, the values of the fitted exponents give insight into the water diffusion dynamics. In white matter, the exponent is close to $1/2$, which indicates that the signal is dominated by water confined to thin tubes, which may be identified as axons. This behavior is the foundation for FBI and FBWM, which we introduced in this work. Gray matter, in contrast, has a much larger exponent that is closer to 1. Here we investigated power-law fits for the direction-averaged dMRI signal for one neonate brain at 44 weeks Gestational Age (GA). The microstructure of neonate brain differs substantially from adult brain in the degree of white matter myelination, which could potentially alter the water diffusion dynamics [202, 203].

Methods

A neonate, 44 weeks GA, (born at 31 weeks GA weighing $1355\,\mathrm{grams}$) was scanned on a Siemens Prisma. The subject was enrolled in a vagus nerve stimulation study at 42 weeks GA to treat the inability to master oral feeding. The patient received 14 treatment sessions and was discharged at 44 weeks GA. Clinical MRI findings included anterior pituitary hypoplasia, enlarging cisterna magna with mild hydrocephalus, and cavum septum pellucidum.

Data were acquired using a twice-refocused dMRI sequence for $b = 1000$, 2000, 4000, 6000, 8000, and $10.000\,\mathrm{s/mm^2}$ and 64 diffusion-encoding directions. Other imag-

ing parameters were: TE=$109\,\mathrm{ms}$, TE=$3800\,\mathrm{ms}$, voxel size = $3\,\mathrm{mm}$, number slices=36, FOV=$198\,\mathrm{mm}^2$. Each dMRI dataset included 11 $b = 0\,\mathrm{s/mm}^2$ images. Subject was swaddled, fed, and given Sweet-Ease to induce natural sleep. The total acquisition time was 31min and 51s.

Data quality was improved by reducing signal noise [85], removing Gibbs ringing artifacts [86] and correcting for Rician noise bias [142] and motion [186]. Conventional diffusion metrics were calculated [84] from dMRI data with $b = 0 - 2000\,\mathrm{s/mm}^2$. The direction-averaged dMRI signal ($\bar{S}$) was calculated for each b-value by averaging over all gradient directions. Only voxels with a mean diffusivity lower than $2\,\mathrm{m}^2/\mathrm{ms}$ and an larger than 3.9 at $b = 6000\,\mathrm{s/mm}^2$ were included.

The b-value dependence of $\bar{S}$ was fit to both a power law $\bar{S} = C_p \cdot b^{-\alpha}$ and, as a comparison, a monoexponential $\bar{S} = C_m \cdot e^{-\nu b}$. All fits had two parameters and were performed using a non-linear least squares fitting procedure. Monoexponential fits were performed both with and without $b = 0$ as a sample point. All power-law fits excluded the $b = 0$ data. Goodness of fit was assessed by the AIC and the coefficient of determination R^2.

Results

Of the 1395 voxels, 361 had an $\bar{s} > 3.9$ for all b-values; 601 and 433 voxels had an $\bar{s} > 3.9$ for $b = 8000$ and $b = 6000 s/mm^2$, respectively. Figure 5.3 shows the anatomical location of these ROIs.

The semi-log plotted non-linear fits are shown in Figure 5.4 for the power-law and monoexponential fits, for all ROIs. All data points below the red line were excluded. For all ROIs the data is best described by a power-law behavior with the exponent varying between $\alpha = 1.08 \pm 0.07$, $\alpha = 1.19 \pm 0.14$, $\alpha = 1.35 \pm 0.14$ for data up to $b = 10,000$, $b = 8000$, and $b = 6000$ respectively. Figure 5.5 shows the distribution of α within all

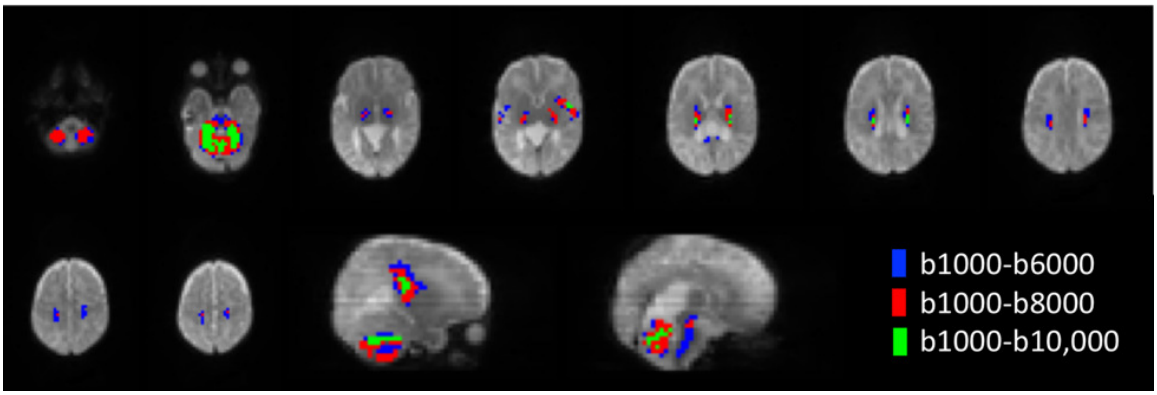

Figure 5.3: Anatomical location of the three ROIs considered in the analyses. Voxels were grouped according to the largest b-value for which the direction-averaged dMRI signal exceeded a noise threshold of 3.9 (arbitrary units). Only voxels for which this largest b-value was at least $b = 6000\,\mathrm{s/mm^2}$ were included, so that the power-law fits would all have at least 4 data points above the noise. The ROIs with largest b-values of 6000, 8000, and $10.000\,\mathrm{s/mm^2}$ are shown in blue, red, and green, respectively. These largely coincide with the cerebellum, brain stem, corticospinal tracts, external capsule, and splenium.

the considered voxels. The AIC does not depend significantly on the FA and the power law outperforms the monoexponential over the entire range of FA values (Figure 5.6).Interestingly, the FA only has minimal influence on α suggestive of little differences in the microstructural environment beyond diffusion anisotropy (Figure 5.7).

Discussion

Our results demonstrate a power-law scaling of the direction-averaged dMRI signal in neonate brain over $b = 1000 - 10.000\,\mathrm{s/mm^2}$ with $\alpha = 1.08 \pm 0.07$. Even though the majority of studied voxels are white matter, Figure 5.5 shows that none demonstrate a scaling behavior with $\alpha = 0.5$ as is observed in adult white matter [30, 166]. A plausible explanation for this could be that, since myelination is scarce at this stage of development, contributions of exchange cannot be neglected. Other contributing factors could be the increased water content as well as the large population of glial cells present in the developing brain. In any case, our results point to substantial differences in water diffusion dynamics in white matter for neonate in comparison to adults. Therefore, microstructural models for

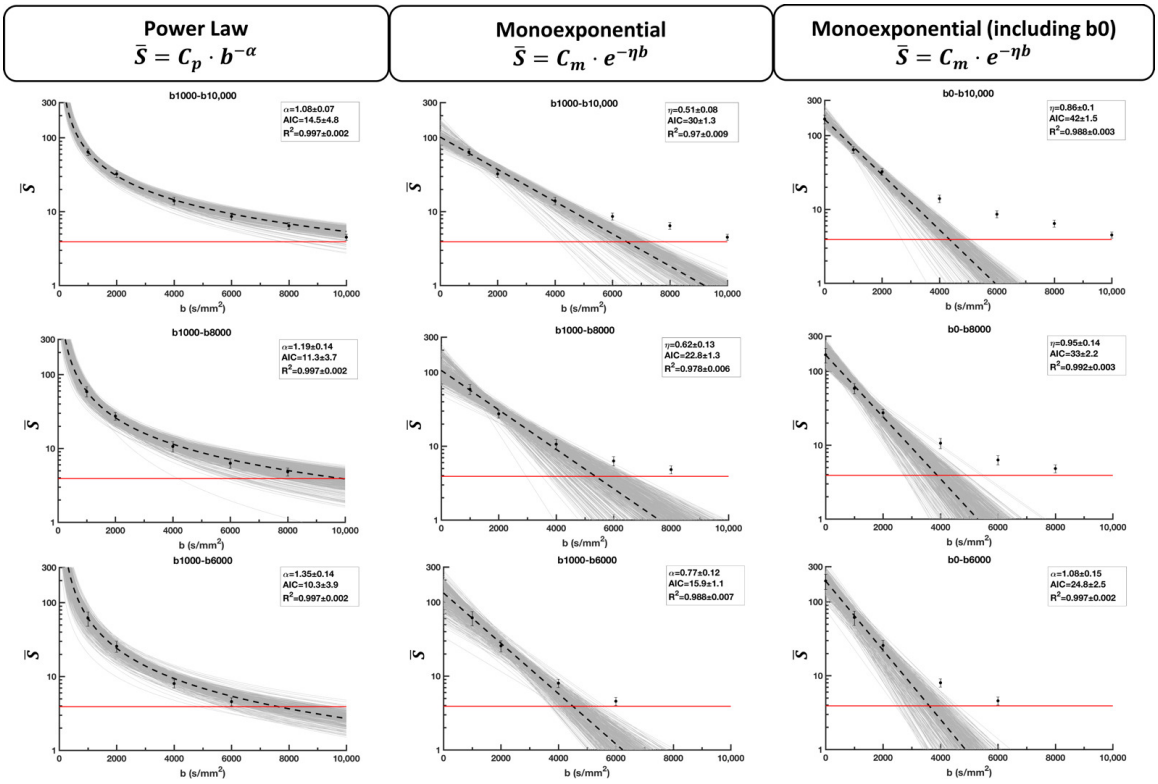

Figure 5.4: Semi-log plots showing the relationship between the direction-averaged diffusion weighted signal ($\bar{S}$) and the b-values for all three ROIs. The first column has the power-law fits, with the black dashed line showing fits to data points averaged over all voxels within each ROI and the gray lines indicating fits for individual voxels. As a comparison, the second and third columns show similar monoexponential fits without and with including $b = 0$ as a fitting point. The red line indicates the noise threshold of 3.9.

the dMRI signal developed for adult white matter may not be valid for neonates. Interestingly, the power-law exponent we find here is roughly similar to the exponent for adult gray matter. A limitation of this study is that the neonate had multiple health problems that may have affected brain maturation, complicating the generalization of our findings. Nonetheless, our results encourage caution when using microstructural models that are developed for adults without validation.

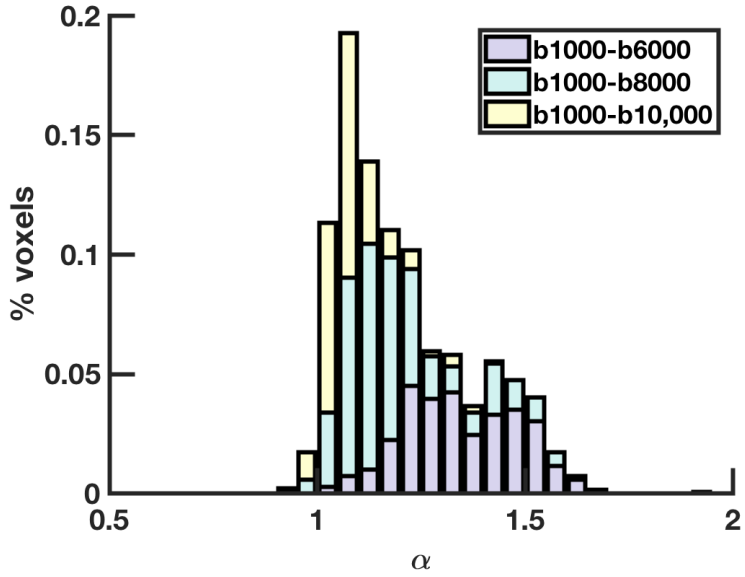

Figure 5.5: Histogram for the power-law exponent α from all the voxels included in the three ROIs. The overall average value for α is 1.21 ± 0.16.

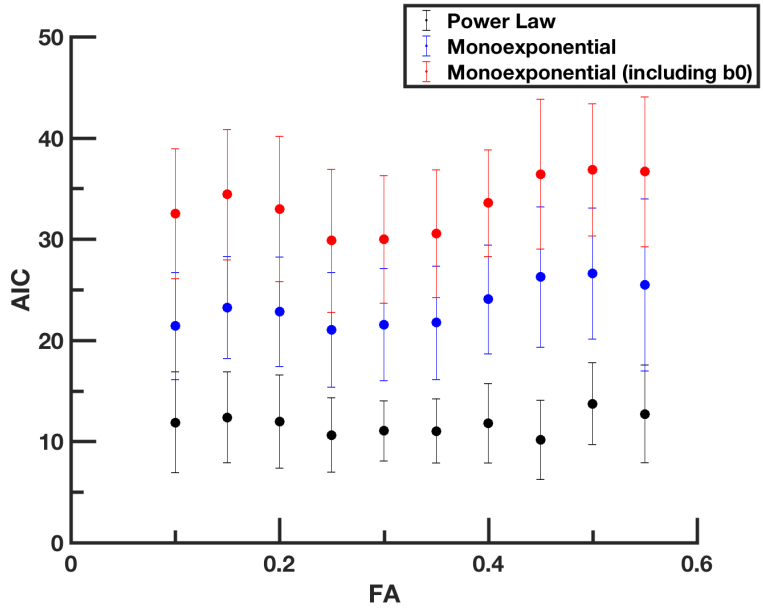

Figure 5.6: The AIC as a function of FA (bin size $= 0.05$) for power-law and both types of monoexponential fits. The power law outperforms the monoexponential fits for the full range of considered FA values. The goodness of fit is largely independent of FA.

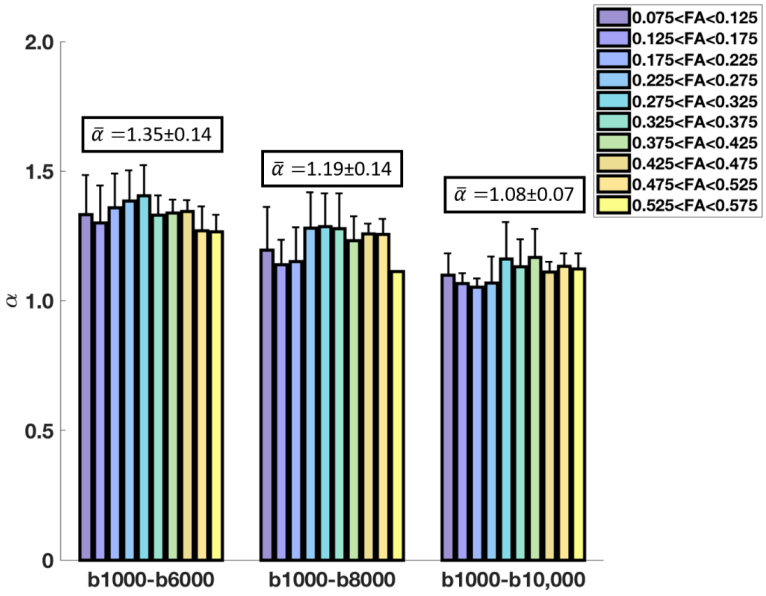

Figure 5.7: The power law exponent α grouped according to FA for all three ROIs. The average values decrease from 1.35 ± 0.14, for the ROI with a largest b-value of $6000\,\mathrm{s/mm^2}$, to 1.08 ± 0.07 for the ROI with a largest b-value of $10.000\,\mathrm{s/mm^2}$. Notice that α is not strongly dependent of FA.

CHAPTER 6
OVERALL CONCLUSION

The aim of this work was two-fold: 1) To study the impact of white matter integrity on post-stroke naming impairments, and 2) To improve upon the conventional methods of quantifying white matter microstructure using dMRI. This final chapter summarizes the original contributions outlined in this dissertation with their implications, and proposes avenues for future research.

The brain is often described as being composed of a collection of cortical hubs supporting complex cognitive function. However the emerging picture is that mental faculties, such as language, are controlled not only by these hubs but also by their interconnection. In spite of this, the specific role of white matter remains largely unexplored. Chapter 3 was devoted to the impact of white matter integrity on chronic post-stroke language impairments. We demonstrated that when predicting aphasia severity from brain microstructure, quantifying white matter integrity is most informative in patients with intermediate cortical damage. Additionally, the integrity of white matter pathways can be an independent predictor of naming impairments. Our results were in line with the dual stream model of language, supporting the existence of a ventral stream network that is responsible for providing meaning to words and a dorsal stream network responsible for their sound structure. Lastly, we provided preliminary evidence for the implication of white matter in stroke recovery. The microstructure of the perilesional white matter at baseline was predictive of naming recovery and, remarkably, therapy induced changes in white matter microstructure were strongly correlated with improvements in naming. These preliminary results pave the way for the development of more objective and individually tailored treatment strategies. Ideally, such strategies would improve predictability of language recovery in chronic aphasia. To de-

velop them we would need at a minimum: 1) A clear understanding of the neurobiology of language, 2) To unravel how residual post-stroke integrity impacts functionality and recovery, and 3) To figure out how neuroplasticity supports repair. The studies in Chapter 3 partially fulfill these requirements. In conclusion, in addition to evaluating gray matter, there is value in assessing the integrity of white matter connections. Future work should focus on quantifying the integrity of the language network at its entirety. It should assess all white matter connections simultaneously and include information on the cortical regions that are being connected by the white matter fibers under study. The imaging pipeline proposed in Chapter 3 of this thesis is ideally suited to take this work forward.

dMRI has great potential to describe brain microstructure in vivo. However, the interpretation of the dMRI signal has proven to be complex and has hampered its success clinically. Over the last 15 years many different physical models have been proposed to improve the specificity of conventional dMRI metrics. Unfortunately, results amongst the different models are inconsistent with some metrics differing by a factor of 2. This disparity is driven by the lack of consensus on the appropriate modeling assumptions for a particular imaging regime. Chapter 4 provided evidence supporting a commonly used assumption that states axons can be approximated by impermeable thin cylinders. Additionally, we found preliminary data to reinforce the assumption that high b-values can be used to isolate the axonal compartment. These two assumptions are the foundation of the FBI model. Thus, with validation of FBI, we extended the model as part of this dissertation to provide compartment specific microstructural parameters. This extension was named the FBWM model. Compartment specific diffusion metrics can be useful to distinguish between different pathological processes that affect the intra- and extra- axonal compartments differently. Lastly, we introduced a straightforward method of calculating the T_2 of both intra- and extra- axonal water. Compartmental T_2 can be used either as a biomarker, aid in the calculation of the myelin content, or alleviate bias in the AWF. Future work should involve performing histology to relate FBWM metrics to tissue microstructure. One important re-

maining question is to determine if the axonal compartment, as defined by dMRI, includes both myelinated and unmyelinated axons. Another such question would be to study the impact of glial cell infiltration on the FBWM compartmental diffusion metrics.

In parallel to histological validation, future work should also include the application of FBWM to post-stroke chronic aphasia. As shown extensively in Chapter 3, the use of conventional dMRI strategies is useful but since FBWM provides a more in depth picture of white matter integrity it may help distinguish between different pathological processes post-stroke. If processes like inflammation and axonal degeneration are made distinguishable, it is possible that salvageable white matter could be better identified. FBWM could also improve our understanding of recovery by providing more specific metrics to analyze neuroplasticity. Additionally, since high b-value dMRI can be used to isolate intra-axonal water, its use for tractography should be explored. The delineation of white matter pathways in stroke could especially benefit from this due to the presence of perilesional edema. While several of the assumptions underlying FBWM were partially validated in this dissertation, the experiments were done for healthy white matter. This work should ideally be extended to confirm the validity of FBWM for post-stroke subjects. Nonetheless, if FBWM shows a greater sensitivity to post-stroke recovery than conventional dMRI, this could justify its application to stroke even without complete validation of its biophysical foundation.

To conclude, this dissertation improves our understanding of the importance of white matter in determining baseline impairments, brain plasticity, and recovery in post-stroke anomia. A better understanding of the neurobiology of anomia could lead to improved knowledge about the mechanisms supporting speech production, better treatment outcome prediction, and possibly better treatments in the future. We also introduced a new biophysical dMRI model to study the white matter post-stroke in greater detail. The clinical validation of FBWM is essential and future work should assess if FBWM better elucidates the relationship between neural network integrity and plasticity in anomia.

Appendices

APPENDIX A

SECTION 3.2

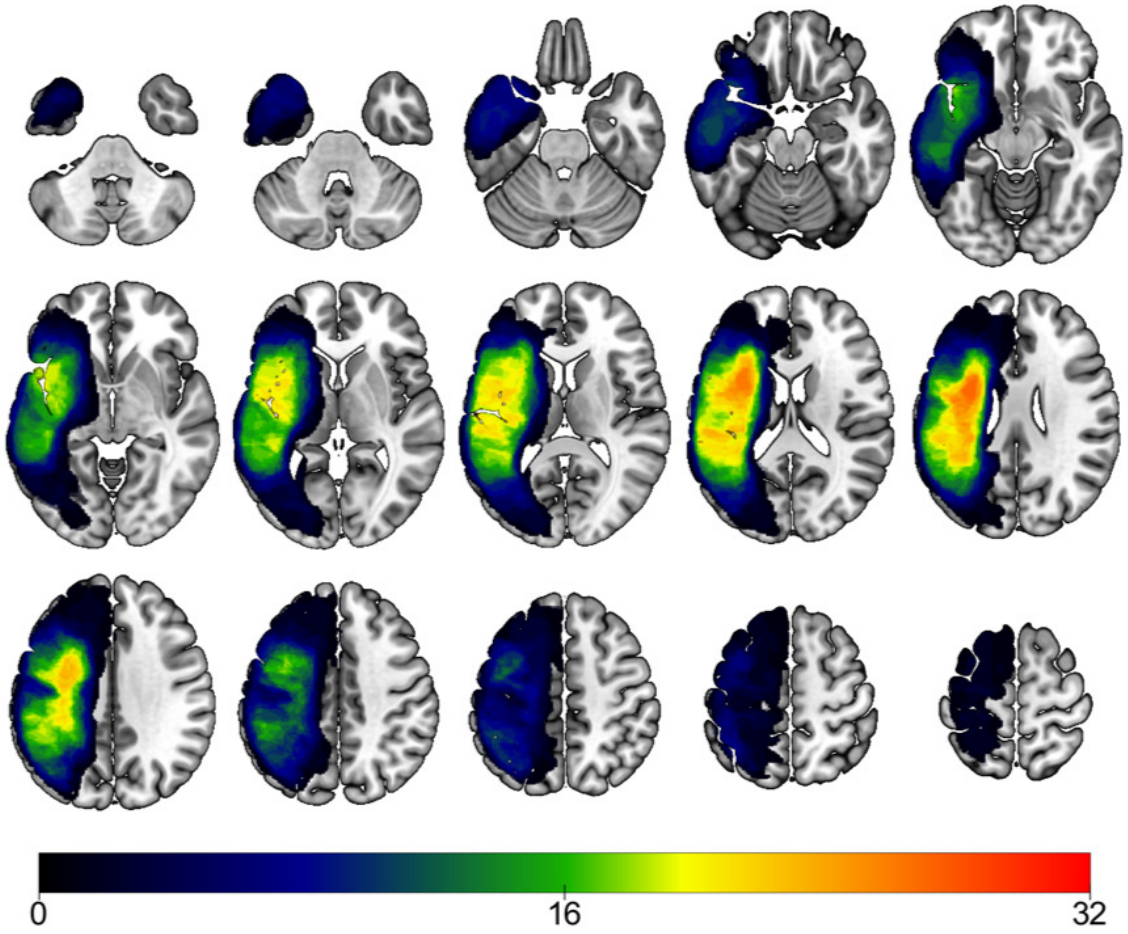

Supplementary Figure 1: Lesion Location: Lesion overlap of all participants (N = 32). The different colors represent a different amount of patients with lesions in that area.

Figure A.1

Table A.1: Subject demographics and language battery results. (M=male; F=female)

Participant	Gender	Race	Age (years)	Time Post-Stroke (months)	WAB AQ	Aphasia Type	Correct Responses (%)	Semantic Paraphasias (%)	Phonemic Paraphasias (%)
1	M	white	76	9	87.8	Anomic	72.35	12.01	0
2	F	white	66	13	80.3	Anomic	61.19	24.14	1.89
3	M	white	70	101	62.7	Broca's	34.96	3.61	0.3
4	M	white	68	48	87.2	Broca's	71.19	15.3	0.29
5	M	white	38	20	41.8	Broca's	42.54	27.55	13.76
6	M	white	66	47	77.8	Anomic	47.81	1.46	0
7	M	black	50	78	80.8	Broca's	44.48	6.09	22.08
8	M	white	49	6	20.1	Broca's	26.37	15.3	27.04
9	M	black	42	108	31.2	Global	38.18	51.11	3.07
10	F	white	37	21	52.8	Broca's	66.84	19.69	3.85
11	M	white	69	9	59.9	Broca's	25.63	12.6	11.64
12	M	black	64	6	45.2	Conduction	1.74	5.28	5.25
13	M	black	58	25	93.7	Anomic	77.07	8.63	0

Table A.1: Subject demographics and language battery results. (M=male; F=female)

Participant	Gender	Race	Age (years)	Time Post-Stroke (months)	WAB AQ	Aphasia Type	Correct Responses (%)	Semantic Paraphasias (%)	Phonemic Paraphasias (%)
14	M	black	47	25	27.9	Broca's	10.57	11.32	14.74
15	F	white	64	86	42.9	Wernicke's	9.06	14.86	10.45
16	M	white	49	15	29.3	Broca's	1.02	1.68	5.69
17	M	white	55	84	23.4	Global	3.64	6.02	1.04
18	F	Asian	46	27	39.6	Broca's	30.14	19.24	13.6
19	F	white	48	21	32.3	Broca's	0.33	1.57	0.95
20	M	white	60	26	27.8	Broca's	0.66	8.97	20.07
21	M	white	55	9	67.9	Conduction	35.78	6.95	24.3
22	M	black	51	72	41.6	Broca's	17.27	35.94	8.33
23	M	white	62	60	86.8	Anomic	78.38	2.89	2.38
24	M	white	56	65	74	Conduction	79.44	8.73	0
25	M	white	64	8	50.9	Wernicke's	10.19	42.73	0.87
26	F	white	70	11	41.9	Wernicke's	7.21	27.41	0.92

Table A.1: Subject demographics and language battery results. (M=male; F=female)

Participant	Gender	Race	Age (years)	Time Post-Stroke (months)	WAB AQ	Aphasia Type	Correct Responses (%)	Semantic Paraphasias (%)	Phonemic Paraphasias (%)
27	M	white	74	7	60.2	Wernicke's	24.01	8.88	4.61
28	M	white	56	23	47.3	Brocas	29.77	14.36	1.34
29	F	black	29	19	49.3	Brocas	43.81	33.62	0.38
30	F	white	73	16	92.1	Anomic	85.01	8.25	0
31	M	white	50	23	30.1	Brocas	60.15	13.86	5.67
32	M	white	61	22	43.3	Brocas	23.52	1.65	21.34

APPENDIX B

SECTION 4.3

Here we sketch the derivations of Equations 4.16 through 4.18. The diffusion tensor for the intra-axonal space may be expressed as

$$\boldsymbol{D_a} = \int d\Omega_u \mathbf{D}_{axon}(\mathbf{u}) F(\mathbf{u}), \tag{B.1}$$

where $\mathbf{D}_{axon}(\mathbf{u})$ is the diffusion tensor for an individual axon oriented in a direction $\mathbf{u}$. If axons are idealized as thin, straight cylinders (i.e., a stick model), we then have

$$\mathbf{D}_{axon}(\mathbf{u}) = D_a \mathbf{u}\mathbf{u}^T = D_a \begin{pmatrix} \sin^2\theta\cos^2\phi & \sin^2\theta\cos\phi\sin\phi & \cos\theta\sin\theta\cos\phi \\ \sin^2\theta\cos\phi\sin\phi & \sin^2\theta\sin^2\phi & \cos\theta\sin\theta\sin\phi \\ \cos\theta\sin\theta\cos\phi & \cos\theta\sin\theta\sin\phi & \cos^2\theta \end{pmatrix}. \tag{B.2}$$

where (θ, ϕ) are the spherical angles for $\mathbf{u}$. From Equations 4.12, B.1 and B.2, one sees that

$$\mathbf{D}_{axon}(\mathbf{u}) = D_a \sum_{l=0}^{\infty} \sum_{m=-2l}^{2l} c_{2l}^m \int d\Omega_u Y_{2l}^m(\theta,\phi) \begin{pmatrix} \sin^2\theta\cos^2\phi & \sin^2\theta\cos\phi\sin\phi & \cos\theta\sin\theta\cos\phi \\ \sin^2\theta\cos\phi\sin\phi & \sin^2\theta\sin^2\phi & \cos\theta\sin\theta\sin\phi \\ \cos\theta\sin\theta\cos\phi & \cos\theta\sin\theta\sin\phi & \cos^2\theta \end{pmatrix}. \tag{B.3}$$

The spherical integrals in Equation B.3 may be evaluated with the help of Equations 4.10 and 4.11, which leads directly to Equations 4.16 and 4.17. All the needed integrals correspond to elementary trigonometric forms, with those for $l > 1$ yielding zero.

In order to derive Equation 4.18, we exploit the fact that the FAA is given by

$$FAA = \sqrt{\frac{3}{2}} \cdot \frac{\|\boldsymbol{D_a} - \frac{1}{3} tr(\boldsymbol{D_a}\mathbf{I})\|}{\|\boldsymbol{D_a}\|}, \tag{B.4}$$

where $\mathbf{I}$ indicates the identity matrix, $tr(...)$ indicates the trace, and $norm...$ indicates the Frobenius norm [13, 204]. By applying Equation B.4 to Equation 4.17, one finds the result of Equation 4.18.

APPENDIX C

SECTION 4.4

Neglecting myelin water, the MRI signal without diffusion weighting can be written as

$$S_0(TE) = A[f \cdot e^{-TE/T_{2a}} + (1 - f \cdot e^{-TE/T_{2e}}], \tag{C.1}$$

where f is the intra-axonal water fraction and A is a constant. For large b-values, the theory underlying fiber ball imaging [29] predicts

$$\bar{S}(TE) = \frac{1}{2} f^*(TE) S_0(TE) \sqrt{\frac{\pi}{bD_a}}, \tag{C.2}$$

where

$$f^* \equiv \frac{f \cdot e^{-TE/T_{2a}}}{f \cdot e^{-TE/T_{2a}} + (1 - f) \cdot e^{-TE/T_{2e}}} \tag{C.3}$$

is the apparent axonal water fraction for a given echo time [166]. By combining Equations C.1-C.3, one sees that

$$\bar{S}(TE) = \frac{Af}{2} e^{-TE/T_{2a}} \sqrt{\frac{\pi}{bD_a}}. \tag{C.4}$$

From Equations C.1 and C.4, it then follows that

$$F(TE) = A(1 - f) \cdot e^{-TE/T_{2e}}, \tag{C.5}$$

which is identical to Equation 4.33 after identifying C_e with $A(1 - f)$.

APPENDIX D

PUBLICATIONS

D.1 Publications in Journals

D.1.1 Related to Dissertation

- **McKinnon, Emilie T.**, and Jens H. Jensen. "Measuring intra-axonal T2 in white matter with direction-averaged diffusion MRI." Magnetic resonance in medicine 81.5 (2019): 2985-2994.

- **McKinnon, Emilie T.**, Julius Fridriksson, Alexandra Basilakos, Gregory Hickok, Argye E. Hillis, M. Vittoria Spampinato, Ezequiel Gleichgerrcht , Chris Rorden, Jens H. Jensen, Joseph A. Helpern, and Leonardo Bonilha. "Types of naming errors in chronic post-stroke aphasia are dissociated by dual stream axonal loss." Scientific reports 8, no. 1 (2018): 14352.

- **McKinnon, Emilie T.**, Joseph A. Helpern, and Jens H. Jensen. "Modeling white matter microstructure with fiber ball imaging." NeuroImage 176 (2018): 11-21.

- **McKinnon, Emilie T.**, Julius Fridriksson, G. Russell Glenn, Jens H. Jensen, Joseph A. Helpern, Alexandra Basilakos, Chris Rorden, Andy Y. Shih, M. Vittoria Spampinato, and Leonardo Bonilha. "Structural plasticity of the ventral stream and aphasia recovery." Annals of neurology 82, no. 1 (2017): 147-151.

- **McKinnon, Emilie T.**, Jens H. Jensen, G. Russell Glenn, and Joseph A. Helpern. "Dependence on b-value of the direction-averaged diffusion-weighted imaging signal in brain." Magnetic resonance imaging 36 (2017): 121-127.

D.1.2 Unrelated to Dissertation

- Nie, Xingju, Maria Fatima Falangola, Ralph Ward, **Emilie T. McKinnon**, Joseph A. Helpern, Paul J. Nietert, and Jens H. Jensen. "Diffusion MRI detects longitudinal white matter changes in the 3xTg-AD mouse model of Alzheimer's disease." Magnetic resonance imaging 57 (2019): 235:242.

- Mohanty, Vaibhav, **Emilie T. McKinnon**, Joseph A. Helpern, and Jens H. Jensen. "Comparison of cumulant expansion and q-space imaging estimates for diffusional kurtosis in brain." Magnetic resonance imaging 48 (2018): 80-88.

- Summers, Philipp M., David A. Hartmann, Edward S. Hui, Xingju Nie, Rachael L. Deardorff, **Emilie T. McKinnon**, Joseph A. Helpern, Jens H. Jensen, and Andy Y. Shih. "Functional deficits induced by cortical microinfarcts." Journal of Cerebral Blood Flow & Metabolism 37, no. 11 (2017): 3599-3614

- Jensen, Jens H., **Emilie T. McKinnon**, G. Russell Glenn, and Joseph A. Helpern. "Evaluating kurtosisbased diffusion MRI tissue models for white matter with fiber ball imaging." NMR in Biomedicine 30, no. 5 (2017): e3689.

D.2 Publications in Conference Proceedings

D.2.1 Oral Presentations

- **McKinnon, Emilie T.** Where to go beyond DTI: DKI and multi-shell acquisitions. Invited talk to be presented at ISMRM 2019.

- **McKinnon, Emilie T.**, Marebwa B., Rorden C.,Basilakos A., Gleichgerrcht E., Fridriksson J. and Bonilha Leonardo. Synergism between cortical damage and white matter disconnection contributes to aphasia severity. Oral presented at SNL 2018. Proceedings of the Society for the neurobiology of language; 2018 August 16-18; Quebec City, Canada.

- **McKinnon, Emilie T.**, and Jensen, Jens H. Simple scheme for correcting bias in axonal water fraction due to differences in compartmental transverse relaxation times. Oral presented at ISMRM 2019. Proceedings of the 27th meeting of the International Society of Magnetic Resonance in Medicine; 2019 May; Montreal, Canada.

- **McKinnon, Emilie T.**, Jensen, Jens H., and Helpern Joseph A. Diffusion Anisotropy of the Extra-Axonal Environment is Linked to Axon Alignment. Power Pitch presented at ISMRM 2018. Proceedings of the 26th meeting of the International Society of Magnetic Resonance in Medicine; 2018 June; Paris, France.

- **McKinnon, Emilie T.** Advanced diffusion MRI methods for studying white matter integrity in Aphasia. Invited talk at C-STAR lecture series, 2017-2018. September 28, 2017. Columbia, South Carolina.

- **McKinnon, Emilie T.** Advanced Neuroimaging Methods for Stroke Recovery: Diffusion-weighted Imaging and Anatomical Connectivity in Stroke Patients. Invited Oral Presentation. Proceedings of the American Heart Association; 2017 February 22-24; Houston, Texas, USA.

- **McKinnon, Emilie T.**, Glenn, G. Russell, Jensen, Jens H., Helpern, Joseph A., Bonilha Leonardo and Fridriksson Julius. Examining the relationship between semantic performance and inferior longitudinal fasciculus integrity in chronic post-stroke aphasia using advanced diffusion MRI techniques. Oral presented at MUSC Research Day 2016.; 2016 November 4; Charleston, South Carolina, USA.

D.2.2 Abstracts

- Moss, Hunter, **McKinnon, Emilie T.**, Helpern, Joseph A., and Jensen, Jens H. Dependence of harmonic power on b-value for fiber ball imaging: comparison of theory and experiment. Abstract presented at ISMRM 2019. Proceedings of the 27th meet-

ing of the International Society of Magnetic Resonance in Medicine; 2019 May; Montreal, Canada.

- Falangola, Maria Fatima, Nie, Xingju, **McKinnon, Emilie T.**, Helpern, Joseph A., and Jensen, Jens H. Diffusion MRI detects changes in the Hippocampus and Fimbria-Fornix Circuit in 2 months-old 3xTg-AD mice. Abstract presented at ISMRM 2019. Proceedings of the 27th meeting of the International Society of Magnetic Resonance in Medicine; 2019 May; Montreal, Canada.

- **McKinnon, Emilie T.**, Jensen H. J., Rorden C.,Basilakos A., Gleichgerrcht E., Fridriksson J, Helpern A. Joseph and Bonilha Leonardo. Perilesional white matter microstructure and aphasia recovery. Abstract presented at SNL 2018. Proceedings of the Society for the neurobiology of language; 2018 August 16-18; Quebec City, Canada.

- Nie, Xingju, Falangola F. Fatima,**McKinnon, Emilie T.**, Oddo Salvatore, Helpern Joseph A., and Jensen H. Jens. Diffusion MRI changes in brain for the 3xTg Mouse Model of Alzheimers Disease. Abstract presented at ISMRM 2018. Proceedings of the 26th meeting of the International Society of Magnetic Resonance in Medicine; 2018 June; Paris, France.

- Moss Hunter, **McKinnon, Emilie T.**, Benitez Andreana, Jenkins D. Dorothea, Glenn, G. Russell, Jensen, Jens H., and Helpern Joseph A. Intra-axonal Fractional Anisotropy from Fiber Ball Imaging. Abstract presented at ISMRM 2018. Proceedings of the 26th meeting of the International Society of Magnetic Resonance in Medicine; 2018 June; Paris, France.

- Bryant Lorna, Alonazi, Batil K., Bonilha, Leonardo, **McKinnon, Emilie T.**, Jensen, Jens H., Das, Kumar, Marson, Anthony G., Sluming, Vanessa, Keller, Simon S. Subcortical diffusional kurtosis imaging and antiepileptic drug treatment outcome in-

newly diagnosed focal epilepsy. Abstract presented at the European Congress for Epileptology. Proceedings of the 13th European congress on Epileptology, 2018 June 26-30, Vienna, Austria.

- **McKinnon, Emilie T.**, Jensen, Jens H., Fridriksson J., Rorden C., Helpern J. and Bonilha Leonardo. Lower axon density in residual temporal white matter is related to semantic paraphasia prevalence. Abstract presented at SNL 2017. Proceedings of the Society for the neurobiology of language; 2017 November 8-10; Baltimore, Maryland.

- **McKinnon, Emilie T.**, Jensen, Jens H.,Glenn, G. Russell, , Shih A, Helpern, Joseph A. Exploring Cortical Fiber Crossings in Mice using Diffusional Kurtosis Imaging. Abstract presented at ISMRM 2017. Proceedings of the 25th meeting of the International Society of Magnetic Resonance in Medicine; 2017 April 22 April 27; Honolulu, USA.

- Jensen, Jens H., Mohanty, Vaibhav, McKinnon, **Emilie T., Helpern**, Joseph A. Optimizing the Signal Model for Diffusional Kurtosis Imaging. Abstract presented at ISMRM 2017. Proceedings of the 25th meeting of the International Society of Magnetic Resonance in Medicine; 2017 April 22 April 27; Honolulu, USA.

- Moss H., Glenn, G. Russell, **McKinnon, Emilie T.**, Jensen, Jens H. White Matter Fiber Tractography with Fiber Ball Imaging. Abstract presented at ISMRM 2017. Proceedings of the 25th meeting of the International Society of Magnetic Resonance in Medicine; 2017 April 22 April 27; Honolulu, USA.

- **McKinnon, Emilie T.**, Glenn, G. Russell, Jensen, Jens H., Helpern, Joseph A., Bonilha Leonardo and Fridriksson Julius. Investigating the post-stroke integrity of the inferior longitudinal fasciculus and its relation with semantic performance using diffusional kurtosis imaging. Abstract presented at ISC 2017. Proceedings of the

American Heart Association; 2017 February 22-24; Houston, Texas, USA.

- **McKinnon, Emilie T.**, Glenn, G. Russell, Jensen, Jens H., Helpern Joseph A., Bonilha Leonardo and Fridriksson Julius. Investigating microstructural changes of the ipsilateral SLF and ILF underlying speech therapy using advanced diffusion MRI techniques. Abstract presented at SNL 2016. Proceedings of the Society for the neurobiology of language; 2016 August 17-20; London, United Kingdom.

- **McKinnon, Emilie T.**, Glenn, G. Russell, Benitez, Adreana, Jensen, Jens H., Falangola, Maria F., Chan, Clifford H. and Helpern Joseph A. Quantifying the Number of Crossing Fibers in the Aging Brain Using DKI Tractography. Poster presented at AAIC 2015. Proceedings of the Alzheimers Association International Conference; 2015 July 18-23; Washington DC.

- Deardorff RL, **McKinnon Emilie T.** , Sokolowski T, Jensen JH, Hori M, Govind V, Helpern JA. Kurtosis Imaging Network: a Collaborative, Open-Source Imaging Database. Poster presented at ISMRM 2015. Proceedings of the 23rd meeting of the International Society of Magnetic Resonance in Medicine; 2015 May 30 June 5; Toronto, Canada.

REFERENCES

[1] K. Brodmann, *Vergleichende lokalisationslehre dergrobhirnrinde in ihren prinzipien dargestellt auf grunddes zellenbaues*. Leipzig: J.A. Barth, 1909.

[2] D. K. Jones (Editor), *Diffusion mri: Theory, methods, and applications*. New York: Oxford, 2010.

[3] R. Brown, "A brief account of microscopical observations made in the months of june, july, and august, 1827, on the particles contained in the pollen of plants; and on the general existence of active molecules in organic and inorganic bodies.," *Philosophical Magazine*, vol. 4, pp. 161–173, 1828.

[4] A. Einstein, "Uber die von der molekularkinetischen theorie der warme gefordete bewegung von in ruhenden flussigkeiten suspendierten teilchen," *Annals of Physics*, vol. 4, pp. 549–560, 1905.

[5] E. O. Stejskal and J. Tanner, "Spin diffusion measurements: Spin echoes in the presence of a timedependent field gradient," *J. Chem. Phys.*, vol. 42, p. 288, 1965.

[6] E. L. Hanh, "Free nuclear induction," *Physics Today*, vol. 6, no. 11, p. 4, 1953.

[7] D. S. Novikov, V. G. Kiselev, and S. N. Jespersen, "On modeling," *Magn Reson Med*, vol. 79, no. 6, pp. 3172–3193, 2018.

[8] D. S. Novikov, E. Fieremans, S. N. Jespersen, and V. G. Kiselev, "Quantifying brain microstructure with diffusion mri: Theory and parameter estimation," *NMR Biomed*, vol. 32, no. 4, e3998, 2019.

[9] Y. Cohen and Y. Assaf, "Extracting geometric properties of white matter with q-space diffusion mri (qsi)," in *Diffusion MRI: Theory, Methods, and Applications*, D. K. Jones, Ed. New York: Oxford, 2011, ch. 9, pp. 125–151.

[10] P. J. Basser, J. Mattiello, and D. LeBihan, "Estimation of the effective self-diffusion tensor from the nmr spin echo," *J Magn Reson B*, vol. 103, no. 3, pp. 247–54, 1994.

[11] ——, "Mr diffusion tensor spectroscopy and imaging," *Biophys J*, vol. 66, no. 1, pp. 259–67, 1994.

[12] J. Tanner, "Transient diffusion in a system partitioned by permeable barriers. application to nmr measurements with a pulsed field gradient.," *J. Chem. Phys.*, vol. 69, pp. 1748–1754, 1978.

[13] P. J. Basser and C. Pierpaoli, "Microstructural and physiological features of tissues elucidated by quantitative-diffusion-tensor mri," *J Magn Reson B*, vol. 111, no. 3, pp. 209–19, 1996.

[14] S. Mori, B. J. Crain, V. P. Chacko, and P. C. van Zijl, "Three-dimensional tracking of axonal projections in the brain by magnetic resonance imaging," *Ann Neurol*, vol. 45, no. 2, pp. 265–9, 1999.

[15] P. J. Basser, S. Pajevic, C. Pierpaoli, J. Duda, and A. Aldroubi, "In vivo fiber tractography using dt-mri data," *Magn Reson Med*, vol. 44, no. 4, pp. 625–32, 2000.

[16] J. H. Jensen, J. A. Helpern, A. Ramani, H. Lu, and K. Kaczynski, "Diffusional kurtosis imaging: The quantification of non-gaussian water diffusion by means of magnetic resonance imaging," *Magn Reson Med*, vol. 53, no. 6, pp. 1432–40, 2005.

[17] D. S. Tuch, T. G. Reese, M. R. Wiegell, and V. J. Wedeen, "Diffusion mri of complex neural architecture," *Neuron*, vol. 40, no. 5, pp. 885–95, 2003.

[18] J. H. Jensen, J. A. Helpern, and A. Tabesh, "Leading non-gaussian corrections for diffusion orientation distribution function," *NMR Biomed*, vol. 27, no. 2, pp. 202–11, 2014.

[19] R. V. Mulkern, H. Gudbjartsson, C. F. Westin, H. P. Zengingonul, W. Gartner, C. R. Guttmann, R. L. Robertson, W. Kyriakos, R. Schwartz, D. Holtzman, F. A. Jolesz, and S. E. Maier, "Multi-component apparent diffusion coefficients in human brain," *NMR Biomed*, vol. 12, no. 1, pp. 51–62, 1999.

[20] C. A. Clark and D. Le Bihan, "Water diffusion compartmentation and anisotropy at high b values in the human brain," *Magn Reson Med*, vol. 44, no. 6, pp. 852–9, 2000.

[21] R. V. Mulkern, S. J. Haker, and S. E. Maier, "On high b diffusion imaging in the human brain: Ruminations and experimental insights," *Magn Reson Imaging*, vol. 27, no. 8, pp. 1151–62, 2009.

[22] D. A. Yablonskiy and A. L. Sukstanskii, "Theoretical models of the diffusion weighted mr signal," *NMR Biomed*, vol. 23, no. 7, pp. 661–81, 2010.

[23] P. van Gelderen, D. DesPres, P. C. van Zijl, and C. T. Moonen, "Evaluation of restricted diffusion in cylinders. phosphocreatine in rabbit leg muscle," *J Magn Reson B*, vol. 103, no. 3, pp. 255–60, 1994.

[24] G. J. Stanisz, A. Szafer, G. A. Wright, and R. M. Henkelman, "An analytical model of restricted diffusion in bovine optic nerve," *Magn Reson Med*, vol. 37, no. 1, pp. 103–11, 1997.

[25] Y. Assaf, R. Z. Freidlin, G. K. Rohde, and P. J. Basser, "New modeling and experimental framework to characterize hindered and restricted water diffusion in brain white matter," *Magn Reson Med*, vol. 52, no. 5, pp. 965–78, 2004.

[26] Y. Assaf and P. J. Basser, "Composite hindered and restricted model of diffusion (charmed) mr imaging of the human brain," *Neuroimage*, vol. 27, no. 1, pp. 48–58, 2005.

[27] E. Fieremans, J. H. Jensen, and J. A. Helpern, "White matter characterization with diffusional kurtosis imaging," *Neuroimage*, vol. 58, no. 1, pp. 177–88, 2011.

[28] H. Zhang, T. Schneider, C. A. Wheeler-Kingshott, and D. C. Alexander, "Noddi: Practical in vivo neurite orientation dispersion and density imaging of the human brain," *Neuroimage*, vol. 61, no. 4, pp. 1000–16, 2012.

[29] J. H. Jensen, G. Russell Glenn, and J. A. Helpern, "Fiber ball imaging," *Neuroimage*, vol. 124, no. Pt A, pp. 824–833, 2016.

[30] E. T. McKinnon, J. H. Jensen, G. R. Glenn, and J. A. Helpern, "Dependence on b-value of the direction-averaged diffusion-weighted imaging signal in brain," *Magn Reson Imaging*, vol. 36, pp. 121–127, 2017.

[31] J. Veraart, E. Fieremans, and D. S. Novikov, "On the scaling behavior of water diffusion in human brain white matter," *Neuroimage*, vol. 185, pp. 379–387, 2019.

[32] S. N. Jespersen, C. D. Kroenke, L. Ostergaard, J. J. Ackerman, and D. A. Yablonskiy, "Modeling dendrite density from magnetic resonance diffusion measurements," *Neuroimage*, vol. 34, no. 4, pp. 1473–86, 2007.

[33] C. P. Hess, P. Mukherjee, E. T. Han, D. Xu, and D. B. Vigneron, "Q-ball reconstruction of multimodal fiber orientations using the spherical harmonic basis," *Magn Reson Med*, vol. 56, no. 1, pp. 104–17, 2006.

[34] B. Jeurissen, M. Descoteaux, S. Mori, and A. Leemans, "Diffusion mri fiber tractography of the brain," *NMR Biomed*, vol. 32, no. 4, e3785, 2019.

[35] A. Alexander, J. M. G. Parker, T. E. Behrens, J. Zhang, and C. I. Nigel, "Fiber tracking," in *Diffusion MRI: Theory, Methods, and Applications*, D. K. Jones, Ed. New York: Oxford, 2011.

[36] M. Drake-Perez, J. Boto, A. Fitsiori, K. Lovblad, and M. I. Vargas, "Clinical applications of diffusion weighted imaging in neuroradiology," *Insights Imaging*, vol. 9, no. 4, pp. 535–547, 2018.

[37] M. E. Moseley, Y. Cohen, J. Mintorovitch, L. Chileuitt, H. Shimizu, J. Kucharczyk, M. F. Wendland, and P. R. Weinstein, "Early detection of regional cerebral ischemia in cats: Comparison of diffusion- and t2-weighted mri and spectroscopy," *Magn Reson Med*, vol. 14, no. 2, pp. 330–46, 1990.

[38] National Institute on Deafness and Other Communication Disorders, *NIDCD fact sheet: Aphasia,* [PDF] [NIH Pub. No. 97-4257], Web Page, Retrieved from *https://www.nidcd.nih.gov/sites/default/files/Documents/health/voice/Aphasia6-1-16.pdf*, 2015.

[39] J. Marshall, J. Atkinson, E. Smulovitch, A. Thacker, and B. Woll, "Aphasia in a user of british sign language: Dissociation between sign and gesture," *Cogn Neuropsychol*, vol. 21, no. 5, pp. 537–54, 2004.

[40] W. J. Levelt, "Spoken word production: A theory of lexical access," *Proc Natl Acad Sci U S A*, vol. 98, no. 23, pp. 13 464–71, 2001.

[41] W. Levelt, "Models of word production," *Trends Cogn Sci*, vol. 3, no. 6, pp. 223–232, 1999.

[42] D. Kemmerer, "Speech production," in *Cognitive Neuroscience of Language*. New York: Psychology Press, 2015.

[43] P. Broca, "Nouvelle observation daphmie produite par une lsion de la troisime circonvolution frontale," *Bulletins de la Socit danatomie (Paris)*, vol. 6, no. 2e serie, pp. 398–407, 1861.

[44] C. Wernicke, *Der aphasische symptomencomplex: Eine psychologische studie auf anatomischer basis*. Breslau : Max Cohn & Weigert, 1874.

[45] L. Lichtheim, "Uber aphasia," *Deutsches Archiv fur klinische Medicin*, vol. 36, pp. 204–268, 1885.

[46] N. Geschwind, "Disconnexion syndromes in animals and man. i," *Brain*, vol. 88, no. 2, pp. 237–94, 1965.

[47] P. Tremblay and A. S. Dick, "Broca and wernicke are dead, or moving past the classic model of language neurobiology," *Brain Lang*, vol. 162, pp. 60–71, 2016.

[48] D. A. Allport, "Distributed memory, modular subsystems, and dysphasia.," in *Current perspectives on dysphasia*, S. Newman and R. Epstein, Eds. New York: Churchill Livingstone, 1985, pp. 207–244.

[49] P. Indefrey and W. J. Levelt, "The spatial and temporal signatures of word production components," *Cognition*, vol. 92, no. 1-2, pp. 101–44, 2004.

[50] D. Poeppel, "The neuroanatomic and neurophysiological infrastructure for speech and language," *Curr Opin Neurobiol*, vol. 28, pp. 142–9, 2014.

[51] G. Hickok and D. Poeppel, "The cortical organization of speech processing," *Nat Rev Neurosci*, vol. 8, no. 5, pp. 393–402, 2007.

[52] C. Rorden and H. O. Karnath, "Using human brain lesions to infer function: A relic from a past era in the fmri age?" *Nat Rev Neurosci*, vol. 5, no. 10, pp. 813–9, 2004.

[53] E. Bates, S. M. Wilson, A. P. Saygin, F. Dick, M. I. Sereno, R. T. Knight, and N. F. Dronkers, "Voxel-based lesion-symptom mapping," *Nat Neurosci*, vol. 6, no. 5, pp. 448–50, 2003.

[54] Y. H. Mah, M. Husain, G. Rees, and P. Nachev, "Human brain lesion-deficit inference remapped," *Brain*, vol. 137, no. Pt 9, pp. 2522–31, 2014.

[55] Y. Zhang, D. Y. Kimberg, H. B. Coslett, M. F. Schwartz, and Z. Wang, "Multivariate lesion-symptom mapping using support vector regression," *Hum Brain Mapp*, vol. 35, no. 12, pp. 5861–76, 2014.

[56] D. T. Wade, R. L. Hewer, R. M. David, and P. M. Enderby, "Aphasia after stroke: Natural history and associated deficits," *J Neurol Neurosurg Psychiatry*, vol. 49, no. 1, pp. 11–6, 1986.

[57] S. E. Kohn and H. Goodglass, "Picture-naming in aphasia," *Brain Lang*, vol. 24, no. 2, pp. 266–83, 1985.

[58] K. Hilari, J. J. Needle, and K. L. Harrison, "What are the important factors in health-related quality of life for people with aphasia? a systematic review," *Arch Phys Med Rehabil*, vol. 93, no. 1 Suppl, S86–95, 2012.

[59] E. Gleichgerrcht, J. Fridriksson, and L. Bonilha, "Neuroanatomical foundations of naming impairments across different neurologic conditions," *Neurology*, vol. 85, no. 3, pp. 284–92, 2015.

[60] T. Ueno, S. Saito, T. T. Rogers, and M. A. Lambon Ralph, "Lichtheim 2: Synthesizing aphasia and the neural basis of language in a neurocomputational model of the dual dorsal-ventral language pathways," *Neuron*, vol. 72, no. 2, pp. 385–96, 2011.

[61] D. Mirman, Q. Chen, Y. Zhang, Z. Wang, O. K. Faseyitan, H. B. Coslett, and M. F. Schwartz, "Neural organization of spoken language revealed by lesion-symptom mapping," *Nat Commun*, vol. 6, p. 6762, 2015.

[62] M. F. Schwartz, O. Faseyitan, J. Kim, and H. B. Coslett, "The dorsal stream contribution to phonological retrieval in object naming," *Brain*, vol. 135, no. Pt 12, pp. 3799–814, 2012.

[63] M. F. Schwartz, D. Y. Kimberg, G. M. Walker, O. Faseyitan, A. Brecher, G. S. Dell, and H. B. Coslett, "Anterior temporal involvement in semantic word retrieval: Voxel-based lesion-symptom mapping evidence from aphasia," *Brain*, vol. 132, no. Pt 12, pp. 3411–27, 2009.

[64] D. P. Corina, B. C. Loudermilk, L. Detwiler, R. F. Martin, J. F. Brinkley, and G. Ojemann, "Analysis of naming errors during cortical stimulation mapping: Implications for models of language representation," *Brain Lang*, vol. 115, no. 2, pp. 101–12, 2010.

[65] Y. Zhang, D. Y. Kimberg, H. B. Coslett, M. F. Schwartz, and Z. Wang, "Multivariate lesion-symptom mapping using support vector regression," *Hum Brain Mapp*, vol. 35, no. 12, pp. 5861–76, 2014.

[66] M. Vigneau, V. Beaucousin, P. Y. Herve, H. Duffau, F. Crivello, O. Houde, B. Mazoyer, and N. Tzourio-Mazoyer, "Meta-analyzing left hemisphere language areas: Phonology, semantics, and sentence processing," *Neuroimage*, vol. 30, no. 4, pp. 1414–32, 2006.

[67] G. S. Dell, M. F. Schwartz, N. Nozari, O. Faseyitan, and H. Branch Coslett, "Voxel-based lesion-parameter mapping: Identifying the neural correlates of a computational model of word production," *Cognition*, vol. 128, no. 3, pp. 380–96, 2013.

[68] H. Duffau, "The anatomo-functional connectivity of language revisited. new insights provided by electrostimulation and tractography," *Neuropsychologia*, vol. 46, no. 4, pp. 927–34, 2008.

[69] C. Pierpaoli and P. J. Basser, "Toward a quantitative assessment of diffusion anisotropy," *Magn Reson Med*, vol. 36, no. 6, pp. 893–906, 1996.

[70] H. M. Feldman, J. D. Yeatman, E. S. Lee, L. H. Barde, and S. Gaman-Bean, "Diffusion tensor imaging: A review for pediatric researchers and clinicians," *J Dev Behav Pediatr*, vol. 31, no. 4, pp. 346–56, 2010.

[71] E. Fieremans, J. Jensen, J. Helpern, K. Sungheon, R. I. Grossman, M. Inglese, and D. Novikov, "Diffusion distinguishes between axonal loss and demyelination in brain white matter," in *International Society for Magnetic Resonance in Medicine (ISMRM)*.

[72] A. Kertesz, *The western aphasia battery - revised.* New York: Grune & Stratton, 2007.

[73] D. Howard and K. Patterson, *The pyramids and palm trees test: A test of semantic access from words and pictures*. London: Harcourt Assessment, 1992.

[74] A. Roach, M. F. Schwartz, N. Martin, R. Grewal, and A. Brecher, "The philadelphia naming test: Scoring and rationale," *Clinical Aphasiology*, vol. 24, pp. 121–133, 1996.

[75] G. R. Glenn, J. A. Helpern, A. Tabesh, and J. H. Jensen, "Optimization of white matter fiber tractography with diffusional kurtosis imaging," *NMR Biomed*, vol. 28, no. 10, pp. 1245–56, 2015.

[76] G. R. Glenn, L. W. Kuo, Y. P. Chao, C. Y. Lee, J. A. Helpern, and J. H. Jensen, "Mapping the orientation of white matter fiber bundles: A comparative study of diffusion tensor imaging, diffusional kurtosis imaging, and diffusion spectrum imaging," *AJNR Am J Neuroradiol*, vol. 37, no. 7, pp. 1216–22, 2016.

[77] T. E. Behrens, H. J. Berg, S. Jbabdi, M. F. Rushworth, and M. W. Woolrich, "Probabilistic diffusion tractography with multiple fibre orientations: What can we gain?" *Neuroimage*, vol. 34, no. 1, pp. 144–55, 2007.

[78] G. R. Glenn, J. H. Jensen, J. A. Helpern, M. V. Spampinato, R. Kuzniecky, S. S. Keller, and L. Bonilha, "Epilepsy-related cytoarchitectonic abnormalities along white matter pathways," *J Neurol Neurosurg Psychiatry*, vol. 87, no. 9, pp. 930–6, 2016.

[79] E. S. Hui, E. Fieremans, J. H. Jensen, A. Tabesh, W. Feng, L. Bonilha, M. V. Spampinato, R. Adams, and J. A. Helpern, "Stroke assessment with diffusional kurtosis imaging," *Stroke*, vol. 43, no. 11, pp. 2968–73, 2012.

[80] S. Van Cauter, J. Veraart, J. Sijbers, R. R. Peeters, U. Himmelreich, F. De Keyzer, S. W. Van Gool, F. Van Calenbergh, S. De Vleeschouwer, W. Van Hecke, and S. Sunaert, "Gliomas: Diffusion kurtosis mr imaging in grading," *Radiology*, vol. 263, no. 2, pp. 492–501, 2012.

[81] J. Zhuo, S. Xu, J. L. Proctor, R. J. Mullins, J. Z. Simon, G. Fiskum, and R. P. Gullapalli, "Diffusion kurtosis as an in vivo imaging marker for reactive astrogliosis in traumatic brain injury," *Neuroimage*, vol. 59, no. 1, pp. 467–77, 2012.

[82] L. Bonilha, C. Y. Lee, J. H. Jensen, A. Tabesh, M. V. Spampinato, J. C. Edwards, J. Breedlove, and J. A. Helpern, "Altered microstructure in temporal lobe epilepsy: A diffusional kurtosis imaging study," *AJNR Am J Neuroradiol*, vol. 36, no. 4, pp. 719–24, 2015.

[83] E. T. McKinnon, J. Fridriksson, G. R. Glenn, J. H. Jensen, J. A. Helpern, A. Basilakos, C. Rorden, A. Y. Shih, M. V. Spampinato, and L. Bonilha, "Structural plastic-

ity of the ventral stream and aphasia recovery," *Ann Neurol*, vol. 82, no. 1, pp. 147–151, 2017.

[84] A. Tabesh, J. H. Jensen, B. A. Ardekani, and J. A. Helpern, "Estimation of tensors and tensor-derived measures in diffusional kurtosis imaging," *Magn Reson Med*, vol. 65, no. 3, pp. 823–36, 2011.

[85] J. Veraart, D. S. Novikov, D. Christiaens, B. Ades-Aron, J. Sijbers, and E. Fieremans, "Denoising of diffusion mri using random matrix theory," *Neuroimage*, vol. 142, pp. 394–406, 2016.

[86] E. Kellner, B. Dhital, V. G. Kiselev, and M. Reisert, "Gibbs-ringing artifact removal based on local subvoxel-shifts," *Magn Reson Med*, vol. 76, no. 5, pp. 1574–1581, 2016.

[87] J. Veraart, E. Fieremans, I. O. Jelescu, F. Knoll, and D. S. Novikov, "Gibbs ringing in diffusion mri," *Magn Reson Med*, vol. 76, no. 1, pp. 301–14, 2016.

[88] M. Jenkinson, P. Bannister, M. Brady, and S. Smith, "Improved optimization for the robust and accurate linear registration and motion correction of brain images," *Neuroimage*, vol. 17, no. 2, pp. 825–41, 2002.

[89] S. Mori, S. Wakana, P. van Zijl, and L. Nagae-Poetscher, *Mri atlas of human white matter*. Amsterdam: Elsevier, 2005, vol. 1, p. 276.

[90] P. Nachev, E. Coulthard, H. R. Jager, C. Kennard, and M. Husain, "Enantiomorphic normalization of focally lesioned brains," *Neuroimage*, vol. 39, no. 3, pp. 1215–26, 2008.

[91] C. Rorden, L. Bonilha, J. Fridriksson, B. Bender, and H. O. Karnath, "Age-specific ct and mri templates for spatial normalization," *Neuroimage*, vol. 61, no. 4, pp. 957–65, 2012.

[92] E. T. McKinnon, J. A. Helpern, and J. H. Jensen, "Modeling white matter microstructure with fiber ball imaging," *Neuroimage*, vol. 176, pp. 11–21, 2018.

[93] J. Veraart, D. H. Poot, W. Van Hecke, I. Blockx, A. Van der Linden, M. Verhoye, and J. Sijbers, "More accurate estimation of diffusion tensor parameters using diffusion kurtosis imaging," *Magn Reson Med*, vol. 65, no. 1, pp. 138–45, 2011.

[94] J. D. Yeatman, R. F. Dougherty, N. J. Myall, B. A. Wandell, and H. M. Feldman, "Tract profiles of white matter properties: Automating fiber-tract quantification," *PLoS One*, vol. 7, no. 11, e49790, 2012.

[95] S. Wakana, A. Caprihan, M. M. Panzenboeck, J. H. Fallon, M. Perry, R. L. Gollub, K. Hua, J. Zhang, H. Jiang, P. Dubey, A. Blitz, P. van Zijl, and S. Mori, "Reproducibility of quantitative tractography methods applied to cerebral white matter," *Neuroimage*, vol. 36, no. 3, pp. 630–44, 2007.

[96] J. B. Colby, L. Soderberg, C. Lebel, I. D. Dinov, P. M. Thompson, and E. R. Sowell, "Along-tract statistics allow for enhanced tractography analysis," *Neuroimage*, vol. 59, no. 4, pp. 3227–42, 2012.

[97] I. Blank, N. Kanwisher, and E. Fedorenko, "A functional dissociation between language and multiple-demand systems revealed in patterns of bold signal fluctuations," *J Neurophysiol*, vol. 112, no. 5, pp. 1105–18, 2014.

[98] A. V. Faria, S. E. Joel, Y. Zhang, K. Oishi, P. C. van Zjil, M. I. Miller, J. J. Pekar, and S. Mori, "Atlas-based analysis of resting-state functional connectivity: Evaluation for reproducibility and multi-modal anatomy-function correlation studies," *Neuroimage*, vol. 61, no. 3, pp. 613–21, 2012.

[99] L. Cloutman, R. Gottesman, P. Chaudhry, C. Davis, J. T. Kleinman, M. Pawlak, E. H. Herskovits, V. Kannan, A. Lee, M. Newhart, J. Heidler-Gary, and A. E. Hillis, "Where (in the brain) do semantic errors come from?" *Cortex*, vol. 45, no. 5, pp. 641–9, 2009.

[100] M. Tochadse, A. D. Halai, M. A. Lambon Ralph, and S. Abel, "Unification of behavioural, computational and neural accounts of word production errors in post-stroke aphasia," *Neuroimage Clin*, vol. 18, pp. 952–962, 2018.

[101] D. Saur, B. W. Kreher, S. Schnell, D. Kummerer, P. Kellmeyer, M. S. Vry, R. Umarova, M. Musso, V. Glauche, S. Abel, W. Huber, M. Rijntjes, J. Hennig, and C. Weiller, "Ventral and dorsal pathways for language," *Proc Natl Acad Sci U S A*, vol. 105, no. 46, pp. 18 035–40, 2008.

[102] M. F. Schwartz, D. Y. Kimberg, G. M. Walker, A. Brecher, O. K. Faseyitan, G. S. Dell, D. Mirman, and H. B. Coslett, "Neuroanatomical dissociation for taxonomic and thematic knowledge in the human brain," *Proc Natl Acad Sci U S A*, vol. 108, no. 20, pp. 8520–4, 2011.

[103] M. Catani, R. J. Howard, S. Pajevic, and D. K. Jones, "Virtual in vivo interactive dissection of white matter fasciculi in the human brain," *Neuroimage*, vol. 17, no. 1, pp. 77–94, 2002.

[104] S. Mori and P. C. van Zijl, "Fiber tracking: Principles and strategies - a technical review," *NMR Biomed*, vol. 15, no. 7-8, pp. 468–80, 2002.

[105] G. Hickok, K. Okada, and J. T. Serences, "Area spt in the human planum temporale supports sensory-motor integration for speech processing," *J Neurophysiol*, vol. 101, no. 5, pp. 2725–32, 2009.

[106] K. Patterson and J. Morton, "A new attempt at an interpretation, or, an attempt at a new interpretation," in *Deep Dyslexia*, C. M., P. K., and M. JC., Eds. London: Routledge and Kegan Paul, 1980, ch. 91-118.

[107] A. D. Halai, A. M. Woollams, and M. A. Lambon Ralph, "Triangulation of language-cognitive impairments, naming errors and their neural bases post-stroke," *Neuroimage Clin*, vol. 17, pp. 465–473, 2018.

[108] A. L. Holland, D. S. Fromm, F. DeRuyter, and M. Stein, "Treatment efficacy: Aphasia," *J Speech Hear Res*, vol. 39, no. 5, S27–36, 1996.

[109] W. D. Heiss and A. Thiel, "A proposed regional hierarchy in recovery of post-stroke aphasia," *Brain Lang*, vol. 98, no. 1, pp. 118–23, 2006.

[110] G. Schlaug, S. Marchina, and A. Norton, "Evidence for plasticity in white-matter tracts of patients with chronic broca's aphasia undergoing intense intonation-based speech therapy," *Ann N Y Acad Sci*, vol. 1169, pp. 385–94, 2009.

[111] C. Y. Wan, X. Zheng, S. Marchina, A. Norton, and G. Schlaug, "Intensive therapy induces contralateral white matter changes in chronic stroke patients with broca's aphasia," *Brain Lang*, vol. 136, pp. 1–7, 2014.

[112] S. van Hees, K. McMahon, and A. Angwin, "Changes in white matter connectivity following therapy for anomia post stroke," *Neuro-rehabil Neural Repair*, vol. 28, pp. 325–334, 2014.

[113] J. H. Jensen and J. A. Helpern, "Mri quantification of non-gaussian water diffusion by kurtosis analysis," *NMR Biomed*, vol. 23, no. 7, pp. 698–710, 2010.

[114] F. Pulvermuller, B. Neininger, T. Elbert, B. Mohr, B. Rockstroh, P. Koebbel, and E. Taub, "Constraint-induced therapy of chronic aphasia after stroke," *Stroke*, vol. 32, no. 7, pp. 1621–6, 2001.

[115] G. M. Walker and M. F. Schwartz, "Short-form philadelphia naming test: Rationale and empirical evaluation," *Am J Speech Lang Pathol*, vol. 21, no. 2, S140–53, 2012.

[116] K. Hua, J. Zhang, S. Wakana, H. Jiang, X. Li, D. S. Reich, P. A. Calabresi, J. J. Pekar, P. C. van Zijl, and S. Mori, "Tract probability maps in stereotaxic spaces: Analyses of white matter anatomy and tract-specific quantification," *Neuroimage*, vol. 39, no. 1, pp. 336–47, 2008.

[117] J. Latt, M. Nilsson, R. Wirestam, F. Stahlberg, N. Karlsson, M. Johansson, P. C. Sundgren, and D. van Westen, "Regional values of diffusional kurtosis estimates in the healthy brain," *J Magn Reson Imaging*, vol. 37, no. 3, pp. 610–8, 2013.

[118] S. Umesh Rudrapatna, T. Wieloch, K. Beirup, K. Ruscher, W. Mol, P. Yanev, A. Leemans, A. van der Toorn, and R. M. Dijkhuizen, "Can diffusion kurtosis imaging improve the sensitivity and specificity of detecting microstructural alterations in brain tissue chronically after experimental stroke? comparisons with diffusion tensor imaging and histology," *Neuroimage*, vol. 97, pp. 363–73, 2014.

[119] A. W. Yang, J. H. Jensen, C. C. Hu, A. Tabesh, M. F. Falangola, and J. A. Helpern, "Effect of cerebral spinal fluid suppression for diffusional kurtosis imaging," *J Magn Reson Imaging*, vol. 37, no. 2, pp. 365–71, 2013.

[120] N. Dancause, S. Barbay, S. B. Frost, E. J. Plautz, D. Chen, E. V. Zoubina, A. M. Stowe, and R. J. Nudo, "Extensive cortical rewiring after brain injury," *J Neurosci*, vol. 25, no. 44, pp. 10 167–79, 2005.

[121] J. Wang, S. Marchina, A. C. Norton, C. Y. Wan, and G. Schlaug, "Predicting speech fluency and naming abilities in aphasic patients," *Front Hum Neurosci*, vol. 7, p. 831, 2013.

[122] S. J. Forkel, M. Thiebaut de Schotten, F. Dell'Acqua, L. Kalra, D. G. Murphy, S. C. Williams, and M. Catani, "Anatomical predictors of aphasia recovery: A tractography study of bilateral perisylvian language networks," *Brain*, vol. 137, no. Pt 7, pp. 2027–39, 2014.

[123] E. Panagiotaki, T. Schneider, B. Siow, M. G. Hall, M. F. Lythgoe, and D. C. Alexander, "Compartment models of the diffusion mr signal in brain white matter: A taxonomy and comparison," *Neuroimage*, vol. 59, no. 3, pp. 2241–54, 2012.

[124] T. Niendorf, R. M. Dijkhuizen, D. G. Norris, M. van Lookeren Campagne, and K. Nicolay, "Biexponential diffusion attenuation in various states of brain tissue: Implications for diffusion-weighted imaging," *Magn Reson Med*, vol. 36, no. 6, pp. 847–57, 1996.

[125] C. A. Clark, M. Hedehus, and M. E. Moseley, "In vivo mapping of the fast and slow diffusion tensors in human brain," *Magn Reson Med*, vol. 47, no. 4, pp. 623–8, 2002.

[126] S. E. Maier and R. V. Mulkern, "Biexponential analysis of diffusion-related signal decay in normal human cortical and deep gray matter," *Magn Reson Imaging*, vol. 26, no. 7, pp. 897–904, 2008.

[127] K. M. Bennett, K. M. Schmainda, R. T. Bennett, D. B. Rowe, H. Lu, and J. S. Hyde, "Characterization of continuously distributed cortical water diffusion rates with a stretched-exponential model," *Magn Reson Med*, vol. 50, no. 4, pp. 727–34, 2003.

[128] D. A. Yablonskiy, G. L. Bretthorst, and J. J. Ackerman, "Statistical model for diffusion attenuated mr signal," *Magn Reson Med*, vol. 50, no. 4, pp. 664–9, 2003.

[129] E. Kaden, F. Kruggel, and D. C. Alexander, "Quantitative mapping of the per-axon diffusion coefficients in brain white matter," *Magn Reson Med*, vol. 75, no. 4, pp. 1752–63, 2016.

[130] M. Eden, "Computer simulations in solidstate nmr. iii. powder averaging," *Concepts in Magnetic Resonance Part A*, no. 18, pp. 24–55, 2003.

[131] P. J. Basser and C. Pierpaoli, "A simplified method to measure the diffusion tensor from seven mr images," *Magn Reson Med*, vol. 39, no. 6, pp. 928–34, 1998.

[132] N. Shemesh, E. Ozarslan, M. E. Komlosh, P. J. Basser, and Y. Cohen, "From single-pulsed field gradient to double-pulsed field gradient mr: Gleaning new microstructural information and developing new forms of contrast in mri," *NMR Biomed*, vol. 23, no. 7, pp. 757–80, 2010.

[133] S. N. Jespersen, H. Lundell, C. K. Sonderby, and T. B. Dyrby, "Orientationally invariant metrics of apparent compartment eccentricity from double pulsed field gradient diffusion experiments," *NMR Biomed*, vol. 26, no. 12, pp. 1647–62, 2013.

[134] E. S. Hui, G. Russell Glenn, J. A. Helpern, and J. H. Jensen, "Kurtosis analysis of neural diffusion organization," *Neuroimage*, vol. 106, pp. 391–403, 2015.

[135] S. Lasic, F. Szczepankiewicz, S. Eriksson, M. Nilsson, and D. Topgaard, "Microanisotropy imaging: Quantification of microscopic diffusion anisotropy and orientational order parameter by diffusion mri with magic-angle spinning of the q-vector.," *Frontiers in Physics*, vol. 2, no. 11, 2014.

[136] J. A. McNab, B. L. Edlow, T. Witzel, S. Y. Huang, H. Bhat, K. Heberlein, T. Feiweier, K. Liu, B. Keil, J. Cohen-Adad, M. D. Tisdall, R. D. Folkerth, H. C. Kinney, and L. L. Wald, "The human connectome project and beyond: Initial applications of 300 mt/m gradients," *Neuroimage*, vol. 80, pp. 234–45, 2013.

[137] T. G. Reese, O. Heid, R. M. Weisskoff, and V. J. Wedeen, "Reduction of eddy-current-induced distortion in diffusion mri using a twice-refocused spin echo," *Magn Reson Med*, vol. 49, no. 1, pp. 177–82, 2003.

[138] D. K. Jones, M. A. Horsfield, and A. Simmons, "Optimal strategies for measuring diffusion in anisotropic systems by magnetic resonance imaging," *Magn Reson Med*, vol. 42, no. 3, pp. 515–25, 1999.

[139] E. Saff and A. Kuijlaars, "Distributing many points on a sphere.," *Math Intelligencer*, vol. 19, no. 1, pp. 5–11, 1997.

[140] B. Fischl, D. H. Salat, E. Busa, M. Albert, M. Dieterich, C. Haselgrove, A. van der Kouwe, R. Killiany, D. Kennedy, S. Klaveness, A. Montillo, N. Makris, B. Rosen, and A. M. Dale, "Whole brain segmentation: Automated labeling of neuroanatomical structures in the human brain," *Neuron*, vol. 33, no. 3, pp. 341–55, 2002.

[141] R. M. Henkelman, "Measurement of signal intensities in the presence of noise in mr images," *Med Phys*, vol. 12, no. 2, pp. 232–3, 1985.

[142] H. Gudbjartsson and S. Patz, "The rician distribution of noisy mri data," *Magn Reson Med*, vol. 34, no. 6, pp. 910–4, 1995.

[143] H. Young, *Statistical treatment of experimental data*. New York: McGraw-Hill, 1962.

[144] B. Keil, J. N. Blau, S. Biber, P. Hoecht, V. Tountcheva, K. Setsompop, C. Triantafyllou, and L. L. Wald, "A 64-channel 3t array coil for accelerated brain mri," *Magn Reson Med*, vol. 70, no. 1, pp. 248–58, 2013.

[145] K. Setsompop, R. Kimmlingen, E. Eberlein, T. Witzel, J. Cohen-Adad, J. A. McNab, B. Keil, M. D. Tisdall, P. Hoecht, P. Dietz, S. F. Cauley, V. Tountcheva, V. Matschl, V. H. Lenz, K. Heberlein, A. Potthast, H. Thein, J. Van Horn, A. Toga, F. Schmitt, D. Lehne, B. R. Rosen, V. Wedeen, and L. L. Wald, "Pushing the limits of in vivo diffusion mri for the human connectome project," *Neuroimage*, vol. 80, pp. 220–33, 2013.

[146] W. H. Press, S. Teukolsky, W. Vetterling, and B. Flannery, "Numerical recipes in c: The art of scientic computing," in. New York: Cambridge University Press, 1992, p. 305.

[147] O. Dietrich, J. G. Raya, S. B. Reeder, M. F. Reiser, and S. O. Schoenberg, "Measurement of signal-to-noise ratios in mr images: Influence of multichannel coils, parallel imaging, and reconstruction filters," *J Magn Reson Imaging*, vol. 26, no. 2, pp. 375–85, 2007.

[148] C. D. Kroenke, J. J. Ackerman, and D. A. Yablonskiy, "On the nature of the naa diffusion attenuated mr signal in the central nervous system," *Magn Reson Med*, vol. 52, no. 5, pp. 1052–9, 2004.

[149] I. O. Jelescu, J. Veraart, E. Fieremans, and D. S. Novikov, "Degeneracy in model parameter estimation for multi-compartmental diffusion in neuronal tissue," *NMR Biomed*, vol. 29, no. 1, pp. 33–47, 2016.

[150] M. Roding, D. Bernin, J. Jonasson, A. Sarkka, D. Topgaard, M. Rudemo, and M. Nyden, "The gamma distribution model for pulsed-field gradient nmr studies of molecular-weight distributions of polymers," *J Magn Reson*, vol. 222, pp. 105–11, 2012.

[151] F. Szczepankiewicz, S. Lasic, D. van Westen, P. C. Sundgren, E. Englund, C. F. Westin, F. Stahlberg, J. Latt, D. Topgaard, and M. Nilsson, "Quantification of microscopic diffusion anisotropy disentangles effects of orientation dispersion from microstructure: Applications in healthy volunteers and in brain tumors," *Neuroimage*, vol. 104, pp. 241–52, 2015.

[152] D. Le Bihan and H. Johansen-Berg, "Diffusion mri at 25: Exploring brain tissue structure and function," *Neuroimage*, vol. 61, pp. 324–341, 2012.

[153] D. Le Bihan and M. Iima, "Diffusion magnetic resonance imaging: What water tells us about biological tissues," *PloS Biol*, vol. 13, no. e1002203, 2015.

[154] D. C. Alexander, T. B. Dyrby, M. Nilsson, and H. Zhang, "Imaging brain microstructure with diffusion mri: Practicality and applications," *NMR Biomed*, vol. 32, no. 4, e3841, 2019.

[155] U. Ferizi, T. Schneider, E. Panagiotaki, G. Nedjati-Gilani, H. Zhang, C. A. Wheeler-Kingshott, and D. C. Alexander, "A ranking of diffusion mri compartment models with in vivo human brain data," *Magn Reson Med*, vol. 72, no. 6, pp. 1785–92, 2014.

[156] I. O. Jelescu and M. D. Budde, "Design and validation of diffusion mri models of white matter," *Front Phys*, vol. 28, 2017.

[157] M. Reisert, E. Kellner, B. Dhital, J. Hennig, and V. G. Kiselev, "Disentangling micro from mesostructure by diffusion mri: A bayesian approach," *Neuroimage*, vol. 147, pp. 964–975, 2017.

[158] R. L. Harms, F. J. Fritz, A. Tobisch, R. Goebel, and A. Roebroeck, "Robust and fast nonlinear optimization of diffusion mri microstructure models," *Neuroimage*, vol. 155, pp. 82–96, 2017.

[159] J. H. Jensen, E. T. McKinnon, G. R. Glenn, and J. A. Helpern, "Evaluating kurtosis-based diffusion mri tissue models for white matter with fiber ball imaging," *NMR Biomed*, vol. 30, no. 5, 2017.

[160] D. S. Tuch, "Q-ball imaging," *Magn Reson Med*, vol. 52, no. 6, pp. 1358–72, 2004.

[161] I. O. Jelescu, M. Zurek, K. V. Winters, J. Veraart, A. Rajaratnam, N. S. Kim, J. S. Babb, T. M. Shepherd, D. S. Novikov, S. G. Kim, and E. Fieremans, "In vivo quantification of demyelination and recovery using compartment-specific diffusion mri metrics validated by electron microscopy," *Neuroimage*, vol. 132, pp. 104–114, 2016.

[162] M. Nilsson, J. Latt, D. van Westen, S. Brockstedt, S. Lasic, F. Stahlberg, and D. Topgaard, "Noninvasive mapping of water diffusional exchange in the human brain using filter-exchange imaging," *Magn Reson Med*, vol. 69, no. 6, pp. 1573–81, 2013.

[163] A. L. MacKay and C. Laule, "Magnetic resonance of myelin water: An in vivo marker for myelin," *Brain Plast*, vol. 2, no. 1, pp. 71–91, 2016.

[164] T. E. Behrens, M. W. Woolrich, M. Jenkinson, H. Johansen-Berg, R. G. Nunes, S. Clare, P. M. Matthews, J. M. Brady, and S. M. Smith, "Characterization and propagation of uncertainty in diffusion-weighted mr imaging," *Magn Reson Med*, vol. 50, no. 5, pp. 1077–88, 2003.

[165] S. N. Jespersen, C. R. Bjarkam, J. R. Nyengaard, M. M. Chakravarty, B. Hansen, T. Vosegaard, L. Ostergaard, D. Yablonskiy, N. C. Nielsen, and P. Vestergaard-Poulsen, "Neurite density from magnetic resonance diffusion measurements at ultrahigh field: Comparison with light microscopy and electron microscopy," *Neuroimage*, vol. 49, no. 1, pp. 205–16, 2010.

[166] J. Veraart, D. S. Novikov, and E. Fieremans, "Te dependent diffusion imaging (teddi) distinguishes between compartmental t2 relaxation times," *Neuroimage*, vol. 182, pp. 360–369, 2018.

[167] J. Jackson, *Classical electrodynamics*, second ed. New York: Wiley, 1975.

[168] M. Holz, S. Heil, and A. Sacco, "Temperature-dependent self-diffusion coefficients of water and six selected molecular liquids for calibration in accurate 1h nmr pfg measurements.," *Phys. Chem. Chem. Phys.*, vol. 2, pp. 4740–4742, 2000.

[169] T. Bailey, M. Eastwood, R. Gover, and L. J. Mason, "Complex analysis and the funk transform," *J. Korean Math. Sociol.*, vol. 40, pp. 577–593, 2003.

[170] P. J. Basser and D. K. Jones, "Diffusion-tensor mri: Theory, experimental design and data analysis - a technical review," *NMR Biomed*, vol. 15, no. 7-8, pp. 456–67, 2002.

[171] B. Dhital, M. Reisert, E. Kellner, and V. G. Kiselev, "Intra-axonal diffusivity in brain white matter," *Neuroimage*, vol. 189, pp. 543–550, 2019.

[172] B. Dhital, E. Kellner, V. G. Kiselev, and M. Reisert, "The absence of restricted water pool in brain white matter," *Neuroimage*, vol. 182, pp. 398–406, 2018.

[173] S. N. Jespersen, J. L. Olesen, B. Hansen, and N. Shemesh, "Diffusion time dependence of microstructural parameters in fixed spinal cord," *Neuroimage*, vol. 182, pp. 329–342, 2018.

[174] D. Topgaard, "Multidimensional diffusion mri," *J Magn Reson*, vol. 275, pp. 98–113, 2017.

[175] C. F. Westin, H. Knutsson, O. Pasternak, F. Szczepankiewicz, E. Ozarslan, D. van Westen, C. Mattisson, M. Bogren, L. J. O'Donnell, M. Kubicki, D. Topgaard, and M. Nilsson, "Q-space trajectory imaging for multidimensional diffusion mri of the human brain," *Neuroimage*, vol. 135, pp. 345–62, 2016.

[176] M. D. Does, "Inferring brain tissue composition and microstructure via mr relaxometry," *Neuroimage*, vol. 182, pp. 136–148, 2018.

[177] M. D. Does and R. E. Snyder, "Multiexponential t2 relaxation in degenerating peripheral nerve," *Magn Reson Med*, vol. 35, no. 2, pp. 207–13, 1996.

[178] C. Beaulieu, F. R. Fenrich, and P. S. Allen, "Multicomponent water proton transverse relaxation and t2-discriminated water diffusion in myelinated and nonmyelinated nerve," *Magn Reson Imaging*, vol. 16, no. 10, pp. 1201–10, 1998.

[179] S. Peled, D. Cory, S. Raymond, D. Kirschner, and F. A. Jolesz, "Water diffusion, t2, and compartmentation in frog sciatic nerve.," *Magn. Reson. Med.*, vol. 42, pp. 911–918, 1999.

[180] M. D. Does and J. C. Gore, "Compartmental study of t(1) and t(2) in rat brain and trigeminal nerve in vivo," *Magn Reson Med*, vol. 47, no. 2, pp. 274–83, 2002.

[181] K. Wachowicz and R. E. Snyder, "Assignment of the t(2) components of amphibian peripheral nerve to their microanatomical compartments," *Magn Reson Med*, vol. 47, no. 2, pp. 239–45, 2002.

[182] A. MacKay, C. Laule, I. Vavasour, T. Bjarnason, S. Kolind, and B. Madler, "Insights into brain microstructure from the t2 distribution," *Magn Reson Imaging*, vol. 24, pp. 515–525, 2006.

[183] R. D. Dortch, G. A. Apker, W. M. Valentine, B. Lai, and M. D. Does, "Compartment-specific enhancement of white matter and nerve ex vivo using chromium," *Magn Reson Med*, vol. 64, no. 3, pp. 688–97, 2010.

[184] L. W. Kuo, J. H. Chen, V. J. Wedeen, and W. Y. Tseng, "Optimization of diffusion spectrum imaging and q-ball imaging on clinical mri system," *Neuroimage*, vol. 41, no. 1, pp. 7–18, 2008.

[185] T. J. Andrews, M. T. Osborne, and M. D. Does, "Diffusion of myelin water," *Magn Reson Med*, vol. 56, no. 2, pp. 381–5, 2006.

[186] J. L. R. Andersson and S. N. Sotiropoulos, "An integrated approach to correction for off-resonance effects and subject movement in diffusion mr imaging," *Neuroimage*, vol. 125, pp. 1063–1078, 2016.

[187] K. Oishi, K. Zilles, K. Amunts, A. Faria, H. Jiang, X. Li, K. Akhter, K. Hua, R. Woods, A. W. Toga, G. B. Pike, P. Rosa-Neto, A. Evans, J. Zhang, H. Huang, M. I. Miller, P. C. van Zijl, J. Mazziotta, and S. Mori, "Human brain white matter atlas: Identification and assignment of common anatomical structures in superficial white matter," *Neuroimage*, vol. 43, no. 3, pp. 447–57, 2008.

[188] B. Bender and U. Klose, "The in vivo influence of white matter fiber orientation towards b(0) on t2* in the human brain," *NMR Biomed*, vol. 23, no. 9, pp. 1071–6, 2010.

[189] P. Sati, A. C. Silva, P. van Gelderen, M. I. Gaitan, J. E. Wohler, S. Jacobson, J. H. Duyn, and D. S. Reich, "In vivo quantification of t(2) anisotropy in white matter fibers in marmoset monkeys," *Neuroimage*, vol. 59, no. 2, pp. 979–85, 2012.

[190] C. F. Westin, S. E. Maier, H. Mamata, A. Nabavi, F. A. Jolesz, and R. Kikinis, "Processing and visualization for diffusion tensor mri," *Med Image Anal*, vol. 6, no. 2, pp. 93–108, 2002.

[191] A. N. Dula, D. F. Gochberg, H. L. Valentine, W. M. Valentine, and M. D. Does, "Multiexponential t2, magnetization transfer, and quantitative histology in white matter tracts of rat spinal cord," *Magn Reson Med*, vol. 63, no. 4, pp. 902–9, 2010.

[192] K. D. Harkins, A. N. Dula, and M. D. Does, "Effect of intercompartmental water exchange on the apparent myelin water fraction in multiexponential t2 measurements of rat spinal cord," *Magn Reson Med*, vol. 67, no. 3, pp. 793–800, 2012.

[193] B. Lampinen, F. Szczepankiewicz, D. topgaard, O. Hansson, D. Van Westen, and M. Nilsson, "Constrained analysis of b-tensor encoding diffusion data with multiple echo times allows estimation of compartment-specific t2 relaxation times in white matter," in *In proceedings of the 26th Annual Meeting of ISMRM*, p. 5240.

[194] S. Tomasi, R. Caminiti, and G. M. Innocenti, "Areal differences in diameter and length of corticofugal projections," *Cereb Cortex*, vol. 22, no. 6, pp. 1463–72, 2012.

[195] R. Bartha, S. Michaeli, H. Merkle, G. Adriany, P. Andersen, W. Chen, K. Ugurbil, and M. Garwood, "In vivo 1h2o t2+ measurement in the human occipital lobe at 4t and 7t by carr-purcell mri: Detection of microscopic susceptibility contrast," *Magn Reson Med*, vol. 47, no. 4, pp. 742–50, 2002.

[196] B. Stefanovic, J. G. Sled, and G. B. Pike, "Quantitative t2 in the occipital lobe: The role of the cpmg refocusing rate," *J Magn Reson Imaging*, vol. 18, no. 3, pp. 302–9, 2003.

[197] C. A. Clark, M. Hedehus, and M. E. Moseley, "Diffusion time dependence of the apparent diffusion tensor in healthy human brain and white matter disease," *Magn Reson Med*, vol. 45, no. 6, pp. 1126–9, 2001.

[198] M. Nilsson, J. Latt, E. Nordh, R. Wirestam, F. Stahlberg, and S. Brockstedt, "On the effects of a varied diffusion time in vivo: Is the diffusion in white matter restricted?" *Magn Reson Imaging*, vol. 27, no. 2, pp. 176–87, 2009.

[199] J. H. Jensen and J. A. Helpern, "Characterizing intra-axonal water diffusion with direction-averaged triple diffusion encoding mri," *NMR Biomed*, vol. 31, no. 7, e3930, 2018.

[200] V. Vasilescu, E. Katona, V. Simplaceanu, and D. Demco, "Water compartments in the myelinated nerve. iii. pulsed nmr results," *Experientia*, vol. 34, no. 11, pp. 1443–4, 1978.

[201] D. S. Novikov, J. Veraart, I. O. Jelescu, and E. Fieremans, "Rotationally-invariant mapping of scalar and orientational metrics of neuronal microstructure with diffusion mri," *Neuroimage*, vol. 174, pp. 518–538, 2018.

[202] C. B. McArdle, C. J. Richardson, D. A. Nicholas, M. Mirfakhraee, C. K. Hayden, and E. G. Amparo, "Developmental features of the neonatal brain: Mr imaging. part i. gray-white matter differentiation and myelination," *Radiology*, vol. 162, no. 1 Pt 1, pp. 223–9, 1987.

[203] I. Jakovcevski, R. Filipovic, Z. Mo, S. Rakic, and N. Zecevic, "Oligodendrocyte development and the onset of myelination in the human fetal brain," *Front Neuroanat*, vol. 3, p. 5, 2009.

[204] G. R. Glenn, J. A. Helpern, A. Tabesh, and J. H. Jensen, "Quantitative assessment of diffusional kurtosis anisotropy," *NMR Biomed*, vol. 28, no. 4, pp. 448–59, 2015.